

Nanosystems in Ceramic Oxides
Created by Means of Ion Implantation



The research performed in this thesis was performed at the Department of Defects in Materials of the Interfaculty Reactor Institute, Delft University of Technology, Mekelweg 15, 2629 JB Delft, The Netherlands.

Nanosystems in Ceramic Oxides Created by Means of Ion Implantation

PROEFSCHRIFT

ter verkrijging van de graad van doctor
aan de Technische Universiteit Delft,
op gezag van de Rector Magnificus prof. dr. ir. J.T. Fokkema
voorzitter van het College voor Promoties
in het openbaar te verdedigen

op dinsdag 25 november 2003 om 13:00 uur

door

Marijn Arnout VAN HUIS

natuurkundig ingenieur
geboren te Managua, Nicaragua

Dit proefschrift is goedgekeurd door de promotoren:

Prof. dr. A. van Veen

Prof. dr. J.Th.M. de Hosson

Samenstelling promotiecommissie:

Rector Magnificus,	voorzitter
Prof. dr. A. van Veen,	Rijksuniversiteit Groningen, promotor
Prof. dr. J.Th.M. de Hosson,	Rijksuniversiteit Groningen, promotor
Prof. dr. H.W. Zandbergen,	Technische Universiteit Delft
Prof. dr. R.W. Grimes,	Imperial College, Verenigd Koninkrijk
Prof. dr. T. Hibma,	Rijksuniversiteit Groningen
Prof. dr. G.J. Kearley,	Technische Universiteit Delft
Dr. R. Fromknecht,	Forschungszentrum Karlsruhe, Duitsland

Published and distributed by: DUP Science

DUP Science is an imprint of
Delft University Press
P.O. Box 98
2600 MG Delft
The Netherlands
Telephone: +31 15 27 85 678
Telefax.: +31 15 27 85 706
Email: info@library.tudelft.nl

ISBN 90-407-2442-3

Keywords: nanoclusters, ion implantation, positron annihilation.

Copyright ©2003 by M.A. van Huis

All rights reserved. No part of the material protected by this copyright notice may be reproduced or utilised in any form or any means, electronic or mechanical, including photocopying, recording or by any information storage and retrieval system, without permission from the publisher: Delft University Press.

Printed in The Netherlands.

CONTENTS

CHAPTER 1. INTRODUCTION	1
1.1. CLUSTER SCIENCE AND NANOTECHNOLOGY	2
1.2. MGO AS AN EMBEDDING MATRIX	5
1.3. ION BEAM SYNTHESIS AND DEFECT EVOLUTION	7
CHAPTER 2. METHODS AND TECHNIQUES	11
2.1. ION IMPLANTATION	12
2.1.1. <i>Ion implanters</i>	12
2.1.2. <i>SRIM ion implantation code</i>	14
2.2. OPTICAL ABSORPTION SPECTROSCOPY (OAS)	15
2.3. RUTHERFORD BACKSCATTERING SPECTROMETRY AND CHANNELING (RBS-C)	16
2.4. NEUTRON DEPTH PROFILING (NDP)	16
2.5. X-RAY DIFFRACTION (XRD)	17
2.6. TRANSMISSION ELECTRON MICROSCOPY (TEM)	17
2.6.1. <i>Specimen preparation</i>	18
2.6.2. <i>Electron microscopes</i>	19
2.7. POSITRON BEAM ANALYSIS (PBA)	20
2.7.1. <i>Doppler Broadening (DB)</i>	22
2.7.2. <i>VEPFIT positron depth profiling code</i>	24
2.7.3. <i>Two-dimensional angular correlation of annihilation radiation (2D-ACAR)</i>	25
2.7.4. <i>Positron affinity and positron confinement</i>	26
CHAPTER 3. NOBLE GAS NANOCLUSTERS	31
3.1. VACANCY CLUSTERS AND HE BUBBLES IN MGO	32
3.1.1. <i>Introduction</i>	32
3.1.2. <i>CASCADE atomistic simulation code</i>	32
3.1.3. <i>Predicted vacancy cluster structures in MgO</i>	34
3.1.4. <i>Predicted He defect interactions in MgO</i>	36
3.1.5. <i>He desorption from bubbles in MgO</i>	41
3.1.6. <i>Conclusions</i>	42
3.2. FORMATION, GROWTH AND DISSOCIATION OF HE BUBBLES IN AL ₂ O ₃	43
3.2.1. <i>Introduction</i>	43
3.2.2. <i>Experimental</i>	44
3.2.3. <i>Defect evolution</i>	44
3.2.4. <i>XTEM results</i>	47
3.2.5. <i>He desorption from bubbles in Al₂O₃</i>	49
3.2.6. <i>Conclusions</i>	52

3.3. SOLID KR NANOCCLUSERS IN MGO	52
3.3.1. <i>Introduction</i>	52
3.3.2. <i>Experimental</i>	53
3.3.3. <i>Structural properties and defect evolution</i>	53
3.3.4. <i>Positron trapping in Kr nanoclusters</i>	63
3.3.5. <i>Formation of shallow nanovoids created by Kr ion irradiation damage</i>	67
3.3.6. <i>Conclusions</i>	71
CHAPTER 4. METAL NANOCCLUSERS	73
4.1. LI NANOCCLUSERS IN MGO	74
4.1.1. <i>Introduction</i>	74
4.1.2. <i>Positron confinement</i>	75
4.1.3. <i>Experimental</i>	78
4.1.4. <i>Positron beam analysis</i>	78
4.1.5. <i>Calculation of positron affinities</i>	86
4.1.6. <i>Positron trapping</i>	88
4.1.7. <i>Conclusions</i>	90
4.2. ZN NANOCCLUSERS IN MGO	91
4.2.1. <i>Introduction</i>	91
4.2.2. <i>Experimental</i>	91
4.2.3. <i>Results and discussion</i>	92
4.2.4. <i>Conclusions</i>	98
4.3. AU AND AG NANOCCLUSERS IN MGO	99
4.3.1. <i>Introduction</i>	99
4.3.2. <i>Experimental</i>	99
4.3.3. <i>Optical and structural properties</i>	100
4.3.4. <i>Discussion and conclusions</i>	104
4.4. IN-SITU AU NANOCCLUSTER NUCLEATION, GROWTH AND REFINEMENT IN MGO	105
4.4.1. <i>Introduction</i>	105
4.4.2. <i>Experimental</i>	106
4.4.3. <i>Results and discussion</i>	106
4.4.4. <i>Conclusions</i>	110
CHAPTER 5. SEMICONDUCTOR NANOCCLUSERS	111
5.1. INTRODUCTION	112
5.2. EXPERIMENTAL	112
5.3. FORMATION OF CDSE NANOCCLUSERS	112
5.4. CONCLUSIONS	118
CHAPTER 6. OUTLOOK: NANOPATTERNING USING E-BEAM LITHOGRAPHY	121
6.1. COMBINING E-BEAM LITHOGRAPHY WITH ION IRRADIATION	122
6.2. PRELIMINARY RESULTS	124
6.3. OUTLOOK	126

REFERENCES	127
SUMMARY	135
SAMENVATTING	139
LIST OF PUBLICATIONS	143
ACKNOWLEDGEMENTS	147
CURRICULUM VITAE	149

Chapter 1

Introduction

Cluster science offers the opportunity to tailor material properties to fit one's wishes. In the selection of materials for a design, the properties of materials are often considered to be fixed. These properties apply to bulk materials, which contain a large number of atoms (with a volume of more than 1 mm^3). However, when the number of atoms is reduced below a critical amount, the material properties can change dramatically. Examples are structural phase transformations, metal-insulator transitions, changing linear and non-linear optical properties, different melting temperatures and widening of the band gap of semiconductors [Ekardt 1999, Halperin 1986, Kreibig et al. 1995, Kamat et al. 1997, Alivisatos 1996a, Peng et al. 2000]. Most changes occur below a number of atoms of approximately 10,000. These small quantities of material are called clusters (in the literature, other names are used as well, partly depending on the formation process: zero-dimensional materials, nanocrystallites, precipitates, nanoparticles, colloids). When these clusters are used in nanotechnological devices, the material properties of the cluster materials can be tailored (within certain limits) by selecting the size of the clusters. In order to stabilise the crystallographic and electronic properties of the nanoclusters and to prevent them from agglomerating, nanoclusters are often embedded in solutions or solid matrices. Ion implantation of the cluster atoms into solid target materials is a convenient way to achieve embedded nanoclusters [White et al. 1989]. In general, additional post-implantation treatment (thermal annealing, laser exposure, ion irradiation) is necessary in order to induce clustering of the implanted atoms. In this study, all clusters were created by means of ion implantation and, mainly, large clusters in the nanometer size range (1 to 10 nm) are investigated. At an atomic density of typically $10^{29} \text{ atoms m}^{-3}$, these clusters contain some 100 to 10,000 atoms. In this thesis the focus is both on the creation of the nanoclusters by ion implantation and subsequent thermal annealing, and on the study of the material properties of these nanoclusters.

1.1. Cluster science and nanotechnology

In cluster science, a distinction is made between intrinsic and extrinsic size effects. Intrinsic size effects occur only because of the reduction in the number of atoms that comprises the nanocluster, while extrinsic size effects exist because of interaction with the environment. The difference becomes clear when comparing the properties of free nanoclusters (in vacuum) with embedded nanoclusters of the same size. The properties and possible applications of nanoclusters vary widely and here only very general properties of gas, metal and semiconductor nanoclusters will be discussed. More detailed information can be found in the references and in the introductions to Chapters 3 to 5.

Gas nanoclusters

Gas nanoclusters are usually referred to as bubbles, and vacancy nanoclusters as cavities or nanovoids. The behaviour of gas atoms, gas bubbles and nanovoids in materials is often of technological interest. For example, gas atoms are used to create empty voids in Si wafers, which act as gettering centres to impurities in order to make the remainder of the Si more chemically pure [Myers et al. 1994, Zhang et al. 1999a]. The process of creating nanovoids in Si by He ion implantation and subsequent thermal annealing was developed in the 1980s by the Defects in Materials group at the Interfaculty Reactor Institute [Griffioen et al. 1987, Van Veen 1991]. Recently, much attention is also given to gas ion implantation in ceramics. The behaviour of He atoms in ceramic oxides such as MgO, Al₂O₃ and MgAl₂O₄ is of major importance. These materials are candidates for serving as an embedding matrix for the transmutation of actinides [Cocuaud et al. 1997] and must be able to resist long irradiations with α particles, which end up as He atoms.

Metal nanoclusters

After gas ion implantation effects in Si, embedded metal nanoclusters receive most commercial attention. For example, computer and telecommunication companies are investigating the nanocluster system Cu in MgO because of the linear and non-linear optical properties that are of interest for use in optical computer components. Metal nanoclusters give rise to optical absorption bands due to Mie surface plasmon resonance [Kreibig et al. 1995] and show strong nonlinear optical features. A material is said to be optically nonlinear when the response of a material to an applied optical field depends on the strength of that optical field [Boyd 2003a]. In practice, only laser light is sufficiently intense to render non-linear optical properties significant. One of the consequences of nonlinearity is the generation of light beams with frequencies different from the frequencies of the input beams. The difference between linear and nonlinear systems is schematically shown in Fig. 1.1.

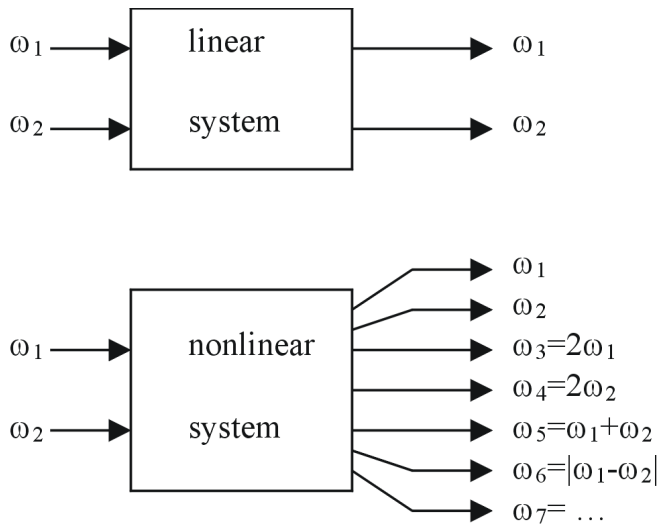


Fig. 1.1. Schematic representation of the frequency response of linear and nonlinear optical systems.

The frequency $\omega_5 = \omega_1 + \omega_2$ corresponds to sum frequency generation (SFG) while the frequency $\omega_6 = |\omega_1 - \omega_2|$ corresponds to difference frequency generation (DFG). If ω_1 is a fixed frequency generated by a laser and ω_2 a tuneable frequency generated by a second laser, then the frequency spectrum of the tuneable laser can be shifted by an amount ω_1 . In this way, the laser system can be operated at frequencies that cannot be reached using the tuneable laser alone. Theoretically, the nonlinear optical response of materials can be expressed in terms of the dependence of the polarisation \mathbf{P} (dipole moment per unit volume) on the electric field \mathbf{E} . For a lossless and dispersionless linear system,

$$\mathbf{P} = \epsilon_0 \chi^{(1)} \mathbf{E}. \quad (1.1)$$

Here \mathbf{P} is the polarisation (Cm^{-2}), \mathbf{E} is the electric field (Vm^{-1}), ϵ_0 is the free-space permittivity ($= 8.85 \times 10^{-12} \text{ F m}^{-1}$), and $\chi^{(1)}$ is the linear susceptibility (dimensionless). \mathbf{P} and \mathbf{E} are vectors, while χ is a tensor. For a nonlinear optical system [Boyd 2003a],

$$\mathbf{P} = \epsilon_0 \{ \chi^{(1)} \mathbf{E} + \chi^{(2)} \mathbf{E} \mathbf{E} + \chi^{(3)} \mathbf{E} \mathbf{E} \mathbf{E} + \dots \} \quad (1.2)$$

where $\chi^{(2)}$ is the second-order nonlinear susceptibility (mV^{-1}), $\chi^{(3)}$ is the third-order nonlinear susceptibility ($\text{m}^2 \text{V}^{-2}$), etc.. Particularly $\chi^{(3)}$ is very strong for metal and semiconductor clusters embedded in glasses [Boyd 2003b, Chakraborty 1998]. For Sn, Ag and Au nanoclusters in silica glass, $\chi^{(3)}$ can be as high as $10 \text{ m}^2 \text{V}^{-2}$, which is 4 orders of magnitude larger than for bulk metals where $\chi^{(3)} \sim 10^{-3} \text{ m}^2 \text{V}^{-2}$ (please note that here, SI units rather than esu (electrostatic units) are used). Materials with strong third-order susceptibility also have a refractive index and absorption coefficient that are dependent on the intensity of the light beam, offering possibilities for optical switching [Chakraborty 1998]. One application based

on these features is a pulse sorter that can differentiate and separate optical pulses of different intensity. Another field of application where metal nanoclusters are used is in the development of memory devices. Si, Ge and Au nanoclusters embedded in SiO₂ are under study for use as non-volatile memory units by electrical charging and discharging of individual clusters [Boer et al. 2001, Thees et al. 2000, Tiwari et al. 1996].

Semiconductor nanoclusters

Most of the recent scientific attention is dedicated to semiconductor nanoclusters [Kamat et al. 1997]. Complicated semiconductor nanosystems such as multi-layer quantum dots have often been the cover stories of top-ranking physics journals. In these systems, single electron hopping can be observed, which provides an opportunity for developing ‘single electron switches’. The electronic properties of semiconductor nanoclusters change already at quite large cluster sizes of ~10 nm [White et al. 1998, Alivisatos 1996a, Alivisatos 1996b, Peng et al. 2000] in comparison to metal nanoclusters. Bulk materials have electronic bands filled with electronic states, while single atoms have non-overlapping, discrete energy levels. Of course, there is a certain range in between these extremes where the density of electronic states is large but still cannot be considered a continuum. As the cluster size is reduced, the discretisation of energy levels begins at the (top and bottom) edges of the electronic energy bands, as shown in Fig. 1.2 [Alivisatos 1996b]. In the case of metal nanoclusters, this does not greatly affect the conduction electrons since they are positioned around the Fermi level, which is in the middle of an energy band. However, in semiconductors the discretisation of energy levels at the top of the valence band and at the bottom of the conduction band directly affects the band gap and the energy levels of (intrinsic) charge carriers. One of the best-investigated features of semiconductor nanoclusters is the widening of the band gap with decreasing nanocluster size. For example, the band gap of the semiconductor CdSe can change from 1.8 eV for bulk CdSe to 2.5 eV for CdSe clusters with a size of 2 nm. Also, the melting temperature of semiconductor nanoclusters is often lower than the melting temperature of the bulk material [Goldstein et al. 1992, Kamat et al. 1997]. Materials containing semiconductor nanoclusters also exhibit non-linear optical properties, similar to embedded metal nanoclusters as discussed above [Boyd 2003a, Chakraborty 1998].

Well-established techniques such as X-ray diffraction and transmission electron microscopy have been employed to characterise the nanoclusters. A special aspect of this work is the use of positron annihilation techniques as a complementary method for investigating embedded nanoclusters. When the positron affinity of the nanocluster material is lower than the positron affinity of the embedding material, the vast majority of the positrons implanted in the composite become trapped in the embedded nanoclusters, thereby becoming a self-seeking probe for nanocluster material.

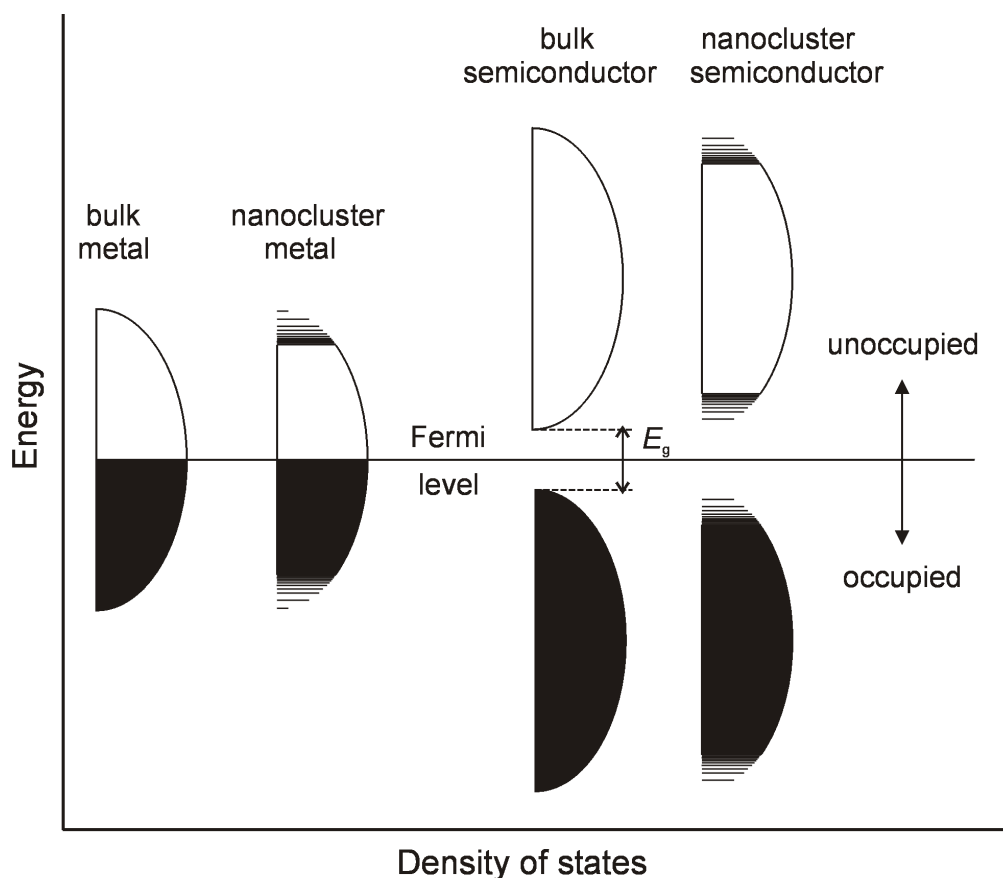


Fig. 1.2. Schematic diagram showing the discretisation of electronic bands in nanoclusters composed of metals and of semiconductors. The discretisation of the electronic states in semiconductors leads to a widening of the band gap.

When a positron technique such as two-dimensional angular correlation of annihilation radiation (2D-ACAR) is used, the positrons reveal the electronic structure of the nanoclusters, which is very interesting when the structural and electronic properties of the nanocluster begin to change. The three-dimensional spatial confinement of the positron wavefunction in the nanoclusters is called *positron confinement*. This phenomenon is explained in Section 2.7.4. Host-nanocluster systems investigated very successfully are Li in MgO [Van Huis et al. 2002, Falub et al. 2002] and Cu in Fe [Nagai et al. 2000, Nagai et al. 2001]. Both these systems are examples of structural phase transformations (an extrinsic size effect): here the Li and Cu nanoclusters adopt the unusual fcc Li and bcc Cu structures, respectively, in order to be more coherent with the host matrices.

1.2. MgO as an embedding matrix

One feature of nanoclusters is the large fraction of surface atoms. The first few atomic layers at the outside of free nanoclusters will have other properties than the interior of the

nanoclusters (due to surface reconstruction, presence of defects, different electronic configuration, presence of other charge carriers). In general, this inhomogeneity is not desirable from the point of view of applications. One way to prevent surface effects is to passivate the nanocluster surface by embedding the nanoclusters in hosts with a large band gap and similar structural properties. MgO has a high melting temperature (> 3000 K) and a large electronic band gap of 7.8 eV. Amongst the crystalline ceramic oxides used as an embedding matrix, MgO is probably the easiest material to work with because of its very simple and symmetric crystal structure (rock-salt, see Fig. 1.3). Furthermore, it is optically transparent so that the optical properties of the nanoclusters can still be investigated. The most important material properties of MgO are listed in Table 1.1. One feature that has to be considered when conducting optical studies, is the intrinsic and extrinsic optical absorption centres that appear after ion implantation in MgO. Most common are the F^+ and F centres (O monovacancies, which have trapped one or two electrons, respectively) and V^- and V^0 centres (Mg monovacancies, which have trapped one or two holes, respectively). Here it should be noted that O monovacancies are positively charged (because of the absence of a negative ion), while Mg monovacancies are negatively charged (because of the absence of a positive ion). The most important absorption centres are listed in Table 1.2 with their absorption energies and corresponding wavelengths.

Table 1.1. Material properties of MgO.

Property			Reference
Chemical composition		50% Mg, 50% O	
Specific gravity	ρ_{sp}	$3.58 \times 10^3 \text{ kg m}^{-3}$	[Handbook 1986]
Melting point	T_m	3125 K	[Handbook 1986]
Boiling point	T_b	3900 K	[Handbook 1986]
Crystal structure		rock-salt	[JCPDS]
Lattice parameter	a_0	4.213 Å	[JCPDS]
Atomic density		$1.07 \times 10^{29} \text{ atoms m}^{-3}$	
Impurity level		< 50 ppm (mainly Si)	
Young Modulus	E	317 GPa	[Munz et al. 1999]
Linear thermal expansion coefficient	a_{lin}	$12 \times 10^{-6} \text{ K}^{-1}$	[Wengeler et al. 1981]
Poisson ratio	ν	0.17	[Munz et al. 1999]
Electrical resistivity at $T=300$ K	ρ_{el}	$10^{14} \Omega \text{ cm}$	[Munz et al. 1999]
Band gap	E_g	7.83 eV	[Whited et al. 1973]
Electron work function	ϕ	3.8 eV	[Namba et al. 1984]
Surface energy	$\gamma_{\{100\}}$	1.25 J m^{-2}	[Watson et al. 1996]
Index of refraction	n	1.736	[Handbook 1986]

Table 1.2. Optical absorption centres in MgO. Values are obtained from Kotomin et al. (1997) and from Las et al. (1984). The wavelengths have been calculated from the absorption energies.

Centre	Description	Wavelength (nm)	Energy (eV)
F	O vacancy (V_O) with 2 trapped electrons	250	5.0
F ⁺	O vacancy (V_O) with 1 trapped electron	255	4.9
F ₂	dimer of F centres	347	3.6
F ₂ ²⁺	dimer of F ⁺ centres	329	3.8
V ⁰	Mg vacancy (V_{Mg}) with 2 trapped holes	568	2.2
V ⁻	Mg vacancy (V_{Mg}) with 1 trapped hole	543	2.3
Fe ³⁺	substitutional impurity on Mg site	284	4.4

1.3. Ion beam synthesis and defect evolution

Nowadays, ion implantation is a standard technique in science and commercial technology. Excellent reviews on radiation effects in ceramics have been written by H. Matzke (1982), J.H. Crawford, Jr. (1984), L.W. Hobbs et al. (1994) and S.J. Zinkle et al. (1997). The Defects in Materials group at the Interfaculty Reactor Institute has followed the history of ion implantation. At first, the focus was mainly on radiation damage in nuclear reactor environments. Much attention was thus given to ion radiation effects in metals [Van der Kolk et al. 1986, Van Veen 1991]. In the 1990s, research for the semiconductor industry became more important than research for the nuclear industry. The focus shifted to semiconductor targets: smart-cut of Si wafers by H ion implantation, creation of buried oxide layers (BOX) by oxygen ion implantation into Si wafers, doping of intrinsic semiconductors by ion implantation of dopant atoms (e.g., B and P doping of Si). Also the generation of nanovoids by means of He ion implantation and impurity gettering in these nanovoids was extensively investigated [Griffioen et al. 1987, Van Veen 1991, Myers et al. 1994]. Finally, there has been a dramatic growth in research in the field of ion implantation into ceramics during the last five years. The embedded metal and semiconductor nanoclusters created by means of ion implantation and subsequent annealing exhibit very interesting structural, electronic, magnetic and optical properties.

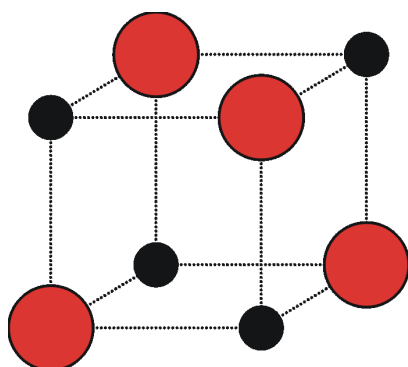


Fig. 1.3. The rock-salt structure of MgO. The large atoms represent the O atoms, the small atoms the Mg atoms.

Ion implantation machines are produced commercially and sold in a large variety. In general, such a machine consists of an ion source (gas, evaporation or sputtering), an accelerator section and a mass-selection analyser magnet. When an energetic ion hits the target material, it is stripped of most of its electrons. The large electronic charge results in a very strong Coulombic interaction with the target material. Therefore, when the energy of the implanted ion is still high, the ion loses energy mostly by creation of electron-hole pairs in the target material. This is called electronic stopping with linear energy loss $(dE/dx)_{el}$. When the kinetic energy of the ion decreases, the electron shells are (partly) refilled with electrons, and the cross-section for nuclear collisions with target atoms becomes more important. The ion loses energy by displacing target atoms from their lattice sites, i.e., by creating vacancy-interstitial (IV) pairs, also called Frenkel defects. A certain minimum energy is required to displace a target atom from its position. This is called the threshold displacement energy, E_d , and is about 55 eV for the Mg as well as the O atoms in MgO [Zinkle et al. 1997]. The threshold displacement energy is often a factor of 3-5 larger than the formation energy of a Frenkel defect. The reason for this paradox is that ion implantation is a physical situation during which thermal equilibrium is not established at all, so that entities defined under the condition of thermal equilibrium (such as the formation energy of Frenkel defects) cannot be used. The formation energy does not include the energy that gets lost to phonon excitations when the defect is created in a dynamical way. Stopping by displacement of target atoms is called nuclear stopping with linear energy loss $(dE/dx)_{nucl}$, and the total energy loss is the sum of the electronic and nuclear losses:

$$\left(\frac{dE}{dx}\right)_{total} = \left(\frac{dE}{dx}\right)_{el} + \left(\frac{dE}{dx}\right)_{nucl} . \quad (1.3)$$

Which of the two contributions is more important depends mainly on the ion species, the type of target atoms and the energy of the ion at a certain moment during the stopping. The stopping cross-sections are documented in the literature and implemented in the SRIM code, which will be discussed in Section 2.1. The displaced target atoms themselves are often energetic enough to create secondary ionisations and target displacements. On the path of the ion through the solid, a track is created of primary and secondary displacements. The total of primary and secondary tracks is called the *displacement cascade*. The average total number (primary and secondary) of displaced target atoms per ion is called the number of *displacements per ion* (dpi). In general, it is more relevant to consider the number of *displacements per target atom* (dpa level). Although the ion implantation dose is usually given in ions cm^{-2} and is in the order of 10^{16} - 10^{17} , it is better to consider the concentration of implanted species in the target material, usually expressed in at. % (or in mol.% if one means per MgO molecule). Unless specified otherwise, the concentration in at. % refers to the peak of the depth distribution of implanted atoms.

As mentioned previously, nuclear stopping results in the creation of many vacancy-interstitial pairs. However, not all of the Frenkel defects survive. Because of recombination, only 10-40% of the Frenkel pairs survive in MgO even at cryogenic temperatures [Zinkle et al. 1997]. Thus, if the implantation is carried out at room temperature, even fewer IV pairs will survive. Another process (other than recombination) that occurs is the migration of interstitials to the surface of the sample, resulting in the creation of Schottky defects (vacancies remain in the bulk, interstitials are added at the surface). This happens because the interstitials in MgO are mobile at room temperature while the monovacancies are not [Zinkle et al. 1997, Kotomin et al. 1998]. Of course, other defects are created as well, such as interstitial clusters, vacancy clusters and dislocation loops. Usually an annealing procedure is performed after ion implantation in order to grow nanoclusters from the implanted species and to get rid of part of the implantation damage in the MgO matrix. During the annealing procedure, the smallest defects dissociate and/or agglomerate into larger defects (clusters, platelets, dislocation loops). Principally, two processes are discussed in the literature to describe the growth of nanoclusters: Ostwald ripening and migration coalescence. During Ostwald ripening, the clusters are not very mobile and there is a concentration of dissolved defect species in the embedding matrix between the clusters (extrinsic atoms in the case of nanoclusters, vacancies in the case of nanovoids). These point defects can leave clusters but also segregate at (other) clusters, thereby enabling both growth and shrinkage of clusters [Bonafos et al. 2001, Claverie et al. 2002]. Migration coalescence means that the clusters themselves are moving (for example by interface diffusion), and two clusters combine into one when they are within a certain range [Birtcher et al. 1999]. In general, the defects grow when the annealing time and the annealing temperature increase. However, upon reaching certain temperatures, defects begin to shrink and eventually dissociate. For example, nanoclusters consisting of a certain chemical element will probably dissociate when the system is annealed at the temperature corresponding to the solution energy of that element in the host matrix. Nanovoids will dissociate when the temperature is high enough to create monovacancies or self-interstitials in the matrix, so that the nanovoids can be filled with atoms that (effectively) are taken from the surface of the sample.

In the following chapter, most of the experimental methods and techniques employed in this work are explained. Chapters 3 to 5 are organised according to the nature of the implanted species. Gas nanoclusters (He, Kr) and nanocavities are discussed in Chapter 3, metal nanoclusters (Li, Zn, Ag, Au) in Chapter 4, while in Chapter 5 an example is presented of a composite semiconductor nanocluster in MgO (CdSe). Finally, in Chapter 6 the first results are presented of an ambitious project to create monodispersed nanoclusters in a controlled geometry by combining e-beam lithography techniques with ion beam irradiation.

Chapter 2

Methods and techniques

In this chapter, the principal experimental techniques employed in this study are addressed. For well-established techniques such as X-ray diffraction and electron microscopy, only the specifications of the machines are given. Other experimental methods such as ion implantation and neutron depth profiling are described in more detail. The positron annihilation techniques and the concepts of positron affinity and positron confinement are discussed extensively.

2.1. Ion implantation

From the title of this thesis it is obvious that ion implantation is of major importance to this work. Nowadays, ion implantation is a standard technique in the nuclear field and in semiconductor industry; an introduction to ion implantation and defect evolution can be found in Section 1.3.

2.1.1. Ion implanters

Various ion implanters were used to create nanoclusters. Table 2.1 gives an overview of these machines. Ion implanters consist of three sections: the source section, the transport and beam tuning section and a target section. In the source, ions are created by bombarding gaseous atoms or molecules with energetic electrons. In this way, a plasma is created which is confined by means of magnetic fields. Ions are extracted from the plasma using an electric field (~30 kV) and enter the transport section. Here the ion beam passes a mass-selection analyser magnet for isotope selection, and is subsequently further accelerated (or decelerated) to the required energy. By means of deflection plates and quadrupole magnets, a homogeneous beam is created that impinges on the target, which is mounted in the target section. The ion current on the target is measured using sensitive current meters. The ion flux is then calculated from the current and the exposed area. To implant a dose of 10^{16} ions cm^{-2} takes about one hour, so that the dose rate is in the order of 10^{12} ions $\text{s}^{-1}\text{cm}^{-2}$. The actual dose rate strongly depends on the isotope to be implanted. It is dependent on the ionisation energy of the ions to be implanted, the abundance of the isotopes of a chemical element, and the stability of the plasma in the ion source.

Table 2.1. Properties of ion implantation systems used in this work. See Section 2.1 for discussion and the meaning of abbreviations. The maximal inhomogeneity is the maximal variation in the planar concentration of implanted ions over the implanted area. The values given for the inaccuracy of the total dose and for the maximal inhomogeneity are estimates.

System	University/ Institute	Max. acceleration voltage	Implanted ion species	Dose inaccuracy, max. inhomogeneity
DANFYSIK 911	TU Delft, Netherlands	30 kV	H, D, ^3He , ^4He , Li, B, Si, Ar, Au	30%
VARIAN 350D	TU Delft, Netherlands	140 kV	H, D, ^4He , Zn, Ne, Ar, Kr, Se, Cd, Xe	10%
DANFYSIK	FZK, Germany	260 kV	Xe, Au	25%
NEC (IVEM- TANDEM)	ANL, IL, USA	600 kV	O, Zn, Kr, Cd, Xe, Au	20%
TANDEM	AAMURI, AL, USA.	2.0 MV	Ag, Au	20%

In general, it is very easy to create a plasma containing ionised gas atoms, but metals require more effort. Metals (or materials like Si) have to be evaporated in a furnace and a carrier gas (usually Ar) is required for stabilisation of the ion plasma. Sputtering sources are sometimes also used to implant elements that cannot be evaporated, but in this work only evaporation ion sources were used.

At the Interfaculty Reactor Institute (IRI) in Delft, two ion implanters were employed. The DANFYSIK 911 ion implanter has a maximum acceleration voltage of 30 kV. It was mainly used for ^3He and Li ion implantations. Most other implantations were performed with a VARIAN 350D commercial ion implanter with a maximum operating voltage of 140 kV, see Fig. 2.1. Sometimes, multiply ionised ions were used to achieve larger effective acceleration energies (e.g., Kr^{2+} ions to generate Kr ions with a kinetic energy of 280 keV). The 600 keV Ag and 1 MeV Au ion implantations described in Chapter 4 were performed with a 2 MV Tandem accelerator at the Center for Irradiation of Materials at the Alabama A&M University Research Institute (AAMURI), Normal, AL, USA. The Au nanoclusters discussed in Chapter 6 were created using the 260 kV DANFYSIK ion implanter at the Institut für Festkörperphysik at the Forschungszentrum Karlsruhe (Germany). Finally, a number of experiments were performed using the IVEM-TANDEM facility at Argonne National Laboratory (ANL), Argonne, IL, USA. This set-up consists of a Hitachi H-9000 transmission electron microscope (TEM) operating at 300 kV, coupled to a NEC ion implanter with a maximum acceleration energy of 600 keV. See Section 2.6 for details.



Fig. 2.1. Varian 350D ion implanter

All implanters can expose an area of typically 1 cm^2 . Only the VARIAN machine in Delft can expose very large areas ($\sim 80 \text{ cm}^2$) since it was developed for the semiconductor industry where large Si wafers (with a diameter of 4" or larger) are the standard. Because of its design for commercial use, the VARIAN is also very easy to operate. The large exposure area and sophisticated control mechanisms result in a very good dose homogeneity over the implanted area (the maximum variation of the dose over the implanted area is 5-10 %). Of course, the homogeneity also depends on the settings of the machine. If the cross-sectional area of the beam is much larger than the area to be implanted, the homogeneity should be good. In all other machines, the homogeneity is worse and the ion dose per unit area at the edges of the implanted area can be 20% less than at the centre of the implanted area. The only disadvantages of the VARIAN are the high consumption rate of source material (e.g., ^3He is expensive) and the fact that its analyser magnet is not strong enough to implant heavy elements like Xe and Au (although multiply ionised heavy elements such as Xe^{2+} and Au^{2+} can be implanted). The DANFYSIK 911 ion implanter in Delft has a high efficiency for source material (smaller implanted area) and has a magnet that can select the heaviest elements. However, its ion source is very unstable, the maximum acceleration voltage can (for most experiments and applications) only be used for light elements, and the homogeneity and dose accuracy are mediocre. For all ion implanters it can be said that the inaccuracy of the total implanted dose is approximately 20%. Although a Faraday cup is used to take into account the effect of secondary electron emission, it is observed by means of neutron depth profiling (NDP, see Section 2.4) that the concentration of implanted ^3He and ^6Li atoms per unit area deviates from the dose settings of the ion implanters to this extent.

2.1.2. SRIM ion implantation code

The SRIM ion implantation code was developed by Ziegler et al. [Ziegler et al. 1985]. It is a Monte Carlo code that predicts the stopping and range of ions in matter (SRIM). The heart of the code is the description of binary collision events. Recent extensions include the description of collision cascades in compound materials. Distributions are obtained of the implantation depths of the ions, the displacements created by nuclear stopping, and the energy deposited in the target due to electronic stopping. With some simple calculations the ion depth distribution can be translated into the atomic density of the implanted element, and vacancy distributions can be translated into dpa levels (displacements per atom). Important input parameters are the ion species and the acceleration energy, the composition and density of the target and the threshold displacement energy of every element in the target. The threshold displacement energy E_d is the minimum energy required to displace a target atom from its position. This entity is not equal to the formation energy of a Frenkel defect (E_d is typically a factor of 5 higher) since the system is not in thermal equilibrium during ion implantation. Much work has been done on the determination of the displacement energies in ceramic oxides, and nowadays most of these displacement energies are known [Pells 1982, Matzke

1982, Crawford, Jr. 1984, Hobbs et al. 1994 and Zinkle et al. 1997]. The SRIM code assumes a random and homogeneous distribution of atoms in the material, so effects like channelling are not taken into account. Furthermore, processes such as recombination, migration, diffusion and annealing (keeping samples at room temperature is also annealing, at 300 K) are not taken into account. Fig. 2.2 shows an example of displacement damage in MgO due to electron irradiation in an electron microscope at elevated temperature. Nanometer-scale Mg ‘dendrites’ are formed at the edge of the hole of an MgO TEM specimen. The observation was made in the IVEM-TANDEM facility at Argonne National Labs (IL, USA, see Section 2.6). The target Mg and O atoms in the MgO are displaced by 300 keV electrons. When these displaced atoms reach the surface of the specimen, the O atoms disappear into the vacuum of the electron microscope chamber while the Mg atoms accumulate at the surface, whereby a wood of nanotrees is formed.

2.2. Optical absorption spectroscopy (OAS)

Optical absorption spectroscopy was performed using a Perkin Elmer Lambda 40 spectrophotometer with a scan range of 190-1100 nm (corresponding to 1.1-6.5 eV), a slit width of 2 nm and a data interval of 1 nm. In the machine, a deuterium lamp is used for the ultraviolet part of the spectrum (UV) and a tungsten lamp is used for the visible (VIS) part of the spectrum. The lamps were turned on 20 mins. before carrying out the baseline scan and subsequent measurements, so that the lamps were warmed up and the emission spectrum of the lamps was stable during the measurements. The baseline scans were performed without reference samples (ambient air was used as a reference).

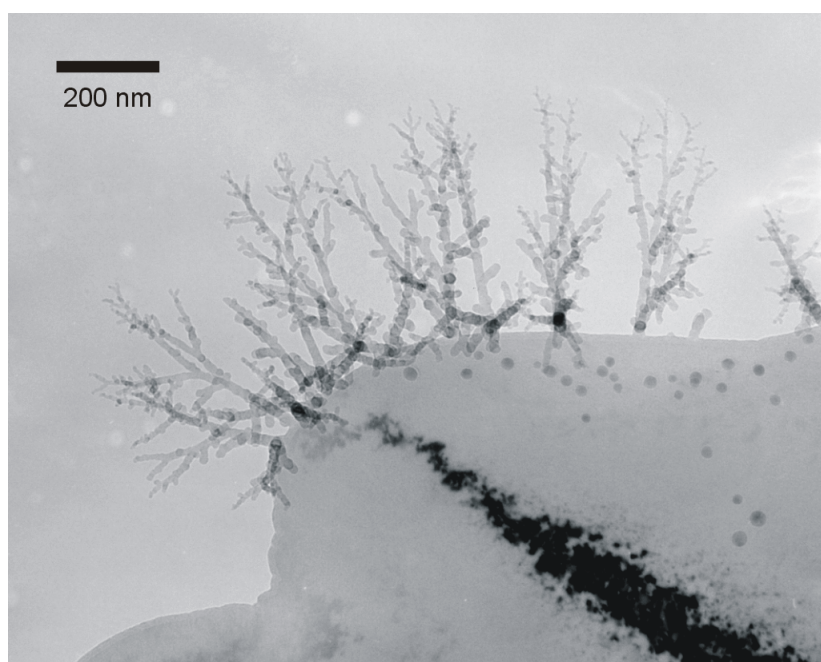


Fig. 2.2. Accumulation of Mg atoms forming nanometer-scale ‘dendrites’ at the surface of an MgO specimen due to 300 keV electron irradiation at elevated temperature in an electron microscope.

2.3. Rutherford backscattering spectrometry and channeling (RBS-C)

The Rutherford backscattering spectrometry/channelling (RBS-C) was performed at the Institut für Festkörperphysik at the Forschungszentrum Karlsruhe (Germany). In the RBS technique, light ions such as H or He ions are used as probes. Depths up to $\sim 1 \mu\text{m}$ can be probed and the best depth resolution can be as good as 5 nm. The sample under investigation is irradiated with a mono-energetic beam of probe ions (energy of the order of MeV). In some cases (about 1 ppm), the probe atom will collide elastically with a target atom in the sample and be backscattered. On its trajectory in and out of the material, the projectile loses energy by electronic interactions. The number of backscattered probe atoms is detected by an energy-sensitive detector, placed at a certain deflection angle. When the number of detected probe atoms is plotted as a function of energy, edges can be distinguished which correspond to collisions with a target atom of a particular mass, see Subsection 4.2.3 for an example. A low (high) energy loss of the backscattered atoms corresponds to a shallow (large) depth of the target atom that participated in the collision. If the specimen under investigation is monocrystalline, the incoming beam is not aligned with any of the crystal axes. This case is called general RBS, also denoted as ‘random’. In channelling experiments, the incoming beam is aligned with one of the crystal axes. In this case, many probe atoms channel through interstitial channels between the rows of atoms so that fewer probe atoms are backscattered. When channelling occurs, the yield (number of counted particles) is strongly reduced. When comparing the ‘random’ experiment with the ‘channelling’ experiment, information can be obtained about the damage in the host matrix and about the position (interstitial or substitutional) of the implanted atoms. In this work, MgO samples were analysed using 1.5-2.0 MeV He ions with a triple-axis goniometer to determine the ion and damage distributions. Angular scans around the [001] axial direction were measured, detecting signals from the impurity and the host lattice atoms as a function of depth. The beam exposes an area of a few square millimetres, and the spectra were taken on sample parts previously not affected by the analysing beam. If this procedure is followed, the method can be considered non-destructive in ceramic oxides. A more extensive description of the technique can be found in Feldman (1991).

2.4. Neutron depth profiling (NDP)

In order to monitor ^3He retention in MgO and Al_2O_3 , the NDP facility at the Interfaculty Reactor Institute (IRI) in Delft was used [Damen et al. 2003, Krings et al. 1999, Eleveld et al. 1994]. The neutron depth profiling (NDP) technique makes use of thermal neutrons, which enter the material and engage in a nuclear reaction with a target atom (if the cross-section for neutron capture is significant). The reaction products are particles with well-defined energies

when they are created. These particles leave the sample and are detected by an energy-sensitive detector. ^3He was detected using the nuclear reaction $^3\text{He}(n,p)^3\text{H}$:



These particles lose kinetic energy on their way to the surface. By measuring the energy distribution of the particles, the depth distribution of the target nuclei can be derived using the stopping cross-sections of the reaction products in the material. The measurements were carried out in a vacuum box that allowed a filtered thermal neutron beam with a flux of 3×10^7 neutrons $\text{s}^{-1}\text{cm}^{-2}$ to enter via a diaphragm and impinge upon the sample. The detector was a Canberra PIPS Si detector with 12 keV energy resolution. The detection limit is about 10^{14} $^3\text{He} \text{ cm}^{-2}$. The NDP set-up was calibrated by measuring a silicon wafer implanted with a calibrated amount of ^{10}B atoms (the cross-section of thermal neutron capture for ^{10}B is well known).

The planar concentration of target atoms can be derived from the total amount of detected reaction products. The inaccuracy of the derived number of target atoms depends on the calibration, the measurement time and the background. The measurement time is chosen to achieve an accuracy of 5-10 %. A more detailed description of the NDP technique can be found in Downing et al. (1993).

2.5. X-ray diffraction (XRD)

High-resolution XRD measurements were performed in collaboration with the Materials Research Centre at the University of Groningen, The Netherlands. XRD was mainly used to study the orientation relationship of nanoclusters with the host matrix and to derive the nanocluster size from the broadening of the diffraction peak using the Scherrer formula [Langford et al. 1978]. The set-up used is a Philips X'Pert materials research diffractometer system with a ceramic X-ray tube, which provides Cu K_α radiation with a wavelength $\lambda_0 = 1.54056 \text{ \AA}$.

2.6. Transmission Electron Microscopy (TEM)

Transmission electron microscopy is very important for investigating the structural properties of nanoclusters. It is the only technique that gives a good impression of the morphology, size distribution and spatial configuration of the nanoclusters.

2.6.1. Specimen preparation

Most of the specimens for (cross-sectional) transmission electron microscopy were prepared at the department of Defects in Materials in Delft. Considering that all the investigated materials were ion implanted layers, almost all specimens were of the cross-sectional type in order to enable investigation of nanoclusters and implantation defects as a function of depth. In general, the implanted samples were of size $10 \times 10 \times 1 \text{ mm}^3$ with an implanted area of $10 \times 10 \text{ mm}^2$. Two rods were cleaved from the sample (size $\sim 3 \times 1 \times 1 \text{ mm}^3$ with implanted area $3 \times 1 \text{ mm}^2$). MgO is a material that is very easy to cleave along the (100) planes, and thus no disc cutting was required for the preparation. In the case of sapphire Al_2O_3 however, the rods had to be cut. In order to create cross-section specimens, the rods were glued together with the implanted surfaces facing each other. A slab of amorphous silica glass (thickness $150 \text{ }\mu\text{m}$) was glued in between the two implanted surfaces for protection of the sample edges during the grinding and polishing. Gatan G-1 epoxy was used as glue because it is strong and can resist temperatures up to 1300 K (important for in-situ heating experiments). The glue was hardened in an air furnace at 380 K for more than two hours. Next, the specimens were ground on both sides (perpendicular to the implanted layers) with a Gatan Model 623 disc grinder, using SiC paper with grit sizes of 1000 and 1200. The samples were ground down to a thickness of $300 \text{ }\mu\text{m}$.

Subsequently, the specimens were polished on both sides using polishing cloth and diamond paste, using crystal sizes of 14, 8, 3 and $1 \text{ }\mu\text{m}$, respectively. After polishing one side (specimen thickness $\sim 170 \text{ }\mu\text{m}$), the polished side was glued onto a copper planar ring (inner/outer diameter of 1.5/3.0 mm) for support. Next, the other side was polished until the specimen reached a thickness of $15\text{-}20 \text{ }\mu\text{m}$. For the polishing, a tripod (South Bay Technology, Model 590) was used in combination with an Olympus PME3 inverted microscope. Finally, the specimens were ion milled to electron transparency using a high-intensity Gatan 691 PIPS (precision ion polishing system) at the University of Groningen. The ion milling was performed with two Ar guns operating at 4.0 keV energy and at an angle of incidence of $6\text{-}7^\circ$. The ion milling was halted when a hole was formed in the specimen. The areas at the edge of holes are usually thin enough ($<100 \text{ nm}$) for successful imaging. The success rate of the specimens increased with experience, reaching about 70% at the end. Planar TEM specimens were prepared for the experiments carried out at Argonne National Laboratory (Argonne, IL, USA), see the subsection below. Because these MgO specimens were to be ion irradiated in-situ in the electron microscope, untreated and as-received MgO samples were used as base material for specimens. For planar TEM specimens, the grinding and polishing procedure is analogous to the procedure used for cross-section specimens described above. Squares with sizes of $3 \times 3 \times 1 \text{ mm}^3$ were cleaved from the MgO crystals, glued onto a copper grid with one of the $3 \times 3 \text{ mm}^2$ surfaces, and then ground and polished

only from one side down to a thickness of 15-20 μm . The quality of the surface of as-received MgO crystals was already of good quality, so the other side (which was glued to the copper) did not need to be ground or polished. Again, ion milling was used to create areas with electron transparency. Unfortunately, these thin areas around the hole broke off along the MgO(100) planes during the transport to the United States and additional ion milling at Argonne was required.

2.6.2. Electron microscopes

Cross-sectional and planar transmission electron microscopy (TEM) was performed in collaboration with the Materials Science and Engineering group at the University of Groningen, The Netherlands. The TEM was performed using a JEOL 4000 EX/II operating at 400 kV (point-to-point resolution 0.17 nm). Planar TEM was also performed, at the IVEM-TANDEM facility at Argonne National Laboratory (Argonne, IL, USA). This facility allows in-situ TEM observation of defect evolution during ion implantation and (simultaneous) thermal annealing [Allen et al. 1989]. The facility was used in collaboration with the Materials Science Center of ANL. The set-up consists of a Hitachi H-9000 transmission electron microscope operating at 300 kV coupled to a NEC ion implanter with a maximum acceleration energy of 600 keV. Because of the different design when an incoming ion beam is used, the resolution of the microscope is reduced to 0.3 nm. The specimens were mounted on a temperature-controlled stage (from 300 to 1100 K) and tilted towards the ion beam ($\sim 30^\circ$ off the electron beam axis) during ion implantation. A schematic drawing is shown in Fig. 2.3. Micrographs and video recordings were made to record the observations. In general, it was very difficult to maintain the same diffraction conditions during the ion implantation/thermal annealing. During ion implantation of in particular the heavy ion species, the insulator MgO foil was strongly vibrating, completely blurring the image. The ion implantation was halted from time to time to check the state of the specimen.

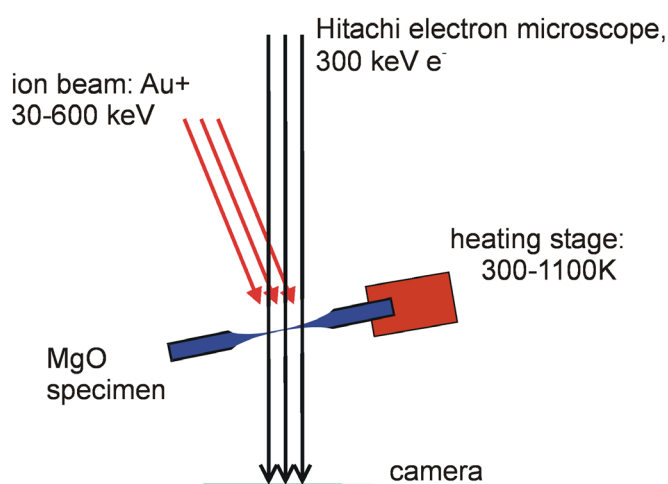


Fig. 2.3. Schematic drawing of the IVEM-TANDEM facility at Argonne National Laboratory (Argonne, IL, USA).

The fact that the vibrations were stronger when the heavy ions were used (with the same electric charge but higher mass) is probably due to secondary electron emission from the MgO specimen. During ion irradiation, the thin areas around the hole were at first bending and in some cases completely curling over more than 360° , which is surprising for a ceramic that is supposed to be brittle. Fig. 2.4 shows thin parts of a MgO specimen that was exposed to 100 keV Au ion irradiation. The bending most likely occurs because of stresses in the MgO slab. With such extreme bending occurring, diffraction conditions were varying continuously.

2.7. Positron beam analysis (PBA)

Positrons are known as sensitive self-seeking probes for defects in materials and can provide detailed information on the electronic structure of defects or bulk materials [Dupasquier et al. 1995, Puska et al. 1994], such as the morphology of Fermi surfaces [Nagai et al. 2001, West 1995, Rajput et al. 1993]. Annihilation of positrons with electrons in solids provides information on the momentum distribution of these electrons. In the centre-of mass coordinate system, the positron-electron pair has zero net momentum as shown in Fig. 2.5(a). Upon annihilation, two annihilation photons are emitted collinearly and in opposite directions. The energy of the electron-positron system is equally distributed between the two annihilation quanta so that their energy is $mc^2 - \frac{1}{2}E_b \approx 511$ keV, with m the mass of the electron (which is equal to the mass of the positron), c the speed of light and E_b the binding energy of the electron and positron in the material. The binding energy of a conduction electron is of the order of a few eV while the rest mass energy mc^2 equals 511 keV, so that the binding energy is usually negligible.



Fig. 2.4. Bending and curling of a MgO foil due to stresses induced by 100 keV Au ion irradiation.

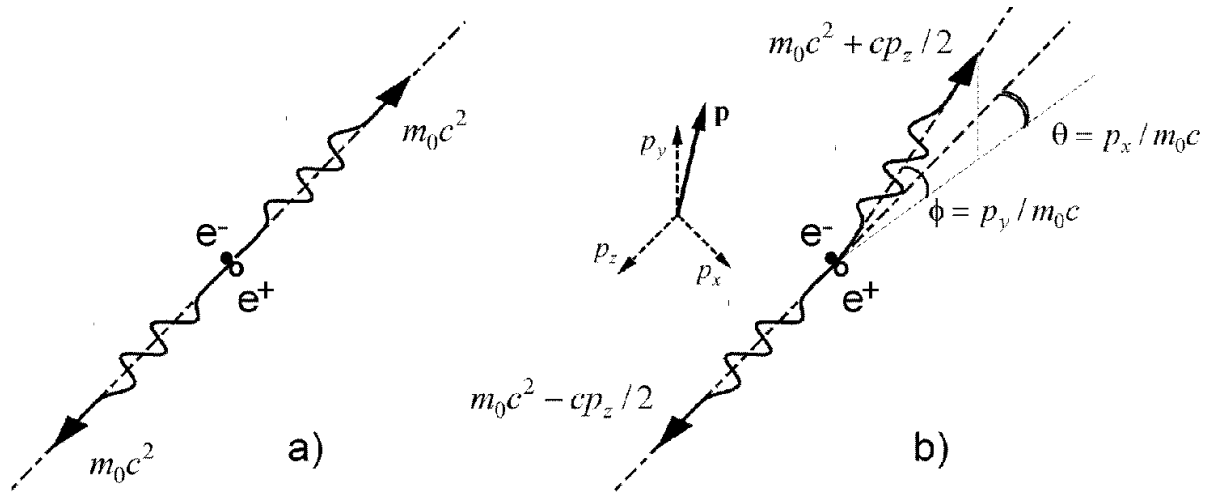


Fig. 2.5. Positron annihilation (a) if the positron-electron pair is at rest and (b) if the positron-electron pair has nonzero net momentum.

When the electron-positron pair has zero momentum in the laboratory system, the centre-of-mass system coincides with the laboratory system and the energies of the annihilation quanta will be equal. However, if the electron has a non-zero momentum at the moment of annihilation, the energies of the two quanta are not exactly equal and the angle between the two γ quanta is not exactly 180° . The first feature is called Doppler broadening and is caused by the component of the electron momentum along the emission direction of the annihilation photons. Please consider Fig. 2.5(b). Due to the longitudinal component p_z , the photons are emitted at energies of $mc^2 + \Delta E$ and $mc^2 - \Delta E$, respectively, where

$$\Delta E = \frac{p_z c}{2}. \quad (2.2)$$

The energy shift ΔE is called the Doppler shift and is of the order of several keV. The transversal components p_x and p_y in Fig. 2.5(b) cause the angle between the emitted photons to deviate from 180° . The deviation equals

$$\theta = \frac{p_x}{mc} \quad (2.3)$$

in the x -direction, and

$$\phi = \frac{p_y}{mc} \quad (2.4)$$

in the y -direction. Here, the approximations $\sin(\theta) \approx \theta$ and $\sin(\phi) \approx \phi$ are made; θ and ϕ are in the order of 1-10 mrad. The energy of positrons in the ground state is of the order of tens of meV, while the energy of electrons in the ground state is of the order of eV. In general, the energy (and momentum) of the positrons can be neglected with respect to the energy of the electrons. Therefore, the Doppler shift and the angular deviation provide the opportunity to measure the energy (and momentum) distribution of the electrons in the material where the positrons annihilate. An electron with an energy of 1.0 eV has a total momentum $p = \sqrt{2mE} = 5.4 \times 10^{-25}$ Ns with $p^2 = p_x^2 + p_y^2 + p_z^2$. Considering Fig. 2.5(b) and Eq. (2.2), this electron can cause a maximum Doppler shift (if $p=p_z$ and $p_x=p_y=0$) of 0.51 keV. Considering Eqs. (2.3) and (2.4), it can cause a maximum angular deviation (if $p_z=0$) of 1.98 mrad. Positrons emitted, e.g., by a ^{22}Na radioactive source, have a wide energy distribution so that only bulk materials can be investigated. To investigate ion implanted layers, the positron analysis needs to be depth-sensitive, which requires a beam of mono-energetic positrons (energy spread less than 200 eV). The positrons are obtained from radioactive sources or produced by pair production, then moderated to thermal energies and subsequently accelerated to the required energy. The probe depth of the positrons is varied by varying the implantation energy of the positrons. When positron beams are coupled to positron annihilation detection techniques, we speak of positron beam analysis (PBA) [Van Veen et al. 2000] similar to ion beam analysis (IBA). These detection techniques include positron lifetime (PL), Doppler broadening (DB) and two-dimensional angular correlation of annihilation radiation (2D-ACAR). The latter two techniques were employed in this study and are discussed in the following subsections.

2.7.1. Doppler broadening (DB)

As explained above, the non-zero momentum of the electrons leads to a shift in the energy of the annihilation quanta. If the energies of many annihilation quanta are measured using an energy-sensitive detector and accumulating the events in a multi-channel analyser (MCA), the non-zero momentum of the electrons can be observed as a Doppler broadening of the 511 keV annihilation peak. Positron annihilation with low-momentum valence or conduction electrons results in a small Doppler shift, contributing to the centre of the peak. Annihilation with high-momentum core electrons results in a large Doppler shift and contributes to the wings of the 511 keV annihilation peak. The shape of the 511 keV peak is characterised by the so-called S and W parameters [Van Veen et al. 2000, Clement et al. 1996] defined in Fig. 2.6. Here the S (shape) parameter indicates the relative contribution from valence and conduction electrons while the W (wing) parameter represents the relative contribution from core electrons. Materials consisting of atoms with a high (low) Z number have many (few) core electrons, and, as a rule of thumb, have a high (low) W parameter.

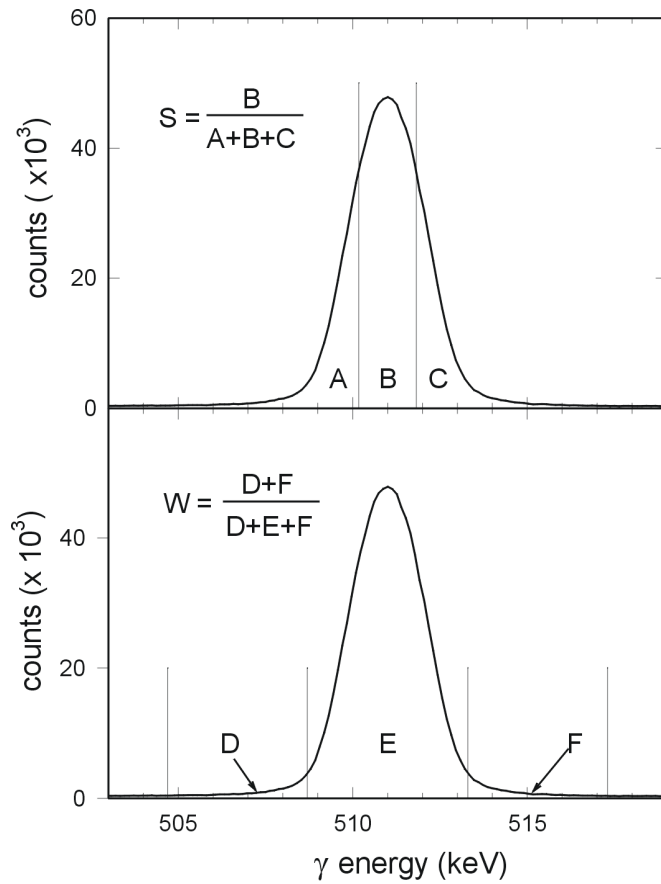


Fig. 2.6. Definition of the S and W parameters. The S parameter denotes the relative contribution of valence and conduction electrons while the W parameter represents the relative contribution of core electrons.

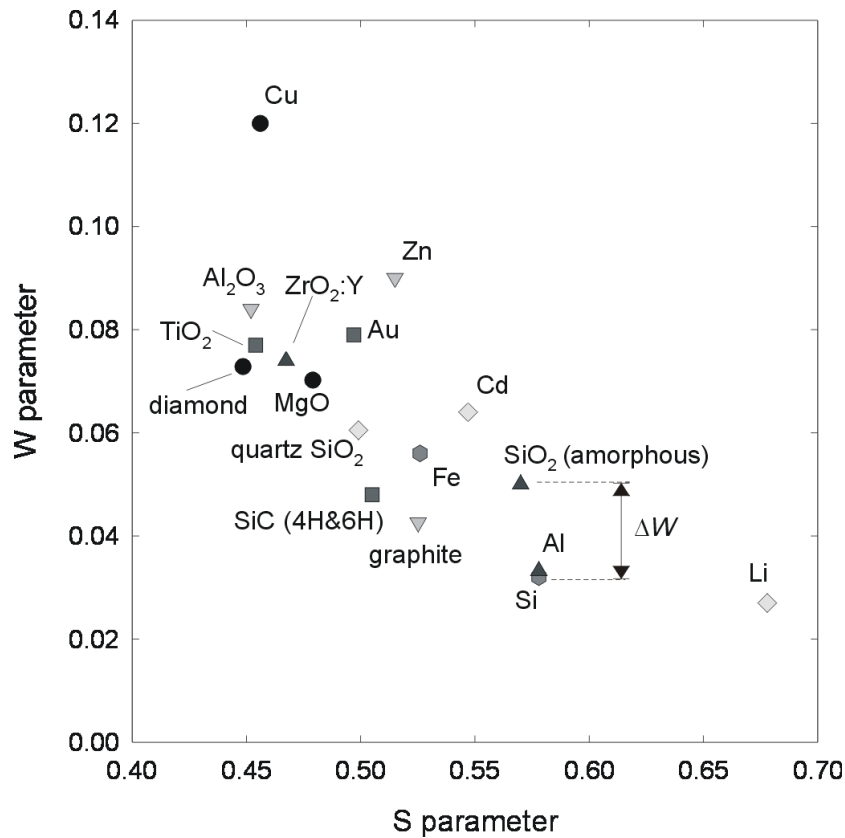


Fig. 2.7. (S, W) cluster points for a number of reference materials measured at room temperature. The difference in the W parameter between Si and amorphous SiO₂ is indicated.

When combined with a slow positron beam, this method is called Doppler broadening positron beam analysis (DBPBA or simply PBA). The S and W parameters can be considered specific bulk properties for every material. Both parameters are usually plotted as a function of positron implantation energy. Alternatively, S can also be plotted vs. W with the positron energy as the running parameter, yielding a so-called SW -plot. Combined use of the S and W parameters can be very essential for investigating materials, because the (S, W) combination can reveal the presence of materials or defects that cannot be identified if only the S parameter is used [Clement et al. 1996, Fedorov et al. 2001a, Rivera 2003]. The (S, W) values for a number of reference materials (measured at room temperature) are plotted in Fig. 2.7. Thus, for example, the S parameters of Si and amorphous SiO₂ are similar, while the W parameters are quite different. In Delft, the PBA measurements were performed using a mono-energetic positron beam with a variable energy of 0-30 keV, corresponding to a probe depth of approximately 0-2 μm . The energy resolution of the detection system is 1.2 keV.

In the case of composite materials (e.g., nanoclusters embedded in ceramic oxides), the overall annihilation distribution can be modelled as a linear combination of the annihilation distributions of the constituting materials. The S parameter of the composite material then equals

$$S_{\text{comp}} = f_{\text{cluster}} S_{\text{cluster}} + f_{\text{host}} S_{\text{host}}, \quad (2.5)$$

where S_{cluster} and S_{host} are the bulk S parameters of the nanoclusters and the embedding material, respectively. f_{cluster} and f_{host} are the fractions of annihilation in the clusters and in the embedding host material ($f_{\text{cluster}} + f_{\text{host}} = 1$). Here it is assumed that the composite material is defect-free and that positrons do not annihilate at the cluster-host interface. If any of the materials contain defects where positrons become trapped and annihilate, these defects will also contribute to the overall S parameter. Any annihilation site i of the positron can be added to Eq. (2.5) as a term $f_i S_i$, while the sum of all the fractions remains unity: $f_1 + \dots + f_m = 1$, where m is the number of annihilation sites. S_i and f_i are the S parameter and the fraction of annihilation at site i . Of course, the principle of superposition of annihilation distributions can be applied to other positron annihilation techniques as well, including two-dimensional angular correlation of annihilation radiation (2D-ACAR).

2.7.2. VEPFIT positron depth profiling code

When a positron beam is used, the S and W parameters can be determined as a function of depth in the sample. Unfortunately, the depth resolution is limited by the positron implantation profile and diffusion processes; the higher the positron implantation energy, the worse the depth resolution. Therefore, the S and W parameters are usually plotted as a function of positron implantation energy rather than as a function of depth. However, the

VEPFIT depth profiling code [Van Veen et al. 1990, Van Veen et al. 1995] takes these effects into account and can translate the experimental curves into an S and W parameter as a function of depth. In the case of, e.g., an ion implanted layer, the S parameter obtained at a certain positron implantation energy consists of contributions from the surface and various layers,

$$S(E) = f_{\text{surf}}(E)S_{\text{surf}} + f_1(E)S_1 + f_2(E)S_2 + \dots + f_n(E)S_n. \quad (2.6)$$

Here the material consists of n layers and the distribution of the layer fractions ($f_{\text{surf}} + f_1 + \dots + f_n = 1$) depends on the positron implantation energy E . Please note that Eq. (2.5) refers to defect (or material) fractions while Eq. (2.6) refers to layer fractions. Formulas analogous to Eqs. (2.5) and (2.6) are valid for the W parameter. The VEPFIT code can fit the S parameter curves to find accurate values for the S and W parameters of the various layers and the fractions of positrons annihilating in these layers as a function of positron implantation energy. This is achieved by solving the time-averaged diffusion equation [Van Veen et al. 1990]. Once the S parameter of a certain layer has been found using the VEPFIT code, Eq. (2.5) can be used to further analyse the defect fractions within that layer. So if, e.g., layer 2 is the ion implanted layer that contains nanoclusters, then $S_2 = S_{\text{comp}}$.

2.7.3. Two-dimensional angular correlation of annihilation radiation (2D-ACAR)

2D-ACAR stands for two-dimensional angular correlation of annihilation radiation [West 1995]. The Doppler broadening technique discussed above uses the difference in energy between the two annihilation γ quanta emitted in opposite directions. The angular correlation techniques use the deviation from collinearity of the two γ quanta, which depends on the momentum of the electron at the moment of annihilation (see Eqs. (2.3) and (2.4)). ACAR set-ups need position-sensitive detectors working in coincidence mode. The advantage of the ACAR techniques is their high resolution (when translated into momentum of the electrons), the disadvantage is their relatively low count rate. The detectors have to be far away from the sample to achieve a good angular resolution, which strongly reduces the solid angle for detection. The 2D-ACAR set-up at the Interfaculty Reactor Institute (IRI) in Delft is of the Anger-camera type with an angular resolution of $1.1 \times 1.4 \text{ mrad}^2$. The 2D-ACAR system is coupled to a high-intensity positron beam with a flux of $\sim 4 \times 10^8 \text{ e}^+ \text{ s}^{-1}$ [Van Veen et al. 1999b], which allows depth-selective 2D-ACAR measurements [Falub et al. 2001, Eijt et al. 2001]. At the time of writing this thesis, it is the only positron facility of this kind in the world. The relationship between energy/momentum of the electron, the angular deviation and the Doppler shift is as follows. An electron with an energy of 1.0 eV (momentum 5.4×10^{-25}

Ns) can give a maximal Doppler shift of 1 keV and a maximal angular deviation of 3.91 mrad, depending on the direction of the momentum of the electron.

2.7.4. Positron affinity and positron confinement

Recently, great advances have been made in the investigation of the electronic structure of metallic nanoclusters by means of positron annihilation spectroscopy. The so-called positron affinity is of major importance for the behaviour of positrons in host-nanocluster systems. The positron will preferentially be present and thus annihilate in the material with the lowest positron affinity. Thus, if the positron affinity of the nanocluster material is lower than the positron affinity of the host, almost all positrons will become trapped in the nanoclusters, thereby becoming a self-seeking probe for nanocluster material. By means of the 2D-ACAR technique the electronic structure of the nanoclusters can be investigated. This offers the opportunity to find properties of nanocluster materials different to those of bulk materials (see Section 1.1). The three-dimensional spatial confinement of the positron wavefunction in the nanoclusters is called 'positron confinement'. Host-nanocluster systems investigated successfully are Li in MgO [Van Huis et al. 2002, Falub et al. 2002] and Cu in Fe [Nagai et al. 2000, Nagai et al. 2001]. The 2D-ACAR experiments in the studies mentioned above provided a unique opportunity to investigate the Fermi surface of these unusual crystal structures. This can only be performed effectively if the vast majority of the positrons trap in the nanoclusters. Assuming that the nanoclusters are homogeneously distributed, the annihilation fractions f_{cluster} and f_{host} in Eq. (2.5) are determined by the diffusion length of the positrons, the concentration of clusters and the difference in positron affinity between the two materials. Although the overall concentration of atoms constituting the clusters in the host material is usually small, the annihilation fraction in the clusters can be high with respect to the annihilation fraction in the host material when the positrons are trapped in the clusters.

In order to find the definition of positron affinity, we follow the derivation by Puska et al. [Puska et al. 1989a, Boev et al. 1987]. Let us first consider Fig. 2.8. The electronic and positronic energy levels in a material are both defined with respect to the crystal zero (CZ). The crystal zero level is defined as the Coulomb potential far away from a single atomic sphere [Boev et al. 1987]. The electron chemical potential μ_{-} is defined as the energy difference between the top of the conduction band (coinciding with the Fermi level) and the crystal zero. The positron chemical potential μ_{+} is defined as the energy difference between the bottom of the positron band $E_{+,0}$ and the crystal zero. Both μ_{-} and μ_{+} are usually negative. The electronic work function φ . (positron work function φ_{+}) is the work necessary to bring an electron (positron) from the Fermi level (positron ground state level) to vacuum. The surface dipole potential step Δ is the potential difference for electrons between the vacuum level and the crystal zero. Positrons experience the same potential step, but with opposite sign: $-\Delta$.

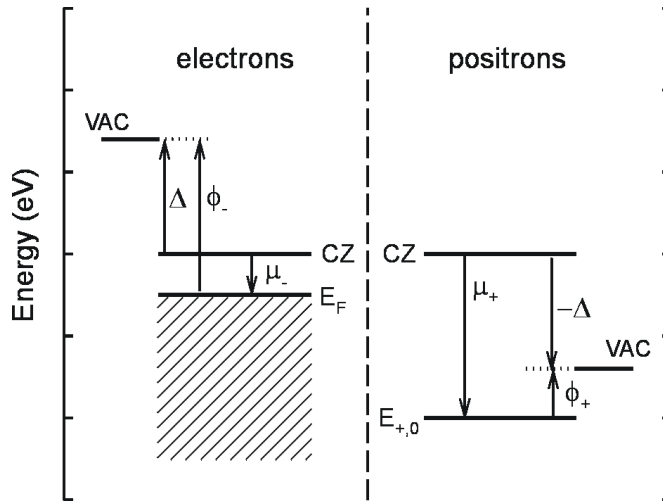


Fig. 2.8. Schematic diagram showing the relevant electronic and positronic energy levels with respect to the crystal zero (CZ) for the case of a metal.

The following relationships hold:

$$\phi_- = -\mu_- + \Delta, \quad (2.7)$$

$$\phi_+ = -\mu_+ - \Delta \quad (2.8)$$

When two metal surfaces are in contact, electrons will flow from one material to the other until the Fermi levels are aligned, thereby establishing thermal equilibrium. This situation is shown in Fig. 2.9. The result is an interface dipole with potential difference $\Delta_{align}^{METAL} = \mu_-^A - \mu_-^B$. For positrons, this potential step is equal in magnitude but opposite in direction. The difference between the lowest positron energies of material A and B equals [Puska et al. 1989a]:

$$\Delta E_{AB,+}^{METAL} = E_{0,+}^A - E_{0,+}^B = \mu_+^A - \mu_+^B + \mu_-^A - \mu_-^B \quad (2.9)$$

which is also clear from Fig. 2.9. When the positron affinity is defined as

$$A_+^{METAL} = \mu_+ + \mu_- = -(\phi_+ + \phi_-), \quad (2.10)$$

the difference in positron ground state levels between the two metals is simply the difference between the positron affinities:

$$\Delta E_+^{AB} = A_+^A - A_+^B. \quad (2.11)$$

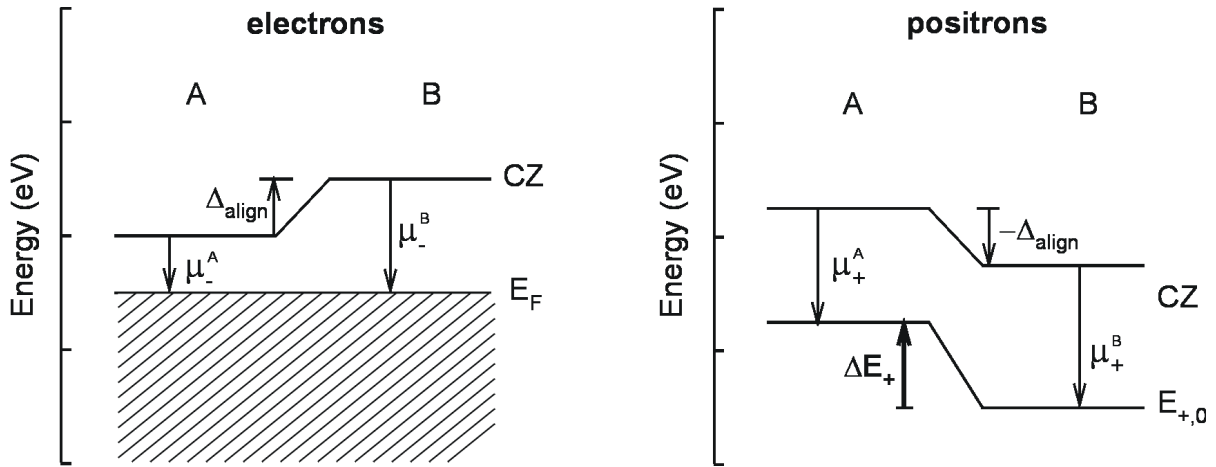


Fig. 2.9. Schematic diagram showing alignment of the Fermi levels for the case of two metals in contact. Note that the alignment shift of the crystal zeros is $\Delta = \mu_-^A - \mu_-^B$ for electrons and $-\Delta$ for positrons.

Although definition (2.10) is commonly used as the general definition of positron affinity, it is only valid for metals. In Section 3.3.4, a definition valid for insulators will be derived. Values for the positron affinity are commonly expressed in eV and are negative for most materials. The affinity has been calculated for almost all metals [Puska et al. 1989a], a number of semiconductors [Panda et al. 2000], a few insulators [Van Huis et al. 2002, Kuriplich et al. 2002] and for rare gases [Puska et al. 1992]. In Fig. 2.10, several possibilities for the positron potential energy as a function of the distance from the centre of the nanocluster are plotted schematically. In Fig. 2.10(a), $\Delta E_+^{AB} < 0$. Here the nanocluster acts as a positronic potential well of depth ΔE_+^{AB} so that positrons can be confined in this nanocluster. In Fig. 2.10(b), $\Delta E_+^{AB} > 0$. The nanocluster now acts as a three-dimensional potential barrier and cannot confine positrons. Fig. 2.10(c) shows a situation where the positron affinity of the nanocluster material is lower than the positron affinity of the host material, but positron confinement is unlikely as the positron is trapped at the interface. Often there is some lattice mismatch due to the different crystal structures of the cluster and the embedding matrix. At the interface, this may result in structural and electronic defects, which can act as a trap for positrons. In the case of, e.g., the Si/SiO₂ interface, preferential trapping at this interface has been claimed by Asoka-Kumar et al. (1994).

As mentioned above, a necessary condition for positron quantum confinement in a cluster (A) embedded in a host (B) is that $\Delta E_+^{AB} < 0$. An additional condition is that there must be at least one bound state in such a well, which determines the minimum size of the cluster. Assuming a spherical potential well this condition reads [Puska et al. 1989a]

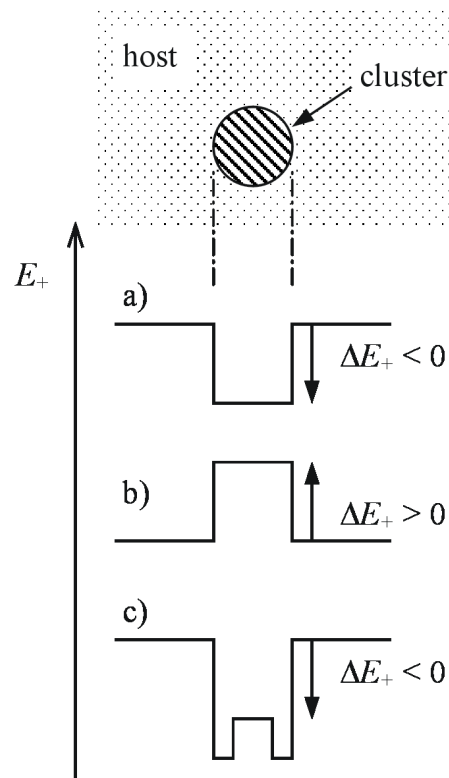


Fig. 2.10. Diagram of the positron potential energy as a function of the distance from the centre of the nanocluster. a) Nanocluster acts as a positronic potential well with depth ΔE_+ . b) Nanocluster acts as a potential barrier with step size ΔE_+ . c) Positron trapping at defects present at the cluster-host interface.

$$R > \frac{\pi \hbar}{\sqrt{8m_0 \Delta E_+^{AB}}}, \quad (2.12)$$

where R is the radius of the cluster and m_0 the positron mass.

Chapter 3

Noble gas nanoclusters

In this chapter, the formation and dissociation of gas bubbles and empty voids are investigated. Gas impurities are an important subject of investigation in materials science since these impurities can alter the material properties. Gas precipitates and radiation damage induce swelling in ceramic oxides, which is of major importance for the design of nuclear reactors (both for fission and for fusion) and for the choice of host matrices for the transmutation of actinides [Cocuaud et al. 1997]. Another application of gas ion implantation is the fabrication of vacancy clusters and voids in ceramic materials. After implantation and subsequent annealing, gas bubbles will be formed in the material. During annealing at higher temperatures the gas atoms escape, often leaving behind empty voids. These voids, which usually have sizes in the nanometer range, can be very functional as they act as gettering centres to impurities, which provides an alternative way of producing nanoclusters [Fedorov et al. 2000]. Finally, ion implantation offers the opportunity to create van der Waals solids in a relatively easy way. Van der Waals solids are crystal structures consisting of noble gas atoms that become solid only at low temperatures and/or high pressures. Ion implantation is a suitable method of creating these solid gases since the pressure in embedded nanoclusters is very high, so that, e.g., the optical and structural properties of these solid noble gases can be investigated at room temperature. In this chapter, the creation of solid Kr nanoclusters is reported and the structural and positronic properties of Kr are investigated.

3.1. Vacancy clusters and He bubbles in MgO

3.1.1. Introduction

Interest in the behaviour of helium in MgO has two diverse origins. The first one concerns MgO as a host material for the generation of non-linear and other optical properties by introducing nanometer-sized metallic or semiconductor clusters [Ueda et al. 1997, White et al. 1998]. Control over the size and shape of these nanoclusters might be obtained by a two-step process when metallic ions are introduced into previously generated nanometer-sized voids in MgO. It is suggested that the cavities will act as gettering centres to metallic ions as has been observed for nanocavities in silicon [Zhang et al. 1999a]. The nanovoids are created by helium ion implantation in single crystals of (100) MgO and subsequent annealing. After isothermal annealing at 1323 K all helium has left the sample, leaving behind voids in the implantation zone [Van Veen et al. 2000]. TEM investigations have revealed that these large vacancy clusters or nanocavities have unusual rectangular shapes [Kooi et al. 2000]. The cavities are shaped as rectangular plates aligned in the (100) plane, with the short sides in the range of 0-3 nm and the long sides varying from 5-20 nm. The second application for MgO is as a candidate uranium-free host matrix for the transmutation of actinides generated in nuclear reactor fuels [Cocuaud et al. 1997]. Alpha decay of actinides introduces helium atoms into the MgO matrix, which interact with radiation damage defects. It is therefore of interest to investigate the relevant activation energies of helium dissociation from various defects in which the helium might be trapped. In this section, the nucleation of voids is investigated by calculating the formation energies of small vacancy clusters. Defect formation energies are compared with calculations and experimental data from the literature [Kotomin et al. 1997, Kotomin et al. 1998, Zinkle et al. 1997]. Furthermore, the activation energies associated with helium migration and dissociation from vacancy-type defects are calculated. These energies are compared with the activation energy for permeation of helium through a 100 nm thick layer of (100) MgO as observed with NDP.

3.1.2. CASCADE atomistic simulation code

The calculations were carried out using the Mott-Littleton methodology as implemented in the code CASCADE [Leslie 1982]. Atomistic simulations are based on a classical Born description of the lattice with pair potentials acting between atomic species. The ionic interactions consist of two components: a long-range Coulombic interaction and a short-range interaction, which accounts for the effect of electron cloud overlap and Van der Waals energies. In this study short-range terms are approximated using parameterised pair potentials of the Buckingham form where A , ρ and C are the potential parameters:

$$S(r_{ij}) = A_{ij}e^{-r_{ij}/\rho} - C_{ij}/r_{ij}^6 \quad (3.1)$$

Two distinct sets of potential parameters, listed in Table 3.1, are used in this study. The potential set for the so-called full charge model was derived with the assumption that the lattice ions assume their full charge states of $+2.0 e$ and $-2.0 e$ for Mg and O respectively. The potential set for the partial charge model was derived for Mg and O ions with a partial charge of $+1.7 e$ and $-1.7 e$. The oxygen partial charge is close to the centre of the values predicted by Mulliken population analyses of periodic quantum mechanical calculations [Ellis et al. 1991, Gale et al. 1992, Jacobs et al. 1992]. An oxygen charge of $-1.7 e$ has also been successfully used to model solutions of MgO, CaO, and TiO₂ in α -Al₂O₃ [Grimes 1994]. The parameters of both potential sets were derived by simultaneous fitting to the relevant crystal properties (e.g. lattice parameter, elastic and dielectric constants).

Table 3.1. Potential parameters for the full and partial charge model.

			Full charge model	Partial charge model	Ref.
Short-range potentials					
O-O	Buckingham	A (eV)	9547.96	2230386.3	[Grimes 1994]
		ρ (\AA^{-1})	0.21916	0.1429	
		C (eV \AA^6)	32	32	
Mg-O	Buckingham	A	1284.38	959.3	[Grimes 1994]
		ρ	0.29969	0.2994	
		C	0	0	
He-He	Buckingham	A	166.8	166.8	^a
		ρ	0.28096	0.28096	
		C	0	0	
He-Mg	Buckingham	A	975.5	975.5	^a
		ρ	0.2229	0.2229	
		C	0	0	
He-O	Lennard-Jones	A	2247.836	2247.836	[Grimes et al. 1990b]
		B	11.762	11.762	
Shell model parameters					
		O shell charge	-2.04	-2.23	[Grimes 1994]
		O core charge	0.04	0.53	
		O total charge	-2	-1.7	
		Mg total charge	2	1.7	
		O harmonic constant	K (eV \AA^{-2}) 6.3	32.2	

^a The He-He and Mg-He energies were calculated within the electron-gas approximation and subsequently fitted to a Born-Mayer potential form.

In addition to the pair potentials, the Dick and Overhauser shell model is used to describe polarisation effects. The shell model parameters are also listed in Table 3.1. The method is further explained in Ref. [Grimes et al. 1990a]. The variation of helium-magnesium and helium-helium energies as a function of atomic separation were calculated within the electron-gas approximation [Harding 1990] with a subsequent fit to a Born-Mayer potential form. The important helium-oxygen potential was taken from Grimes et al. (1990), where energies were calculated within the Hartree-Fock approximation based on a distribution of oxygen ions characteristic of the UO_2 lattice.

Throughout this section, defects will be written in a modified Kröger-Vink notation (see Table 3.3). Activation energies for migration of vacancies and interstitials are obtained by calculating defect formation energies at discrete positions along the migration path and subtracting the minimum formation energy at the interstitial position from the maximum formation energy at the saddle point (see Fig. 3.1). The migration paths for charged magnesium and oxygen vacancies V_{Mg}'' , $V_{\text{O}}^{\bullet\bullet}$, and charged magnesium and oxygen interstitials $\text{Mg}_i^{\bullet\bullet}$, O_i' , follow straightforwardly from the simple structure of MgO [Kotomin et al. 1997]. Interstitial helium atoms He_i^\times follow the same migration path as charged oxygen and magnesium interstitials, in a $\langle 100 \rangle$ direction (see also Fig. 3.4).

3.1.3. Predicted vacancy cluster structures in MgO

First, the formation energies of Schottky and Frenkel defects, the migration activation energies of oxygen and magnesium vacancies and interstitials as well as the migration activation energy of helium interstitials in MgO were calculated. The results are listed in Table 3.2. The energies reported here show good agreement with earlier INDO and pair potential calculations [Kotomin et al. 1997, Kotomin et al. 1998] and with experimental results [Zinkle et al. 1997].

In general, values reported in the literature are in between the full charge and partial charge values of Table 3.2. Although the absolute values calculated with the partial charge model agree better with the experimental data, the relative energies predicted by each model are essentially the same. Thus, for example, Schottky disorder is favoured over Frenkel disorder by both models. Next, the energetically most favourable configuration of selected vacancy clusters composed of up to eight vacancies were determined. A number of possible configurations is displayed in Fig. 3.2 and the corresponding formation energies are listed in Table 3.3. Again both partial and full charge models yield equivalent relative geometric preferences.

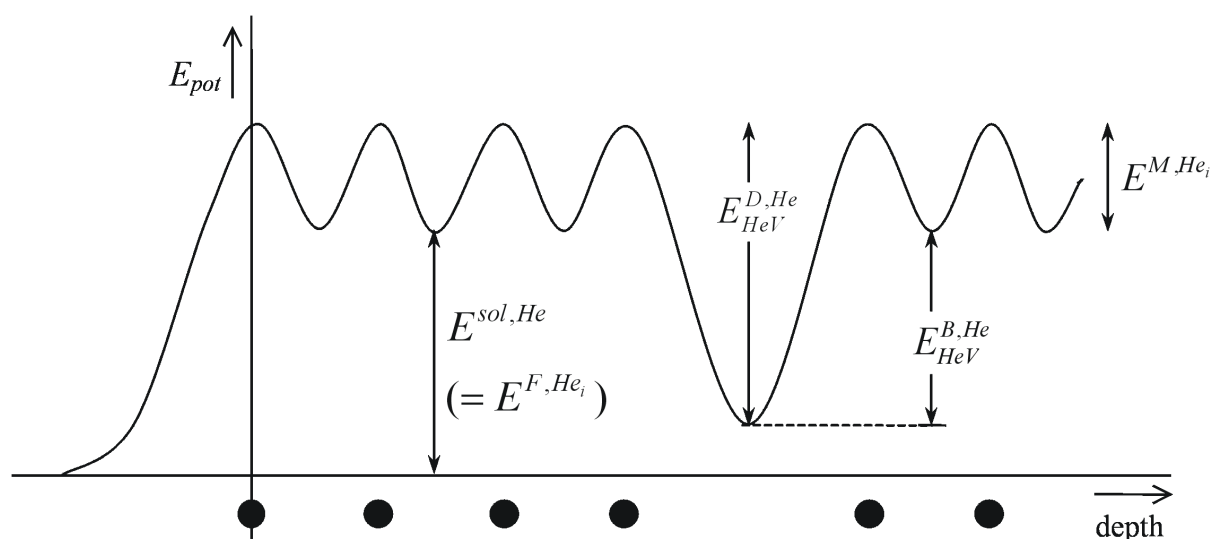


Fig. 3.1. Schematic diagram of the potential energy of a He atom in a solid. The maxima in the graph correspond to ‘saddle points’ at crystal planes (indicated by the large dots at the bottom of the figure) that have to be crossed in order to move from one interstitial site to another. The solution energy of a He atom in the matrix equals the formation energy of a He interstitial. In addition, the binding and the dissociation energy for a He atom in a monovacancy are indicated.

Table 3.2. Formation energies of Schottky and Frenkel defects, migration energies of oxygen and magnesium vacancies and interstitials, and the formation and migration energy of helium in MgO. Definitions of the formation and migration energies can be found in Section 1.3 and Fig. 3.1.

Defect energies (eV)		Full charge model	Partial charge model
Lattice energy	E_{MgO}^{latt}	-41.16	-29.74
Schottky pair	$E^{F,V_O^{**}} + E^{F,V_{Mg}^{**}}$	8.44	6.12
Schottky cluster	$E^{F,\{V_{Mg}V_O\}^x}$	5.35	3.90
Frenkel – Mg	$E^{F,V_{Mg}^{**}} + E^{F,Mg_i^{**}}$	13.35	9.58
Frenkel – O	$E^{F,V_O^{**}} + E^{F,O_i^{**}}$	13.81	9.95
Migration energies	$E^{M,V_{Mg}^{**}}$	2.08	1.53
	$E^{M,V_O^{**}}$	2.12	1.56
	$E^{M,Mg_i^{**}}$	0.64	0.46
	$E^{M,O_i^{**}}$	0.58	0.47
	E^{M,He_i}	1.08	0.71
He solution energy	$E^{sol,He} = E^{F,He_i}$	3.19	2.80

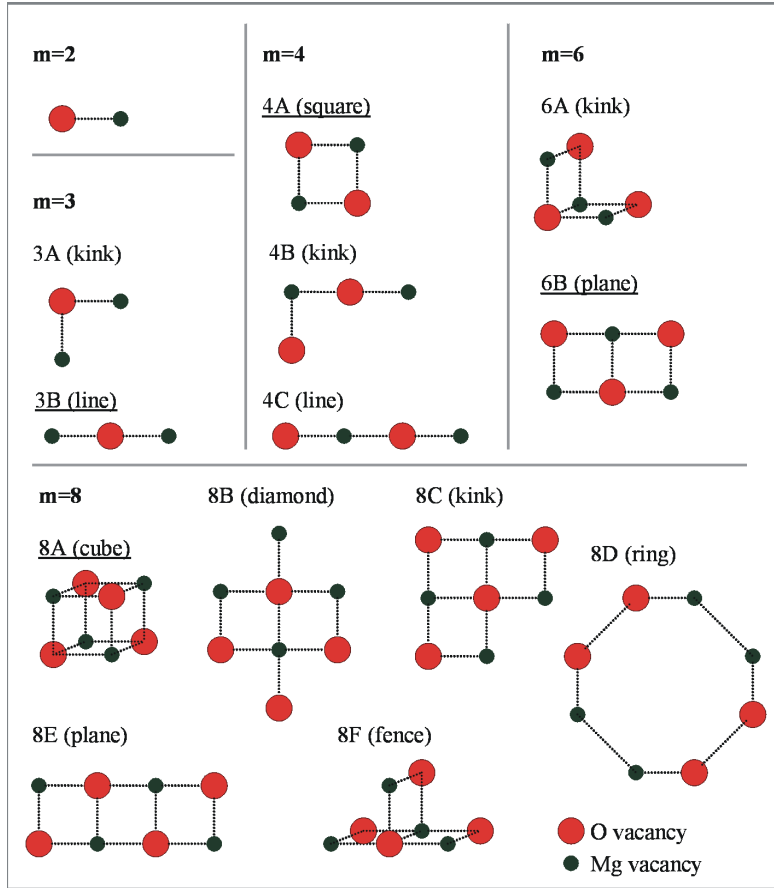


Fig. 3.2. Possible vacancy cluster (V_m) configurations. Note that the depicted atoms represent vacancy sites. The formation energies are listed in Table 3.3. The energetically most favourable configurations are underlined.

By considering Fig. 3.2 and Table 3.3, it is clear that configurations which induce little polarisation around the vacancy cluster are energetically favourable. An interesting extension of this hypothesis is that the energetically most favourable configuration for an eight-vacancy cluster is a cube. Here a three-dimensional configuration is preferred to any planar configuration. A vacancy cluster consisting of a monolayer ‘slab’ induces polarisation oriented perpendicular to the monolayer slab. However, when there are two adjacent monolayers of vacancies, the vertically orientated polarisation induced by the two monolayers cancels to a large extent due to the alternate arrangement of magnesium and oxygen atoms in the MgO matrix. Therefore, three-dimensional growth in an even number of slabs reduces the formation energy of vacancy clusters. This explains why voids in MgO are relatively easy to create [Van Veen et al. 2002].

3.1.4. Predicted He defect interactions in MgO

Now that the configurations of the energetically most favourable vacancy clusters have been determined, an approximation for the activation energies for dissociation of the n^{th} helium atom from a $\text{He}_n V_m$ vacancy-type defect (i.e., $V_m \text{He}_n \rightarrow V_m \text{He}_{n-1} + \text{He}_i$) can be calculated. Here again V_m can be either an oxygen or magnesium monovacancy or a cluster composed of an equal number of oxygen and magnesium vacancies, totalling m vacancies.

Table 3.3. Formation energies of vacancy clusters V_m , $1 \leq m \leq 8$ (here m is the total number of vacancies in the cluster: either oxygen, magnesium or both). The energetically most favourable configurations are underlined.

Number of vacancies m	Configuration of cluster V_m (see Fig. 3.2)	Formation energies (eV)	
		Full charge model	Partial charge model
CHARGED CLUSTERS			
$m=1$	V_{Mg}''	3.93	2.63
	V_O''	4.51	3.49
$m=3$	$[\{V_{Mg}\}_2\{V_O\}_1]''$ 3A: kink	7.85	5.51
	$[\{V_{Mg}\}_2\{V_O\}_1]''$ <u>3B: line</u>	7.31	5.10
	$[\{V_{Mg}\}_1\{V_O\}_2]''$ 3A: kink	8.42	6.37
	$[\{V_{Mg}\}_1\{V_O\}_2]''$ <u>3B: line</u>	7.88	5.97
UNCHARGED CLUSTERS			
$m=2$	$\{V_{Mg}V_O\}^\times$ <u>Schottky cluster</u>	5.35	3.90
$m=4$	$\{V_{Mg}V_O\}_2^\times$ <u>4A: square</u>	7.48	5.48
	$\{V_{Mg}V_O\}_2^\times$ 4B: kink	9.19	6.72
	$\{V_{Mg}V_O\}_2^\times$ 4C: line	9.12	6.66
$m=6$	$\{V_{Mg}V_O\}_3^\times$ 6A: kink	10.69	7.84
	$\{V_{Mg}V_O\}_3^\times$ <u>6B: plane</u>	9.96	7.30
$m=8$	$\{V_{Mg}V_O\}_4^\times$ <u>8A: cube</u>	10.22	7.52
	$\{V_{Mg}V_O\}_4^\times$ 8B: planar diamond	16.46	12.08
	$\{V_{Mg}V_O\}_4^\times$ 8C: planar kink	12.91	9.49
	$\{V_{Mg}V_O\}_4^\times$ 8D: ring	23.56	17.17
	$\{V_{Mg}V_O\}_4^\times$ 8E: rectangle	12.36	9.07
	$\{V_{Mg}V_O\}_4^\times$ 8F: fence	14.28	10.47

He_i is a He interstitial. The dissociation energies $E_{He_nV_m}^{D,He}$ have been calculated by summing the binding energy of the helium atom in the vacancy cluster, $E_{He_nV_m}^{B,He}$, and the migration energy of interstitial helium in defect-free MgO, $E^{M,He}$. The binding energy is calculated from formation energies of helium-filled vacancy clusters, E^{F,He_nV_m} , and the helium interstitial formation energy, E^{F,He_i} .

$$E_{He_n V_m}^{D,He} = E_{He_n V_m}^{B,He} + E^{M,He}, \quad (3.2)$$

$$E_{He_n V_m}^{B,He} = E^{F,He_{n-1} V_m} + E^{F,He_i} - E^{F,He_n V_m}. \quad (3.3)$$

The definitions of some of the energies above are depicted in Fig. 3.1. The calculated activation energies for dissociation are listed in Table 3.4 and shown in Fig. 3.3. It is clear from Table 3.4 and Fig. 3.3 that the dissociation energy of helium from a vacancy or vacancy cluster containing only one helium atom ($n=1$) is more or less constant: 4.4 eV for the full charge model and 3.6 eV for the partial charge model. Helium atoms experience empty vacancy clusters as vacuum and therefore the dissociation energy does not increase with larger cavities. Only the magnesium vacancy is apparently somewhat smaller than the oxygen vacancy. Another result of importance to note is that the fifth helium atom in an oxygen vacancy ($n=5$) is not bound at all, that is, the dissociation energy for the fifth helium atom in a $\{V_O He_5\}^{**}$ defect is less than the helium migration energy in the MgO bulk (Table 3.2, Fig. 3.3) for both the full charge and partial charge model. Thus, the binding energy of the cluster is negative and such a cluster would not be stable.

Table 3.4. Dissociation energies for the n^{th} He atom in $V_{Mg}He_n$, $V_O He_n$ and $V_m He_n$ defects for the full charge and partial charge model. Energies have been calculated using Eqs. (3.2) and (3.3) assuming the energetically most favourable configuration for the vacancy clusters listed in Table 3.3. The data below are displayed in Fig. 3.3.

Full charge model – dissociation energies (eV)						
	V_{Mg}''	V_O^{**}	V_2 (Schottky)	V_4 (square)	V_6 (plane)	V_8 (cube)
n						
1	4.21	4.30	4.37	4.39	4.38	4.37
2	2.01	2.99	4.08	4.26	4.37	4.37
3	1.98	2.33	3.06	4.12	4.22	4.26
4	2.49	2.50	2.61	3.99	4.22	4.27
5	1.60	0.72	2.83	3.09	4.02	4.09
6	2.09	1.52	2.35	0.87	3.82	4.05
Partial charge model – dissociation energies (eV)						
	V_{Mg}''	V_O^{**}	V_2 (Schottky)	V_4 (square)	V_6 (plane)	V_8 (cube)
n						
1	3.46	3.54	3.61	3.63	3.62	3.61
2	1.47	2.27	3.32	3.50	3.61	3.60
3	1.46	1.69	2.16	3.36	3.46	3.50
4	1.97	1.87	2.12	3.23	3.46	3.38
5	1.14	0.37	2.16	2.37	3.26	3.46
6	1.56	1.06	1.06	2.21	3.07	3.30

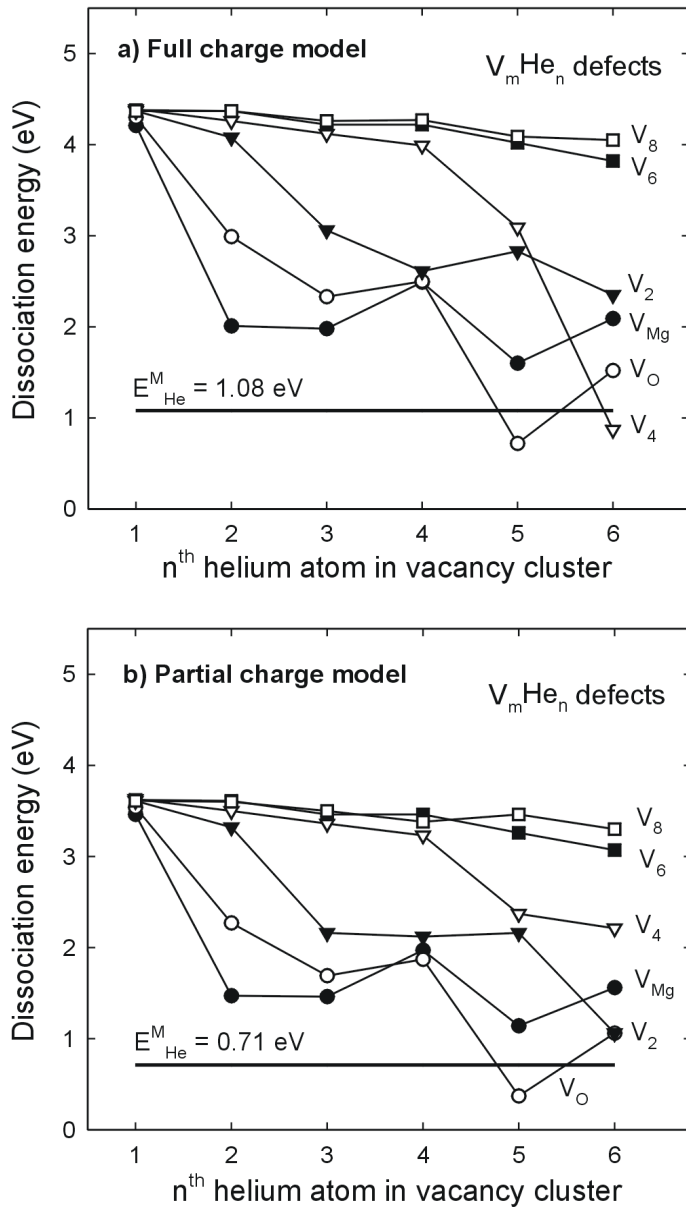


Fig. 3.3. Activation energies for the dissociation of one helium atom from helium-filled vacancy clusters (i.e. $V_m\text{He}_n \rightarrow V_m\text{He}_{n-1} + \text{He}_i$) as a function of the number of helium atoms n in the cluster prior to dissociation. Lines are drawn to guide the eye.

The activation energy for helium atom dissociation from a cluster calculated here based on the assumption that the migration activation energy for a helium atom, $E^{M,He}$, as it moves away from the cluster, is the same as in the bulk defect-free material. However, local relaxation of the lattice surrounding the defect may increase (or decrease) this energy. In order to learn more about the dissociation of a single helium atom from a monovacancy, the potential energy of the helium atom has been calculated along the escape trajectory from an oxygen vacancy as depicted in Fig. 3.4. From here on, only the partial charge model is considered. The helium potential along the trajectory as a function of the distance from the centre of the monovacancy is shown in Fig. 3.5. Regarding the saddle points shown in Fig. 3.5, it is clear that the potential energy at the first saddle point is slightly larger than at the subsequent saddle points. This results in a dissociation energy of 3.9 eV rather than 3.5 eV (obtained with Eqs.

(3.2) and (3.3), Table 3.4). This effect is the result of the charged nature of the monovacancies: an oxygen monovacancy exhibits a charge of $+1.7 e$ with respect to the defect-free MgO matrix. The nearest-neighbour magnesium atoms will be repelled by Coulombic interactions and the second-neighbour oxygen atoms will be attracted to the defect. The expansion and contraction of the first and second ion shells around the oxygen vacancy result in a potential barrier, which increases the activation energy of helium dissociation from a monovacancy. This effect (although without helium) has already been reported by Kotomin and Popov [Kotomin et al. 1998]. The increased activation energy described above for the monovacancy is expected to be higher than for any of the neutral clusters since distortions of the surrounding lattice by neutral defects are much less.

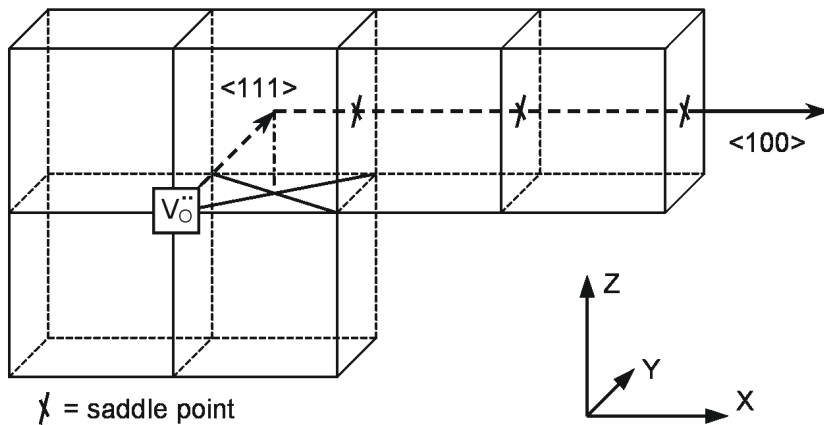


Fig. 3.4. Assumed trajectory of a helium atom dissociating from an oxygen monovacancy.

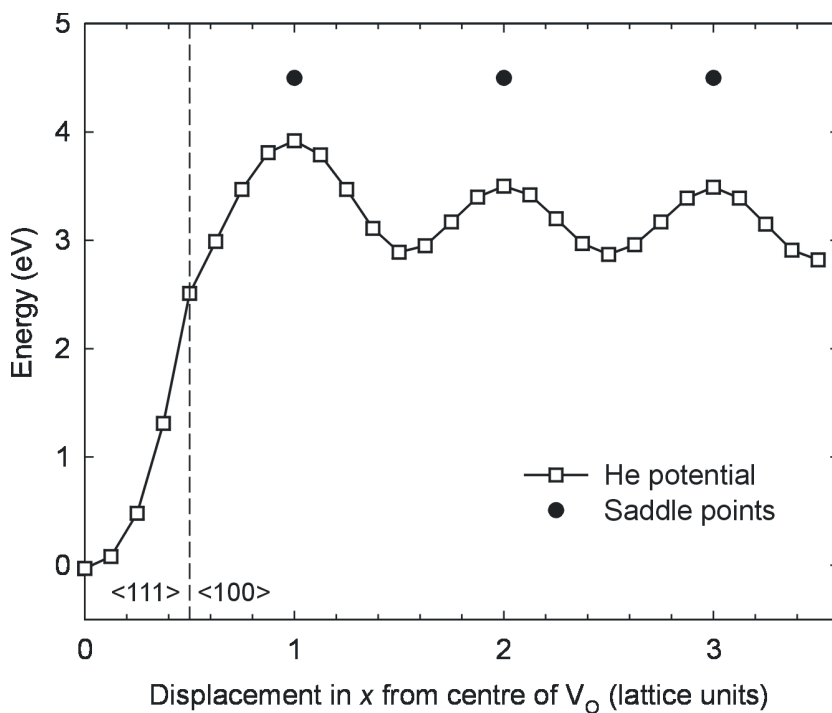


Fig. 3.5. Potential energy diagram of a helium atom dissociating from an oxygen vacancy in MgO, following the trajectory of Fig. 3.4. Only the partial charge model is considered.

3.1.5. He desorption from bubbles in MgO

The calculated values of the helium dissociation energy can be compared with the results of helium permeation from cavities in MgO. A dense layer of helium bubbles at a depth of 100 nm was created by ^3He ion implantation in a single crystal of (100) MgO and subsequent annealing at a temperature of 1200K [Schut et al. 1999]. Using neutron depth profiling (NDP) it is observed that helium permeates to the surface during isochronal annealing at a temperature of 1323 ± 70 K for a period of 30 min. XTEM investigations have shown that the 100 nm thick layer between the layer of cavities and the surface is reasonably defect-free [Kooi et al. 2000]. When dissolving the helium is the rate-determining step, the helium release from the layer of gas bubbles can be modelled as a quasi-stationary flow of gas. This flow is sustained by the concentration gradient which exists between the equilibrium concentration $c_{\text{He},eq}$ of dissolved gas near the cavity layer and the zero concentration near the external surface,

$$\frac{dN_{\text{He}}}{dt} = -D \frac{dc_{\text{He}}}{dx} = -D \frac{c_{\text{He},eq}}{L}, \quad (3.4)$$

where dN_{He}/dt is the flow rate of helium atoms per unit area in $\text{m}^{-2}\text{s}^{-1}$, c_{He} is the volumetric concentration of helium atoms, x is the depth in the sample and L the depth of the cavity layer. D is the helium diffusivity in m^2s^{-1} and is related to the helium migration energy E_M as [Van Veen 1991]

$$D = \frac{1}{6} \lambda^2 \frac{\omega}{2\pi} \exp(-E_M / kT) \quad (3.5)$$

Here, λ is the jumping distance between two interstitial sites (2.1 Å), ω is a fundamental attempt frequency taken as 10^{13} s^{-1} , k is the Boltzmann constant ($8.62 \times 10^{-5} \text{ eV K}^{-1}$) and T the temperature in K. Substituting 0.71 eV for E_M (Table 3.2) in Eq. (3.5), the relaxation time required to establish a stationary flow $\tau_D = L^2/2D$ is of the order of 10^{-4} s , orders of magnitude smaller than the gas release time (of the order of minutes). The model of a quasi-stationary flow is therefore justified. The equilibrium concentration of helium in MgO is [Van Veen 1991]

$$c_{\text{He},eq} = c_{\text{MgO}} \exp(\mu / kT - G_{\text{sol}} / kT), \quad (3.6)$$

with c_{MgO} the atomic concentration of MgO, $1.07 \times 10^{29} \text{ atoms m}^{-3}$, while μ is the chemical potential and G_{sol} the Gibbs free energy of the gas in solution. For a dense bubble layer with gas at low helium pressure and a planar configuration [Godey et al. 2000, Van Veen 1991],

$$\exp(\mu / kT - G_{sol} / kT) = \frac{N_{He}}{d_c} \left(\frac{2\pi\hbar^2}{mkT} \right)^{3/2} \left(\frac{kT}{\hbar\omega} \right)^3 \exp(-E_{sol} / kT). \quad (3.7)$$

Here, N_{He} is the number of helium atoms in the bubble layer per unit area, d_c is the effective thickness of the bubble layer, m is the mass of the ^3He atom and E_{sol} is the helium solution energy as defined in Table 3.2 and Fig. 3.1. Note that N_{He}/d_c represents the density of helium in the cavities. The effective layer thickness d_c equals 0.5 nm, calculated as the product of the thickness of the cavity layer, 20 nm, and the void fraction of 2.5%. Substitution of Eqs. (3.5), (3.6) and (3.7) into Eq. (3.4) and integration with respect to time yields the following expression

$$\frac{N_{He}}{N_0} = e^{-ft}, \text{ with } f = \frac{\lambda^2 \omega}{12\pi L} \frac{c_{MgO}}{d_c} \left(\frac{2\pi\hbar^2}{mkT} \right)^{3/2} \left(\frac{kT}{\hbar\omega} \right)^3 e^{-E_{perm}/kT}. \quad (3.8)$$

The permeation energy, E_{perm} , is defined as $E_{perm} = E_{sol} + E_M$ and t is the time in s during which the permeation occurs. With a decrease in helium content of 86% ($N/N_0 = e^{-2}$) and the values given above, the permeation energy can be calculated. This yields a permeation energy of 3.3 ± 0.3 eV, which agrees reasonably well with the dissociation energy of 3.6 eV for helium desorption from vacancy clusters calculated with the partial charge model.

As the predicted value is still somewhat higher than the experimental value, we have also considered the mechanism of vacancy-assisted migration. The migration energy of a helium-vacancy complex is 2.3 eV calculated with the partial charge model. In order to obtain the activation energy for vacancy-assisted migration, this energy has to be added to the energy required to produce a thermal vacancy (a large concentration of vacancies is required for the process of vacancy-assisted migration). Thermal vacancies are produced at temperatures corresponding to an energy of 3.1 eV (half the Schottky defect energy as defined in Table 3.2) or more. Thus an activation energy of 5.4 eV for vacancy-assisted migration is obtained which makes this process much less likely than helium permeation through the bulk.

3.1.6. Conclusions

The energetically most favourable configurations for vacancy clusters in MgO have been determined. Three-dimensional growth of vacancy clusters is possible, as this introduces less lattice polarisation around the vacancy clusters. As a result, the energetically most favourable configuration of an eight-vacancy cluster is a cube. The partial charge model is more successful at predicting basic defect energies than the full charge model, as the results

calculated with the latter are generally too high when compared to experimental values reported in the literature. The experimentally determined permeation energy of helium in MgO observed with NDP is 3.3 ± 0.3 eV. This agrees reasonably well with the activation energy of 3.6 eV calculated with the partial charge model for helium dissociation from large vacancy clusters. However, the calculated activation energy for helium dissociation from a single oxygen vacancy is expected to be higher: 3.9 eV. This effect is due to lattice relaxation around the charged oxygen vacancy.

In particular, with respect to the helium-defect interactions, more experimental data concerning helium desorption from MgO should be gathered in order to obtain a better understanding of the kinetics of the helium desorption process. This could be achieved, e.g., with thermal desorption spectrometry (TDS). The predictions might be further improved by calculating explicitly the activation energies for the dissociation of helium from (partly filled) vacancy clusters.

3.2. Formation, growth and dissociation of He bubbles in Al₂O₃

3.2.1. Introduction

Like MgO, Al₂O₃ is also a candidate host matrix for the transmutation of actinides generated in nuclear reactor fuels [Cocuaud et al. 1997]. So it is of interest to investigate the activation energies for dissociation of helium from defects. Secondly, Al₂O₃ is a popular host material for the generation of linear and non-linear optical properties by introducing metallic or semiconductor nanoclusters [White et al. 1989, White et al. 1998]. Control over the size and shape of these nanoprecipitates may be obtained by a two-step process [Fedorov et al. 2000]. The first step is the creation of empty voids by He ion implantation and thermal annealing, similar to void fabrication in monocrystalline MgO (see section 3.1). The second step is the introduction of metal ions by means of ion implantation or diffusion from the surface. These metal ions can become trapped at the voids and can eventually fill the voids, so that the size and spatial configuration of the voids determines the size and spatial configuration of the metal nanoclusters. The question is, however, whether vacancy clusters in Al₂O₃ are stable without the presence of He. Although various studies have been performed on He implanted Al₂O₃ [Rechtin 1979, Allen et al. 1992, Sasajima et al. 1999], release of He from monocrystalline alumina has never been reported. In this work, He desorption and the He atomic depth distribution was monitored by means of Neutron Depth Profiling (NDP). The defect evolution in the ion-implanted samples was investigated by means of positron beam analysis (PBA). Positrons are very sensitive tools to probe vacancy-type defects and the formation of bubbles [Schut et al. 1999]. Both techniques are non-destructive and depth-

sensitive. Cross-sectional transmission electron microscopy (XTEM) was employed to determine the size and concentration of He bubbles. These parameters are required for application of a permeation model to the desorption data.

3.2.2. Experimental

Four epi-polished $\text{Al}_2\text{O}_3(0001)$ single crystals of size $10 \times 10 \times 1 \text{ mm}^3$ were implanted at room temperature with 30 keV ^3He ions to four different doses of 0.1, 0.3, 1.0 and 2.0×10^{16} ions cm^{-2} . The samples were isochronally annealed in air for 30 mins. at temperatures varying from 550 K to 1850 K in steps of 100 K. The inaccuracy in the annealing temperature is approximately 20 K. After ion implantation and after each annealing step, the sample was cooled down and the evolution of ion implantation defects was monitored by means of Doppler broadening positron beam analysis (PBA) [Van Veen et al. 2000] and neutron depth profiling (NDP) [Downing et al. 1993]. The PBA set-up uses a 0-30 keV mono-energetic positron beam. This corresponds to a mean positron implantation depth of 0-2.0 μm , which allows depth-resolved monitoring of the defect evolution. The NDP technique uses the $^3\text{He}(n,p)^3\text{H}$ nuclear reaction in order to determine the total amount and the depth distribution of He atoms present in the sample. The inaccuracy in the absolute ^3He content is in general 7% but larger for low doses ($< 10^{15}$ ions cm^{-2}). Finally, XTEM was applied to a fifth sample, which received the same treatment as the sample implanted with the highest He dose (2.0×10^{16} ions cm^{-2}). The TEM specimen was prepared from this sample after annealing at a temperature of 1250 K. This temperature corresponds to the largest bubble volume as observed by means of PBA, see below. The TEM analysis was performed in a JEOL 4000 EX/II electron microscope operating at 400 keV (point-to-point resolution 0.17 nm). First, the defect evolution observed by means of PBA and XTEM is discussed. Next, He release as observed by means of NDP will be presented. The desorption results are analysed using a permeation model.

3.2.3. Defect evolution

Fig. 3.6 shows the S parameter as a function of positron implantation energy for the high-dose (2.0×10^{16} He ions cm^{-2}) implanted sample. The S (shape) parameter is deduced from the Doppler broadening of the 511 keV positron annihilation peak, as explained in Section 2.7. Positrons have a strong preference for trapping in vacancy clusters. When trapped in such a vacancy-type defect, the positron is more likely to annihilate with the nearest outer-shell electrons, which have a low momentum. This leads to an increase in the S parameter. If vacancy clusters are sufficiently large, the S parameter can increase further due to the formation of positronium (Ps) inside the voids. Positronium is a hydrogen-like bound state of a positron and an electron. One-fourth of the positronium atoms is formed in a singlet state with anti-parallel spins of the positron and the electron.

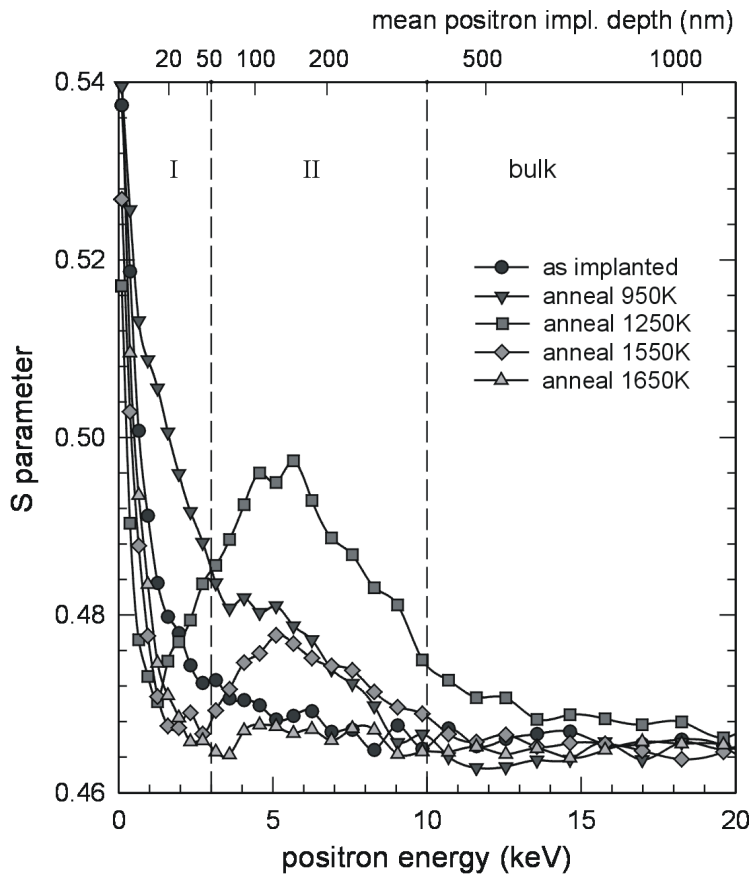


Fig. 3.6. S parameter vs. positron implantation energy for the sample implanted with the high-dose ($2.0 \times 10^{16} \text{ cm}^{-2}$ ^3He) after implantation and after the indicated annealing temperatures. Lines are drawn to guide the eye. The mean positron implantation depth is displayed at the top of the figure.

This so-called para-positronium (p-Ps) annihilates in the 2γ -mode with a lifetime of 125 ps in vacuum. Three-fourth of the positronium formed is in a triplet state with parallel spins of the electron and positron, called ortho-positronium (o-Ps). Because o-Ps can only annihilate in the less probable 3γ -mode, the lifetime in vacuum is considerably longer, 142 ns [Ore et al. 1949, Deutsch 1951]. Due to this long lifetime in vacuum, o-Ps present in a material is much more likely to annihilate by means of so-called pick-off annihilation. Here the positron in the positronium atom does not annihilate with the electron in the positronium atom, but with an electron of opposite spin at the internal surface of the cavity. In that case, the resulting annihilation spectrum will reflect the annihilation spectrum of the surrounding matrix. In the case of p-Ps, the positron annihilates with the electron within the Ps-atom. The Ps-atom has virtually zero momentum and, therefore, the annihilation of p-Ps contributes only to the centre of the 511 keV positron annihilation peak, which causes a considerable increase in the S parameter. Although Ps formation constitutes the principle reason why positrons are able to detect vacancy-type defects, it should be noted that Ps can only be formed in vacancy clusters with a size of ~ 2 nm or more. The presence of helium inside the vacancy clusters is known to suppress the formation of Ps. This was found, e.g., for the case of silicon where Ps formation in empty and in helium-filled voids was compared [Hakvoort et al. 1995, Eijt et al. 2001].

Although the presence of helium in voids (i.e. bubbles) suppresses the Ps formation, the presence of bubbles detected by means of Ps formation is still observable.

Fig. 3.6 shows the S parameter (indicator of open volume) as a function of positron implantation energy, after ion implantation and after several annealing steps. The positron implantation energy on the abscissa of Fig. 3.6 corresponds to a mean positron implantation depth indicated at the top of the figure. For the discussion, we use a two-layer model: a top layer, which contains mainly ion implantation damage (layer I in Fig. 3.6) and a layer containing mainly He-related defects (layer II). The layers indicated in the figure cannot be directly related to the depth scale given at the top of the figure. Due to the broadness of the positron implantation profile and positron diffusion processes, a thin layer of defects will appear much broader in the S parameter curve. The thickness of the layers can only be estimated by means of a simulation code such as VEPFIT [Van Veen et al. 1990], which takes into account the effects mentioned above. We shall now discuss the defect evolution using Fig. 3.6.

1. After implantation, the S parameters of layers I and II increase slightly with respect to the S parameter of the Al_2O_3 bulk (positron energy > 15 keV). Al_2O_3 is a Schottky material in which the interstitials are mobile at room temperature but vacancies are not [Zinkle et al. 1997]. Thus, the interstitials from Frenkel defects created by the implantation will either recombine with vacancies or move to the surface (so that the Frenkel defects turn into Schottky defects). Therefore, mainly vacancies and divacancies are present after implantation (and ‘annealing’ at room temperature) and contribute to the slight increase of the S parameter.
2. Annealing at 550-950 K: The S parameter in layers I and II increases. This means that larger vacancy clusters are formed because vacancies created by the ion implantation agglomerate.
3. Annealing at 950-1250 K: The S parameter decreases in layer I, indicating that the vacancy-type defects in layer I dissociate. Simultaneously, the S parameter increases considerably in layer II, showing that He bubbles are formed. This clearly indicates that at an annealing temperature of approximately 1100 K, defects in Al_2O_3 are not stable unless they are stabilised by the presence of He. The maximum bubble volume is found after annealing at 1250 K.
4. Annealing at 1250-1850 K: The S parameter in layer II decreases and reaches the Al_2O_3 bulk value after annealing at 1650 K. Apparently, the He bubbles shrink and are not observable anymore after annealing at 1650 K. Simultaneously, the NDP results to be discussed below show that 70% of the implanted He is still present in the sample at this temperature. This means that the size of the bubbles decreases to less than approximately 2 nm, a size below which Ps formation is very improbable (see the discussion on

positronium formation at the beginning of this section). Another possibility is that shrinkage of the bubbles increases the helium pressure in the bubbles, which suppresses positronium formation, thereby considerably reducing the S parameter. The observation of strong bubble shrinkage in combination with helium retention in the temperature interval 1250-1650 K is a situation very different from He release in MgO [Schut et al. 1999, Van Veen et al. 1999a] where nanometer-sized voids are stable even when all He has been released.

The low-dose implanted samples ($< 5 \times 10^{15}$ He cm $^{-2}$) showed a similar defect evolution, although the detected bubble volume did not develop as strongly as for the high dose implanted samples.

3.2.4. XTEM results

In order to obtain information on the average size and the size distribution of the He bubbles, a specimen was prepared from the high-dose sample (2×10^{16} He cm $^{-2}$) after the 1250 K annealing step. This temperature was chosen because the S parameter is the highest after annealing at this temperature, indicating a maximum in the bubble volume. An overview image is shown in Fig. 3.7. The ion implantation layer is clearly observable as a band with dark contrast at a depth of 230-340 nm below the surface. At smaller depths, there is a low density of large He bubbles. In this region, the number of displacements per atom (dpa) is lower than in the ion implantation layer. Therefore, monovacancies and He-vacancy defect complexes travel large distances before clustering with other vacancy-type defects. The result is the formation of fewer bubbles, which are larger in size.

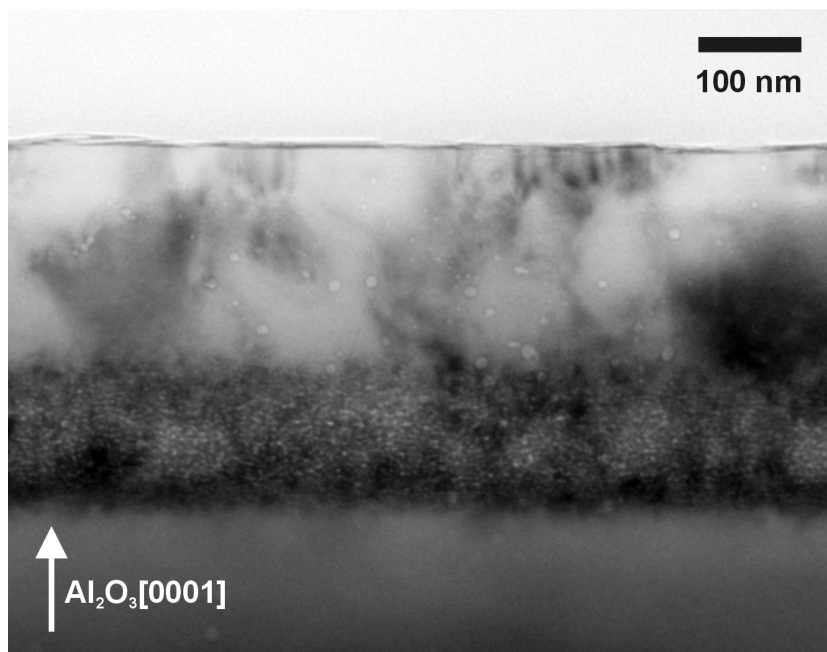


Fig. 3.7. Bright-field XTEM image showing the surface of the specimen and the ion implantation layer at a depth of 230-340 nm.

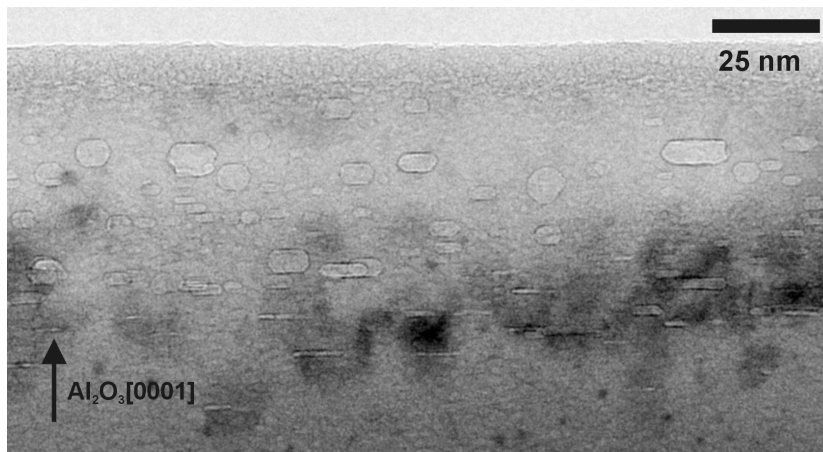


Fig. 3.8. Bright-field XTEM image in underfocus condition showing He bubbles in Al_2O_3 . The average bubble size and the number of bubbles per unit of surface area are deduced from this image (see text).

The PBA results (Fig. 3.6) seem to disagree with the TEM results (Fig. 3.7) on the depth of the ion implantation layer. The peak in the S parameter is found at a positron implantation energy corresponding to a depth of 100-200 nm, while the depth of the helium implantation layer is 230-340 nm as observed by means of TEM. The reason for this difference is that the peak in the S parameter curve does not exactly correspond to the helium implantation layer. As is clear from Fig. 3.7, there are relatively large bubbles present at a depth of 100-200 nm, above the ion implantation layer. To a first approximation, the pressure in the bubbles is inversely proportional to the size, $p=2\gamma/R$, with R the radius of the bubbles [Van Veen 1991]. Therefore, the He pressure is lower in the large bubbles, so that efficient positronium formation takes place, which contributes strongly to the high S parameter at this depth [Hakvoort et al. 1995]. Simultaneously, positronium is not formed or formed to a lesser extent in the smaller, higher-pressurised He bubbles in the ion implantation layer. Therefore, the peak present in the S parameter curve in Fig. 3.6 does not correspond to the ion implantation layer itself.

Fig. 3.8 shows a magnification of the bubbles in the implantation layer in a thin part of the specimen. Considering that the image is a cross-section, it is clear that the bubbles are shaped in the form of discs lying parallel to the surface. The small bubbles are quite flat, the large bubbles are more three-dimensionally shaped, and sizes vary from a few to 16 nm. The reason that the bubbles are disc-shaped rather than spherical can have two causes. First, the interface energy can be different for different facets. So, if the $\text{Al}_2\text{O}_3\{0001\}$ surfaces have a very low surface energy, these facets will be relatively large. Second, there probably exist stresses in the material because of the ion implantation which might also influence the energy balance, inducing a non-spherical shape of the bubbles. The volume of 52 bubbles in Fig. 3.8 was calculated taking account of the disc-like shape of the bubbles. With the size defined as the cube root of the bubble volume, the average size was determined as 5.5 nm. Therefore, the average bubble volume, V_b , is 165 nm^3 . It should be noted that large bubbles are much easier to observe than small bubbles, which leads to an overestimate of the average bubble volume.

The bubble concentration *inside the ion implantation layer* was also estimated from Fig. 3.8, at 1.4×10^{17} bubbles cm^{-3} . Here it was assumed that the part of the specimen displayed in Fig. 3.8 is 30 nm thick (in the direction perpendicular to the image). Since the ion implantation layer is 110 nm thick in depth (Fig. 3.7), the planar bubble concentration *in the sample* is 1.54×10^{12} bubbles cm^{-2} . Now that the bubble concentration and bubble size are known, the number of vacancies constituting the bubbles can be calculated. Using the numbers above and the atomic density of Al_2O_3 (1.2×10^{23} atoms cm^{-3}), the total number of vacancies in the sample is found as 3.0×10^{16} cm^{-2} . Considering that the implanted He dose was 2×10^{16} cm^{-2} , this means that there are 1.5 displacements per He ion that have survived after annealing at 1250 K. From an empirical point of view this is a very reasonable value. It should be realised that all the bubbles displayed in Fig. 3.7 and Fig. 3.8 are still filled with helium. This is proven by the NDP/desorption results presented below.

3.2.5. He desorption from bubbles in Al_2O_3

Fig. 3.9 shows the normalised retained He content in the samples as a function of annealing temperature, measured by means of NDP. All four samples (high and low dose) follow the same trend. The largest decrease in helium content is observed after the 1750 K annealing step for all four doses. However, the desorption process is slower for the low-dose ($< 10^{16}$ cm^{-2}) implanted samples than for the samples implanted with higher He doses. We shall now discuss the experimental desorption results using the same permeation model applied to He desorption in MgO. Therefore, we simulate the He release again using Eq. (3.8), which we repeat here:

$$\frac{N_{\text{He}}}{N_0} = e^{-ft}, \text{ with } f = \frac{\lambda^2 \omega}{12\pi L} \frac{c_{\text{Al}_2\text{O}_3}}{d_c} \left(\frac{2\pi\hbar^2}{mkT} \right)^{3/2} \left(\frac{kT}{\hbar\omega} \right)^3 e^{-E_{\text{perm}}/kT} \quad (3.9)$$

(see Subsection 3.1.5 for a derivation of the formula and for definitions of the symbols). For the case of Al_2O_3 , the atomic concentration $c_{\text{Al}_2\text{O}_3}$ is 1.18×10^{29} atoms m^{-3} , the thickness L of the top layer is 230 nm, the jumping distance λ is 2.0 Å, and the fundamental attempt frequency ω is taken as 10^{12} s^{-1} . The effective thickness of the bubble layer is again denoted by d_c . Note that N_{He}/d_c represents the density of helium in the cavities. The effective thickness is in fact the total bubble volume per unit area and can be written

$$d_c = N_b V_b / A \quad (3.10)$$

if it is assumed that all bubbles have the same diameter. Here N_b is the number of helium bubbles, V_b the bubble volume and A the area of the bubble layer (1.0 cm^2).

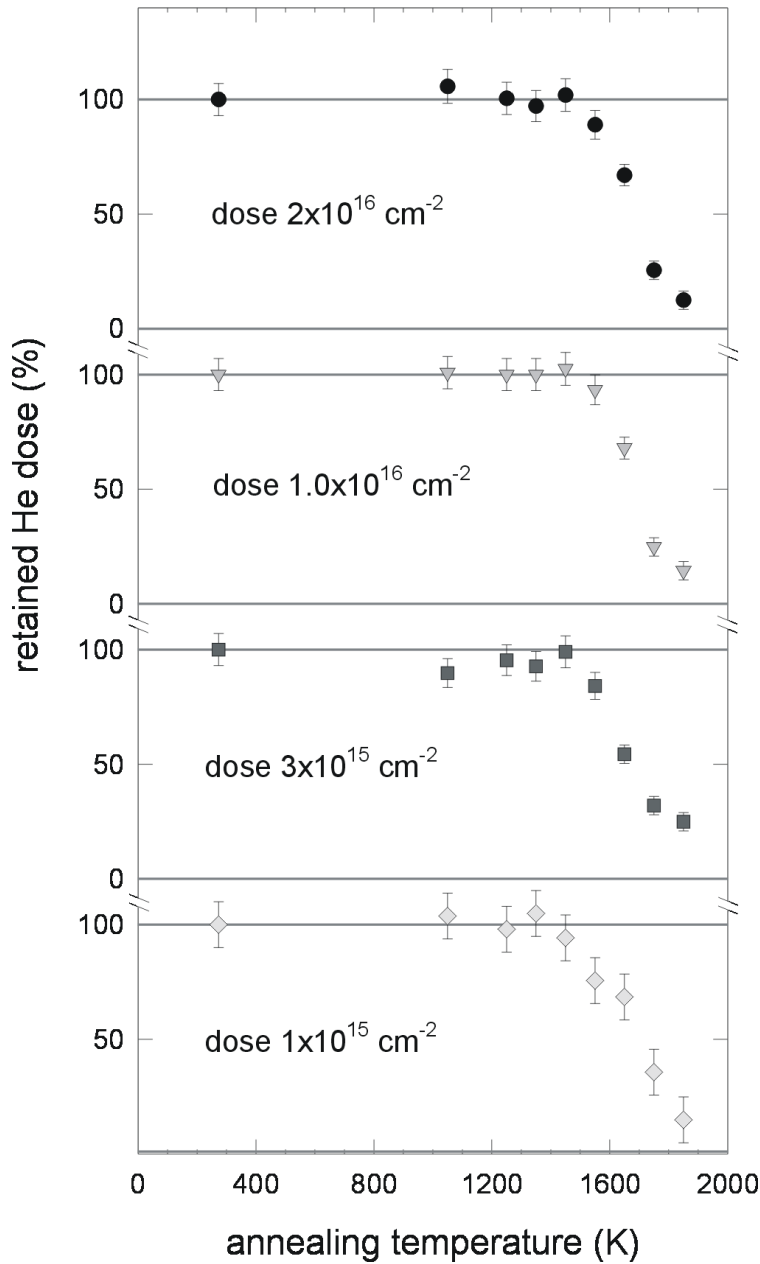


Fig. 3.9. Normalised concentration of He in the sample as observed by NDP, after implantation and during the annealing treatment for the four indicated implantation doses.

In the previous subsection, N_b and V_b were calculated from the TEM analysis as 1.54×10^{12} and 165 nm^3 , respectively. Substitution of Eq. (3.10) into Eq.(3.9) yields the following expression:

$$\frac{N_{He}}{N_0} = e^{-ft}, \text{ with } f = \frac{\lambda^2 \omega}{12\pi L} \frac{A c_{Al_2O_3}}{N_b V_b} \left(\frac{2\pi\hbar^2}{mkT} \right)^{3/2} \left(\frac{kT}{\hbar\omega} \right)^3 e^{-E_{perm}/kT}. \quad (3.11)$$

The desorption curves can now be fitted by variation of the permeation energy E_{perm} . Fig. 3.10 shows the results obtained using the model above for a permeation energy of 4.0 eV.

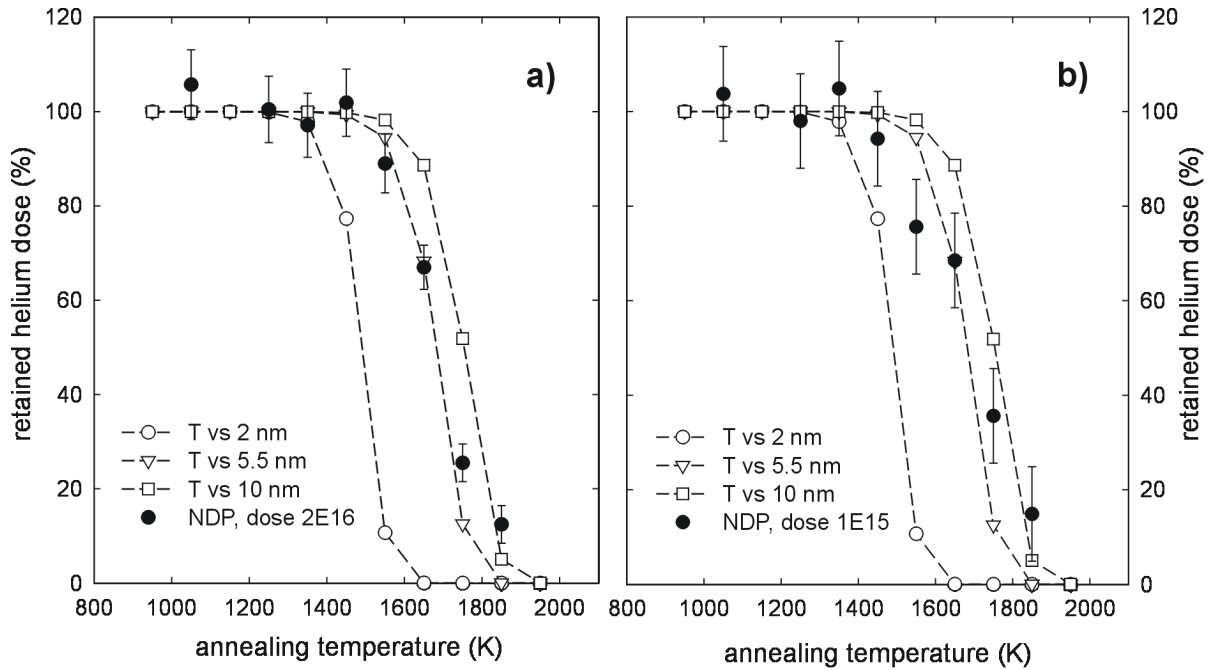


Fig. 3.10. Desorption curves (black symbols) for (a) the high-dose (2×10^{16} He cm⁻²) implanted sample and (b) the low-dose (1×10^{15} He cm⁻²) implanted sample. Added are the desorption curves (open symbols) obtained from the permeation model (Eq. (3.11)) with a permeation energy of 4.0 eV.

The experimental desorption curves for the highest (2×10^{16} cm⁻²) and the lowest helium dose (1×10^{15} cm⁻²) are shown in Fig. 3.10(a) and (b), respectively. In order to show the effect of bubble size distribution and, therefore, of a different pressure inside the bubbles, bubble diameters of 2, 5.5 and 10 nm have been substituted into Eq.(3.11) with the number of bubbles, N_b , fixed to the value given above. The experimental desorption curve falls off slower than the theoretical curves corresponding to the permeation model.

Two reasons can be given for this behaviour. First, there is a bubble size distribution as observed in Fig. 3.8. In this case, the desorption is a multi-stage process where helium is first released from high-pressurised small helium bubbles and later from low-pressurised, large helium bubbles. Second, the annealing is a dynamic process during which the average bubble size and the size distribution are changing. At low temperatures, small bubbles are formed, which will either dissociate (yielding desorption at low temperature) or agglomerate into large bubbles (yielding desorption at higher temperatures). The fact that the desorption curve of the lowest-dose sample falls off much slower than the curve of the high-dose sample (Fig. 3.9) indicates that the size distribution is broader in the case of the low-dose sample.

3.2.6. Conclusions

At a sufficiently high dose, helium bubbles are formed in He ion implanted Al_2O_3 , which reach a maximum volume after annealing at a temperature of 1250K. TEM observations show that after annealing at this temperature, the bubbles are shaped as discs lying parallel to the surface, and that the average bubble size is 5.5 nm for the sample implanted with the highest dose (2.0×10^{16} He ions cm^{-2}). At higher temperatures, bubble shrinkage sets in until no bubbles are observed by means of positrons after annealing at 1650 K. This means that the bubbles have shrunk below the size of a few nm. Helium is released from vacancy-type defects in the Al_2O_3 matrix in the temperature range of 1650-1850 K, which can be explained by a permeation model combined with a bubble size distribution. The activation energy for permeation is estimated at 4.0 eV. Bubble dissociation and He release occur simultaneously, which is very different from the situation in MgO where large, empty voids are left behind when He is released.

3.3. Formation of solid Kr nanoclusters in MgO

3.3.1. Introduction

When certain requirements with respect to the positron affinity are fulfilled, the vast majority of the positrons becomes trapped in embedded nanoclusters, thereby becoming a self-seeking probe for nanocluster material. The three-dimensional spatial confinement of the positron wavefunction in the nanoclusters is called 'positron confinement'. As explained in Section 2.7, quantum confinement of positrons allows the investigation of the electronic structure of the nanoclusters. Host-nanocluster systems successfully investigated are, e.g., Li in MgO [Van Huis et al. 2002, Falub et al. 2002] and Cu in Fe [Nagai et al. 2000, Nagai et al. 2001]. However, positron confinement only takes place when the positron affinity of the nanocluster is lower than the positron affinity of the host material. Looking through the literature that predicts the positron affinity for almost all metals [Puska et al. 1989a], a number of semiconductors [Panda et al. 2000], a few insulators [Van Huis et al. 2002, Kuriplach et al. 2002], and rare gases [Puska et al. 1992], it is obvious that the solid noble gases have by far the lowest positron affinity of all elements (less than -10 eV), which makes them most interesting candidates for further pursuit and exploitation of the phenomenon of positron confinement.

In this section, we present the observation of solid Kr nanoclusters by means of transmission electron microscopy (TEM). We have also investigated positron trapping in this host-nanocluster system. Solid Kr clusters created by means of ion implantation have already been observed in the metals Ti, Ni, Cu, Mo, and Au [Evans et al. 1985, Evans et al. 1986], in

graphite and Grafoil [Tan et al. 1991] and once in MgO [Norton et al. 1992]. Most of the work on solid Kr mentioned above concerns the analysis of diffraction patterns in transmission electron microscopy (TEM) and X-ray absorption studies. To our knowledge, we are the first to show solid Kr clusters in the TEM in high-resolution mode, similar to the high-resolution work already performed on solid Xe clusters [Birtcher et al. 1999].

3.3.2. Experimental

Several epi-polished MgO(100) single crystals of size $10 \times 10 \times 1 \text{ mm}^3$ were implanted at room temperature with 280 keV Kr ions to a dose of $3 \times 10^{16} \text{ ions cm}^{-2}$ and subsequently annealed in ambient air for periods of 30 min. at temperatures of 900 K and 1100 K, respectively. After ion implantation and after each annealing step, the evolution of the ion implantation defects was monitored with the aid of optical absorption spectroscopy and Doppler broadening positron beam analysis (PBA) [Van Veen et al. 2000] using a mono-energetic positron beam with a variable acceleration energy of 0-30 keV. Cross-sectional transmission electron microscopy (XTEM) was applied after the 1100 K annealing step. The TEM was performed using a JEOL 4000 EX/II operating at 400 kV (point-to-point resolution 0.17 nm). The specimen preparation is discussed in Section 2.6.1 [Kooi et al. 2000]. The sample treatment and principal observations are listed in Table 3.5.

3.3.3. Structural properties and defect evolution

First, the results of optical absorption spectroscopy will be presented, followed by the XTEM results, focussing on both the solid Kr nanoclusters and the defects created in the MgO. The result of positron beam analysis is shown as an additional method of obtaining depth-resolved information on the defect evolution in the composite material during the sample treatment. Possible trapping in Kr nanoclusters is discussed in terms of positron affinity.

Table 3.5. Sample treatment and most important experimental observations.

Sample treatment	
Ion implantation	$3 \times 10^{16} \text{ Kr ions cm}^{-2}$ at an energy of 280 keV.
Thermal anneal	at 900 K and 1100 K for a period of 30 min.
Results	
Optical absorption	F- and V-centres present after implantation; dissociation after 900 K anneal.
XTEM	Cubical, solid Kr clusters at 70-130 nm depth, cluster size 2-4 nm. Cubical nanovoids at 15-30 nm depth, cluster size 2-5 nm.
PBA	Defect agglomeration during annealing. High S parameter in nanovoids layer, S parameter in Kr cluster layer higher than that of bulk MgO and lower than the S parameter of MgO with defects.

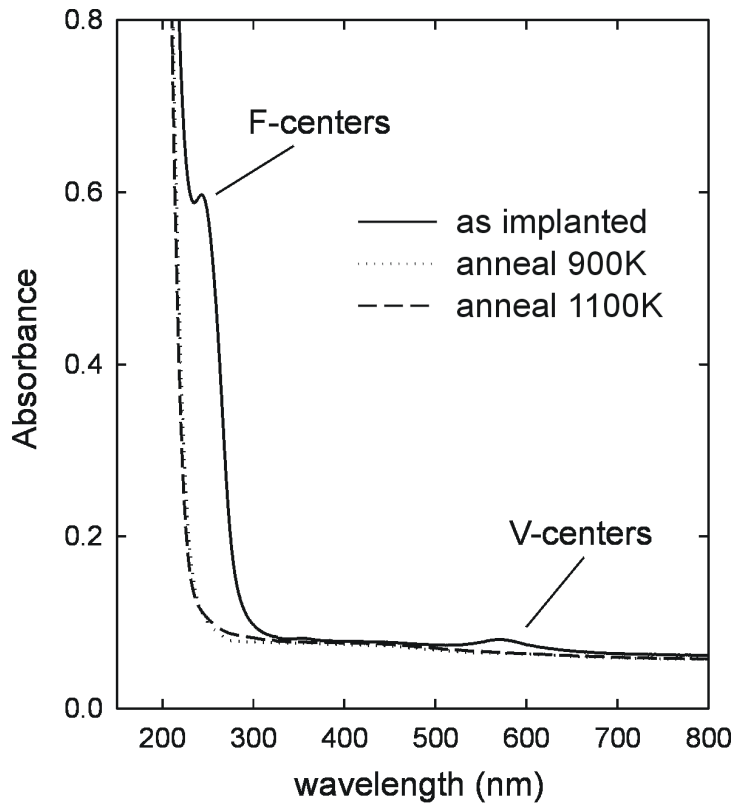


Fig. 3.11. Optical absorption spectra of an MgO(100) crystal implanted with 280 keV 3×10^{16} Kr ions cm^{-2} , as implanted and after annealing in air at various temperatures.

Optical absorption spectroscopy

The results of the optical absorption spectroscopy are displayed in Fig. 3.11. After ion implantation, two types of defects can be distinguished. There is an absorption peak at a wavelength of 570 nm which can be attributed to V-centres (Mg vacancies), while at a wavelength of 250 nm there is another absorption peak attributed to F-centres (O vacancies) [Qian et al. 1997]. Both absorption peaks vanish after annealing at 900 K.

Cross-sectional TEM

Cross-sectional transmission electron microscopy (XTEM) was performed on a sample after the 1100 K anneal step. Fig. 3.12 shows an overview image. The region between 70 and 130 nm depth is a subsurface layer, which contains Kr nanoclusters. The rectangular area in Fig. 3.12 (marked with the white corners) is enlarged in the HRTEM image of Fig. 3.13. Here the Kr nanoclusters can be clearly observed. The clusters are rectangularly shaped and their sizes vary from 2 to 5 nm. Moiré fringes are present due to the lattice mismatch between solid Kr and MgO. The morphology of the nanoclusters is determined by the interface energy corresponding to the various MgO//Kr interface facets; if the interface energies are known the shape of the cluster can be constructed using the Wulff diagram [Lüth 1995, Backhaus-Ricoult 2001]. In this particular case it is clear that the $\{100\}$ interface is energetically favoured over the $\{110\}$ and $\{111\}$ interfaces. The interface energy equals the sum of the surface energies of MgO and Kr minus the work of adhesion:

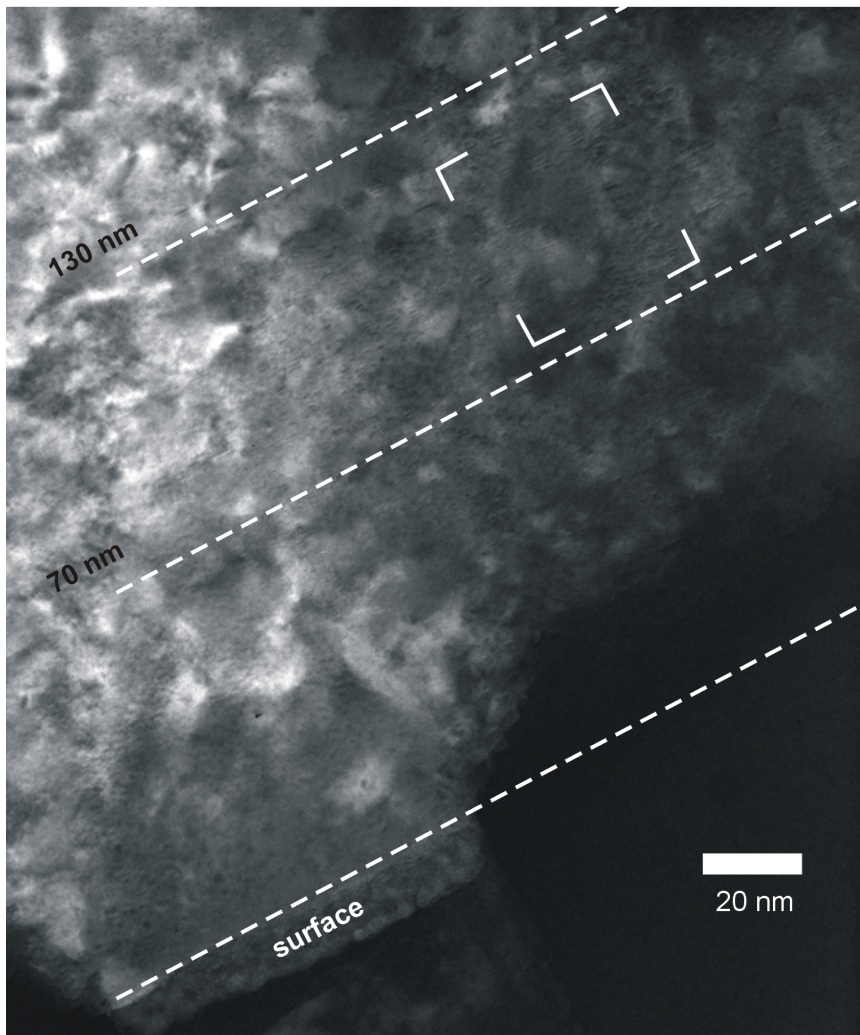


Fig. 3.12. TEM overview image of Kr-implanted MgO. Solid Kr nanoclusters are observed in a band at a depth of 70-130 nm. The white corners indicate the area shown in more detail in Fig. 3.13.

$$\gamma_{MgO//Kr} = \gamma_{MgO} + \gamma_{Kr} - W_{ad}. \quad (3.12)$$

Considering that the Van der Waals bonding of the noble gas Kr atoms is very weak, the interface energy of Kr and the work of adhesion will be negligible with respect to the surface energy of MgO, i.e., the MgO//Kr interface energy approximately equals the MgO surface energy. Watson *et al.* [Watson et al. 1996] calculated surface energies of 1.25 Jm^{-2} for MgO {100}, 1.87 Jm^{-2} for MgO{110}, and 2.5 Jm^{-2} for MgO{111}. The last two values are valid for microfaceted surfaces, but the surface energies for unafaceted {110} and {111} MgO surfaces are even higher [Watson et al. 1996]. Considering the Wulff diagram [Lüth 1995, Backhaus-Ricoult 2001] the absence of the {110} facets in the rectangular Kr nanoclusters means that the MgO{110} surface energy should be at least $\sqrt{2}$ times larger than the MgO{100} surface energy, which is in agreement with the theoretical values given above.

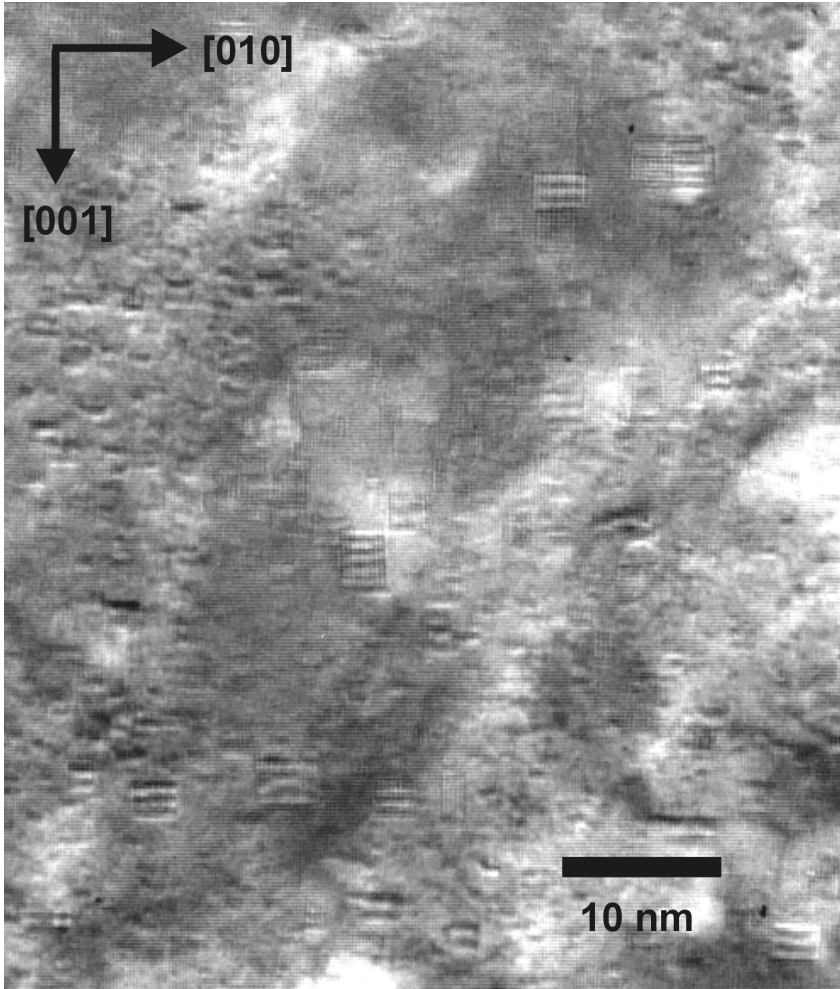


Fig. 3.13. Solid Kr nanoclusters at a depth of 75-120 nm with moiré fringes caused by the lattice mismatch between solid Kr and MgO.

Fig. 3.14 shows a magnification of the large cluster present in the centre of Fig. 3.13. There are 5 moiré fringes in 18 MgO lattice spacings. Since Kr is fcc in fcc host matrices [Evans et al. 1986] and the Kr clusters are in a cube-on-cube orientation relationship with the MgO, the following relationship can be used to calculate the lattice parameter of solid Kr, a_{Kr} :

$$\frac{1}{d_{\text{fringes}}} = \left| \frac{1}{d_{\text{MgO}}} - \frac{1}{d_{\text{Kr}}} \right|. \quad (3.13)$$

With a lattice parameter a_{MgO} of 4.212 Å ($d_{\text{MgO},200} = 2.106$ Å), this yields $d_{\text{Kr},200} = 18/(18-5) \cdot d_{\text{MgO},200} = 2.9$ Å and thus the lattice parameter for solid Kr, a_{Kr} , equals 5.8 Å. This corresponds to the lattice parameter of frozen Kr at a temperature of 110 K [Macrander 1980]. In a similar fashion, the Kr lattice parameters in the other clusters present in Fig. 3.13 can be analysed and values of 5.3-5.8 Å are found. These values for a_{Kr} correspond reasonably well to the values of 5.0-5.5 Å reported in the literature [Evans et al. 1985, Norton et al. 1992].

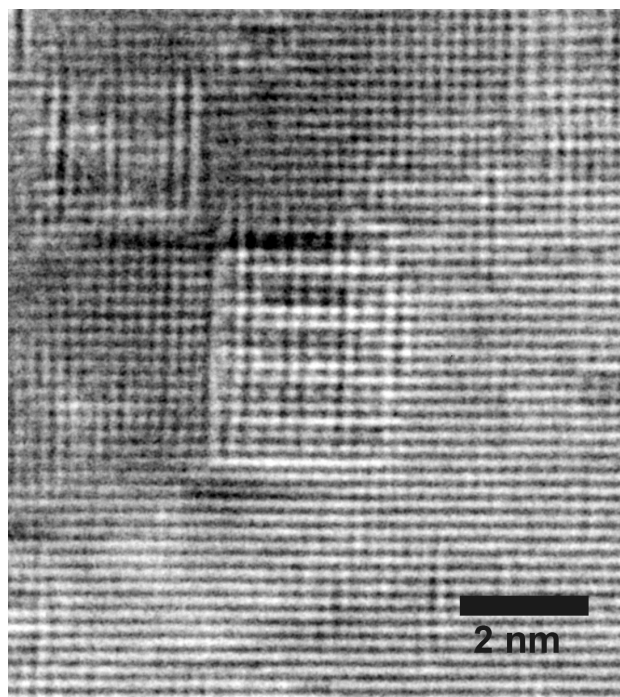


Fig. 3.14. High-resolution TEM image of a solid Kr nanocluster (also present in the centre of Fig. 3.13). The lattice parameter of the solid Kr can be derived from the moiré fringes (see text).

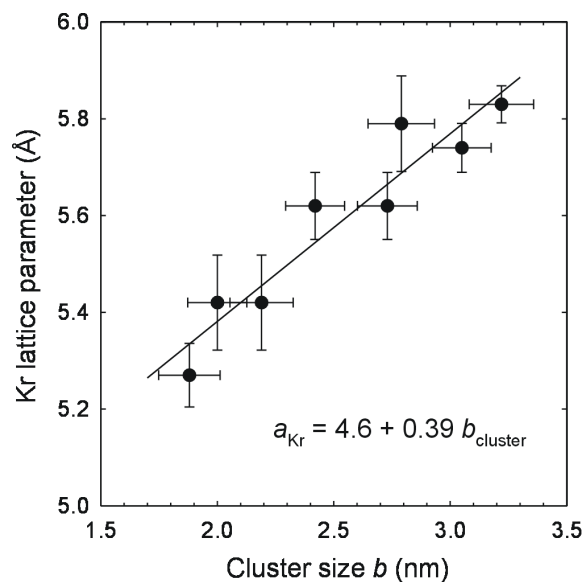


Fig. 3.15. Relationship between the Kr lattice parameter and the cluster size.

The important advantage of the use of moiré fringes in comparison with the experimental methods mentioned in the introduction is that the lattice parameter can be determined for every Kr cluster separately. In Fig. 3.15, the Kr lattice parameter is plotted as a function of the cluster size. It is clear that there is a positive correlation between a_{Kr} and the cluster size; the straight line plotted in the figure is a linear least-squares fit to the data. The cluster size (defined as the cube root of the nanocluster volume) cannot be determined accurately since the cluster dimension perpendicular to the plane in Fig. 3.13 or Fig. 3.14 cannot be determined. Therefore, the cluster size was estimated as the square root of the cluster area visible in the figures. The lattice parameter in small clusters is smaller due to the higher pressure in small clusters. The lattice parameter can be related to the pressure using the Ronchi equation of state (EOS). A lattice parameter of 5.3-5.8 Å for fcc Kr corresponds to a molar volume of 22-30 cm³. Using the EOS for solid Kr [Ronchi 1981] at a temperature of 300 K, the pressure in the largest cluster is 0.6 GPa and the pressure in the smallest cluster 2.5 GPa. These pressures are in reasonable agreement with the minimum pressure of 0.83 GPa necessary for the formation of solid Kr [Norton et al. 1992]. It is also in good agreement with the following equations, which describe the relationship between pressure and interface energy. The energy of the cluster system is minimised when

$$dE = p dV - \gamma dS = 0 \Rightarrow \frac{dE}{da} = p \frac{dV}{da} - \gamma \frac{dS}{da} = 0. \quad (3.14)$$

For the case of a cube of size b , volume $V = b^3$ and surface $S = 6b^2$, it follows that

$$p = \frac{4\gamma}{b}. \quad (3.15)$$

Since the interface energy is completely determined by the surface energy of MgO (see Eq. (3.12) and the discussion above), the pressure in the cluster can be calculated. It should be realised that Eqs. (3.14) and (3.15) are only valid if the material is in thermal equilibrium at the temperature at which the clusters were formed. The pressure and surface energy mentioned in Eq. (3.15) should therefore be considered at 1100 K. The MgO{100} surface energy at 1100 K is 1.17 Jm^{-2} [Taylor et al. 1999]. Using Eq. (3.15), a cluster size of 3 nm then yields a pressure of 1.7 GPa at 1100 K. How can this pressure be compared with the pressures of 0.6-2.5 GPa found in the electron microscope at 300 K? MgO is a rather incompressible material with a linear thermal expansion coefficient which varies with temperature. Over the temperature interval of 300-1100 K, the average linear thermal expansion coefficient a_{lin} is $12 \times 10^{-6} \text{ K}^{-1}$ [Wengeler et al. 1981]. Since MgO is much less compressible than Kr, we assume that the shrinkage of the cluster is completely determined by the MgO. With $a_{\text{vol}} = 3a_{\text{lin}}$, the change in volume of the cluster is 2.9%. Therefore, the molar volumes of $22\text{-}30 \text{ cm}^3$ found at room temperature correspond to molar volumes of $23\text{-}31 \text{ cm}^3$ at 1100 K. Again using the Ronchi equation of state [Ronchi 1981] but now for a temperature of 1100 K, we find pressures of 1.5-4.6 GPa. This is in good agreement with the pressure of 1.7 GPa found from Eq. (3.15).

Fig. 3.16 shows an enlarged TEM image of the subsurface region down to a depth of 60 nm. It is clear that a band of rectangularly shaped nanovoids is present at a depth of 15-30 nm. These large vacancy clusters are 2-5 nm in size and are rectangularly shaped, similar to the nanovoids found previously in ion implanted MgO [Van Veen et al. 2002]. The rectangular shape is again caused by the different surface energies of the various MgO facets (see the discussion above on the rectangular shape of the Kr clusters). These voids are formed due to accumulation of vacancies created by the Kr implantation. It is, however, peculiar that this vacancy band is located so far away from the principal Kr cluster band, since normally the damage depth distribution and the Kr depth distribution from the same implantation overlap to a large extent. Fig. 3.17 shows the Kr depth distribution and the damage created by ion implantation simulated by means of the SRIM2000 code (see Subsection 2.1.2). Here, displacement energies of 55 eV were used for both Mg and O [Zinkle et al. 1997]. At the applied dose of $3 \times 10^{16} \text{ ions cm}^{-2}$, the peak value of the Kr concentration is 4.1 at. % while the peak damage level is 37 dpa (displacements per target atom).

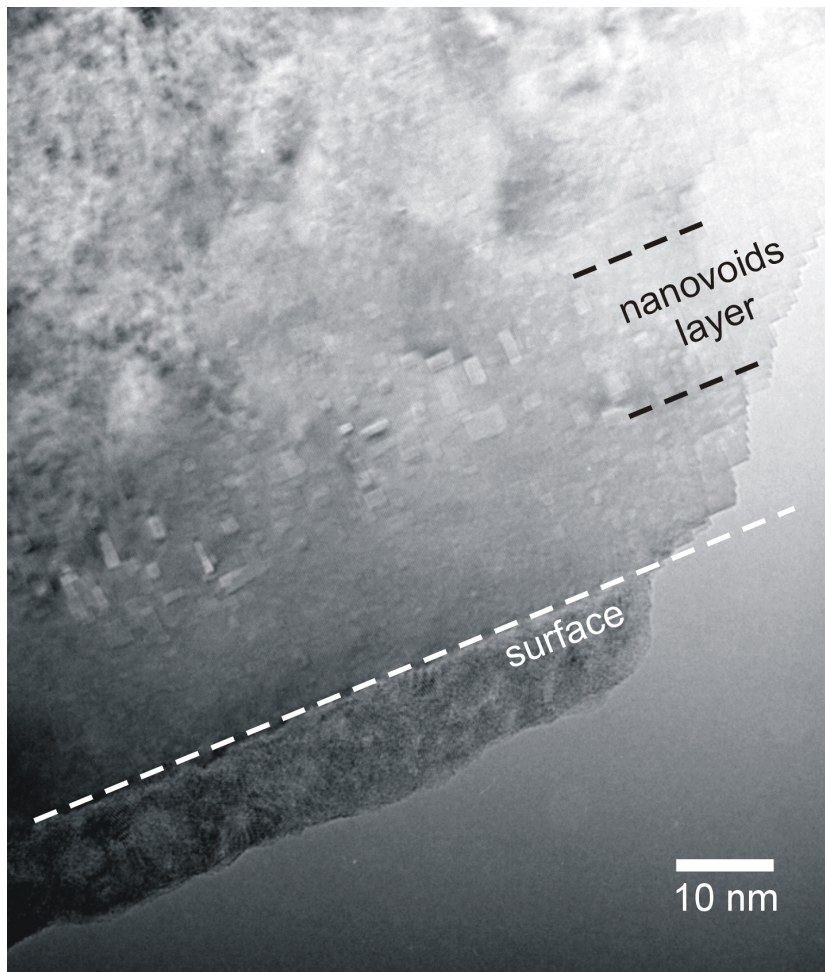


Fig. 3.16. TEM image showing the vacancy cluster band located at a depth of 15-30 nm.

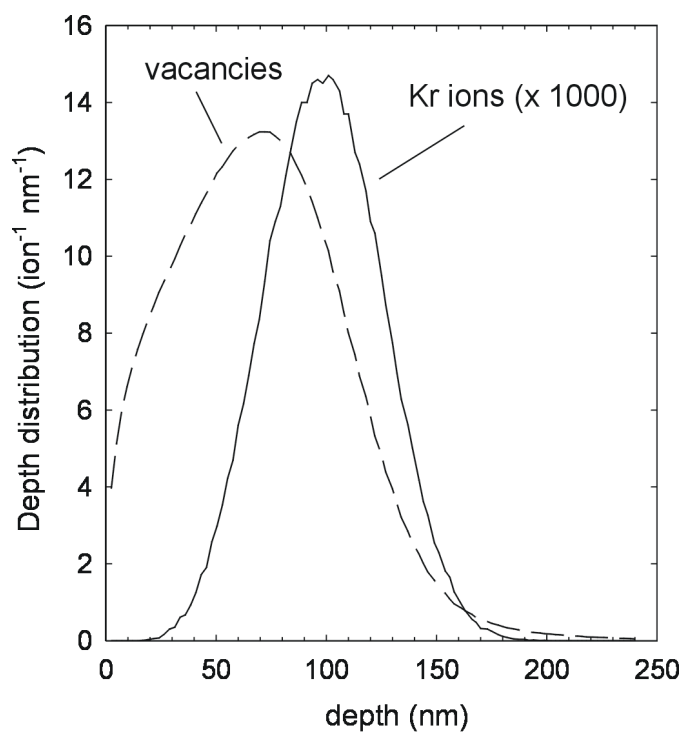


Fig. 3.17. Krypton depth distribution (after implantation, prior to thermal anneal) and damage depth distribution calculated using the SRIM2000 code [Ziegler et al. 1985].

First of all, it is clear that the predicted Kr depth distribution is in excellent agreement with the location of the Kr nanocluster layer at a depth of 70-130 nm observed with the aid of TEM in Fig. 3.12. It is also clear that the predicted damage depth distribution is located at a lesser depth than the predicted Kr distribution. However, this does not explain the presence of a distinct vacancy cluster band at a depth of 15-30 nm observed by TEM: in the SRIM simulation the vacancy and the Kr distribution are not separated but overlap to a large extent. A possible explanation is that the vacancies and the Kr atoms recombine at the intermediate depth range of 30-70 nm: the presence of Kr in the vacancy clusters slows down the mobility of Kr-filled vacancy clusters so that large vacancy clusters are not formed. At the same time, the concentration of Kr in this intermediate layer is not high enough to form solid Kr nanoclusters large enough to be observed by means of TEM.

Positron beam analysis

The defect evolution during the annealing procedure was monitored by Doppler broadening positron beam analysis (PBA) [Van Veen et al. 2000]. As already discussed in Section 2.7, annihilation of positrons with electrons in solids yields information on the momentum distribution of these electrons. The electronic momentum distribution is reflected in the Doppler broadening of the 511 keV annihilation peak. Positron annihilation with low-momentum valence or conduction electrons results in a small Doppler shift, contributing to the centre of the peak. Annihilation with high-momentum core electrons results in a large Doppler shift, contributing to the wings of the 511 keV annihilation peak. The shape of the 511 keV peak is characterised by the so-called *S* (shape) parameter, which gives the ratio of the number of counts in the centre of the peak to the number of counts in the whole peak [Van Veen et al. 2000, Van Huis et al. 2002]. By using a mono-energetic positron beam of variable energy, the *S* parameter can be recorded as a function of depth. However, at larger depths the depth resolution decreases due to broadening of the implantation profile of the implanted positrons.

The *S* parameter is displayed in Fig. 3.18 as a function of positron implantation energy. The average positron implantation depth is indicated at the top of the figure. The solid lines show the results of the VEPFIT simulation to be discussed below. It is clear that after implantation, the *S* parameter increases in the ion implantation zone with respect to reference MgO and it increases further over a wide range of depths after annealing at 900 K and 1100 K. The *S* parameter in ion-implanted MgO always increases after ion implantation due to the efficient formation of vacancy-type defects in the Schottky material MgO [Van Veen et al. 2002]. It is observed that the *S* parameter increases after annealing at 900 K. At this temperature, the optical F- and V-centres dissociate as observed with optical absorption spectroscopy (see Fig. 3.11). This clearly indicates aggregation of vacancy-type defects (the larger the vacancy clusters, the larger the *S* parameter).

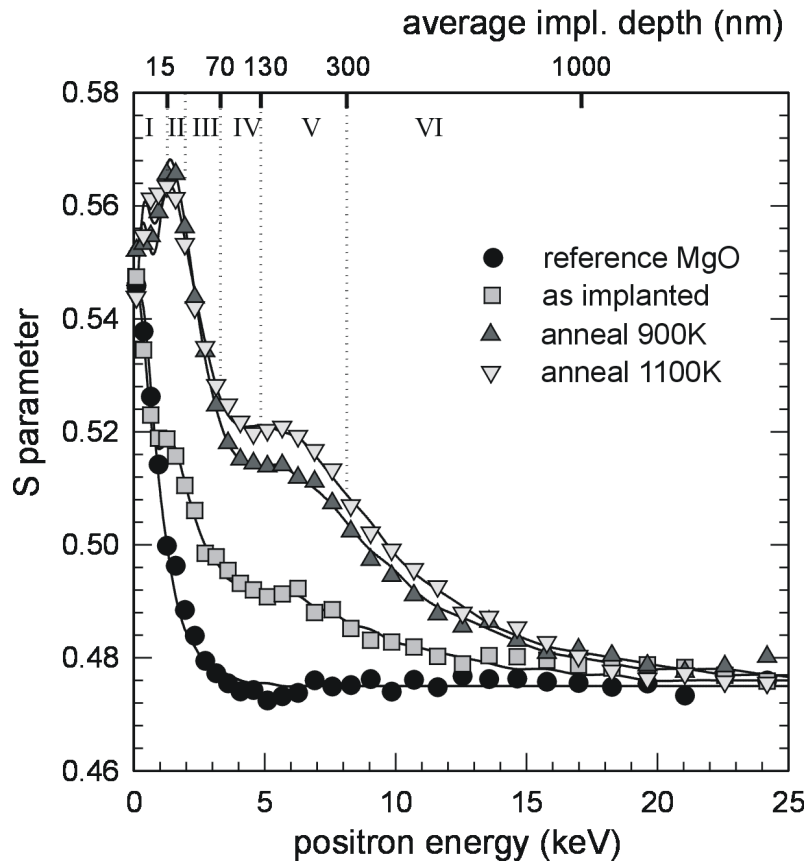


Fig. 3.18. S parameter vs. positron energy measured for reference MgO and for MgO:Kr after implantation and after two thermal annealings. The scale at the top of the graph indicates the average positron implantation depth. The Roman numerals are the layer numbers (see Table 3.6) and the solid lines are the result of VEPFIT fitting (see text).

The peak at 1.5 keV positron implantation energy in Fig. 3.18 can be attributed to the presence of the vacancy cluster band that was observed with TEM in Fig. 3.16. These voids are large enough to form positronium (Ps), a hydrogen-like bound state of a positron (e^+) and an electron (e^-). Positronium formation leads to a dramatic increase in the S parameter [Van Veen et al. 2000]. In order to analyse the PBA results in more detail, the VEPFIT code [Van Veen et al. 1990] was used to find the S parameter corresponding to every defect layer. The S parameter found at a certain positron energy in Fig. 3.18 consists of contributions of various layers due to the broadness of the positron implantation profile (which increases with increasing positron energy) and positron diffusion processes.

The VEPFIT code takes these effects into account and yields the depth-resolved S parameters for every defect layer. Based on the TEM observations, a six-layer model was used as defined in Table 3.6. The chosen diffusion lengths are reasonable estimates. When considering the number of clusters in Fig. 3.13 and Fig. 3.16, it is clear that in that region the diffusion length will be 5 nm or less. The layers and the corresponding depths are indicated at the top of the graph in Fig. 3.18. Layer V at a depth of 130-300 nm is the so-called ion implantation tail. Due to channelling effects, the implantation damage in MgO extends much further than the maximum range predicted by SRIM (Fig. 3.17) as this code assumes the atoms in the target material to be randomly distributed.

Table 3.6. Model used for VEPFIT simulation. Note that the S parameters of layers I, III and V are fitted with the same parameter.

Layer	description	depth (nm)	S parameter	diffusion length (nm)
I	MgO with defects	0-15	S_{def} (fitted)	5
II	nanovoids	15-30	S_{voids} (fitted)	5
III	MgO with defects	30-70	S_{def} (fitted)	5
IV	Kr clusters	70-130	S_{Kr} (fitted)	5
V	MgO with defects	130-300	S_{def} (fitted)	20
VI	MgO bulk	>300	$S_{\text{MgO}}=0.475$	100

Only for the S parameter curve of reference (non-implanted) MgO, a single-layer model was used with the S parameter value of bulk MgO, 0.475. The solid lines in Fig. 3.18 are the result of VEPFIT fitting and it is clear that the model discussed above is able to fit the experimental S parameter curves. Fig. 3.19 shows the depth-resolved S parameters found using VEPFIT for the sample after the 1100 K annealing step (where XTEM was also performed). As expected, the S parameter in the nanovoids layer (layer II) is rather high, 0.59. The S parameter in the layer with Kr nanoclusters (layer IV) is lower than that of the adjacent layers but higher than that of bulk MgO. This explains the 'dip' in the S parameter curve in Fig. 3.18 at 4.5 keV positron implantation energy. The fact that the S parameter in the layer with Kr nanoclusters is not much different from that of adjacent layers points to little interaction of positrons with Kr nanoclusters. The reason that the S parameter in the nanocluster layer is lower than in the adjacent layers (Fig. 3.18 and Fig. 3.19) is probably due to Kr filling of vacancy-type defects. Thus, there are fewer open-volume defects for the positrons to trap in and the value of the S parameter is closer to that of bulk MgO.

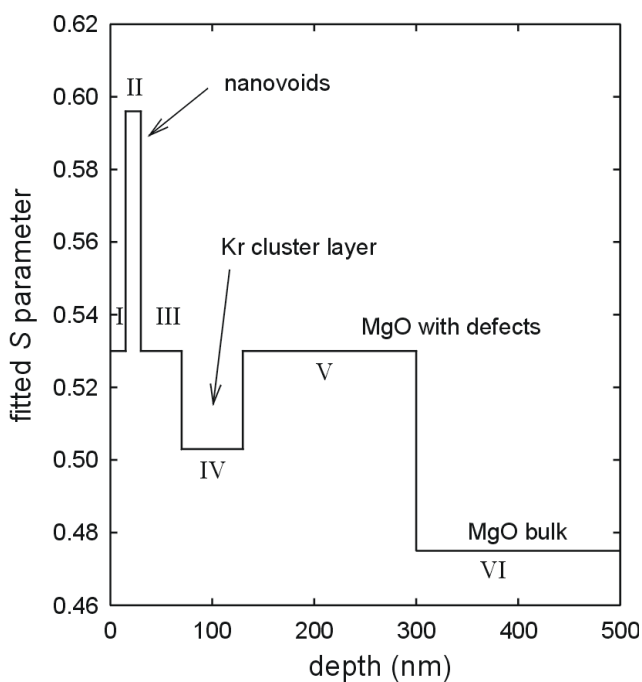


Fig. 3.19. Depth-resolved S parameter as a function of depth in the sample after the 1100 K annealing step, obtained using the VEPFIT code. The applied six-layer model is given in Table 3.6. The layers are labelled with Roman numerals.

In order to investigate the behaviour of positrons with respect to the nanoclusters in more detail, a 2D-ACAR (two-dimensional angular correlation of annihilation radiation) experiment was carried out on the nanoclusters after the 1100 K annealing step. 2D-ACAR allows a detailed investigation of the electronic structure of a material [West 1995, Falub et al. 2002, Nagai et al. 2001]. Experimental details of the set-up can be found in Refs. [Falub et al. 2000, Falub et al. 2001], where positron confinement in Li nanoclusters in MgO is investigated. The positrons were implanted at 4.5 keV energy, corresponding to implantation at the centre of the Kr nanocluster layer. No anisotropic contribution other than that of MgO could be observed in the 2D-ACAR spectrum after accumulation of 7×10^6 2γ -coincidence events [Eijt et al. (pc)], thus supporting the idea of negligible trapping in and interaction with Kr clusters. This runs counter to the expectation that positrons are very effectively trapped in Kr nanoclusters because of the very low positron affinity of solid Kr [Puska et al. 1992] compared to that of MgO [Van Huis et al. 2002]. So why do the Doppler broadening and 2D-ACAR results not provide evidence of positron trapping in the Kr nanoclusters?

3.3.4. Positron trapping in Kr nanoclusters

Whether positrons trap in nanoclusters depends on the positron affinity [Puska et al. 1989, Van Huis et al. 2002, Nagai et al. 2000], as discussed in Section 2.7. Consider Fig. 3.20. When the Fermi levels of two metals in contact become equal, the difference between the positron ground state levels of the two materials is

$$\Delta E_{AB,+}^{METAL} = E_{0,+}^A - E_{0,+}^B = \mu_+^A - \mu_+^B + \mu_-^A - \mu_-^B. \quad (3.16)$$

The positron affinity can then be defined as

$$A_+^{METAL} = \mu_+ + \mu_- = -(\phi_+ + \phi_-) \quad (3.17)$$

so that the positronic potential barrier at the host-nanocluster interface equals

$$\Delta E_+^{AB} = A_+^A - A_+^B, \quad (3.18)$$

(see Section 2.7 for a more extensive discussion). A necessary condition for positron quantum confinement in a cluster (A) embedded in a host (B) is that $\Delta E_+^{AB} < 0$. Then the cluster represents a three-dimensional potential well for positrons. If $\Delta E_+^{AB} > 0$, the cluster acts as a potential barrier. Finally, the possibility should be considered that positrons trap at the interface.

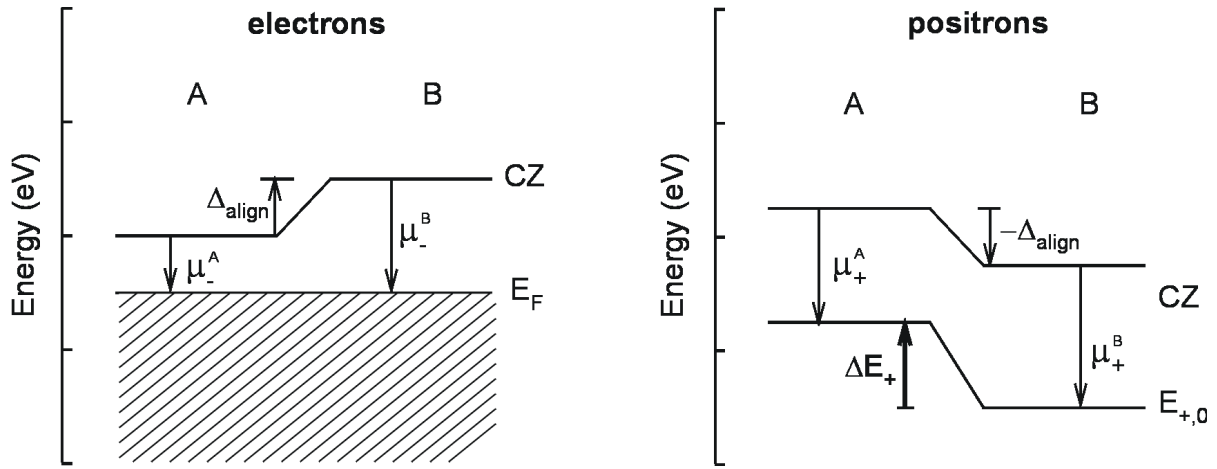


Fig. 3.20. Schematic diagram showing alignment of the Fermi levels for the case of two metals in contact. Note that the alignment shift of the crystal zeros is $\Delta = \mu_-^A - \mu_-^B$ for electrons and $-\Delta$ for positrons.

The question now arises whether the concept of positron affinity as defined in Eq. (3.17) can be applied to an insulator-insulator interface. The alignment of the Fermi levels is expressed in the term $(\mu_-^A - \mu_-^B) = \Delta_{align}^{METAL}$ on the right-hand side of Eq. (3.16), see also Fig. 3.20. This is true for metals where the position of the electronic chemical potentials coincides with the position of the Fermi levels. It is not true, however, for insulators. In insulators the electronic chemical potential is defined as the distance between the top of the valence band and the crystal zero [Puska et al. 1992] as depicted in Fig. 3.21. E_V is the top of the valence band, E_C is the bottom of the conduction band, and E_F is the Fermi level positioned in the middle of the band gap E_g . Fig. 3.21 shows the electronic and positronic energy levels for MgO and Kr in contact for the case that the Fermi levels are aligned. It follows from the figure that $\Delta_{align}^{INS} = (\mu_-^A + \frac{1}{2}E_g^A - \mu_-^B - \frac{1}{2}E_g^B)$. The energies and energy levels displayed in the figure are to scale. The numerical values of the electronic and positronic entities for MgO and Kr are listed in Table 3.7 and are mostly obtained from Refs. [Van Huis et al. 2002, Puska et al. 1992]. Considering Fig. 3.21, it is clear that the difference between the positron ground state potentials of the two materials is not described by Eq. (3.16), but by the following formula:

$$\Delta E_{AB,+}^{INS} = E_+^A - E_+^B = \mu_+^A - \mu_+^B + \mu_-^A - \mu_-^B + \frac{1}{2}E_g^A - \frac{1}{2}E_g^B. \quad (3.19)$$

Therefore, the positron affinity for insulators can be defined alternatively as

$$A_+^{INS} = \mu_+ + \mu_- + \frac{1}{2}E_g. \quad (3.20)$$

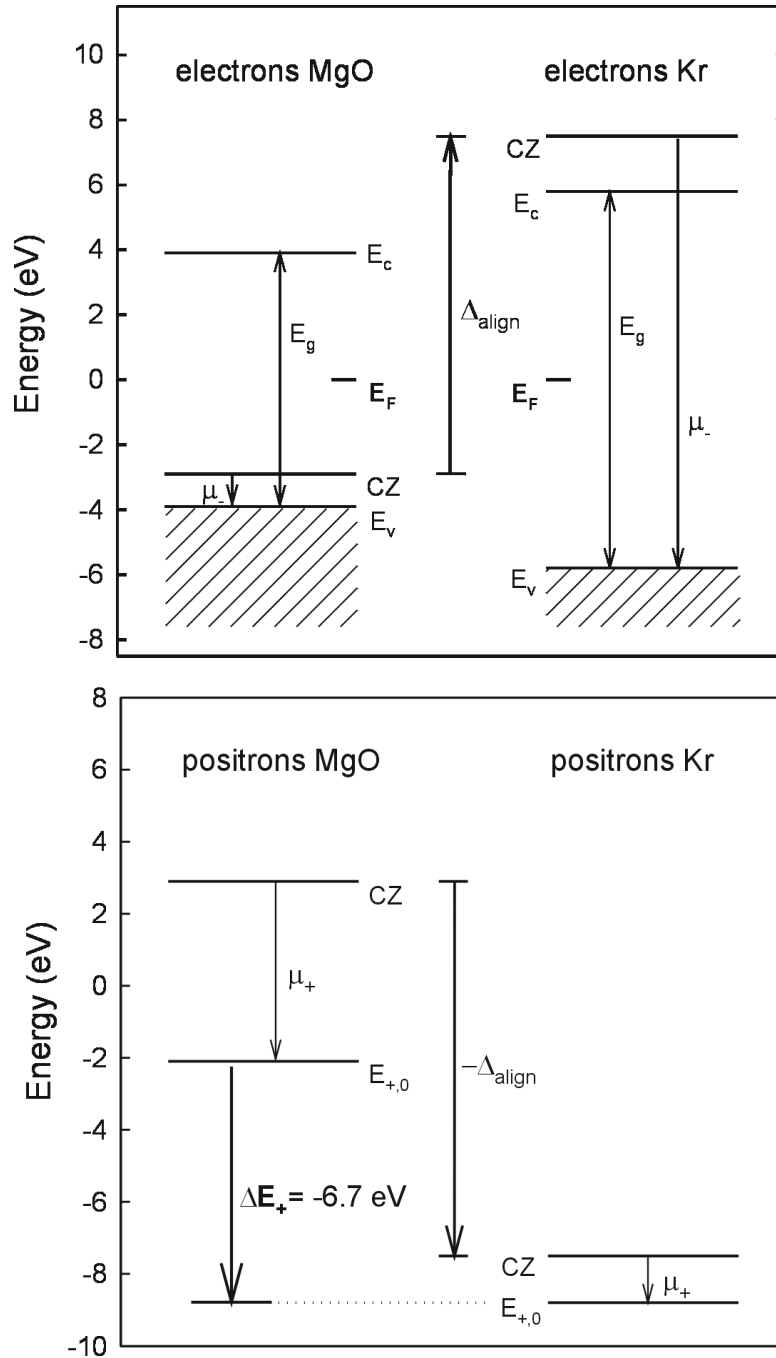


Fig. 3.21. Electronic and positronic energy levels for MgO in contact with solid Kr, based on the data listed in Table 3.7. The alignment of the Fermi levels is achieved by an energy shift $\Delta E_{align}^{INS} = (\mu_-^A + \frac{1}{2} E_g^A - \mu_-^B - \frac{1}{2} E_g^B)$ between the crystal zeros of the two materials.

so that Eq. (3.18) is still valid. Using Eq. (3.19) and the values gives in Table 3.7, we find a difference in positron ground state potentials $\Delta E_{AB,+}^{INS}$ of -6.7 eV. So $\Delta E_{AB,+} < 0$ and the Kr nanoclusters should act as potential wells, in contradiction with our experimental observations, which do not show evidence of positron trapping in Kr.

Table 3.7. Electronic and positronic data for MgO and Kr.

	MgO	Kr	Ref./Eq.
a_0 (Å)	4.212	5.72	^a , [Puska et al. 1992]
μ_- (eV)	-1.0	-13.3	^a , [Puska et al. 1992]
μ_+ (eV)	-5.0	-1.3	^a , [Puska et al. 1992]
ϕ_- (eV)	3.8	11.9	[Namba et al. 1984, Puska et al. 1992]
ϕ_+ (eV)	2.2	2.7	Eq. (2.8), [Puska et al. 1992]
Δ (eV)	2.8	-1.4	Eq. (2.7)
E_c (eV)	6.8	-1.7	^a , [Puska et al. 1992]
E_g (eV)	7.8	11.6	^a , [Puska et al. 1992]
E_F (eV) ^b	2.9	-7.5	$\mu_- + \frac{1}{2} E_g$
A^{METAL} (eV)	-6.0	-14.6	Eq. (3.17)
A^{INS} (eV)	-2.1	-8.8	Eq. (3.20)
$A^{\text{VAC}} = -\phi_+$ (eV)	-2.2	-2.7	Eq. (3.21)

^a Values obtained with the MgO II, GGA model in Ref. [Van Huis et al. 2002].

^b defined with respect to the crystal zero in Fig. 3.21.

One possible explanation is that the Fermi levels are not equalised. MgO and Kr are both insulators with large band gaps of 7.8 and 12 eV [Puska et al. 1992], respectively. When there are no electrons available to align the Fermi levels, thermal equilibrium cannot be established and the vacuum levels will be aligned instead [Nagashima et al. 1996]. In addition, it is well-known that the energy levels of rare-gas solids physisorbed onto various metal surfaces are aligned with the vacuum level [Lang et al. 1982, Hulse et al. 1980, Jacobi 1987]. Therefore, we have also considered alignment of the vacuum levels. This is achieved in a way analogous to the alignment procedure shown in Fig. 3.21. The result is that the difference between the positron ground states of the two materials is simply the difference between the positron work functions,

$$\Delta E_{AB,+}^{\text{VAC}} = -(\phi_+^A - \phi_+^B), \quad (3.21)$$

so that $-\phi_+$ takes the role of the positron affinity when the vacuum levels are aligned (compare with Eq. (3.18)). With the values given in Table 3.7, this yields -0.5 eV for $\Delta E_{AB,+}^{\text{VAC}}$, indicating that the nanocluster still acts as a (shallow) potential well. However, the differences in calculated energies between various theoretical models are approximately 1 eV [Puska et al. 1992, Van Huis et al. 2002]. Furthermore, we have combined experimental and theoretical results, and the electronic and positronic data for Kr given in Table 3.7 are only valid for a lattice parameter of 5.72 Å while in reality, there is a distribution of lattice parameters.

Table 3.8. Positronic potential difference between Kr cluster and MgO in contact assuming alignment of the Fermi levels in metals (Eq. (3.16)), in insulators (Eq. (3.19)), or assuming alignment of the vacuum levels (Eq. (3.21)). The data of Table 3.7 have been used to calculate the numerical values.

Level alignment	$\Delta E_+ = E_+^{Kr} - E_+^{MgO}$	result (eV)
Fermi (metals)	$\Delta E_+^{METAL} = (\mu_+^{Kr} + \mu_-^{Kr}) - (\mu_+^{MgO} + \mu_-^{MgO})$	N.A. ^a
Fermi (insulators)	$\Delta E_+^{INS} = (\mu_+^{Kr} + \mu_-^{Kr} + \frac{1}{2} E_g^{Kr}) - (\mu_+^{MgO} + \mu_-^{MgO} + \frac{1}{2} E_g^{MgO})$	-6.7 ± 1.5
Vacuum	$\Delta E_+^{VAC} = (-\phi_+^{Kr}) - (-\phi_+^{MgO})$	-0.5 ± 1.5

^aDoes not apply to the MgO//Kr insulator-insulator interface.

Therefore, we estimate the systematic error in $\Delta E_{AB,+}$ to be at least 1.5 eV, so that it is not clear whether positrons will trap in Kr nanoclusters when the vacuum levels are aligned. The various possibilities for alignment of the electronic energy levels and the corresponding differences in positronic ground state potentials are summarised in Table 3.8.

Another aspect to be considered is that Kr is commonly used as a moderator because positrons thermalise ineffectively in solid rare gases [Mills, Jr., et al. 1986]. This means that positrons hardly lose energy when moving in 'bulk' solid Kr. So even if the Kr nanoclusters would act as a potential well, a positron entering a nanocluster might not lose enough energy to be thermalised and to remain trapped inside the cluster until annihilation. In the literature, trapping in spherical Kr bubbles in metals (Ni, Cu) is reported [Jensen et al. 1988, Jensen et al. 1990, Britton et al. 1987] and these authors conclude that the trapping occurs at the interface rather than in the nanocluster itself. We cannot fully exclude that positrons are also trapped at the MgO//Kr interface, but it is not likely. First, the TEM results suggest that the cubically shaped Kr clusters fit very well into the MgO lattice, reducing the probability of interface defects that can act as trapping sites. Second, if the positrons would trap at the interface, one would still expect an anisotropic contribution from Kr to the 2D-ACAR spectrum due to overlap of the positron wavefunctions with the solid Kr. Unfortunately, the anisotropy in the electronic/positronic structure for bulk Kr is known neither theoretically nor experimentally, so that we cannot interpret our experimental results in more detail.

3.3.5. Formation of shallow nanovoids created by Kr ion irradiation damage

In the TEM image of Fig. 3.16, a vacancy cluster band, which can be attributed to agglomeration of ion implantation damage, can be observed at a depth much less than the depth of the Kr ion implantation layer. In the present subsection, this phenomenon is investigated further. For this purpose, use was made of the IVEM-TANDEM facility at Argonne National Laboratory [Allen et al. 1989], see Subsection 2.6.2. The facility allows in-

situ observation of defect evolution during ion implantation and (simultaneous) thermal annealing. Thin MgO(100) specimens were prepared from bulk MgO single crystals as described in Subsection 2.6.1. The specimens were mounted on a temperature-controlled stage (from 300 to 1100 K) and were tilted towards the ion beam ($\sim 30^\circ$ off the electron beam axis) during ion implantation. In order to study the void formation, an experiment was performed where 300 keV Kr ions were implanted through an MgO(100) foil to a fluence of $4.0 \times 10^{16} \text{ cm}^{-2}$. Here the Kr ions pass completely through the foil so that there is no interaction between the ion implantation damage and the implanted species. In order to calculate the required acceleration energy and the corresponding ion and damage depth distribution, the SRIM 2000 code was employed [Ziegler et al. 1985], using a value of 55 eV for the displacement energy of both the Mg and O atoms [Zinkle et al. 1997]. The implantation parameters are listed in Table 3.9 and the corresponding ion and vacancy depth distributions are shown in Fig. 3.22 and Fig. 3.23, respectively. Estimating the thickness of thin areas of the MgO specimen at $\sim 50 \text{ nm}$, the 300 keV Kr ions completely pass through the foil (Fig. 3.22). Nevertheless, the irradiation damage deposited inside the 50-nm-thick MgO foil is about 30 dpa (Fig. 3.23). In order to create nucleation centres, the specimen was bombarded with $5 \times 10^{15} \text{ Kr ions cm}^{-2}$ at room temperature. Subsequently, the dose was increased to a final dose of $4 \times 10^{16} \text{ Kr ions cm}^{-2}$ while the specimen was kept at an elevated temperature of 650 K. After an irradiation dose of $2 \times 10^{16} \text{ cm}^{-2}$, nanovoids with a size of $\sim 1 \text{ nm}$ began to develop, growing to a final size of $\sim 3 \text{ nm}$ after $4 \times 10^{16} \text{ Kr ions cm}^{-2}$. No further growth of the nanovoids was observed after post-irradiation thermal annealing at 1100 K.

Table 3.9. Sample treatments, predicted ion implantation data and calculated ion and vacancy concentrations.

Sample treatment		
Ion species		Kr
Energy	keV	300
Fluence	cm^{-2}	4.0×10^{16}
Implantation T	K	650 K
Annealing T	K	1100 K
Calculated properties ^a		
Ion range R_p	nm	105
Ion straggling ΔR_p	nm	28
Implanted ion conc. (peak)	at. %	5.2
Displacements per ion		1400
Electr. energy loss $(dE/dx)_e$	keV/nm	0.88
Nucl. energy loss $(dE/dx)_n$	keV/nm	1.9
Dpa (peak)		49

^acalculated with the SRIM 2000 code [Ziegler et al. 1985].

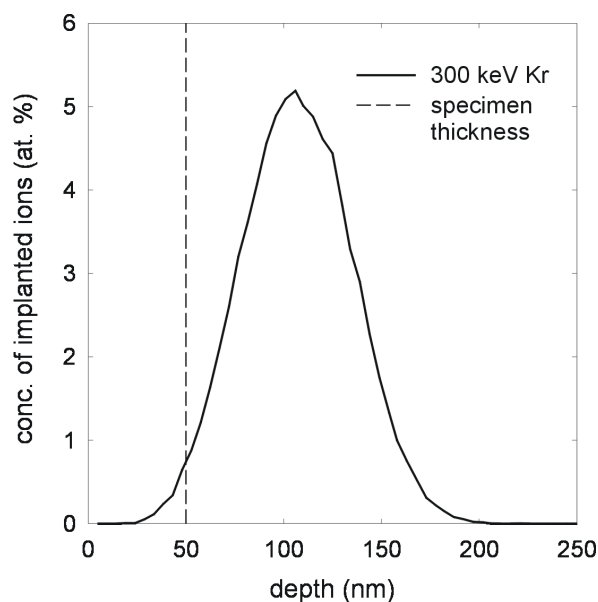


Fig. 3.22. Atomic depth distribution of Kr ions implanted at an energy of 300 keV in MgO

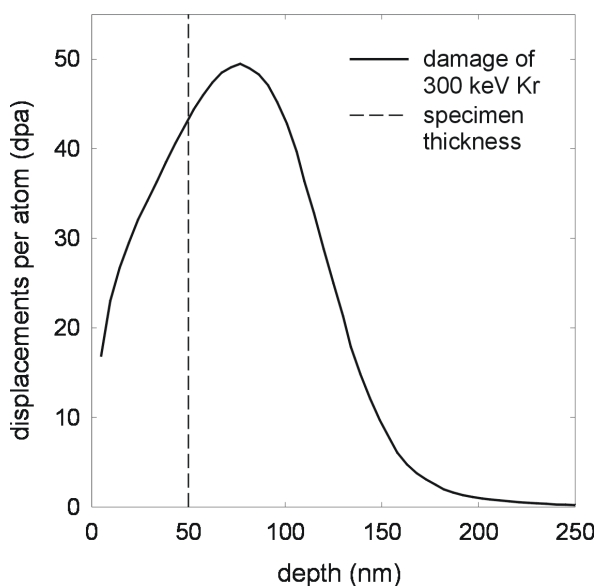


Fig. 3.23. Displacement damage distribution created by implantation of 300 keV Kr ions to a dose of 4×10^{16} ions cm^{-2} .

Fig. 3.24 shows the vacancy clusters in underfocus and overfocus condition. Agglomeration of the displacement damage (~ 30 dpa, see Fig. 3.23) created by the 300 keV Kr ions in the first 50 nm leads to a very dense network of cubical nanoclusters. The edge of the hole in the specimen is visible in the bottom-left corner of Fig. 3.24. The cubical shapes present near the edge might also be surface defects. However, the cubical shapes can be found in the entire specimen, as is also visible in Fig. 3.24 in the top-right corner. Here the specimen is thicker and the (projected) concentration of vacancy clusters is higher. Therefore, the vacancy clusters are present inside the MgO foil. This experiment clearly shows that cubical nanovoids in MgO can be formed due to agglomeration of implantation damage without any interference with the implanted ion. Other examples are discussed in Ref. [Van Veen et al. 2002].

The three-dimensional growth of vacancy clusters in metal oxides is remarkable since vacancy clusters in metals always develop in two-dimensional structures such as platelets and dislocation loops. Vacancies are easily created in MgO because it is a typical Schottky material [Busker et al. 2000]: interstitials are mobile at room temperature and migrate easily to the surface, while the vacancies are not mobile at room temperature and agglomerate into vacancy clusters after thermal annealing or due to radiation-induced annealing. Post-implantation thermal annealing at 1100 K did not change the size distribution of the nanoclusters, showing that the nanovoids are very stable at this temperature. It can be concluded that cubically shaped nanovoids are easily created in MgO by agglomeration of displacement damage (without the presence of the implanted ion) during 300 keV Kr ion irradiation at an elevated temperature of 650 K.

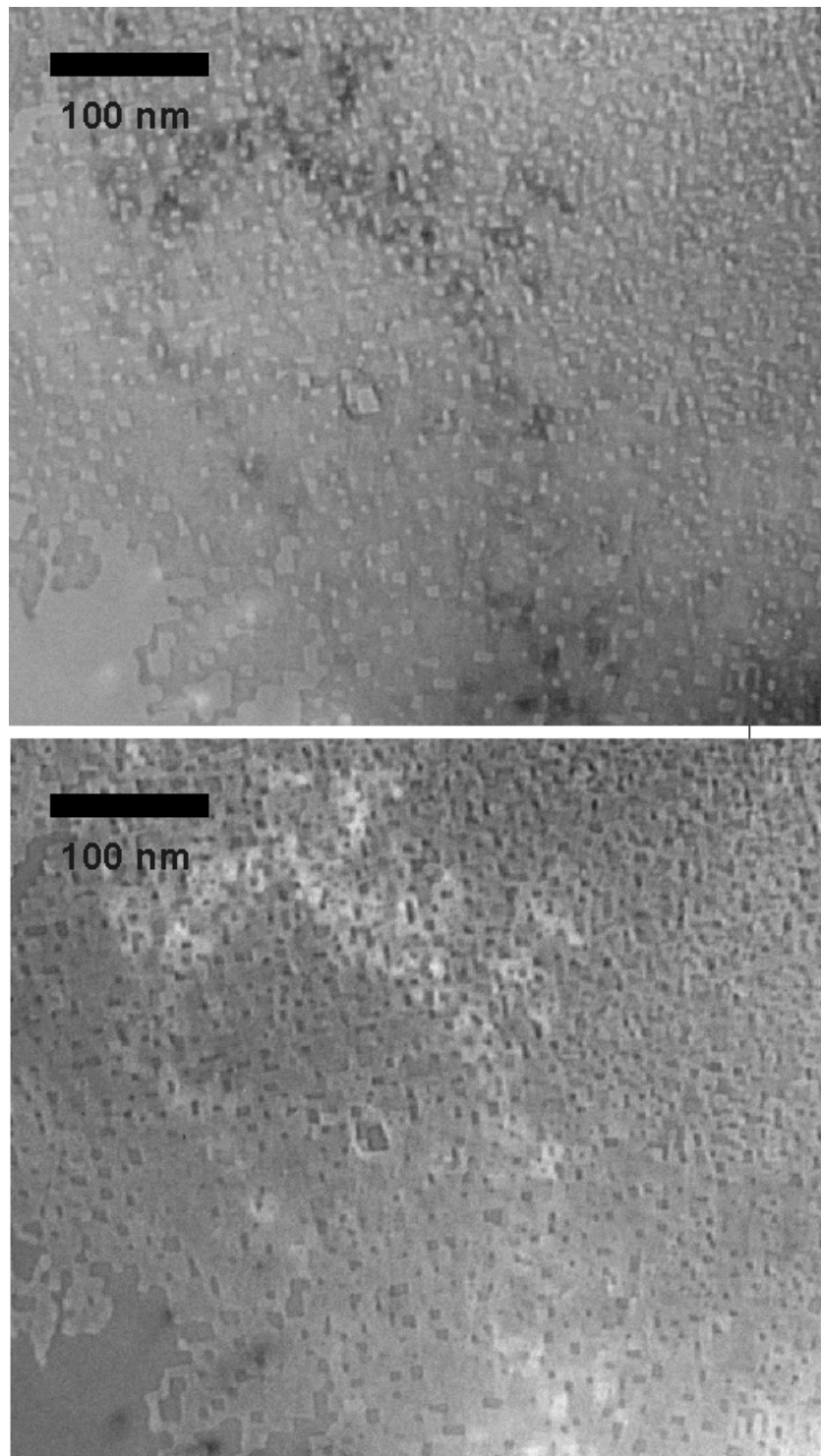


Fig. 3.24. Bright-field TEM images of cubical nanovoids in MgO created by means of 300 keV Kr irradiation through the foil. Dose: $4 \times 10^{16} \text{ cm}^{-2}$ implanted at 650 K. Top: underfocus. Bottom: overfocus.

3.3.6. Conclusions

Solid Kr nanoclusters were successfully created in MgO by means of 280 keV Kr ion implantation and subsequent thermal annealing at 1100 K. The nanoclusters were observed by cross-sectional transmission electron microscopy (XTEM) in the high-resolution mode. The fcc Kr nanoclusters are rectangularly shaped with sizes of 2 to 4 nm. The lattice parameters of the solid Kr in the clusters varies from 5.3 Å for small clusters to 5.8 Å for large clusters, with the lattice parameter increasing with increasing nanocluster size. Using the Ronchi equation of state, this corresponds to local pressures of 0.6-2.5 GPa. Both optical absorption spectroscopy and Doppler broadening positron beam analysis show that small defects are present in the MgO after the ion implantation and that defect aggregation occurs during annealing. In a follow-up experiment, a thin MgO(100) foil was irradiated in-situ in the electron microscope with 300 keV Kr ions at a temperature of 650 K. Here the Kr ions completely pass through the foil. It was found that cubically shaped nanovoids are easily created due to agglomeration of displacement damage, even when the implanted ion is not present to participate in the defect evolution. Experimentally, no evidence was found for positron confinement in Kr nanoclusters. The non-equalisation of Fermi levels, the poor thermalisation of positrons in solid Kr, and the absence of trapping sites at the Kr//MgO interface might be the cause that positrons are not trapped in Kr clusters.

Chapter 4

Metal nanoclusters

Metal nanoclusters are studied extensively because of their linear and non-linear optical properties [Chakraborty 1998, Kreibig et al. 1995, Stepanov et al. 2002, Fukumi et al. 1994] and their electronic features as quantum dots [Ekardt 1999, Halperin 1986, Davidovic et al. 1999]. The optical and electronic properties are strongly dependent on the nanocluster size as a result of quantum size effects such as the confinement of surface plasmons and the discretisation of energy levels below a certain cluster size. Other material properties that can change with the cluster size are the melting temperature, the position of the Fermi level and the paramagnetic susceptibility. Apart from the optical applications such as optical waveguides and optical switches, metal nanoclusters in insulator materials can also be used as non-volatile memory devices. When the clusters in the material are located very close to the surface, they can be charged using an electrode and discharged by exposure to light. The charged/uncharged state of the metal clusters can then be used as a 0/1 memory unit. In this chapter three different types of metal nanoclusters are discussed, all embedded in MgO. The Li nanoclusters are an interesting example of an extrinsic size effect: they undergo a phase transformation (from bcc to fcc) when they become smaller than 20 nm. They also show a very effective positron confinement. The Ag and Au nanoclusters are an example of an almost perfect host-nanocluster system: they have the same crystal structure as MgO (fcc) and have lattice parameters very close to that of MgO. The Zn nanoclusters are an example of metal nanoclusters with a hexagonal crystal structure, which does not fit very well into the MgO lattice.

4.1. Li nanoclusters in MgO

4.1.1. Introduction

Positron confinement is a newly investigated type of quantum confinement in nanoclusters and can serve as a powerful tool for investigating the electronic structure of nanoclusters. The concept of positron confinement was introduced by Nagai et al. (2000). Under certain conditions, nanoclusters act as a potential well to positrons, i.e., the wave function of the positron is spatially confined in three dimensions within the nanocluster. This is explained in Section 2.7. A positron confined in a nanocluster will annihilate there and will thus provide unique information on the electronic and crystal structure of the nanocluster, which can be quite different from the bulk material of the atoms constituting the nanocluster. Previously, positron confinement was investigated in Cu nanoclusters embedded in Fe [Nagai et al. 2000, Nagai et al. 2001]. By analysis of the S and W parameters of the Doppler broadening curves these authors found that, after thermal ageing, approximately 90 % of all positrons annihilate in the Cu nanoclusters while Cu makes up only 1.0 wt.% of the Fe:Cu composite material. The positron confinement was confirmed by coincidence Doppler broadening (CDB) measurements and was ascribed to a difference in positron affinity between Cu and Fe of 1.0 eV. If the positron affinity of the cluster material is lower than the positron affinity of the host material the cluster will act as a potential well to positrons (see Section 2.7).

In this work, positron confinement is investigated in Li nanoclusters embedded in monocrystalline MgO. In order to study the material properties of nanoclusters, it can be useful to embed nanoclusters in stable and inert ceramics such as MgO, which can be achieved by ion implantation and subsequent annealing [White et al. 1998]. It is expected that the wide band gap material MgO (7.8 eV) does not interact with the electronic structure of metal and semiconductor clusters [Vom Felde et al. 1988, Alivisatos 1996a]. It is also optically transparent in a large frequency band, which facilitates optical studies. Furthermore, the high melting point of MgO (3125 K) allows a study of phase transitions of nanoclusters. The optical and structural properties of Li nanoclusters embedded in MgO have been investigated previously by photo-absorption spectroscopy, transmission electron microscopy and electron diffraction [Marichy et al. 1979, Treilleux et al. 1979, Vergara et al. 1998]. It was found that small Li clusters (< 20 nm) adopt the unusual fcc crystal structure while large Li clusters (> 40 nm) adopt the regular bcc crystal structure. This is a so-called extrinsic size-effect: small Li clusters adopt a different phase in order to fit better into the MgO matrix. As is clear from Table 4.1, the lattice parameter of fcc lithium is closer to that of MgO than the lattice parameter of bcc Li, which reduces the formation energy of the MgO//Li interface. The fcc phase for bulk Li is otherwise only observed at low temperatures and high pressures [Christensen et al. 2001, Vaks et al. 1989].

Table 4.1. Structural data of MgO and Li.

	Structure	a_0 (Å)	at. volume (Å ³)
MgO	rock-salt	4.212 ^a	-
Li	fcc	4.40 ^a	21.3
Li	bcc	3.51 ^b	21.6

^a Ref. [Handbook 1986]

^b Ref. [Treilleux et al. 1979]

A similar effect was reported in the work mentioned above [Nagai et al. 2001] where the crystal structure of Cu nanoclusters embedded in Fe was found to be bcc rather than fcc, as is expected on the basis of lattice parameter similarity.

The nanoclusters investigated in this work were created by ion implantation and subsequent annealing. It was shown previously [Van Veen et al. 2001] that Doppler broadening PBA (positron beam analysis) and 2D-ACAR (two-dimensional angular correlation of annihilation radiation) measurements show a very high fraction of positron annihilations in Li nanoclusters, indicating possible positron quantum confinement. Below we shall first discuss the concepts of positron affinity and the positronic potential well. After describing the experimental techniques and procedures, the results from the positron annihilation techniques are presented and analysed in order to obtain a value for the fraction of positrons annihilating in lithium nanoclusters. Furthermore, the positron affinities of MgO and fcc and bcc lithium are calculated in order to determine the drop of the positronic potential at the MgO//Li interface. The confinement of positrons in Li nanoclusters is then discussed using the experimental and computational results.

4.1.2. Positron confinement

In Section 2.7 the definitions of the S parameter, the W parameter, positron affinity and positron confinement have been discussed. We repeat here a few formulas so that the reader does not have to switch between Chapter 2 and Chapter 4. These are formulas describing the contribution of defect or material fractions to the overall S parameter and the formula describing the contribution of various layers to the overall S parameter:

$$S_{\text{comp}} = f_{\text{cluster}} S_{\text{cluster}} + f_{\text{host}} S_{\text{host}}. \quad (4.1)$$

$$S(E) = f_{\text{surf}}(E) S_{\text{surf}} + f_1(E) S_1 + f_2(E) S_2 + \dots + f_n(E) S_n. \quad (4.2)$$

where S_{cluster} , S_{host} , S_{surf} , and S_i , are the S parameters of the nanocluster material, the embedding material, the surface and the i -th layer ($i=1,2,\dots,n$), respectively. f_{cluster} and f_{host} are the fractions of annihilation in the clusters and in the embedding host material ($f_{\text{cluster}} + f_{\text{host}} =$

1). Of course, the sum of the layer fractions f_i also equals one: ($f_{\text{surf}}+f_1+\dots+f_n = 1$). When the S parameter of a certain layer has been determined with the aid of VEPFIT (see Section 2.7) using Eq. (4.2), the annihilation fractions within that layer can be calculated using Eq. (4.1). If the ion implantation layer (containing the nanoclusters) is, e.g., layer 2, then $S_2=S_{\text{comp}}$. When the Fermi levels become equal, the positron affinity is defined as [Puska et al. 1989a]

$$A_+^{METAL} = \mu_+ + \mu_- = -(\phi_+ + \phi_-). \quad (4.3)$$

The potential step at the interface is equal to the difference in the positron affinities of the two materials [Puska et al. 1989a]:

$$\Delta E_+^{AB} = A_+^A - A_+^B. \quad (4.4)$$

A necessary condition for positron confinement in a cluster (A) embedded in a host (B) is that $\Delta E_+^{AB} > 0$. Then the cluster represents a potential well for positrons (cf. Section 2.7 for a more extensive discussion of Eqs. (4.1)-(4.4)). Usually, the positron affinity is determined experimentally by measuring the electron and positron work functions [Weiss et al. 2000] (see Eq. (4.3)). Alternatively, the positron affinity can be derived from the positronium (Ps) formation potential ε_{Ps} , which can be determined experimentally as the negative of the maximum kinetic energy of positronium atoms ejected from the sample into vacuum. The positronium formation potential is related to the positron affinity as [Puska et al. 1989a]

$$\varepsilon_{Ps} = \phi_+ + \phi_- - 6.8 \text{ eV} = -A_+ - 6.8 \text{ eV}. \quad (4.5)$$

where 6.8 eV is the binding energy of the positron-electron pair constituting a positronium atom in vacuum. Two experimental time-of-flight studies on MgO [Sferlazzo et al. 1987, Nagashima et al. 1998] report positronium emission peak energies of 4.5 and 2.6 eV, respectively. Applying Eq. (4.5) then yields values for the positron affinity for MgO of -2.3 and -4.2 eV, respectively. Apart from the quantitative discrepancy, the interpretation of these results is complicated by the fact that the emission energy spectra are quite broad. Furthermore, the unknown binding energy of Ps at the MgO surface (MgO is too dense a material for Ps to be formed in the bulk) and the uncertainty about whether valence or conduction electrons participate in Ps formation obscure a direct translation to the positron affinity for MgO [Sferlazzo et al. 1987, Nagashima et al. 1998]. Summarising, the determination of positronium formation potentials at the surface of insulating oxides such as MgO is experimentally difficult, which results in the different values reported in the literature.

Therefore, we turn to *ab initio* calculations to determine the positron affinities. These calculations were performed by Dr. J. Kuriplach from the Charles University in Prague and are included in this thesis for completeness. As the calculation of electron and positron work functions requires a careful treatment of the surface of the material, we prefer to determine A_+ through the electron and positron chemical potentials (see Eq. (4.3)), the calculation of which is a standard procedure in ‘bulk’ electronic structure computational methods. It should be noted that A_+ is a bulk characteristic of a material (see Refs. [Puska et al. 1994, Puska et al. 1989a] for details). For the calculation of the positron affinities and lifetimes in the materials studied [Puska et al. 1994] the linear-muffin-tin-orbital (LMTO) method was used within the atomic sphere approximation (ASA) [Andersen et al. 1987]. Within the framework of this method the crystal is divided into overlapping spheres (called atomic spheres) centred at the positions of the nuclei. The sum of the volumes of the spheres is equal to the volume of the crystal. However, the rock-salt structure of MgO is not as closely packed as the fcc and bcc structures considered for Li [Treilleux et al. 1979]. Therefore we had to introduce empty spheres [Andersen et al. 1987] into the MgO lattice to describe properly the distribution of the electron and positron densities and potentials in the interstitial region. We considered the case where the empty spheres occupied 30 % of the cell volume. In the following this case is referred to as MgO II, in contrast to MgO I where no empty spheres were included for comparison. Choosing the 30% filling with empty spheres leads to a reasonable overlap between neighbouring Mg-O spheres in the MgO lattice [Andersen et al. 1987].

The lattice constants a_0 used in our calculations are collected in Table 4.1. As for the positron calculations, in Li we used the parametrisations of the positron correlation potential and enhancement factor given by Boroński and Nieminen [Boroński et al. 1986] within the framework of the local density approximation (LDA). The corresponding results will further be denoted as LDA, whereas the results obtained using the generalised gradient approximation [Barbiellini et al. 1995] will be marked GGA. In the case of MgO we also employed the GGA, but instead of the LDA we made use of the so-called semiconductor (SM) and insulator (IM) models [Puska et al. 1989b], which take into account incomplete positron screening in non-metallic systems (i.e., systems having a band gap; MgO is an insulator). A high-frequency dielectric constant $\epsilon_\infty = 3.0$ was employed in the SM and IM calculations. This constant was derived from the optical constants of MgO [Roessler et al. 1991] in the visible spectrum $(n, k)=(1.73, 0.00)$, using the relationship $\epsilon_\infty = n^2 - k^2$. Finally, the exchange-correlation potential for electrons parametrised according to Von Barth and Hedin [Von Barth et al. 1972] was used in the calculations of the electronic structure of MgO and Li. For completeness, the positron lifetime (τ) in defect-free MgO and Li was calculated employing the well known formula [Puska et al. 1994]

$$1/\tau = \pi r_0^2 c \int n_-(\mathbf{r}) n_+(\mathbf{r}) \gamma[n_-(\mathbf{r})] d\mathbf{r}. \quad (4.6)$$

Here, n_- and n_+ denote the electron and positron density, respectively, and γ stands for the enhancement factor describing the pile up of electrons around a positron (r_0 is the classical radius of the electron and c the speed of light). The different forms of γ within the LDA, GGA, SM, and IM approaches were used in the corresponding calculations. Other computational details are described in Kuriplach et al. (1999).

4.1.3. Experimental

Epi-polished single crystals of MgO(100) of size $10 \times 10 \times 1 \text{ mm}^3$ were implanted with $1.0 \times 10^{16} \text{ cm}^{-2}$ ^6Li ions at an energy of 30 keV. After the implantation the crystals were annealed in air in steps from room temperature to 1200 K. The annealing temperatures were 550, 750, 950, 1100 and 1200 K for periods of 30 min. Photo-absorption spectroscopy was used to detect Mie plasmon resonance due to the presence of lithium nanoclusters. Furthermore, the Neutron Depth Profiling (NDP) technique, using the nuclear reaction $^6\text{Li}(n,\alpha)^3\text{H}$, was applied to determine the depth profile of ^6Li after the annealing steps. The results of these two methods have already been discussed in an earlier paper, which focused on the defect evolution during the annealing procedure [Van Veen et al. 2001]. In the present work we address the confinement of positrons in lithium nanoclusters, and therefore only the positron experimental techniques applied to the samples are presented in this paper. After ion implantation and after each annealing step, the samples were analysed with Doppler Broadening positron beam analysis (PBA) using a mono-energetic 0-30 keV positron beam. The energy resolution of the PBA set-up is 1.2 keV. After the 950 K annealing step, one of the samples was also analysed with 2D-ACAR. The 2D-ACAR set-up of the Anger-camera type is coupled to a high-intensity positron beam with a flux of $8 \times 10^7 \text{ e}^+ \text{ s}^{-1}$, allowing depth-selective 2D-ACAR [Falub et al. 2001]. The angular resolution of this system is $1.1 \times 1.4 \text{ mrad}^2$. The sample measured with 2D-ACAR was identical to the other samples, apart from a 15-nm-thick layer of Al deposited on the sample surface after the 950 K annealing step to prevent build-up of electric charge. The 2D-ACAR distribution was collected at a positron implantation energy of 4 keV, which corresponds to a mean positron implantation depth at the centre of the layer containing the lithium nanoclusters. This energy was chosen on the basis of depth-profiling performed on the same sample by means of Doppler broadening PBA. Furthermore, an MgO bulk 2D-ACAR distribution was collected from an as-received sample of MgO(100) for reference purposes. The use of a conventional ^{22}Na source in this latter measurement renders any surface effects negligible.

4.1.4. Positron beam analysis

Doppler broadening positron beam analysis

Fig. 4.1 shows the S and W parameters as a function of positron implantation energy after lithium ion implantation and after annealing at the indicated temperatures. The solid lines

represent the results of simulations performed with the VEPFIT code, discussed below. The S parameter shows a spectacular increase in the lithium ion implantation range (corresponding to a positron energy of 3-4 keV) after annealing at temperatures of 750 K and 950 K. At higher annealing temperatures the S parameter in the ion implantation layer drops considerably and after annealing at 1200 K the peak in this range almost disappears. At larger depths (corresponding to positron implantation energies of 7-15 keV in Fig. 4.1), the S parameter drops below the bulk value of MgO (i.e. 0.468) after annealing at 1200 K. Such a drop of the S parameter below the bulk value of MgO as a result of ion implantation and subsequent annealing has not been observed before. We attribute this effect to positron annihilation in small Li-related defects, as will be discussed in more detail below.

The experimental S and W parameter curves shown in Fig. 4.1 have been fitted using the VEPFIT code [Van Veen et al. 1990] in order to gain more insight into defect evolution and in order to derive the contributions of the various layers to the annihilation distribution. A four-layer model was used. The principal defect types and the corresponding diffusion lengths used as input to the VEPFIT code are listed in Table 4.2. The choice for this model is mainly based on defect analysis performed on previously ion implanted MgO samples which were analysed by means of transmission electron microscopy, positron annihilation spectroscopy and neutron depth profiling [Van Veen et al. 2001, Kooi et al. 2000, Van Huis et al. 2001]. In particular, there is a subsurface layer containing the ion implanted species and the principal implantation defects (layer 2). Dislocation loops are formed at smaller depths in the MgO top layer (layer 1) and below the ion implantation layer [Kooi et al. 2000]. The presence of dislocation loops in MgO does not affect the S parameter significantly, but it does shorten the diffusion length compared to the bulk values. In the layer below the ion implantation layer (layer 3) there are not only dislocation loops but also a tail of implanted species as observed by NDP [Van Veen et al. 2001], possibly because of channelling effects. It was estimated that about 6 % of the implanted species end up in this range. Due to the low atomic concentration of Li in this layer, we expect small Li-related defects rather than metallic Li clusters (see the discussion on the defect evolution of layer 3 in Fig. 4.1 below). The fourth layer is the MgO bulk. In order to monitor the defect evolution, the S and W parameters of layer 2 (ion implantation layer) and layer 3 (ion implantation tail) were fitted. The layer boundaries determining the position of the ion implantation layer have been allowed to relax as the S parameter peak shifts to somewhat lower positron energies when the annealing temperature increases (compare, for example, the 750 K and 1100 K S parameter curves in Fig. 4.1). This might be due to a recombination of implanted lithium atoms and lithium clusters with vacancies and small vacancy clusters created by ion implantation. The range of the implantation damage is always located at a slightly smaller depth than the range of the implanted ions.

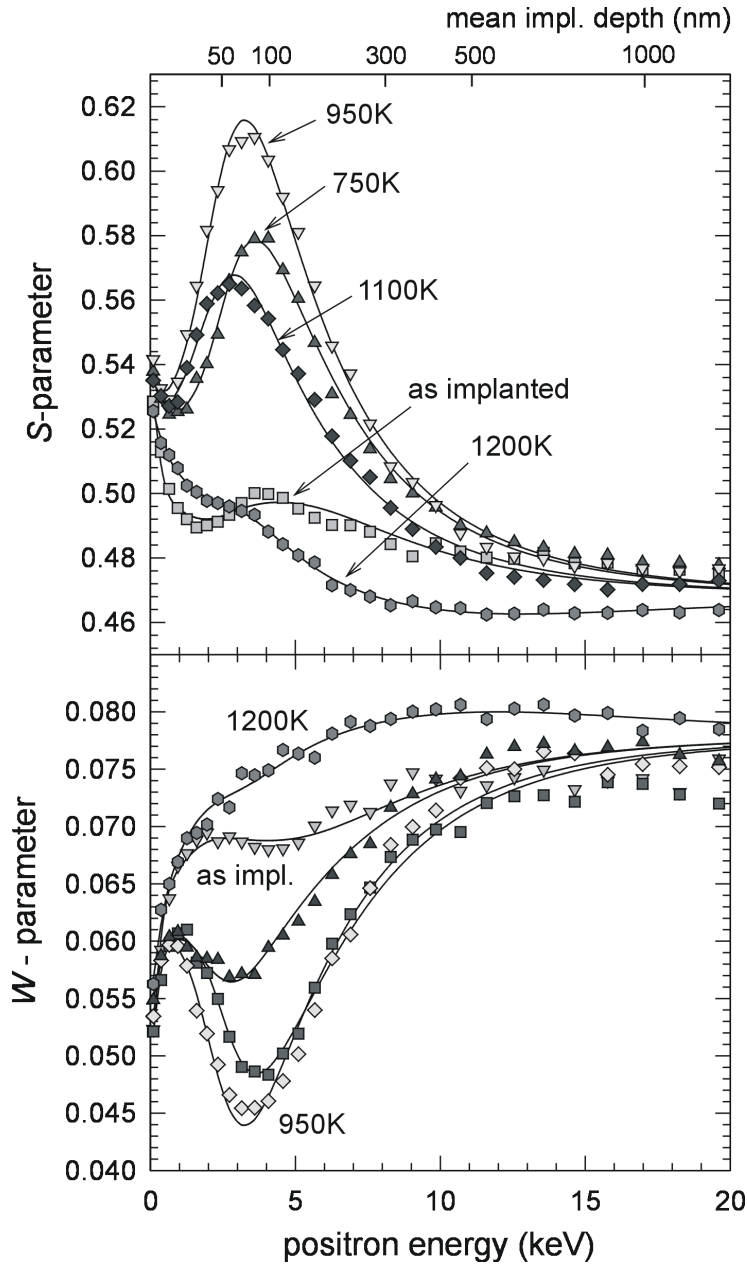


Fig. 4.1. S and W parameters as a function of positron energy. The solid lines are the result of VEPFIT modelling.

Table 4.2. VEPFIT model used to fit the S and W parameter curves shown in Fig. 4.1.

	depth (nm)	diff. length (nm)	S par.	W par.	Description
Layer 1 ^a	$0-d_1$	50	0.468	0.078	MgO top layer
Layer 2	d_1-d_2	15	fitted	fitted	MgO:Li
Layer 3	d_2-300	50	fitted	fitted	ion impl. tail
Layer 4	>300	100	0.468	0.078	MgO bulk

^a Layer 1 was omitted ($d_1=0$) in the case of the 1200 K annealing step.

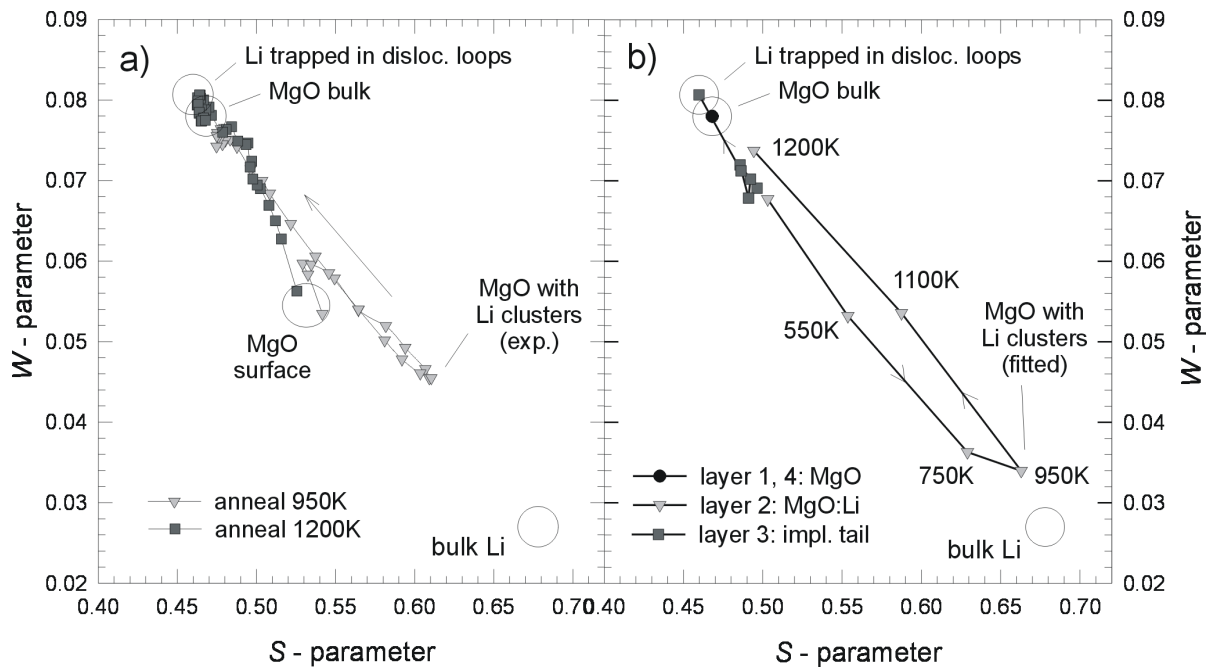


Fig. 4.2. a) S - W plot with the positron energy as running parameter. The experimental data are plotted for the 950 K and 1200 K annealing step only. b) S - W plot with the annealing treatment as running parameter. The fitted values are plotted for all of the four layers (see Table 4.2).

The fitted curves are depicted as solid lines in Fig. 4.1. The agreement with the experimental results is reasonable, considering the fact that the same model has been applied to all data sets. In the case of the S and W graphs corresponding to the 1200 K annealing step the MgO top layer was omitted since it was not possible to distinguish between the ion implanted layer and the MgO top layer. The fitted results yield boundaries d_1 and d_2 of the ion implanted layer of approximately 45 and 115 nm respectively, which shift to slightly lower values with increasing annealing temperature. The fitted values of S and W are presented in Fig. 4.2(b).

Fig. 4.2 shows the S parameter plotted vs. the W parameter. Every bulk material and every defect type has a characteristic S and W parameter. A few of these typical S , W combinations are indicated in Fig. 4.2 with open circles and are called cluster points. The cluster points corresponding to pure MgO and bcc Li were determined experimentally from bulk samples of these materials. By plotting experimental or fitted S - W values in an S - W plot with, e.g., the positron energy as the running parameter, the defect status at a certain depth in the material can be analysed by means of comparison with the characteristic S - W cluster points for defects and bulk materials. In Fig. 4.2(a), the experimentally obtained S - W parameters are plotted with the positron energy as the running parameter. Fig. 4.2(b) shows the S - W plot using the fitted S and W values for every layer with the annealing treatment as the running parameter. The main difference between the two plots is that in Fig. 4.2(a) all layers contribute to the experimental S - W points, while in Fig. 4.2(b) the S - W parameters are layer-resolved with the

aid of the VEPFIT code, i.e., the S and W parameters corresponding to only one layer are shown (see also Eq. (4.2)).

Considering the defect evolution of layer 3 (ion implantation tail) in Fig. 4.2(b), it is clear that the S, W combination moves away from the bulk Li cluster point during the annealing procedure, while the NDP measurements show that a small fraction (approximately 6%) of the implanted Li atoms is present in this layer. Therefore, the Li atoms should be in an electronic state different from metallic bulk Li. Research performed previously on Li-doped MgO crystals has revealed defect types such as Li_2O precipitates, isolated Li^+ ions and so-called $[\text{Li}]^0$ centres [Vergara et al. 1998]. These defects will yield $S-W$ parameters which are quite different from bulk Li or bulk MgO.

Another observation that can be made with respect to Fig. 4.2(b) is that the $S-W$ characteristic points corresponding to the ion implantation layer (layer 2) move roughly along the line connecting the MgO bulk cluster point and the bcc bulk Li cluster point. It is also clear that the experimental $S-W$ point corresponding to MgO containing Li clusters after the 950 K annealing step in Fig. 4.1(a) does not reach the fitted $S-W$ combination of layer 2 (MgO containing lithium clusters) after the 950 K annealing step in Fig. 4.2(b). Due to the broadness of the positron implantation profile and positron diffusion processes, only a certain fraction of the positrons implanted at 3.5 keV (with a mean implantation depth that corresponds to the centre of the implantation layer) annihilate in the MgO:Li layer. This is also clear from Fig. 4.3 where the fraction of annihilations per layer is plotted as a function of positron implantation energy. It is found that 69% of the positrons with 3.5 keV implantation energy annihilate in MgO:Li (layer 2).

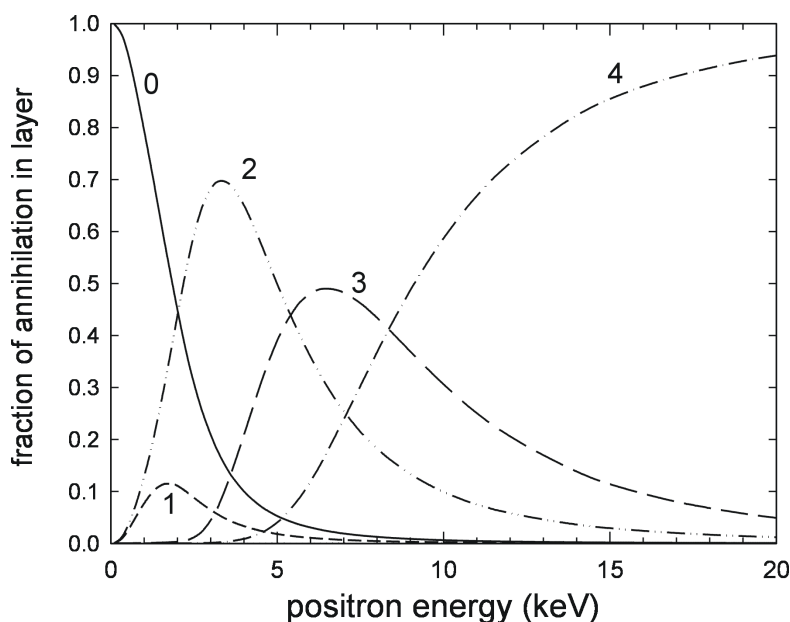


Fig. 4.3. Layer fractions of the PBA sample as a function of the positron implantation energy. Annihilation fractions per layer were found by VEPFIT modelling of the PBA data obtained after the 950 K annealing step. The numbers indicate the layer number listed in Table 4.2. Layer 0 is the surface.

Calculation of the efficiency of positron confinement in Li nanoclusters using Eq. (4.1) requires numerical values for the S parameter of the composite MgO:Li material (i.e., the S parameter of layer 2), the S parameter of bulk lithium and the S parameter of bulk MgO. The S parameter of the MgO:Li layer ($S_{\text{MgO:Li}}$) after the 950 K annealing step was found to be 0.662 by means of VEPFIT modelling (Table 4.2, Fig. 4.2(b)). The S parameters of bulk lithium and bulk MgO were measured using the same Doppler broadening PBA set-up and were evaluated to be 0.678 for polycrystalline bulk bcc Li and 0.468 for monocrystalline bulk MgO. The measurement of the S parameter of bulk Li was carried out at a positron implantation energy of 27 keV. This energy is sufficiently high to make the contribution of the lithium oxide layer at the surface to the measured distribution negligible, as ascertained by means of positron depth profiling. The S parameter for bulk lithium is much higher than that for bulk MgO. This is due to the rather small Fermi cut-off for metallic lithium of 0.58 a.u. [Tanaka et al. 2001] (equivalent to 4.2 mrad) while the window for the measurements of the S parameter is set at energies corresponding to ± 3.2 mrad. Consequently, most of the Doppler broadening curve falls within the window and the S parameter for lithium is therefore relatively high. This is also clear from Fig. 4.4 where the experimentally obtained 511 keV annihilation peaks of bulk MgO, bulk bcc Li and MgO:Li are displayed. The fraction of annihilations in lithium can be calculated rewriting Eq. (4.1) and using $f_{\text{MgO}} + f_{\text{Li}} = 1$:

$$f_{\text{Li}} = \frac{S_{\text{MgO:Li}} - S_{\text{MgO}}}{S_{\text{Li}} - S_{\text{MgO}}}. \quad (4.7)$$

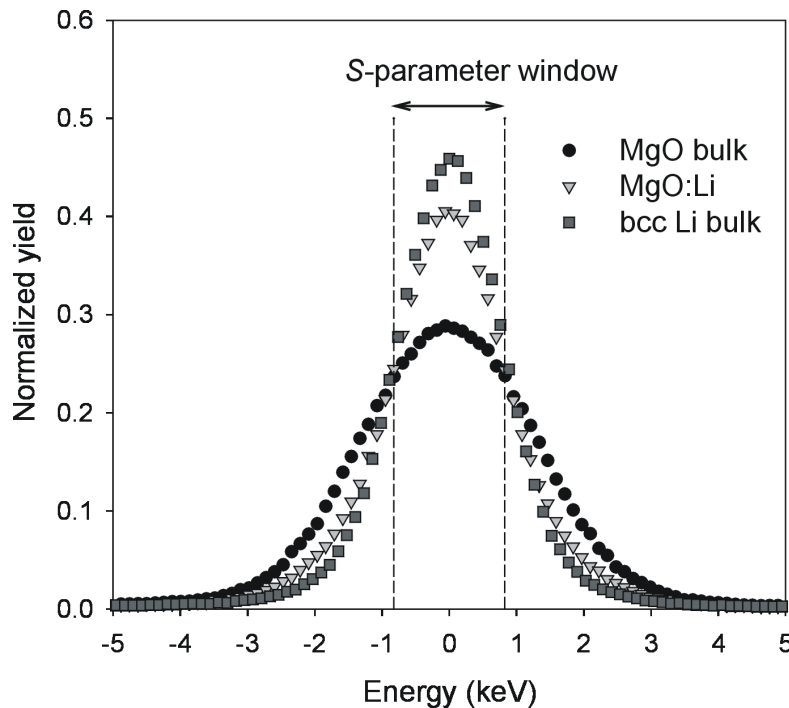


Fig. 4.4. Experimentally obtained 511 keV Doppler Broadening peaks for bulk MgO, bulk bcc Li and MgO containing Li nanoclusters (after the 950 K annealing step).

Here it should be realised that contributions from the surface and any other layers have already been filtered out by the VEPFIT code see also the discussion in Section 2.7. Substituting the S parameters mentioned above then yields a fraction of annihilations in lithium, f_{Li} , of $92 \pm 5\%$. This shows a very effective confinement of positrons in Li nanoclusters, which occupy only 1.3 at.% of the MgO:Li layer. In the calculation above, it is assumed that the S parameters for bcc Li and fcc Li do not differ significantly and that the S parameter of the lithium nanoclusters (without surrounding MgO) is similar to the S parameter of lithium bulk. A question that now arises is whether the positron is really confined within the Li nanocluster or whether it is trapped at the MgO//Li interface prior to annihilation. We shall postpone the discussion of this point until Subsection 4.1.6.

2D-ACAR

The 2D-ACAR results are shown in Fig. 4.5. Part (a) shows the anisotropic contribution of the MgO bulk distribution (total number of counts 6.4×10^7) obtained from an as-received single crystal of MgO(100). The anisotropic part of the 2D-ACAR distribution was determined by subtracting an isotropic distribution that remains everywhere within the measured distribution. The anisotropy is therefore everywhere positive.

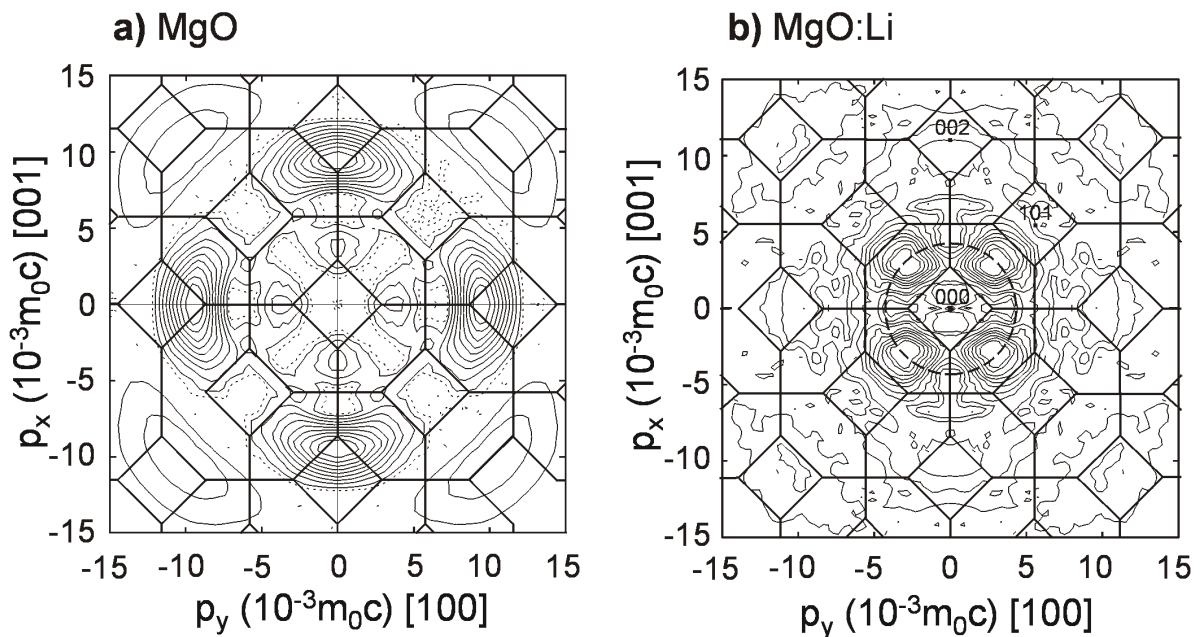


Fig. 4.5. Anisotropic part of the [010]-axis projected momentum distribution obtained by 2D-ACAR measurements for a) bulk MgO(100) and b) MgO containing Li crystalline nanoclusters. The average Fermi cut-off for bulk Li of 4.3 mrad (see Subsection 4.1.4) is displayed as a dashed circle. The distributions have been symmetrised by reflection with respect to the (100) and (001) mirror planes. The contour interval is 10% (5%) of the peak height for solid (dotted) contours. The projection of the Brillouin zones is shown based on the lattice parameters of (a) MgO and (b) fcc Li.

Part (b) of Fig. 4.5 shows the anisotropic part of the 2D-ACAR distribution obtained from a Li-implanted sample after annealing at 950 K (total number of counts 1.0×10^7). This distribution was collected at 4 keV positron implantation energy, which corresponds to a mean positron implantation depth at the centre of the lithium nanocluster layer (MgO:Li material). This energy was chosen on the basis of depth-profiling performed on the 2D-ACAR sample by means of Doppler broadening PBA. Both distributions have been corrected for the difference in resolution between the directions parallel and perpendicular to the sample surface ($1.1 \times 1.4 \text{ mrad}^2$) and were symmetrised by reflection with respect to the (100) and (001) mirror planes. The anisotropy plot of the MgO:Li layer is strikingly different from the bulk MgO anisotropy plot. The bulk MgO anisotropy is still observable in Fig. 4.5(b), but another, very dominant anisotropic contribution is present in the central part of the figure. The major part of this contribution has a nearly perfect fourfold symmetry with peaks positioned near the Fermi radius of lithium (see below). Therefore, we attribute the 2D-ACAR anisotropy at the centre of Fig. 4.5(b) to annihilation in bcc or fcc lithium clusters. Treilleux and Chassagne [Treilleux et al. 1979] found by means of electron diffraction and cross-sectional transmission electron microscopy (X-TEM) analysis that, depending on the nanocluster size, metallic lithium nanoclusters in MgO can adopt either the fcc or a rotated bcc crystal structure. The fact that the anisotropic contributions displayed in Fig. 4.5(a) and (b) both have the same symmetry and identical mirror planes shows that there is a distinct orientation relationship between the crystalline Li clusters and the MgO host matrix. Therefore, the lithium clusters will be coherent or semi-coherent with the MgO crystal lattice.

In complementary work by Falub et al. (2002), it was ascertained that the Li nanoclusters are in the fcc phase. In that case, the lithium nanoclusters are in a simple cube-on-cube orientation relationship with the MgO host matrix. Cube-on-cube bcc Li is excluded by the anisotropy in Fig. 4.5(b) as it would produce peaks along the $\langle 100 \rangle$ directions. The anisotropy in the central part of Fig. 4.5(b) agrees very well with the results of calculations performed on the momentum distribution of fcc Li using the KKR method. The free-electron Fermi sphere for fcc Li ($a_0 = 4.4 \text{ \AA}$, cf. Table 4.1) is displayed in Fig. 4.5(b) as a circle of radius 0.591 a.u., equivalent to 4.3 mrad. The peaks in the anisotropy then derive from bulges of the Fermi surface pointing towards the hexagonal Brillouin zone faces. The results of the momentum density calculations for fcc and bcc Li and a more detailed analysis of the experimental 2D-ACAR distributions have been presented elsewhere [Falub et al. 2002].

The fraction of positron annihilations in Li nanoclusters f_{Li} was also estimated from the 2D-ACAR distribution, using Eq. (4.1) in combination with a VEPFIT layer fraction analysis (giving the relative contributions of the layers to the annihilation distribution at a certain positron implantation energy). The fraction found (90 %) was not significantly different from the one derived from the Doppler broadening PBA results discussed above.

4.1.5. Calculation of positron affinities

In the previous subsection, it was found that the fraction of annihilations in Li in the ion implanted layer, as deduced from the Doppler broadening PBA spectra, is $92 \pm 5 \%$. It will be shown that the effective positron confinement can be ascribed to the different positron affinities of MgO and Li. These positron affinities were calculated using the models discussed in Section 4.1.2. The results of calculations of the positron lifetime, affinity, and electron and positron chemical potentials for Li are shown in Table 4.3. Very similar lifetimes and affinities are obtained for bcc and fcc Li. This is related to the fact that the atomic volumes of bcc and fcc Li are almost equal (Table 4.1). The affinities found are in good agreement with theoretical values in the literature [Farjam et al. 1987, Puska et al. 1989a]. To our knowledge, the positron affinity of Li has never been determined experimentally.

The electron and positron chemical potentials, positron affinity and lifetime for MgO determined using three different models are given in Table 4.4. The IM and GGA approaches yield values for the bulk lifetime that are close to the experimentally obtained lifetime τ of 150-170 ps in MgO [Forster et al. 1989, Pareja et al. 1985], which is not the case for the SM results. We note that the incorporation of empty spheres into the MgO lattice (MgO II case) leads to a slight increase of the lifetime values because the interstitial space is better described compared to the case without empty spheres (MgO I). Table 4.4 also includes the calculated lifetimes by Puska *et al.* [Puska et al. 1989b].

Table 4.3. Calculated positron lifetime, positron affinity and electron and positron chemical potentials for bcc and fcc Li.

	μ^- (eV)	LDA			GGA		
		τ (ps)	μ_+ (eV)	A_+ (eV)	τ (ps)	μ_+ (eV)	A_+ (eV)
bcc Li	-2.8	299	-5.2	-8.0	283	-5.0	-7.8
fcc Li	-2.8	297	-5.3	-8.1	282	-5.0	-7.8

Table 4.4. Calculated lifetimes, positron affinities and electron and positron chemical potentials for MgO without empty spheres (MgO I) and including empty spheres (MgO II). GGA: generalized gradient approximation; SM: semiconductor model; IM: insulator model.

	GGA				SM			IM		
	μ^- (eV)	τ (ps)	μ_+ (eV)	A_+ (eV)	τ (ps)	μ_+ (eV)	A_+ (eV)	τ (ps)	μ_+ (eV)	A_+ (eV)
MgO I	-2.9	139	-3.2	-6.1	121	-4.0	-6.9	141	-2.6	-5.5
MgO II	-1.0	140	-5.0	-6.0	126	-5.5	-6.5	147	-4.0	-5.0
MgO ^a					119			167		

^a [Puska et al. 1989b]

In the present work, the lifetimes found using the SM and the IM are somewhat higher and lower, respectively, than the values reported by Puska *et al.*, while the same SM and IM models have been used. This is mainly due to a different treatment of the core electrons. In addition, the electron density of MgO in Ref. [Puska *et al.* 1989a] was approximated by the superposition of atomic densities without consideration of the charge transfer between Mg and O atoms. Anyhow, it turns out that the semiconductor model does not reasonably describe the lifetime experiment (neither in the present work nor in [Puska *et al.* 1989a]) so that we shall not consider this model when calculating the difference between positron affinities of MgO and Li.

The values of A_+ presented in Table 4.4 depend obviously on the models used to calculate them. The lowest value comes from the SM, whereas the IM yields the largest value. The affinity results also depend slightly on whether the empty spheres are included or not. In the following considerations we shall employ the MgO II case. The positronic energy step at the MgO//Li interface can now be calculated using Eq. (4.4). Combining the GGA and IM positron affinities for MgO II (Table 4.4) and the GGA results for bcc and fcc lithium (Table 4.3; LDA and GGA results differ only marginally), the positronic potential drop at the MgO//Li interface equals 1.8 eV using the GGA and 2.8 eV using the IM. Regardless of this uncertainty in the affinity difference, it is therefore plausible to assume that clusters of Li in MgO act as positron traps.

In this context it is useful to mention recent work [Kuriplach *et al.* 1999] in which the positron affinity was studied in several polytypes of SiC, which is a semiconductor. It was found that all theoretical approaches (GGA, SM, IM) overestimate (in magnitude) the positron affinity in SiC. This was ascribed to certain inadequacies in the theoretical description of both the electron and the positron part of the problem. Considering this conclusion and the above mentioned experimental values of the positron affinity for MgO [Sferlazzo *et al.* 1987, Nagashima *et al.* 1998] it turns out that the values of A_+ calculated here for MgO are probably too large (in magnitude). Further theoretical and experimental work is therefore needed to clarify this point. A final remark in this section concerns the sensitivity of the values of the positron affinity with respect to the choice of the LDA exchange-correlation potential for electrons. In addition to the exchange-correlation potential of Von Barth and Hedin [Von Barth *et al.* 1972] we also examined the potential of Ceperley and Alder [Ceperley *et al.* 1980] as parameterised by Perdew and Zunger [Perdew *et al.* 1981]. Surprisingly, the calculated positron affinities increase (magnitudes decrease) by about 0.5 eV in all cases presented in Table 4.3 and Table 4.4. Inspection of the electron and positron chemical potentials leads to the conclusion that this effect can be attributed to the change of the electron chemical potentials only. It shows that, although the resulting difference of the positron affinity of MgO

and Li remains unchanged, one has to be careful when comparing affinity results obtained using different exchange-correlation potentials for electrons (cf. Ref. [Panda et al. 2000]).

4.1.6. Positron trapping

Our results show a very high fraction of annihilations in lithium, indicating a very effective positron confinement in Li nanoclusters. Two aspects are important when considering the efficiency of positron confinement in nanoclusters: a) the probability of trapping and reflection when a positron encounters a nanocluster acting as a potential well, and b) the probability of reaching a nanocluster, assuming that the positron is thermalised in the embedding MgO material.

The kinetic energy of delocalised positrons is of the order of tens of meV, while the size of the potential step at the MgO//Li interface is a few eV (1.8 eV using the GGA and 2.8 eV using the insulator model). Thus, the depth of the potential well as determined by the difference in positron affinities is two orders of magnitude larger than the kinetic energy of the positron after thermalisation. Therefore, when a positron is thermalised and diffuses within the embedding MgO, the probability of reflection when encountering the MgO//Li interface is negligible at room temperature. Every positron reaching a lithium nanocluster will be confined in that cluster. Once inside the cluster, the positron will be reflected at the walls. A necessary condition for the process described above is that the size of the nanoclusters is large enough to accommodate at least one bound state. Applying the three-dimensional spherical well model with a finite potential, the critical radius is given by Eq. (2.12). Substituting a value of 1.8 eV for the depth of the potential well then yields a critical cluster diameter of 0.4 nm. As the confinement of positrons is quite obvious from the results described in Subsection 4.1.4, the actual size of the nanoclusters will be larger than this value.

The probability of encountering a nanocluster is determined by the positron diffusion length and the concentration and spatial distribution of the Li clusters. Trapping of the vast majority of the positrons is only possible if the mean distance between the Li nanoclusters is smaller than the diffusion length for positrons diffusing in MgO within the MgO:Li layer. Here it is assumed that the positron is present in MgO after thermalisation, as Li occupies only 3 vol. % of the MgO:Li layer. In the diffusion-limited trapping model, described by Hautojärvi and Corbel [Hautojärvi et al. 1995], the diffusion to the defect is slow compared to the transition to the localised state. The depth of the nanocluster potential well is of the order of a few eV, so this condition is well satisfied. The possibility of detrapping is neglected. Assuming spherically shaped clusters, the fraction of positrons annihilating in the clusters is given by

$$f_{Li} = \frac{\kappa}{\kappa + \lambda_{MgO}} = \frac{4\pi r_{cl} D_+ c_{cl}}{4\pi r_{cl} D_+ c_{cl} + \lambda_{MgO}}, \quad (4.8)$$

where κ is the positron trapping rate with respect to the clusters (s^{-1}), λ_{MgO} is the annihilation rate in MgO (s^{-1}), r_{cl} is the radius of the cluster (m), c_{cl} is the concentration of clusters (m^{-3}), and D_+ is the diffusion coefficient ($m^2 s^{-1}$). The diffusion coefficient is related to the diffusion length L_+ (m) and to the positron lifetime τ (s) as

$$L_+ = \sqrt{D_+ \tau}. \quad (4.9)$$

With the aid of Eqs. (4.8) and (4.9), the fraction of annihilations in lithium clusters can be estimated. No detailed information is available on the size of the nanoclusters, so we perform an order-of-magnitude calculation. The mass density of bulk Li is 543 kg m^{-3} , so the 10^{16} implanted Li atoms occupy a total volume of $2.1 \times 10^{-13} \text{ m}^3$ independent of the cluster size. If the radius of the lithium nanoclusters is, e.g., 5.0 nm [Treilleux et al. 1979], the total number of clusters is 4.1×10^{11} and the concentration of clusters will be $5.8 \times 10^{22} \text{ m}^{-3}$, considering that all clusters are present in the ion implantation layer of thickness 70 nm (estimated from VEPFIT, Table 4.2) and area $1.0 \times 1.0 \text{ cm}^2$. At this concentration, the average intercluster distance is 26 nm. The annihilation rate in MgO equals $6.5 \times 10^9 \text{ s}^{-1}$ as it is the inverse of the lifetime τ in MgO, 155 ps [Forster et al. 1989]. A value for the diffusion length for positrons in MgO of 50 nm can be assumed (equal to the diffusion lengths for layers 1 and 3 in the VEPFIT model). Substituting Eq. (4.9) into Eq. (4.8) and using the numerical values given above, the fraction of annihilations in Li, f_{Li} , can be calculated. This yields a fraction of 90 %, which agrees very well with the experimental results. Although the cluster size and the diffusion length are estimated, the above calculation demonstrates that the annihilation fraction in lithium can be lower than 100 % due to diffusion-related processes even if every positron encountering a nanocluster is trapped in that cluster. The calculated fraction is strongly dependent on the cluster size and the diffusion length. For clusters with a radius of 3-7 nm and a diffusion length of 50-100 nm, the trapped fraction varies from 82 % to 99 %.

Finally, the possibility should be discussed that positrons are not present in either MgO or Li but are trapped at the interface, corresponding to the situation depicted in Fig. 2.10(c). This phenomenon is observed, e.g., for the Si//SiO₂ interface [Asoka-Kumar et al. 1994]. Open-volume defects or lattice mismatch at the interface can induce positron trapping. No evidence of positronium formation was found in the analysis of the 2D-ACAR distribution, showing that large vacancy-type defects are not present. Positrons can also trap in interface defects that are too small for the formation of positronium. However, positron annihilation distributions corresponding to positron annihilation at interfaces usually bear characteristics of both

materials. Thus, if positron trapping would occur at the MgO//Li interface, a considerably higher contribution from MgO to the Doppler broadening and 2D-ACAR distributions would be expected. Therefore, interface trapping in the case of the MgO//Li interface is not likely on the basis of the above observations. On the other hand, the fraction of annihilations in Li nanoclusters might be influenced by local electric fields near the interface. These can be present as a result of charge redistribution associated with the equalisation of the Fermi levels of MgO and Li in thermal equilibrium. We have, however, no means to investigate whether this last aspect plays a significant role.

4.1.7. Conclusions

It has been shown that positrons are very effectively confined in crystalline lithium nanoclusters embedded in MgO. The fraction of positron annihilations in lithium nanoclusters was deduced by analysis of the Doppler Broadening PBA spectra and found to be $92 \pm 5\%$. This annihilation fraction is very high, considering the fact that the lithium content in the MgO:Li layer is only 1.3 at. %. The anisotropic contribution of the 2D-ACAR distribution collected in the layer containing Li nanoclusters shows a fourfold symmetry which, together with the symmetry of other projections [Falub et al. 2002], indicates an fcc crystal structure with peaks at positions near the average Fermi radius of lithium. This shows that crystalline bulk lithium is present. The symmetry of the 2D-ACAR anisotropic contributions also shows that the lithium clusters are coherent or semi-coherent with the MgO host matrix. The difference in the positron affinities of lithium and MgO yields a positronic potential step down at the MgO//Li interface. Therefore, the nanoclusters act as a potential well for positrons with a depth equal to the difference in the positron affinities. These positron affinities were calculated using the LMTO-ASA method, and values for the depth of the positronic potential well of 1.8 and 2.8 eV were obtained using the GGA and the insulator model, respectively. The depth of the potential well is so large that the trapping probability of positrons meeting a nanocluster is approximately equal to 1. Positron confinement can facilitate the investigation of metal and semiconductor quantum dots and of unusual crystal structures, such as the electronic structure of fcc Li nanoclusters in MgO or of bcc Cu nanoclusters in Fe. An extensive experimental and theoretical investigation of the system Li in MgO was performed by Falub et al. (2002).

In order to predict beforehand whether positron confinement is feasible, it would be useful to know the experimentally determined or calculated positron affinities of embedding transparent materials commonly used in optical studies, such as SiO₂, TiO₂ and Al₂O₃. These affinities can then be compared with the known positron affinities of many nanocluster materials.

4.2. Zn nanoclusters in MgO

4.2.1. Introduction

Metal and semiconductor nanoclusters embedded in glasses are composite materials with promising optical properties. Semiconductor ZnO nanoclusters are known for their photoluminescence [Wong et al. 1999, Mahamuni et al. 1999, Zu et al. 1997] and also exhibit strong third-order optical nonlinearity [Zhang et al. 1999b]. Metallic Zn nanoclusters show optical absorption due to Mie plasmon resonance [Nakao et al. 2003] and possess a paramagnetic susceptibility that depends on the nanocluster size [Pasche et al. 1989]. In this section, it is attempted to create ZnO nanoclusters in MgO by Zn ion implantation and internal oxidation by thermal annealing in an oxidising environment. Earlier investigations of Zn ion implantation concerned implantation into silica [Liu et al. 2002, Chen et al. 1998] and into sapphire Al_2O_3 [White et al. 1999b].

4.2.2. Experimental

In order to create nanoclusters, monocrystalline MgO(001) samples were implanted with doses of 1.4×10^{16} and 1×10^{17} Zn ions cm^{-2} at an energy of 140 keV. This corresponds to a peak concentration of implanted Zn of 20 at. %. After ion implantation, isochronal annealing was performed in ambient air at temperatures up to 1550 K in steps of 200 K for periods of 0.5 h. After ion implantation and after each annealing step, the defect evolution in the sample was monitored using optical absorption spectroscopy (OAS), Doppler broadening positron beam analysis (PBA), Rutherford backscattering and channelling (RBS-C) and cross-sectional transmission electron microscopy (XTEM). Optical absorption spectroscopy was used to detect metal nanoclusters, which exhibit Mie surface plasmon resonance. Strictly speaking, the conduction electrons of Zn cannot be considered as free electrons, which is required for the application of the Drude-Lorentz-Sommerfeld model on which the Mie theory is based [Kreibig et al. 1995]. However, the interband transitions in Zn result in plasmon behaviour [Rubloff 1971] and we apply the Mie theory as an approximation. Positron beam analysis (PBA) [Van Veen et al. 2000] was used to follow the defect evolution. The so-called S (shape) parameter is a good indicator of open-volume defects, see Section 2.7. PBA is also a depth-sensitive technique; the probe depth in the sample can be varied by varying the implantation energy of the positron beam. A mono-energetic positron beam with a variable energy of 0-30 keV was used, allowing detection up to a depth of 2 μm . One sample was also examined by means of cross-sectional transmission electron microscopy (XTEM) after the 1150 K annealing step. The microscope was a JEOL 4000 EX/II operating at 400 kV with a point-to-point resolution of 0.17 nm. The specimen preparation is discussed elsewhere [Kooi et al. 2000]. RBS-C was used to detect damage recovery in the MgO and migration of

implanted Zn atoms. The samples measured with RBS-C were implanted under different implantation conditions, because they were produced in an older experimental program. Here a lower total dose of 1.4×10^{16} Zn ions cm^{-2} was implanted at energies ranging from 35 to 280 keV in order to create a flat Zn implantation profile. The RBS set-up consists of a beam of 2.0 MeV He ions in combination with a triple-axis goniometer. By using these complementary techniques, one attempts to create a good understanding of the defect evolution.

4.2.3. Results and discussion

Optical absorption spectroscopy

Fig. 4.6 shows the optical absorption spectra after implantation of 1.0×10^{17} Zn ions cm^{-2} and after various annealing steps. The presence of Zn nanoclusters results in optical absorption due to Mie plasmon resonance [Kreibig et al. 1995]. Unfortunately, the wavelength-dependent optical constants of MgO and Zn [Van Huis et al. 2003] are such that the Mie plasmon resonance peak interferes with the F-centres of MgO (O vacancies) at a photon energy of 4.9 eV and with Fe^{3+} impurity centres at 4.4 eV [Las et al. 1984]. After annealing at 950 K, it is clear that the Fe^{3+} impurity peak is superimposed on a broader absorption peak. After annealing at 1150 K this broad absorption peak, which is due to Mie plasmon resonance, is well developed and has a centroid at a photon energy of 4.2 eV. Results published in the literature show that ZnO nanoclusters have an absorption edge at 3.3 eV at room temperature [Zu et al. 1997, Zhang et al. 1999b].

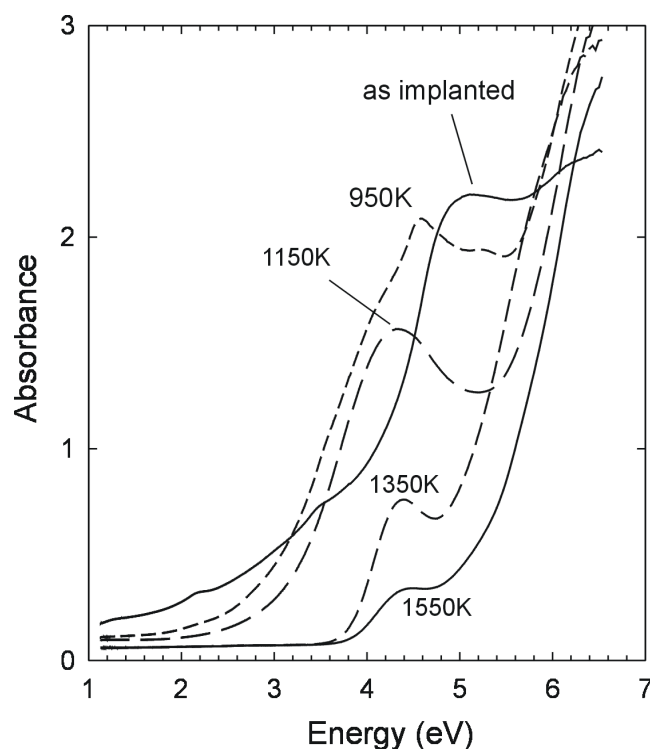


Fig. 4.6. Optical absorption spectra of MgO as-implanted with 1×10^{17} Zn ions cm^{-2} and after annealing at various temperatures.

Comparing the absorption curves in Fig. 4.6 with the absorption curves of ZnO nanoclusters in the literature, it can be concluded that there is no evidence of ZnO nanocluster formation. The TEM analysis discussed below shows that after annealing at 1150 K, the clusters are made up of metallic Zn rather than semiconductor ZnO. Therefore, both the optical and TEM results show that the clusters are metallic up to a temperature of at least 1150 K. The absorption peak at 4.2 eV decreases upon annealing at 1350 K and almost vanishes after annealing at 1550 K, suggesting shrinkage and dissociation of the Zn nanoclusters.

RBS-C

The strong reduction in the Mie plasmon absorption peak after annealing at 1150 K implies that the Zn has dissolved in the MgO matrix, which was confirmed by RBS-C measurements performed on an MgO sample implanted with Zn ions under the slightly different ion implantation conditions mentioned above (Section 4.2.2). These samples were subjected to the same annealing treatment as the high-dose 140 keV Zn implanted samples. The RBS-C results are displayed in Fig. 4.7. Part (a) of the figure shows the RBS-C spectra obtained after annealing at 550 K, while the spectra shown in Fig. 4.7(b) were obtained after annealing at 1550 K. It is clear that the channelling in the MgO improved during the annealing sequence, showing recovery of ion implantation damage in the MgO matrix. The shape of the Zn peak shows only very minor changes during annealing up to a temperature of 1350 K (compared to the shape of the Zn peak prior to thermal annealing).

The shape of the Zn peak in Fig. 4.7(a) does not resemble at all a flat implantation profile. Possibly this is due to processes such as channelling and radiation-induced annealing and diffusion. The channelling observed in the Zn peak in (a) was also observed in the as-implanted sample. Apparently, Zn is already mobile at room temperature. From the angular scans (not shown) it was found that Zn mainly occupies substitutional Mg sites in the MgO lattice. The shape of the Zn peak only changed (very drastically) upon annealing at 1550 K. Instead of a peak, a very broad Zn band stretches towards larger depths. The Zn atoms have diffused into the MgO matrix, and the MgO surface does not act as a sink since the Zn is not accumulating there. The question now arises as to the chemical state in which the Zn is present. Probably Zn is completely dissolved in the MgO and is present in substitutional lattice sites. Another possibility is that a composite ceramic structure $Zn_xMg_yO_{x+y}$ has been formed. This has been observed previously for the case of Zn ions implanted in sapphire Al_2O_3 , where $ZnAl_2O_4$ spinel was formed after thermal annealing at 1300 K [White et al. 1999b]. Another feature in Fig. 4.7(b) is the appearance of a strong carbon (C) peak after the annealing at 1550 K. The carbon contamination is probably introduced in the sample during thermal annealing. The sample investigated by means of RBS-C was not annealed in Delft, but in an air oven at the Forschungszentrum Karlsruhe.

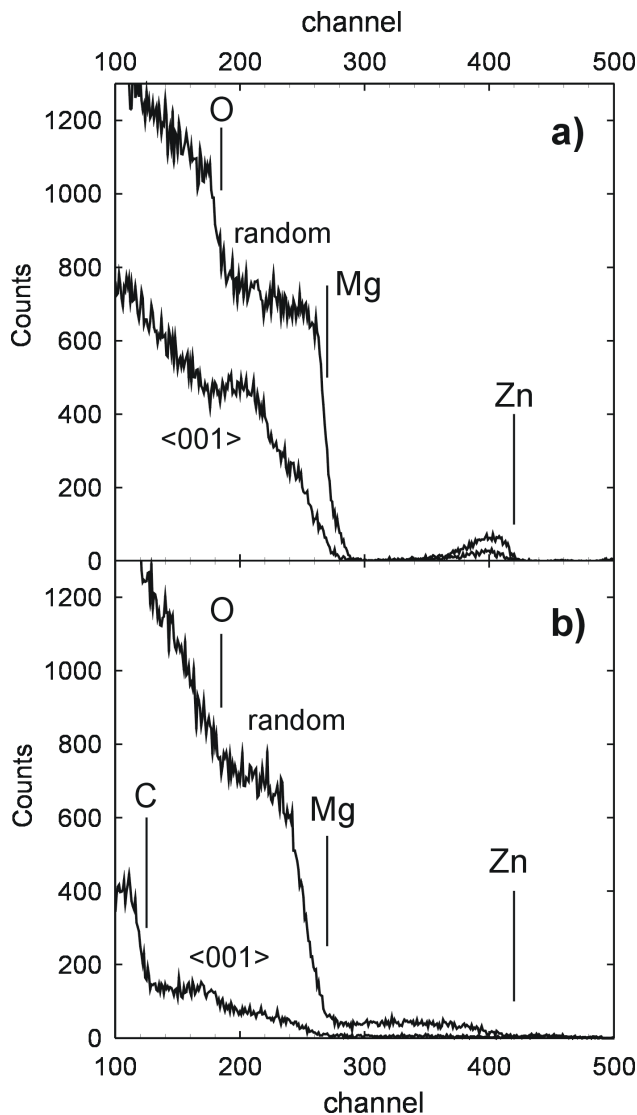


Fig. 4.7. RBS and $\langle 001 \rangle$ channelling spectra obtained on a sample implanted with 1.4×10^{16} Zn ions cm^{-2} after (a) annealing at 500 K and (b) annealing at 1550 K. The shape of the Zn peak did not change much during the annealing sequence until a temperature of 1550 K was reached.

Positron beam analysis

Doppler broadening positron beam analysis (PBA) is a very sensitive technique to monitor ion implantation damage; a high S parameter indicates open volume defects. Fig. 4.8 shows the S parameter as a function of the positron implantation energy for the sample after implantation of 1×10^{17} Zn ions cm^{-2} and after annealing at various temperatures. The depth resolution is limited (in particular at higher positron implantation energies) due to the broadness of the positron implantation profile and positron diffusion processes. The positron implantation energy corresponds to an average depth indicated at the top of the figure. In order to facilitate the discussion, four layers are indicated in Fig. 4.8. The top layer I contains mainly displacement damage created by the ion implantation. Layer II represents the ion implantation range, layer III contains a 'tail' of ion implantation defects (caused by channelling effects), and layer IV is the MgO bulk. Comparing the curve of the as-implanted sample with that of reference MgO, it is clear that the S parameter rises in layers I and II.

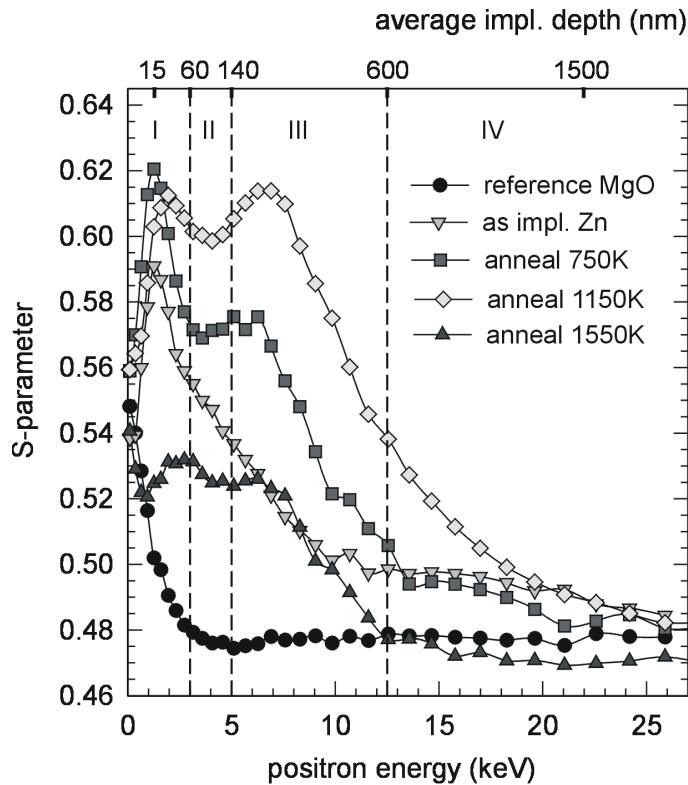


Fig. 4.8. S parameter as a function of positron implantation energy, after ion implantation of 1×10^{17} Zn ions cm^{-2} and after annealing at various temperatures. The average positron implantation depth is indicated at the top of the figure.

After annealing at 1150 K, there are two peaks in the S parameter corresponding to open-volume defects created by agglomeration of vacancy-type defects. Of course, vacancies have also been created in the ion implantation range (layer II), but there they recombine with the implanted Zn ions. Thus, in layer II the S parameter is lower because there are fewer open volume defects. After annealing at 1350 and 1550 K, the S parameter decreases in layers I, II and III, indicating recovery of ion implantation damage. Furthermore, the S parameter in the MgO bulk (layer IV) is lower than that of bulk MgO after annealing at 1550 K. This unusual observation suggests that the MgO bulk has changed, in agreement with the RBS results discussed above, which show that the Zn dissolves into the MgO bulk upon annealing at 1550 K.

XTEM

The evolution of ion implantation defects always starts with recombination and dissociation of the smallest defects and evolution into larger defects (vacancy cluster agglomeration, formation of nanoclusters and dislocation loops). Above a certain temperature, this process is followed by the shrinkage and dissociation of larger defects. From the optical and PBA results, the sample annealed at 1150 K was chosen as the most interesting one to perform an XTEM analysis on. Fig. 4.9 shows a bright-field XTEM image of this sample. The Zn clusters can be easily observed from the moiré fringes and are about 5-10 nm in size. Fig. 4.10(a) shows a high-resolution image of a Zn nanocluster.

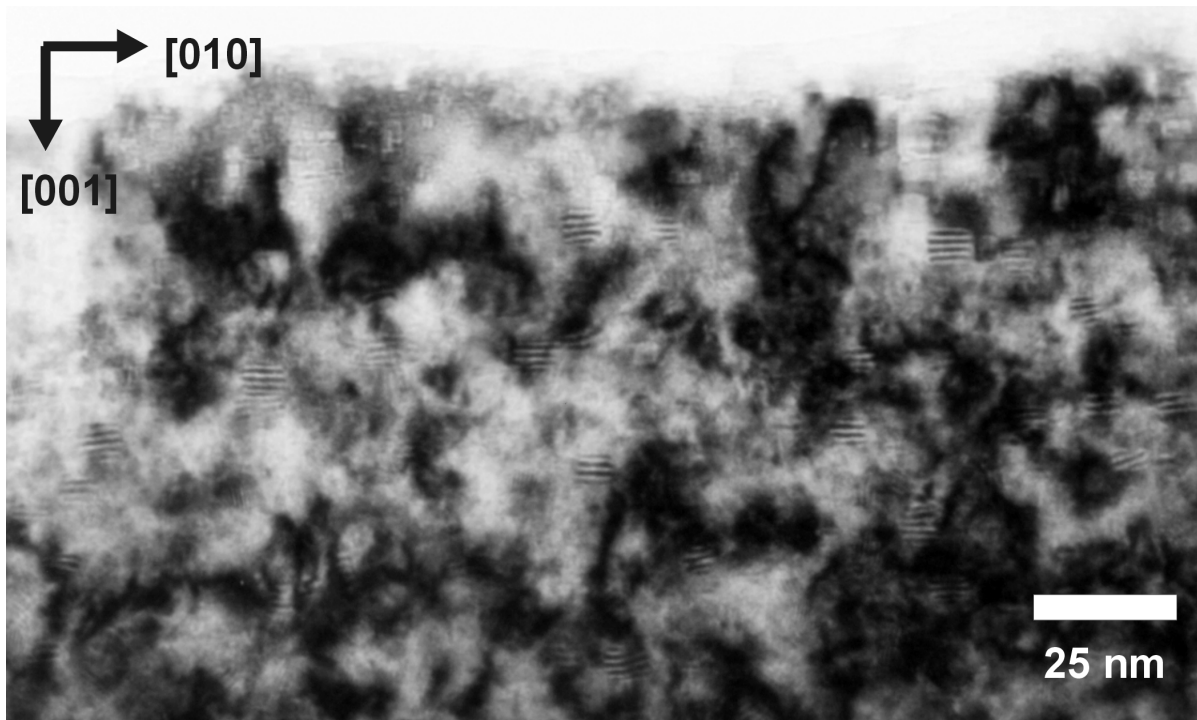


Fig. 4.9. Bright-field TEM image showing moiré fringes belonging to Zn nanoclusters created by implantation of 1×10^{17} Zn ions cm^{-2} and subsequent annealing at 1150 K. Only those clusters are visible that have the c -axis aligned with the MgO[001] axis.

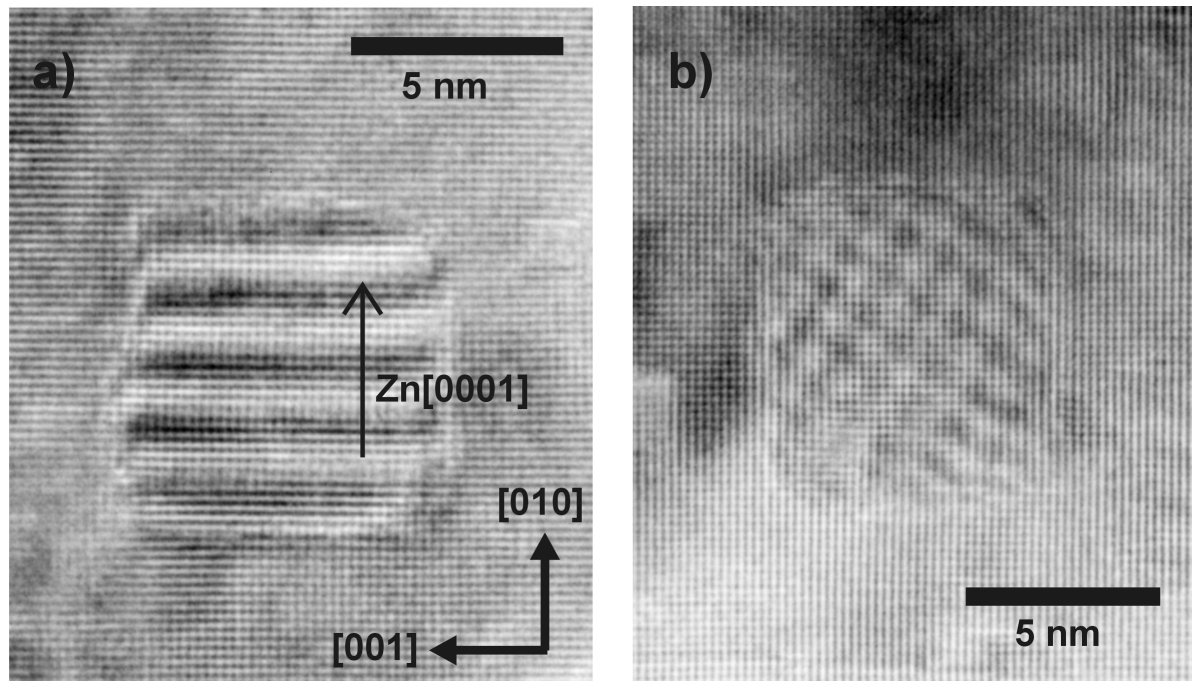


Fig. 4.10. High-resolution TEM images showing a Zn nanocluster (a) with translational moiré fringes along the MgO[010] axis and (b) with general moiré fringes.

From Fig. 4.9, it appears that all the clusters exhibit the same orientation and that only translational moiré fringes are found. However, when selecting other diffraction conditions or when operating in the high-resolution mode, other types of moiré fringes (non-translational) are observed as well. Fig. 4.10(b) shows a high-resolution image of a Zn nanocluster with general moiré fringes. In Fig. 4.10(a) the translational moiré fringes run in the [010] direction. Simultaneously though, clusters can be found that have the same moiré fringes running in the [001] direction (with the clusters close to each other, in the same area, observed under the same diffraction conditions). From these observations and the spacing of the moiré fringes discussed below, it is most likely that the c -axis of hexagonal Zn is aligned with one of the cubic MgO[001] axes. The lattice spacing of Zn crystals in the [010] direction can be determined from the relationship between d_{fringes} observed in Fig. 4.10(a) and the lattice spacings:

$$\frac{1}{d_{\text{fringes}}} = \left| \frac{1}{d_{\text{MgO}}} - \frac{1}{d_{\text{Zn}}} \right|. \quad (4.10)$$

MgO has a lattice parameter of 4.212 Å, so that $d_{\text{MgO}(002)}=2.106$ Å. There are four moiré fringes in 29 MgO lattice spacings and application of Eq. (4.10) then yields $d_{\text{Zn}}=2.44$ Å. The lattice parameters of hexagonal zinc are $a=2.665$ Å and $c=4.947$ Å [JCPDS]. Therefore, $d_{\text{Zn}(0002)}=2.47$ Å, which corresponds very well to the d_{Zn} calculated from the moiré fringes. Thus, the Zn nanoclusters have the usual hcp crystal structure and the c -axis is aligned with one of the cubic MgO axes: MgO(001)//Zn(0001).

Considering Fig. 4.10(a), the translational moiré fringes will run in the [010] direction when the c -axis is aligned with the MgO[010] axis and in the [001] direction when the c -axis is aligned with the MgO[001] axis. The rotational moiré observed in Fig. 4.10(b) can occur when the c -axis is perpendicular to the images in Fig. 4.10, i.e., in the [100] direction. The MgO//Zn alignment within the basal plane (i.e., perpendicular to the c -axis) is not clear from the TEM results.

X-ray diffraction

High-resolution X-ray diffraction was performed on the sample implanted with 1×10^{17} Zn ions cm^{-2} and annealed at 1150 K; the result is shown in Fig. 4.11. A small peak is present in the figure, which corresponds to the Zn(002) diffraction peak. This means that the c -axis of Zn is indeed aligned with the MgO[001] axis: MgO(001)//Zn(0001). The centroid of the Zn(002) peak is at 36.10° . Using Bragg's law, $\lambda = 2d_{hkl} \sin(\vartheta)$, with $\lambda=1.54056$ Å, it follows that the lattice parameter for Zn is $c_{\text{exp}}=4.973$ Å. Considering that the bulk lattice parameter for the c -axis is $c_{\text{ref}}=4.947$ Å [JCPDS], there is a tensile strain along the c -axis of +0.5%.

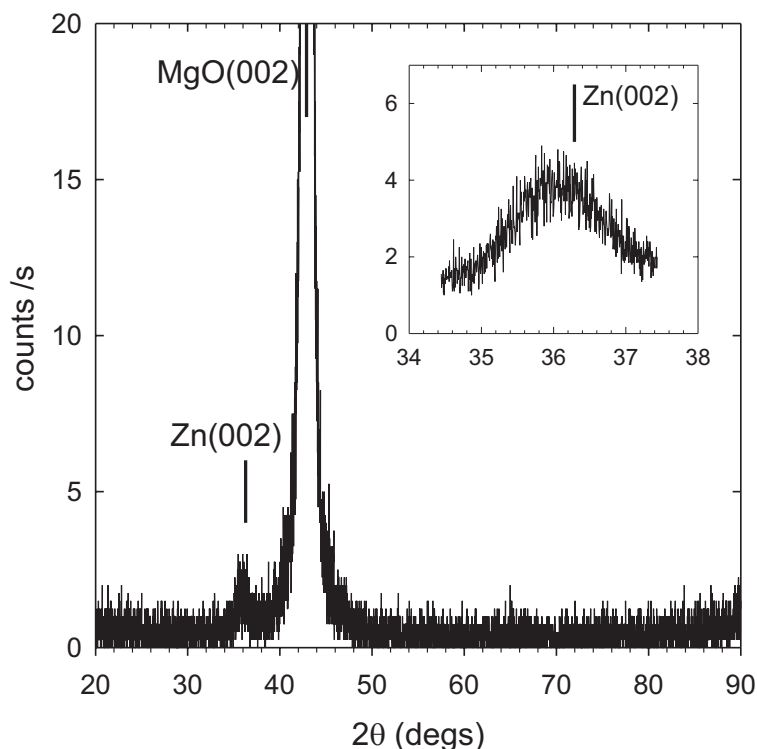


Fig. 4.11. XRD θ - 2θ scan of an MgO sample implanted with 1×10^{17} Zn ions cm^{-2} after annealing at 1150 K. The Zn(002) peak is shown in the inset on an expanded scale.

This conclusion is only valid for those Zn clusters that have the c -axis aligned with the MgO[001] axis (perpendicular to the ion implantation layer) because only these Zn clusters contribute to the Zn(002) peak observed in Fig. 4.11. In an attempt to determine the orientation relationship within the basal plane of the hcp Zn, a texture scan was made of the Zn(101) reflection, which is the most intense diffraction peak of Zn. From this texture scan, indications were found that alignments other than MgO(001)//Zn(0001) are present as well. More measurements and analysis are necessary to assess all possible orientation relationships.

4.2.4. Conclusions

Metallic zinc nanoclusters were created in MgO by means of ion implantation and subsequent annealing. An optical absorption peak appears at 4.2 eV after annealing at 1150 K caused by Mie plasmon resonance in metallic Zn nanoclusters. TEM investigations performed after annealing at 1150 K show that the nanoclusters have sizes of 5-10 nm and possess the usual hcp Zn crystal structure. From the XRD and TEM results it was found that the c -axis of Zn is aligned with the cubic MgO axes, MgO(001)//Zn(0001), although this is not the only possible orientation relationship. Optical, RBS-C and PBA results show that the nanoclusters dissociate during annealing at a temperature of 1550 K; the Zn is dissolved and diffuses into the MgO matrix. No evidence was found for the presence of ZnO nanoclusters. For future attempts to create ZnO nanoclusters it is recommended to use co-implantation of the same dose of Zn and O ions instead of relying on internal oxidation.

4.3. Au and Ag nanoclusters in MgO

4.3.1. Introduction

Gold and silver nanoclusters are the most extensively studied nanoclusters. Of all the elements, they show the strongest optical absorption due to Mie plasmon resonance and have the strongest non-linear optical properties [Kreibig et al. 1995, Stepanov et al. 2002, Fukumi et al. 1994, Chakraborty 1998, Zimmerman et al. 1999]. Unless the implantation doses are very high, the precipitation of the implanted atoms starts only after subsequent annealing. Many factors influence the size and the size distribution of these precipitates, such as the ion implantation dose, ion implantation energy, annealing temperature, annealing time and chemical environment where the annealing takes place (inert, oxidising or reducing environment). The average size and the size distribution are best determined from cross-sectional transmission electron microscopy (X-TEM). However, this technique often implies destruction of the sample while the specimen preparation is time consuming. Therefore, many authors performing annealing studies try to estimate the precipitate size from the broadening of the optical absorption peak present because of Mie plasmon resonance [Zimmerman et al. 1999]. Here the Doyle theory [Doyle 1958] is used to estimate the nanocluster size during the annealing procedure. Alternatively, the size can be estimated from the broadening of the XRD diffraction peaks using the Scherrer formula [Langford et al. 1978]. In this section, we compare the nanocluster size obtained from the three methods mentioned above. XRD and XTEM are also employed to determine the coherency and the orientation relationship of the gold and silver clusters with the surrounding matrix.

4.3.2. Experimental

In order to create silver and gold nanoclusters, epi-polished MgO(100) single crystals of size $10 \times 10 \times 1 \text{ mm}^3$ were implanted at room temperature with 1.0×10^{16} Au or Ag ions cm^{-2} at an energy of 1.0 MeV and 600 keV, respectively. These energies were chosen in order to obtain the same ion distribution depth so that the atomic concentration of implanted species in the ion implanted layer is approximately equal for Au and Ag as predicted by the SRIM ion implantation code [Ziegler et al. 1985, Fedorov et al. 2001b]. After ion implantation, the samples were annealed in ambient air at temperatures up to 1473 K for a period of 22 hrs. The sample treatment data are listed in Table 4.5. The following techniques were employed for the characterisation of the optical and structural properties of the nanoclusters: optical absorption spectroscopy (OAS), high-resolution X-ray diffraction (XRD) and cross-sectional transmission electron microscopy (XTEM). The XRD measurements were performed using a Philips X'Pert materials research diffractometer system with a ceramic X-ray tube providing Cu K_α radiation.

Table 4.5. Sample treatment and structural properties of the Au and Ag nanoclusters.

	MgO:Au	MgO:Ag
Sample treatment		
implantation	1 MeV, 10^{16} Au ⁺ cm ⁻²	600 keV, 10^{16} Ag ⁺ cm ⁻²
thermal anneal	1473K, 22 hrs	1473K, 22 hrs
Cluster size and shape		
Optical abs. (Doyle)	4.3 nm	5.1 nm
XRD (Scherrer), (113) peak	4.0 nm ($K_w=0.8290$)	9.8 nm ($K_w=0.8863$)
XTEM mean size	4.6 nm	11 nm
distribution	2-14 nm	6-24 nm
shape	spherical	octahedral
Lattice parameter a		
literature	4.078 Å	4.085 Å
misfit ($a_{MgO}=4.212$ Å)	3.2 %	3.0%
experimental a (XRD)	4.09 Å	4.12 Å
coherency strain $\epsilon_{[100]}$ (XRD)	+0.4%	+0.9%

The TEM was performed using a JEOL 4000 EX/II operating at 400 kV (point-to-point resolution 0.17 nm). The specimen preparation is discussed in Subsection 2.6.1.

4.3.3. Optical and structural properties

The results of the optical absorption measurements carried out on the MgO:Au and MgO:Ag samples were published by Fedorov et al. (2001b) and are shown in Fig. 4.12. Optical absorption bands are present due to Mie plasmon resonance. The size of the nanoclusters can be estimated from the width of the peaks using the Doyle theory. In this theory, the mean free path of the electrons constituting the plasmon is limited by the size of the nanocluster. This allows estimation of the cluster size from [Doyle 1958]

$$D = 2 \frac{v_F}{\Delta\omega_{1/2}} = 2 \frac{v_F}{2\pi c} \frac{\lambda_{\max}^2}{\Delta\lambda_{1/2}}. \quad (4.11)$$

Here D is the diameter of the precipitate (m), v_F the Fermi velocity (1.39×10^6 m/s for both gold and silver [Kittel 1986]), $\Delta\omega_{1/2}$ the FWHM of the peak when plotted as a function of the circular frequency ω (rad/s), c the speed of light, λ_{\max} the position of the centroid of the peak and $\Delta\lambda_{1/2}$ the FWHM of the peak when plotted as a function of wavelength. The background in the optical spectra was fitted with an exponential function and the Mie plasmon resonance peak was fitted with a Gaussian. The FWHM of the Gaussian and the parameters mentioned above were substituted into Eq. (4.11), yielding cluster diameters of 4.3 and 5.1 nm for the Au and Ag clusters, respectively.

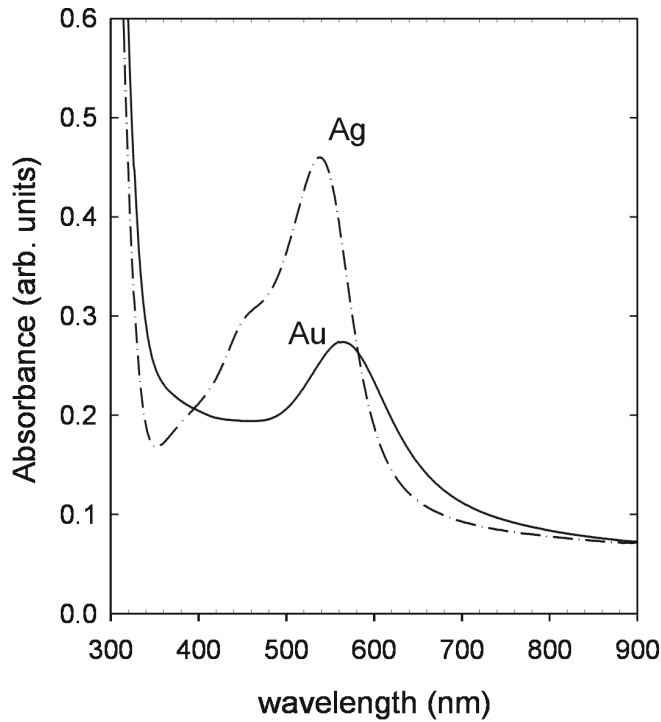


Fig. 4.12. Optical absorption spectra of Au and Ag implanted MgO after annealing at a temperature of 1473 K. The absorption peaks are caused by Mie plasmon resonance.

High-resolution XRD measurements were carried out on the MgO(002), (113), (004) and (024) diffraction peaks. Fig. 4.13 (a) and (b) show the contour plots of the (113) diffraction peaks of the MgO:Au and MgO:Ag samples, respectively. The $q_{[001]}$ axis corresponds to diffraction along the [001] crystal axis (perpendicular to the surface); the $q_{[110]}$ axis corresponds to diffraction along the [110] crystal axis (parallel to the surface). The crystal structure of MgO, Au and Ag is fcc; their lattice parameters are listed in Table 4.5. Because the lattice parameters of Au and Ag are close to that of MgO, Au(113) and Ag(113) satellite peaks are observed near the intense MgO(113) peaks in Fig. 4.13. The broadening of the MgO diffraction peaks is due to mosaic broadening (rocking curve). Au and Ag satellite peaks were also found near the MgO (002), (004) and (024) diffraction peaks, clearly indicating a cube-on-cube orientation relationship with the MgO host matrix. The cluster size was estimated from the width of the (002) and (113) diffraction peaks using the Scherrer formula [Langford et al. 1978]

$$p = K_w \cdot \frac{\lambda_0}{\Delta\theta \cos\theta} = K_w \cdot \frac{2}{\Delta q \sqrt{h^2 + k^2 + l^2}} \quad (4.12)$$

Here p is the precipitate size, defined as the cube root of the precipitate volume. Furthermore, λ_0 is the wavelength (1.540560 Å), θ the position of the (hkl) diffraction peak, $\Delta\theta$ the FWHM of the same diffraction peak and Δq the FWHM of the peak in reciprocal space in m^{-1} .

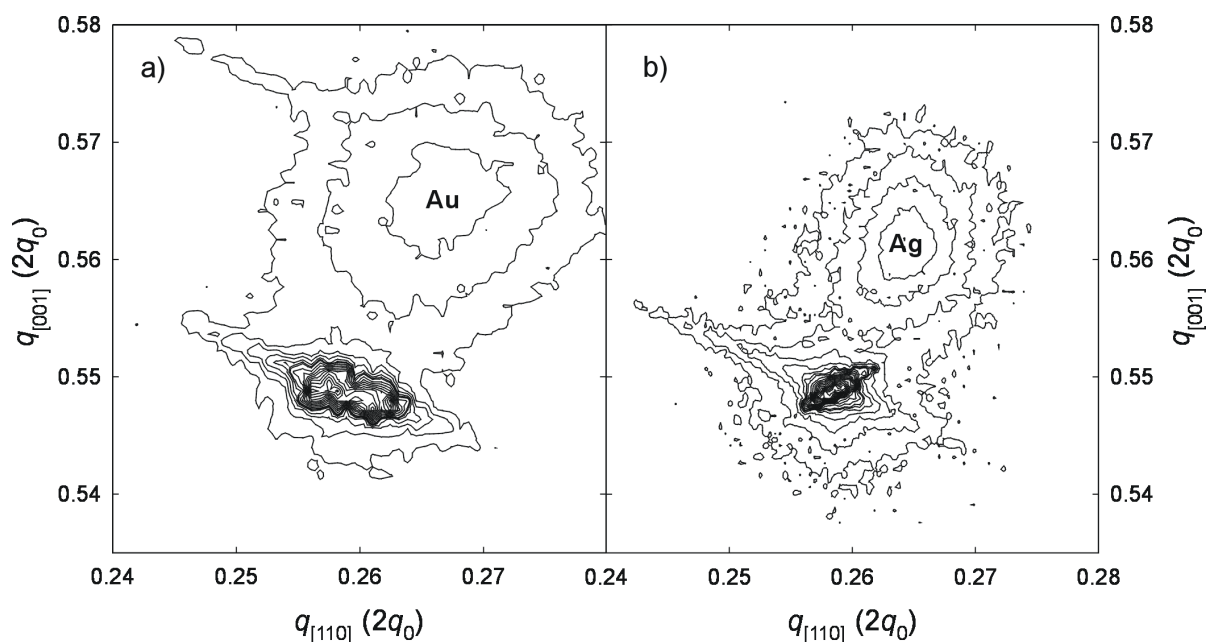


Fig. 4.13. Reciprocal space plots of a) the MgO(113) and Au(113) diffraction peaks of the MgO:Au sample and b) the MgO(113) and Ag(113) diffraction peaks of the MgO:Ag sample. Units are $2q_0=2/\lambda_0$.

The half-width Scherrer constant K_w depends on the shape of the nanocluster and – if the clusters are not spherically shaped – also on the (hkl) index of the diffraction peak [Langford et al. 1978]. The right-hand side of Eq. (4.12) is derived from Bragg's law, $\lambda = 2d_{hkl} \sin(\vartheta)$, and $q \equiv 1/d_{hkl}$. Here $d_{hkl} = d/\sqrt{h^2 + k^2 + l^2}$ where d is the lattice parameter of the material. k is the diffraction vector in reciprocal space and is commonly expressed in units of $2q_0 \equiv 2/\lambda_0$.

The results of the Scherrer analysis are shown in Table 4.5. From the XTEM results discussed below, it was found that the shape of the Au clusters is spherical while the Ag clusters are octahedral. The corresponding values for the Scherrer constant K_w are listed in Table 4.5 and obtained from Ref. [Langford et al. 1978]. The cluster sizes were derived from the (113) rather than from the (002) diffraction peaks, because the (113) diffraction peaks of Au and Ag are better resolved from the corresponding MgO peaks than the (002) peaks. Therefore, the cluster sizes obtained from the (113) peaks are more accurate. From the positions of the Au(002) and Ag(002) peaks, the mean lattice parameters of the nanoclusters perpendicular to the surface were also calculated. It was found that the Au and Ag lattices are extended by 0.4% and 0.9%, respectively, in the direction perpendicular to the surface. This is probably caused by coherency strains since the lattice parameters of Au and Ag are smaller than the lattice parameter of MgO (see Table 4.5). Calculation of the tensile strain from the (113) diffraction peaks yields the same result. We shall now discuss the results of the XTEM analysis so that the results of the three methods can be compared.

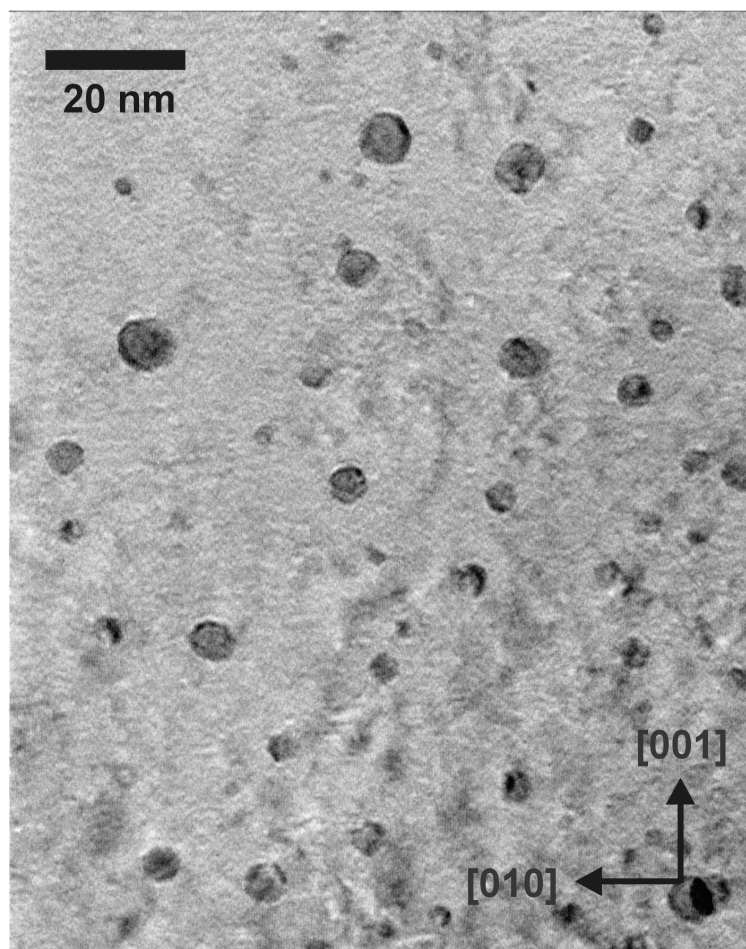


Fig. 4.14. Bright-field TEM image of a part of the Au implanted layer showing a typical size distribution of spherically shaped Au clusters.

The MgO:Au and MgO:Ag samples were analysed with XTEM. In the MgO:Au specimen, a band of Au clusters was found at depths between 140 and 300 nm below the surface. Fig. 4.14 shows a typical size distribution of the spherically shaped Au clusters. The size of the gold clusters varies from 2-14 nm with a mean size of 4.6 nm (average obtained from 40 clusters). Fig. 4.15 shows a high-resolution TEM image of a few gold clusters.

The cube-on-cube orientation relationship is clearly observable since the lines of the MgO lattice spacing continue in the Au nanocluster. XTEM analysis of the MgO:Ag sample yields a depth range of 180-350 nm below the surface, a size distribution of 6-24 nm and a mean cluster size of 11 nm (average obtained from 75 clusters). Fig. 4.16 shows a high-resolution (HR) TEM image of a silver cluster. It can be observed from the image that the Ag clusters have truncated octahedral shapes and that they are, just like Au, in a cube-on-cube orientation relationship with the MgO.

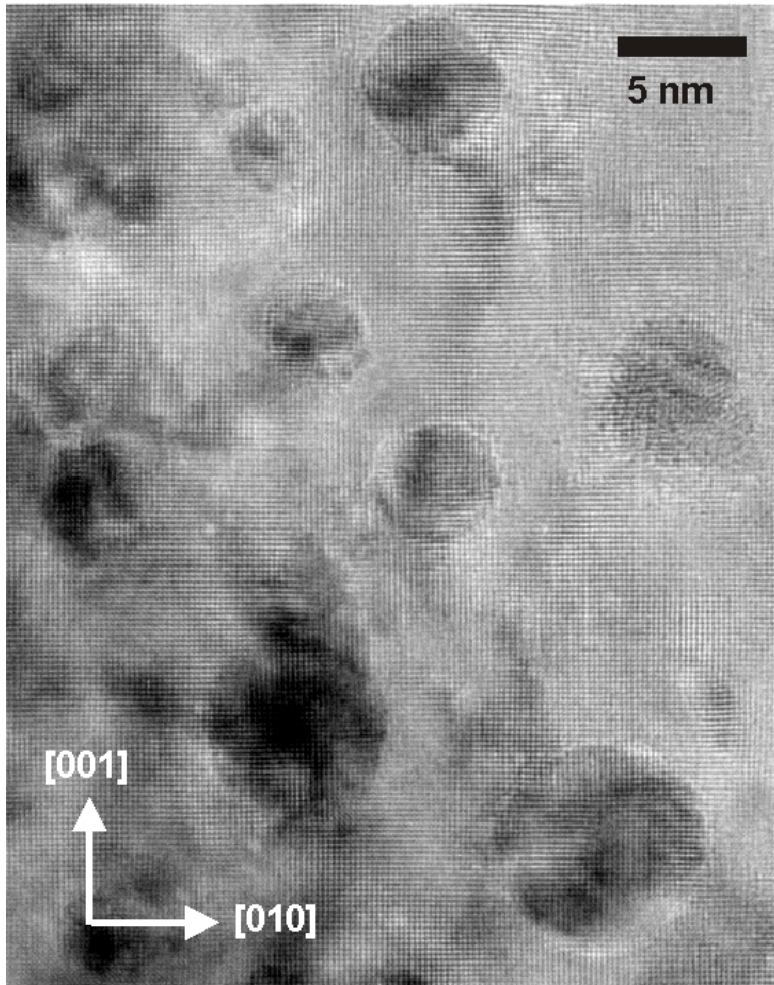


Fig. 4.15. HR-TEM image of a few spherically shaped gold clusters in a cube-on-cube orientation relationship with the embedding MgO matrix.

4.3.4. Discussion and conclusions

In the determination of the mean cluster size, the results of the Scherrer XRD method and the TEM observations are in excellent agreement. In the case of the Ag clusters, the Doyle optical method underestimates the cluster size, which might be attributed to additional broadening due to size dispersion and interface effects.

Kreibig et al. (1996) have shown that embedding of Ag nanoclusters in various matrices leads to additional broadening of the absorption peaks by a factor of 2 to 4, compared to absorption peaks of Ag nanoclusters that are not embedded in a matrix. The additional broadening is dependent on the embedding medium. Consideration of Eq. (4.11) shows that additional broadening of $\Delta\lambda_{1/2}$ leads to an underestimation of the cluster size. XRD and TEM do not suffer from this artefact. However, both the Doyle and the Scherrer method may suffer from the effect of size distribution, which in general also induces additional broadening. Nevertheless, the results shown in Table 4.5 show that the Scherrer method accurately predicts the mean cluster size observed by means of TEM.

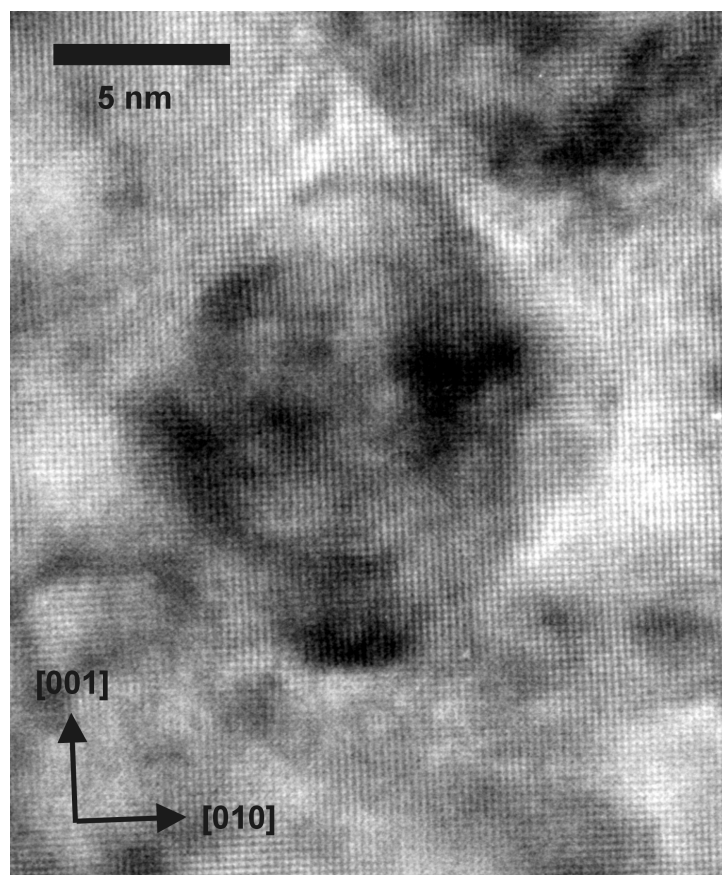


Fig. 4.16. HR-TEM image of a silver cluster with the shape of a truncated octahedron in a cube-on-cube orientation relationship with the embedding MgO matrix.

It was found here that, of these three methods of determining the cluster size, the Doyle optical method is the least accurate. This is caused by the asymmetry of the absorption peaks, inaccurate background subtraction and systematic underestimation due to interface effects. Scherrer XRD and XTEM are both accurate methods of determining the mean cluster size, while XTEM can also provide a good indication of the cluster size distribution. Considering that optical measurements take typically 10 minutes, XRD measurements a few hours and XTEM measurements about 3 days (including specimen preparation), Scherrer XRD is probably the best compromise. However, if one is interested mainly in the optical properties important for applications, optical absorption studies are indispensable.

4.4. In-situ Au nanocluster nucleation, growth and refinement in MgO

4.4.1. Introduction

In the previous section, the properties of Au and Ag nanoclusters were investigated using a number of complementary experimental techniques. Among these techniques, TEM is

indispensable for obtaining information on the spatial configuration, morphology and size distribution of the nanoclusters. In general, planar TEM or cross-sectional TEM is applied only at one point during the defect evolution, e.g., directly after implantation or after a certain post-annealing treatment. The IVEM-TANDEM facility [Allen et al. 1989] at Argonne National Laboratory (USA) offers the possibility of following the defect evolution in the specimen all the way during in-situ ion implantation and post-implantation treatments. Using this facility, we have investigated the formation, growth and degradation of Au clusters in MgO.

4.4.2. Experimental

The IVEM-TANDEM facility at Argonne National Laboratory [Allen et al. 1989] consists of a Hitachi H-9000 transmission electron microscope (TEM) operating at 300 kV coupled to a 650 kV NEC ion implanter. This allows in-situ observation of defect evolution during ion implantation and (simultaneous) thermal annealing. Thin MgO(100) specimens were prepared from bulk MgO single crystals following the procedure described in Subsection 2.6.1. The MgO specimens were mounted on a temperature-controlled stage (from 300 to 1100 K) and were tilted towards the ion beam ($\sim 30^\circ$ off the electron beam axis) during ion implantation. In order to create Au clusters, one specimen was implanted with 100 keV Au ions to a fluence of 1.8×10^{16} ions cm^{-2} while the specimen was kept at an elevated temperature of 700 K. After implantation, the specimen was annealed up to a temperature of 1100 K to induce coarsening and growth of the precipitates. In order to investigate the effect of ion irradiation on the nanoclusters, the specimen was subsequently irradiated with 600 keV Au ions to a fluence of 1.0×10^{16} cm^{-2} . At this acceleration energy the Au ions pass through the thin parts of the specimen and cause only displacement damage in the MgO slab. This will be discussed in detail in the next section. The sample treatments are listed in Table 4.6.

4.4.3. Results and discussion

In order to perform the experiments described above, it is necessary to either deposit the Au ions within the MgO foil or to shoot all ions through the foil, adding only displacement damage. In order to calculate the required acceleration energies and the corresponding ion and damage depth distributions, the SRIM 2000 code was used [Ziegler et al. 1985], using a value of 55 eV for the displacement energy of both the Mg and O atoms [Zinkle et al. 1997]. The implantation parameters are listed in Table 4.6 and the corresponding ion depth distribution and vacancy depth distribution are shown in Fig. 4.17 and Fig. 4.18, respectively. Estimating the thickness of thin areas of the MgO specimen at ~ 50 nm, the 100 keV Au ions will be implanted inside the MgO foil over a depth interval of 20-40 nm.

Table 4.6. Sample treatments, predicted ion implantation data and calculated ion and vacancy concentrations.

		100 keV Au	600 keV Au
Fluence	cm ⁻²	1.8×10 ¹⁶	1.0×10 ¹⁶
Implantation <i>T</i>	K	700 K	RT (300 K)
Annealing <i>T</i>	K	1100 K	-
Range <i>R_p</i> ^a	nm	28	107
Stragging Δ <i>R_p</i> ^a	nm	6	21
Ion conc. (peak)	at. %	12	1.8
Displacements per ion ^a		650	2900
Electr. energy loss ^a (d <i>E</i> /d <i>x</i>) _e	keV/nm	0.64	1.5
Nucl. energy loss ^a (d <i>E</i> /d <i>x</i>) _n	keV/nm	4.5	5.1
Dpa (peak)		41	27

^acalculated with the SRIM 2000 code [Ziegler et al. 1985].

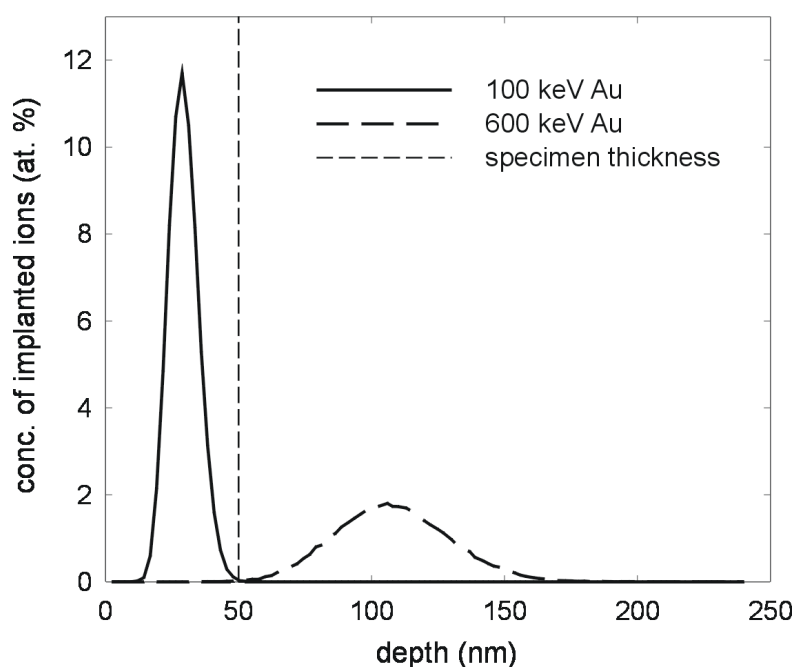


Fig. 4.17. Atomic depth distribution of implanted Au ions. Fluences are 1.8×10^{16} and 1×10^{16} cm⁻² for 100 keV Au and 600 keV Au, respectively.

The 600 keV Au ions pass completely through the foil (Fig. 4.17) but the implantation damage deposited inside the 50 nm MgO foil is about 15 and 30 dpa, respectively (Fig. 4.18). It should be realised that the validity of the SRIM results presented here is limited. The model assumes the material to be amorphous while MgO is monocrystalline. Furthermore, (thermal) effects such as defect migration, diffusion, recombination, agglomeration and dissociation are not taken into account. Sample 1 (MgO:Au) received three treatments: implantation with 100 keV Au ions at a temperature of 700 K to deposit Au ions inside the foil (range 28 nm), a post-implantation thermal annealing at 1100 K to induce coarsening and growth of Au clusters, and a post-irradiation annealing using 600 keV Au ions that pass completely through the foil (range 107 nm).

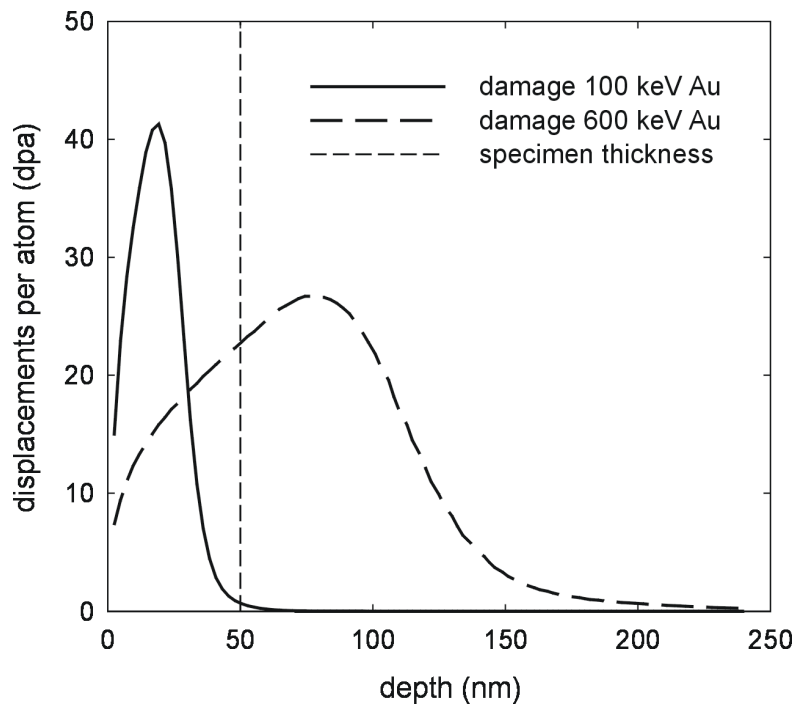


Fig. 4.18. Displacement damage distribution of implanted ion species. Fluences are 1.8×10^{16} and $1 \times 10^{16} \text{ cm}^{-2}$ for 100 keV Au and 600 keV Au, respectively.

The 100 keV Au ions deposited inside the foil reach a Au peak concentration of 12 at. %. Fig. 4.19 shows the defect evolution during the sample treatment. Prior to ion implantation, the MgO material is almost without contrast (Fig. 4.19a). Implantation of $1.8 \times 10^{16} \text{ cm}^{-2}$ 100 keV Au ions at a temperature of 700 K leads to the spontaneous formation of small Au precipitates with sizes of 2-3 nm (Fig. 4.19b). Subsequent thermal annealing at 1100 K leads to coarsening and growth of the nanoclusters to sizes of ~ 9 nm (Fig. 4.19c). Subsequent irradiation with Au ions at room temperature (range 107 nm, all ions go completely through the foil) leads to a refinement of the precipitates. After a fluence of $2 \times 10^{15} \text{ cm}^{-2}$, the cluster size already decreases from ~ 9 nm to ~ 5 nm (Fig. 4.19d). After a fluence of $1 \times 10^{16} \text{ cm}^{-2}$, a further reduction to ~ 3 nm takes place (Fig. 4.19e).

It is very likely that the Au nanoclusters are not very mobile, so that the growth of Au clusters is governed by an Ostwald ripening process rather than by migration coalescence. The ripening continues during post-implantation thermal annealing at temperatures up to 1100 K. The refining of the clusters upon irradiation with 600 keV Au ions results in an inverse ripening process. It is well-known that the damage caused by heavy-ion implantation is deposited very locally along the ion track in elongated defect clusters. These defect areas are reasonably narrow, of the order of 5 nm [Studer et al. 1997]. If one of the defect areas created in the heavy ion track incorporates a gold nanocluster, this cluster can be (partially) destroyed due to the very high, locally deposited, displacement damage.

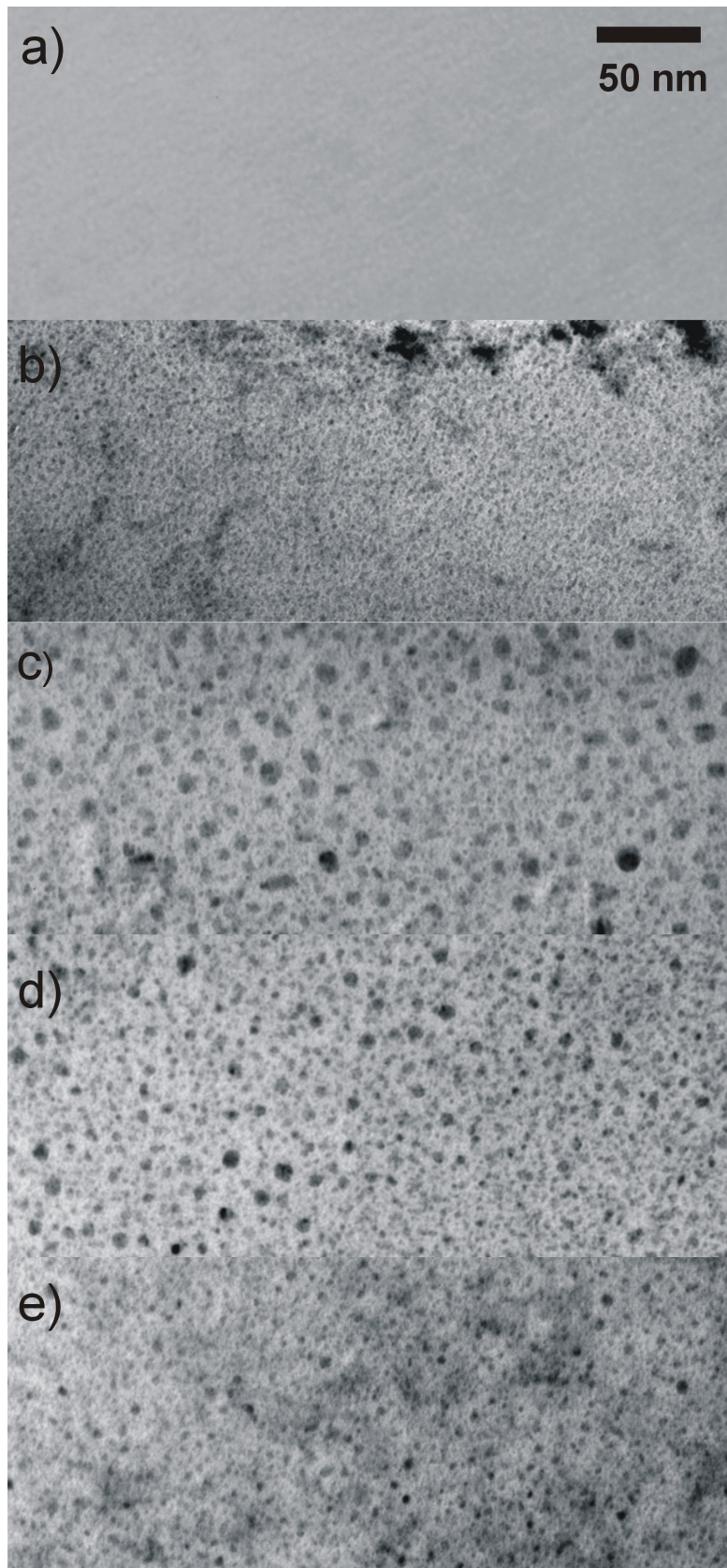


Fig. 4.19. Bright-field TEM images showing the evolution of the Au clusters. a) unimplanted; b) as implanted 100 keV Au, fluence $1.8 \times 10^{16} \text{ cm}^{-2}$; c) After 1100 K anneal; d) after post-irradiation with 600 keV Au, fluence $2 \times 10^{15} \text{ cm}^{-2}$; e) after post-irradiation with 600 keV Au, fluence $1 \times 10^{16} \text{ cm}^{-2}$.

Sufficient energy is available to remove Au atoms from the nanocluster and to reposition them as interstitial or substitutional Au atoms in the MgO. This seems to be in contradiction with the results by Ila et al. [Ila et al. 1999], who found that post-implantation irradiation with energetic ions actually enhances the nucleation and growth of Au clusters in SiO₂ by small energy transfers. The main difference between their work and the present work is that they use relatively light Si ions at an energy of 5.0 MeV, where the electronic stopping $(dE/dx)_e$ is two orders of magnitude larger than the nuclear stopping $(dE/dx)_n$ (see also Section 1.3). They also conclude that the nucleation and growth of nanoclusters is enhanced by the part of the electronic stopping that is deposited in the form of heat ('radiation-induced annealing'). However, in our case of 600 keV heavy Au ion irradiation, the nuclear stopping is five times as large as the electronic stopping (see Table 4.6). Therefore, the nuclear stopping dominates over the electronic stopping, which results in an inverse cluster growth compared to the growth achieved during thermal annealing at 1100 K. During the first stage (100 keV Au implantation at an elevated temperature of 700 K) the mechanisms of thermal annealing and heavy ion irradiation occur simultaneously. As can be seen in Fig. 4.18, the displacement damage deposited inside the foil by the 100 keV ions (~25 dpa) is even higher than the displacement damage deposited by the 600 keV Au ions in the first 50 nm (~15 dpa). The effects can be separated by performing a separate thermal annealing and a separate heavy-ion irradiation. It then becomes clear that in the case of heavy-ion irradiation, thermal annealing and radiation-induced annealing are competing processes, enhancing and reversing the growth of Au clusters, respectively. Although Au clusters form spontaneously during ion implantation at room temperature after reaching a certain threshold dose [Zimmerman et al. 1999], implantation at a higher temperature will induce an earlier and faster growth of the clusters [Fedorov et al. 2000].

4.4.4. Conclusions

TEM with in-situ ion implantation and thermal annealing is a very useful tool to study the defect evolution of nanocluster formation, growth and degradation. It was shown that thermal annealing at 1100 K enhances Au cluster growth while post-annealing irradiation with 600 keV Au ions leads to a refinement of the nanoclusters.

Chapter 5

Semiconductor nanoclusters

The optical, electrical and structural properties of nanoclusters change as a function of size, offering unique opportunities to tailor material properties for future use in applications. Semiconductor nanoclusters are particularly interesting because the electronic properties change already below a size of ~ 10 nm (see Section 1.1). When compared to the bulk properties of semiconductors, semiconductor nanocrystals exhibit uncommon crystal structures, lower melting temperatures and changes in the width of the band gap [Kamat et al. 1997, Goldstein et al. 1992, Alivisatos 1996a, Alivisatos 1996b, Peng et al. 2000]. One feature of nanoclusters is the large fraction of surface atoms. The first few atomic layers at the outside of the nanocluster will have properties different from the interior of the nanocluster (due to surface reconstruction, presence of defects, bending of electron bands, other charge carriers). In order to passivate the surface, the nanoclusters should be embedded in hosts with a large band gap and similar structural properties. Ion implantation into ceramic oxides is a practical method of creating embedded, electronically passivated semiconductor nanoclusters [White et al. 1998, White et al. 1999a]. MgO has a high melting temperature (>3000 K) and a large band gap of 7.8 eV. Furthermore, it is optically transparent so that the optical properties of the nanoclusters can still be investigated. Apart from Si and Ge, most semiconductors are composites and therefore require co-implantation of the elements constituting the semiconductor.

5.1. Introduction

One of the semiconductor cluster systems, which has received much attention is CdSe [Peng et al. 2000, Alivisatos 1996a, Alivisatos 1996b]. The band gap of CdSe nanoclusters increases with decreasing cluster size. So, e.g., the band gap of CdSe clusters with a size of 2 nm is 2.5 eV while the band gap of bulk CdSe is 1.8 eV. In addition, phase transitions occur when the cluster size changes [Jacobs et al. 2002]. In this chapter, the formation of CdSe nanoclusters in MgO by sequential Cd and Se ion implantation is discussed. The defect evolution during the annealing treatment is monitored with the aid of three complementary techniques: optical absorption spectroscopy, positron annihilation spectroscopy and transmission electron microscopy.

5.2. Experimental

In order to create nanoclusters, monocrystalline MgO(100) samples were sequentially implanted with 1×10^{16} Cd and 1×10^{16} Se ions cm^{-2} at an energy of 280 and 210 keV, respectively. After ion implantation, isochronal annealing was performed in ambient air at temperatures up to 1500 K in steps of 200 K for periods of 0.5 h. After ion implantation and after each annealing step, the defect evolution in the sample was monitored using optical absorption spectroscopy and Doppler broadening positron beam analysis (PBA) [Van Veen et al. 2000]. The PBA technique is explained in Section 2.7. The principal parameter considered in the Doppler broadening PBA experiments was the S parameter as it is a good indicator of open-volume defects. For these experiments, a mono-energetic positron beam with a variable energy of 0-30 keV was used. One sample was examined by means of cross-sectional transmission electron microscopy (XTEM) after the 1300 K annealing step. The specimen preparation is discussed elsewhere [Kooi et al. 2000]; the microscope used was a JEOL 4000 EX/II operating at 400 kV (point-to-point resolution 0.17 nm).

5.3. Formation of CdSe nanoclusters

SRIM simulations

The ion implantation energies were chosen in such a way that the Cd and Se ion implantation profiles overlap as much as possible. Fig. 5.1 shows the SRIM calculations [Ziegler et al. 1985] for 280 keV Cd and 210 keV Se. Displacement energies of 55 eV were used for both the Mg and the O atoms [Zinkle et al. 1997].

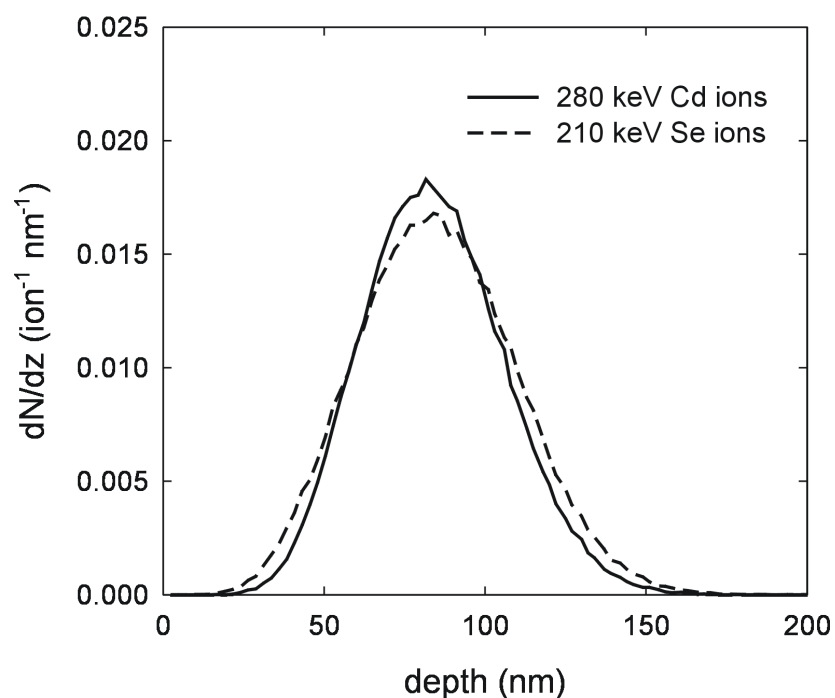


Fig. 5.1. Predicted depth distribution of 280 keV Cd ions and 210 keV Se ions in MgO, calculated with the SRIM code [Ziegler et al. 1997].

As is clear from the figure, the straggling of the Cd profile is somewhat larger than that of the Se profile. However, during the nanocluster formation process, the atoms are somewhat mobile, which is expected to reduce a possible deviation from stoichiometry. Cd and Se have melting points (594 K and 490 K, respectively), which are much lower than that of CdSe (1350 K [Handbook 1986]). Cd and Se nanoclusters will therefore be much less stable during thermal annealing and will easily dissociate to form CdSe nanoclusters. At the peak of the CdSe distribution, the concentration is 3.2 mol. % (CdSe per MgO).

Optical absorption spectroscopy

Fig. 5.2 shows the optical absorption spectra after ion implantation and after various annealing steps. After ion implantation, V-centres (Mg monovacancies) are present at a photon energy of 2.2 eV, as well as F-centres (O monovacancies) at an energy of 4.9-5.0 eV. After annealing at 700 K, an absorption peak appears at 4.4 eV corresponding to Fe³⁺ impurity centres [Las et al. 1984]. During the annealing procedure, the V-centres dissociate and the intensity of the F-centres reduces. Unfortunately, no evidence of CdSe nanoclusters can be found in the optical absorption spectra. These could be expected at a (band gap) energy in the range of 1.8-2.5 eV. It is not likely that the absorption peak at 2.2 eV in Fig. 5.2 corresponds to CdSe nanoclusters (instead of V-centres), because this peak disappears already after annealing at a temperature of 500 K. The broad size distribution of the CdSe nanoclusters created by means of ion implantation (see the discussion of the TEM results below) will give a smeared absorption band originating from a multitude of absorption peaks rather than one or more distinct absorption peaks. The position of the peak is dependent on the size (and therefore the band gap) of the nanocluster.

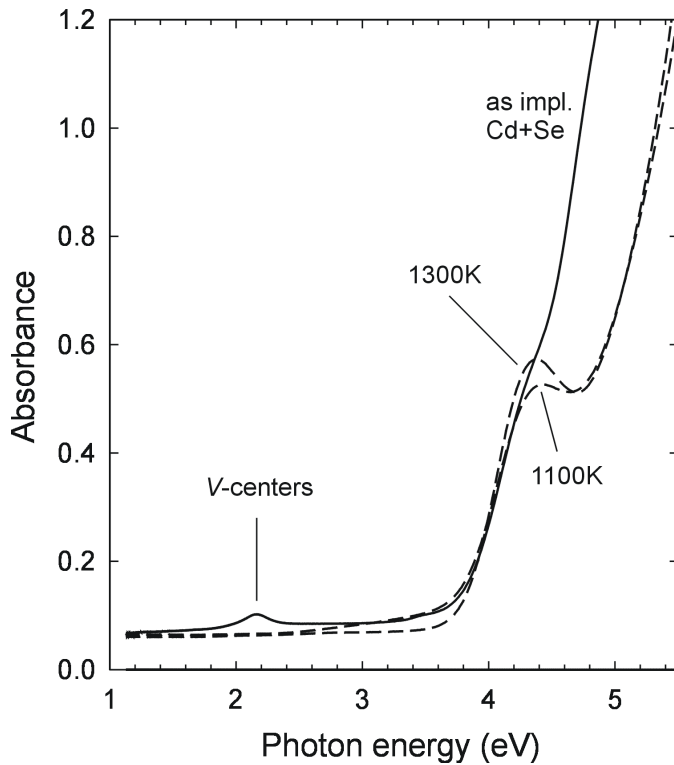


Fig. 5.2. Optical absorption spectra of MgO as-implanted with Cd and Se and after annealing at the indicated temperatures.

For example, nanoclusters with a size of 2 nm give an absorption peak at ~ 2.5 eV while nanoclusters with a size of 4 nm produce an absorption peak at ~ 2.1 eV [Alivisatos 1996a]. Nevertheless, despite the size dispersion, it could still be possible to detect optical absorption by CdSe nanoclusters. In a previous study, CdSe nanoclusters were created by means of ion beam synthesis in sapphire Al_2O_3 [White et al. 1998] where an absorption edge was found at a wavelength of ~ 700 nm, corresponding to a band gap of ~ 1.8 eV. In the present work, the ion implantation doses are lower, indicating that the overall intensity generated by the nanoclusters is too low to be resolved.

Positron beam analysis

Fig. 5.3 shows the S parameter (indicator of open-volume defects) as a function of positron implantation energy. The average positron implantation depth is indicated at the top of the figure. It should be realised that the depth resolution is limited due to the straggling of the positron implantation profile and positron diffusion processes (the resolution is approximately 20% of the implantation energy). In order to facilitate the discussion, a four-layer model is indicated in the figure. Layer I contains mostly displacement damage, layer II is the ion implantation range, layer III is a ‘tail’ of implantation defects mainly caused by channelling effects, and layer IV is the MgO bulk. The boundaries of layer II correspond reasonably well to the ion range predicted by SRIM in Fig. 5.1. Directly after ion implantation, the S parameter in layers I-III increases due to the creation of vacancies and vacancy clusters.

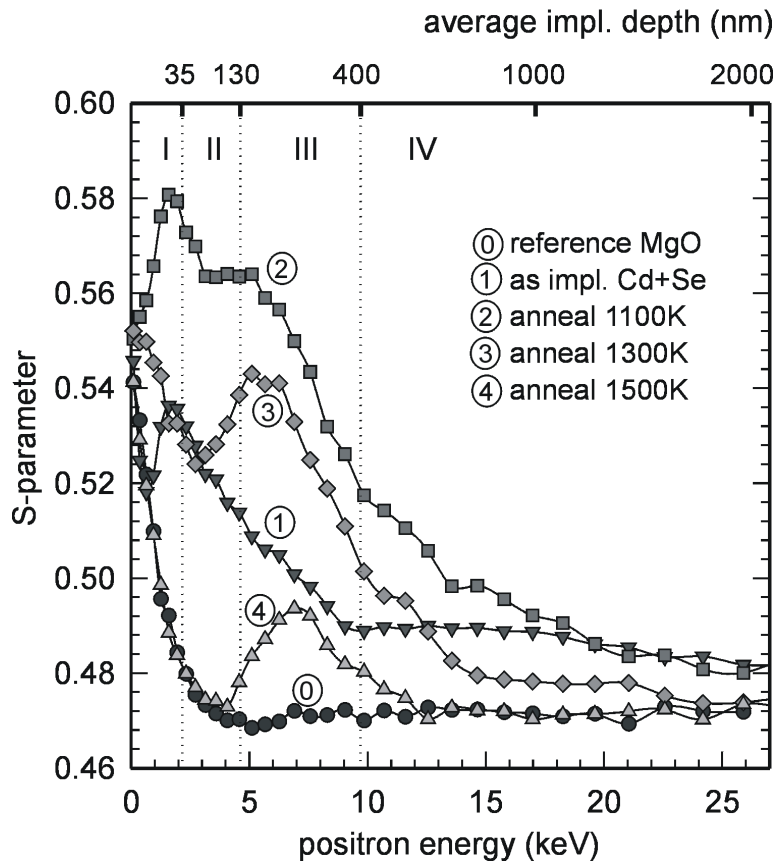


Fig. 5.3. S parameter as a function of positron implantation energy for the MgO sample as-implanted with Cd and Se and after annealing at various temperatures. The average positron implantation depth is indicated at the top of the figure.

During the subsequent annealing steps, the S parameter increases further because of the growth of vacancy clusters until a maximum in the S parameter is reached after annealing at 1100 K. At higher temperatures, the S parameter decreases in layers I-III because of shrinkage and dissociation of vacancy clusters. Considering the S parameter curve after annealing at 1300 K, it is clear that the S parameter in layer II (ion implantation range) has become lower than in layers I and III (containing mostly implantation damage). Of course, layer II also contains implantation damage, but in this layer the vacancy-type defects recombine with the implanted Cd and Se ions so that there are fewer open-volume defects to trap the positrons. This results in a low S parameter in layer II (in comparison to the adjacent layers) after annealing at 1300 K. After annealing at 1500 K, the S parameter in layers I-III reduces even further.

XTEM

TEM analysis was performed on a cross-section of a sample after the 1300 K annealing step. CdSe nanoclusters with size-dependent structural properties were found with sizes ranging from a few to 20 nm. There are three different crystal structures of CdSe: halite (cubic, rock-salt), sphalerite (cubic, zinc-blende) and wurtzite (hexagonal) [Alivisatos 1996b, Jacobs et al. 2002]. The lattice parameters of the three crystal structures are given in Table 5.1.

Table 5.1. Crystal structures and lattice parameters of MgO and CdSe.

Material	structure	type		lattice parameters (Å)	$V_{\text{mol.}}$ (Å ³)	Reference
MgO	rock-salt	halite	cubic	a : 4.213	18.7	[JCPDS]
CdSe	rock-salt ^a	halite	cubic	a : 5.61 ^a	44.1	[Jacobs et al. 2002]
	zinc blende	sphalerite	cubic	a : 6.077	55.4	[JCPDS]
	zincite	wurtzite	hex.	a : 4.298 c : 7.002	56.1	[JCPDS]

^a for CdSe nanoclusters at a pressure of 9 PGa.

The lattice parameter for rock-salt CdSe is deduced from the work of Jacobs et al. (2002). Although the value of the lattice parameter is not mentioned explicitly in this work, it can be deduced from the X-ray diffraction data. The (200) peak of rock-salt CdSe has a centroid at $Q = 2\pi/d_{200} = 2.24 \text{ \AA}^{-1}$ so that $a_{\text{CdSe}} = 5.61 \text{ \AA}$. This value does not refer to bulk CdSe, but to CdSe nanoclusters with a size of $11 \pm 1 \text{ nm}$ and at a pressure of 9 GPa.

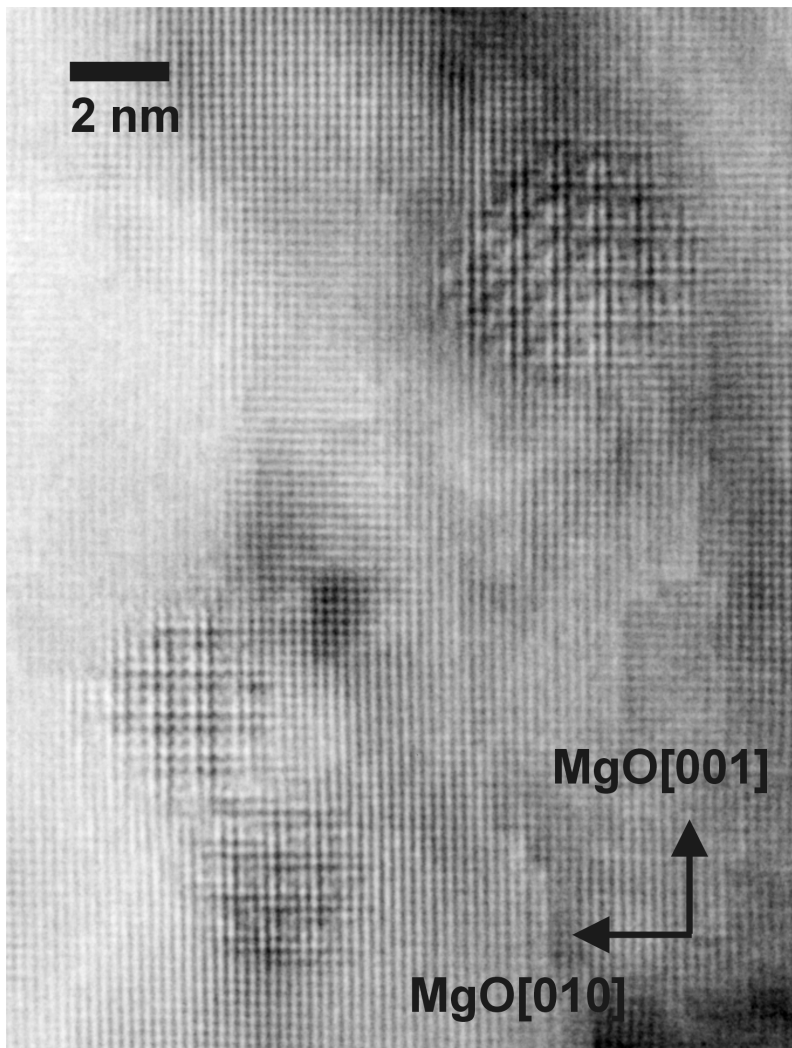


Fig. 5.4. High-resolution TEM image of small (< 5 nm) CdSe nanoclusters with a rock-salt crystal structure, showing translational moiré fringes in both the MgO[001] and MgO[010] directions.

In the high-resolution image of Fig. 5.4, three small CdSe nanoclusters can be observed. Translational moiré fringes were observed to run in both the MgO[010] and the MgO[001] directions for all nanoclusters with a size less than 5 nm. This shows that the CdSe crystal structure is cubic. The lattice parameter can be deduced from the spacing of the moiré fringes, using the following relationship:

$$\frac{1}{d_{fringes}} = \left| \frac{1}{d_{MgO}} - \frac{1}{d_{CdSe}} \right|. \quad (5.1)$$

MgO has a lattice parameter of 4.213 Å so that $d_{MgO(002)}=2.107$ Å. From Fig. 5.4, it is clear that there are exactly four MgO fringes per moiré fringe. This means for CdSe that $d_{CdSe}=4/3 \cdot d_{MgO(002)}=2.81$ Å. Table 5.1 gives a lattice parameter of rock-salt CdSe of 5.61 Å so that $d_{CdSe(002)}=2.81$ Å, which coincides with the value calculated from the moiré fringes. From the observations above it is also clear that the clusters are in a cube-on-cube orientation relationship with the MgO host. Rock-salt CdSe is more ionic than sphalerite or wurtzite CdSe so that it fits better into the ionic MgO lattice. Moreover, the smallest nanoclusters experience the largest pressure, and rock-salt CdSe is more densely packed than the other structures. The molecular volume of rock-salt CdSe is at least 20% smaller than the molecular volume of the sphalerite or wurtzite phase (see Table 5.1). This explains why the smallest clusters prefer to have the rock-salt structure despite the very large lattice mismatch with MgO of 33% (calculated as $(d_{CdSe} - d_{MgO})/d_{MgO}$).

Fig. 5.5 shows three CdSe nanoclusters with sizes of 5-10 nm. Here moiré fringes and high-resolution interference patterns are observed. In the TEM image of Fig. 5.6, a number of small rock-salt CdSe nanoclusters can be observed, together with a very large CdSe nanocluster with clear lattice fringes. The large clusters with size larger than 5 nm have the sphalerite or the wurtzite crystal structure. In the case of sphalerite, the orientation relationship is

$$(111)_s // (002)_{MgO}, [11\bar{2}]_s // [100]_{MgO}; \quad (5.2)$$

in the case of wurtzite

$$(0002)_w // (002)_{MgO}, [11\bar{2}0]_w // [100]_{MgO}. \quad (5.3)$$

Dr. B.J. Kooi at the University of Groningen performed TEM simulations, creating high-resolution images of various projections of the wurtzite and sphalerite CdSe structures.

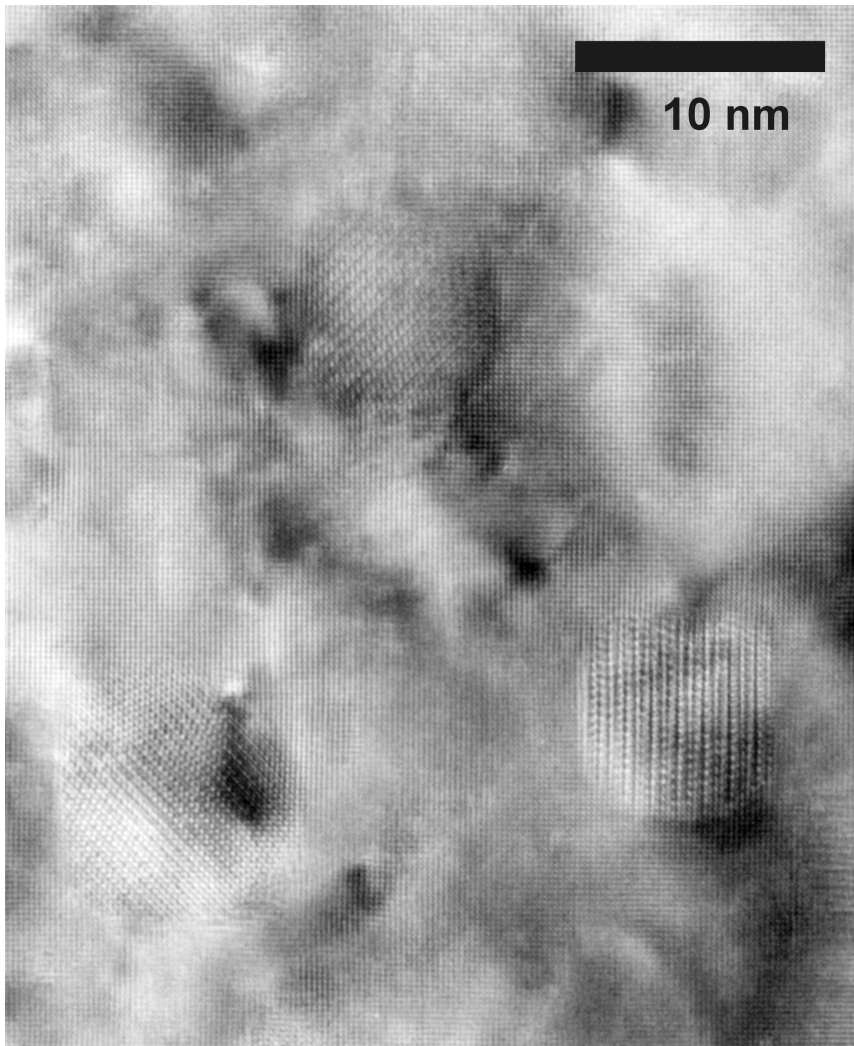


Fig. 5.5. High-resolution TEM image of three CdSe nanoclusters in the size range of 5-10 nm. The clusters probably have the sphalerite phase.

For the large CdSe nanocluster shown in Fig. 5.6, the projection is such that no distinction can be made between the sphalerite and wurtzite phases. More experimental TEM recordings were made of large CdSe nanoclusters with different orientations. These preliminary results (not known) match well with the simulated images of the cubic sphalerite phase.

5.4. Conclusions

CdSe nanoclusters were successfully created in MgO by means of ion beam synthesis with post-implantation thermal annealing at 1300 K. The CdSe nanoclusters have a broad size distribution of 2-20 nm. The clusters smaller than 5 nm have the rock-salt crystal structure and are in a cube-on-cube orientation relationship with the MgO host matrix. Nanoclusters larger than 10 nm have a different crystal structure. The experimental observations have been compared with the results of high-resolution imaging simulations. It follows that the large nanoclusters most likely have the cubic sphalerite crystal structure.

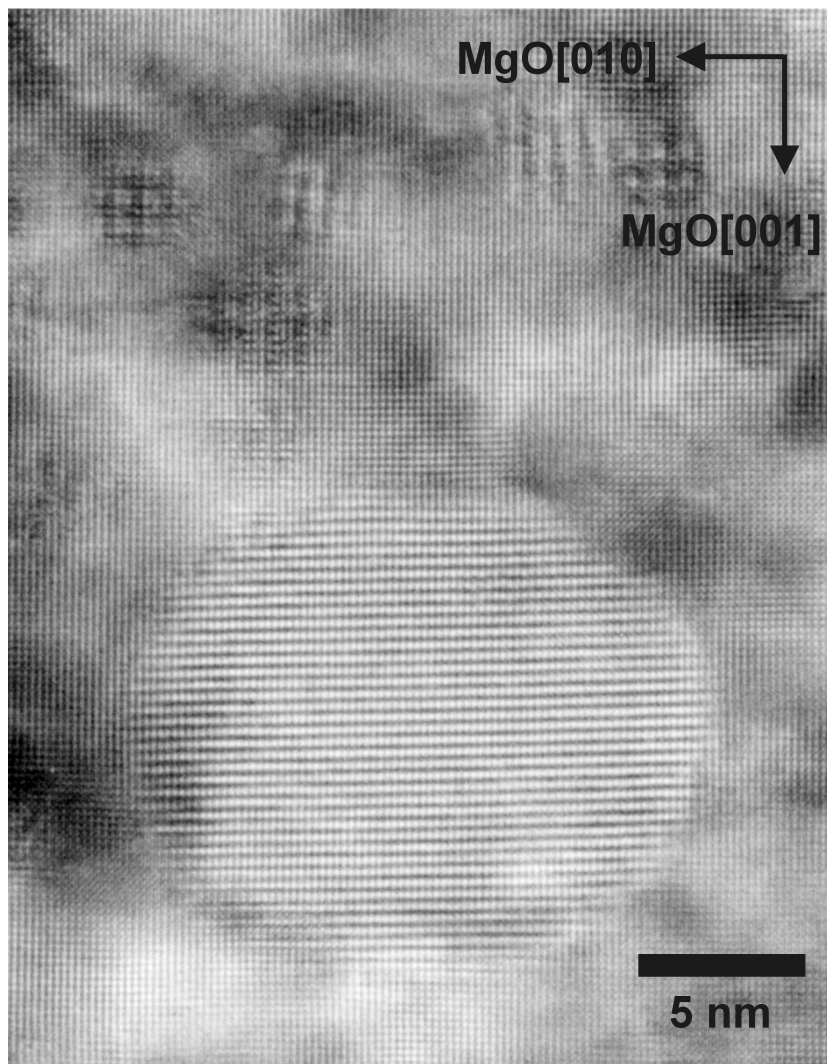


Fig. 5.6. TEM image with a number of small rock-salt CdSe nanoclusters at the top and a very large CdSe nanocluster at the bottom of the figure. The strong fringes in the large nanocluster are not moiré fringes but CdSe lattice fringes.

No optical absorption peaks could be found that could be attributed to CdSe, probably due to the broad size distribution and a number of nanoclusters which is too small to cause significant absorption.

Chapter 6

Outlook: patterned ion implantation using e-beam lithography

In order to systematically study the material properties as a function of cluster size, it is necessary that all the clusters have the same size. From the last three chapters, it is clear that in general this is not the case for clusters created by means of ion implantation and subsequent thermal annealing. Using other annealing treatments such as radiation-induced annealing by bombardment with MeV Si ions, the size distribution can become narrower [Ila et al. 1999, Ila et al. 2000], but the distribution is still quite wide if compared to what has been achieved in physical chemistry [Kamat et al. 1997]. Three European scientific institutes, the Interfaculty Reactor Institute of the Delft University of Technology (The Netherlands), the Institut für Festkörperphysik of the Forschungszentrum Karlsruhe (Germany) and the Physikalischen-Technischen Bundesanstalt in Braunschweig (Germany) have started an ambitious project to create monodispersed metal nanoclusters by combining ion implantation with e-beam lithography techniques. In the following sections, the experimental procedure will be explained and preliminary experimental results will be presented. Although the research program is still at an early stage, the first results are very promising and suggest that ion implantation of Au ions in a small three-dimensional volume can lead to the formation of a single gold cluster. By creating two-dimensional arrays of mutually separated, small three-dimensional implanted volumes, a periodic array of monodispersed Au atoms can be constructed. Another interesting topic is the creation by ion implantation of very thin, embedded gold wires, which can have non-trivial electric properties if the distance between the nanoclusters in the wire is small enough to allow tunnelling of electrons through the MgO between the nanoclusters.

6.1. Combining e-beam lithography and ion implantation

The goal is to create Au nanoclusters with control over their position and size. Ideally, a small implanted area should converge, upon annealing, to one single nanocluster. By choosing the number of implanted ions in this small volume, the number of Au atoms in the nanocluster – and thus the size of the nanocluster – can be determined. Another challenge is the creation of a subsurface Au wire. Thus, certain areas (zero-dimensional, or one-dimensional) should be implanted, while other areas should not be implanted. This is achieved by covering the surface of the target material with a mask prepared using an electron beam pattern generator (EBPG). A resist is spin coated onto the MgO surface, written with a focused electron beam and then developed by chemical etching. The areas that have been exposed to the electron beam will be removed so that the ions can be implanted in the substrate, while in the unexposed areas the ions will be stopped in the mask material. After ion irradiation, the mask is removed and further processing (such as thermal annealing) can be performed. This implies, of course, that the mask is able to stop the implanted ions: the range of the Au ions in the mask material should be smaller than the thickness of the mask. The first trials were performed with a single layer consisting of common PMMA resist. Although SRIM calculations predicted that the Au ions would be completely stopped inside the mask, in reality the mask was burnt and blistered after ion implantation and was not able to stop the 240 keV Au ions. In order to add more stopping power, a three-layer mask including a Ge layer was eventually developed, which proved to be adequate. Fig. 6.1 schematically shows the experimental procedure, which will now be discussed step by step.

0. First, a three-layer PMMA/Ge/PMMA mask was constructed on top of the MgO substrate. A 300-nm-thick PMMA layer was spin coated onto the sample. Next, a 100-nm-thick Ge layer was deposited on the PMMA layer and finally a second PMMA layer with a thickness of 100 nm was spin coated on top of the Ge. The top PMMA layer is the resist that is used to write the e-beam mask, the Ge layer serves as the principal stopping material for the Au ions and the task of the bottom PMMA layer is to enable removal of the mask after ion irradiation (in particular the Ge layer).
1. E-beam writing. Various patterns were designed which served as input to the electron beam pattern generator (type Leica, EBPG-4 HR, 50 keV). Included in all designs were two-dimensional rectangular arrays of circular dots with a pitch (interdot distance) of 250 nm and with dot sizes ranging from 50 to 100 nm.
2. Development. The PMMA resist exposed by the electron beam was removed by chemical etching.
3. Projection of the top PMMA mask onto the Ge layer by chemical dry etching using O₂.
4. Projection of the mask onto the bottom PMMA layer by chemical etching using CF₄. The construction of the mask is now completed.

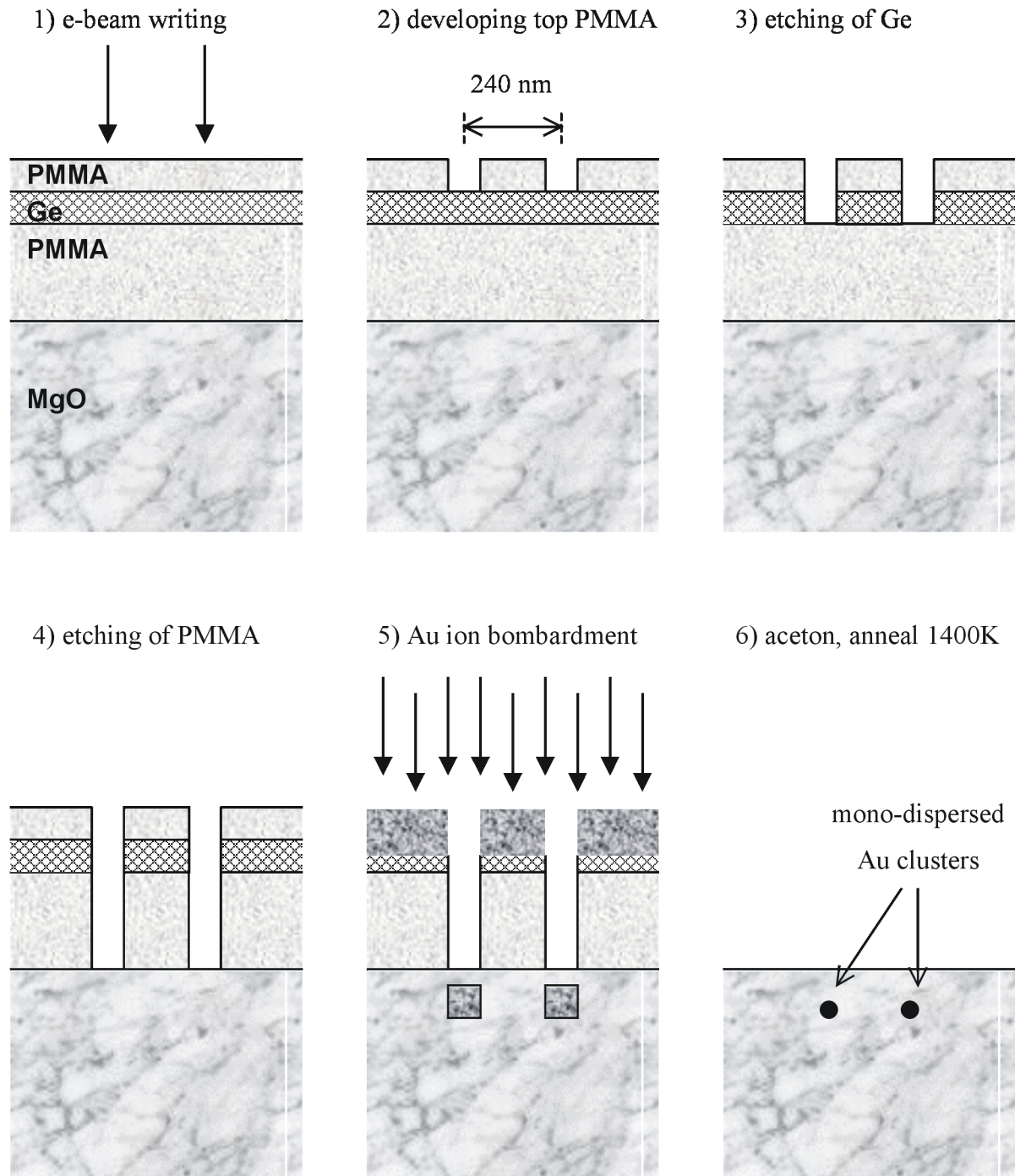


Fig. 6.1. Schematic drawing showing the experimental procedure of creating monodispersed Au clusters in MgO in a controlled geometry.

5. Au ion bombardment to a dose of 4×10^{15} Au ions cm^{-2} at an energy of 240 keV. The total dose was kept low in order not to destroy the mask as a result of stresses, blistering effects etc.
6. Removal of the mask. The three-layer mask was removed by dissolution in acetone with some additional soft mechanical polishing. Surprisingly, the mask could be entirely removed in the patterned (e-beam written) areas, but not in the areas that had been completely covered with the three-layer mask. In the large areas outside the patterned areas, serious blistering had occurred and this had probably destroyed the layered structure of the mask to some extent. In the patterned areas though, blistering did not occur, which is probably because stresses in the Ge layer can be released more easily when holes (or lines) are present.
7. Thermal annealing in ambient air at a temperature of 1400 K for a period of 3 hrs. in order to induce clustering of the implanted Au ions within the confined implanted areas.

The development of the mask has been a trial-and-error process with most of the attention focussed on the stopping of Au ions and the possibility of removing the mask after Au ion implantation.

6.2. Preliminary results

The surface of the sample was investigated by means of scanning electron microscopy (SEM) at a few stages of the experimental procedure. The results are shown in Fig. 6.2. The three-layer mask (prior to ion implantation) looks neatly and orderly in the SEM and is displayed in Fig. 6.2(a). After ion irradiation and removal of the mask, but prior to thermal annealing, the surface of the MgO sample was also investigated in the SEM. The implanted areas could be observed when working in the BSE mode (15 keV backscattered electrons). The result is displayed in Fig. 6.2(b). A weak contrast is visible in the areas where previously the dots had been and the effect of the mask displayed in Fig. 6.2(a) is clearly visible. After thermal annealing at 1400 K for 3 hrs, and again using the SEM in the BSE mode, the result shown in Fig. 6.2(c) is obtained. Clearly, the Au atoms in the implanted areas have agglomerated and precipitated into clusters. The image is blurred, which is not surprising considering that the nanoclusters are present at a depth of ~ 50 nm. It seems that a number of areas have one large Au nanocluster. In every dot with a diameter of 100 nm, a dose of 4×10^{15} Au ions cm^{-2} was implanted, i.e., a total of 3.1×10^5 Au ions was implanted per dot. If all these atoms converge into one nanocluster, this nanocluster would have a diameter of 22 nm.

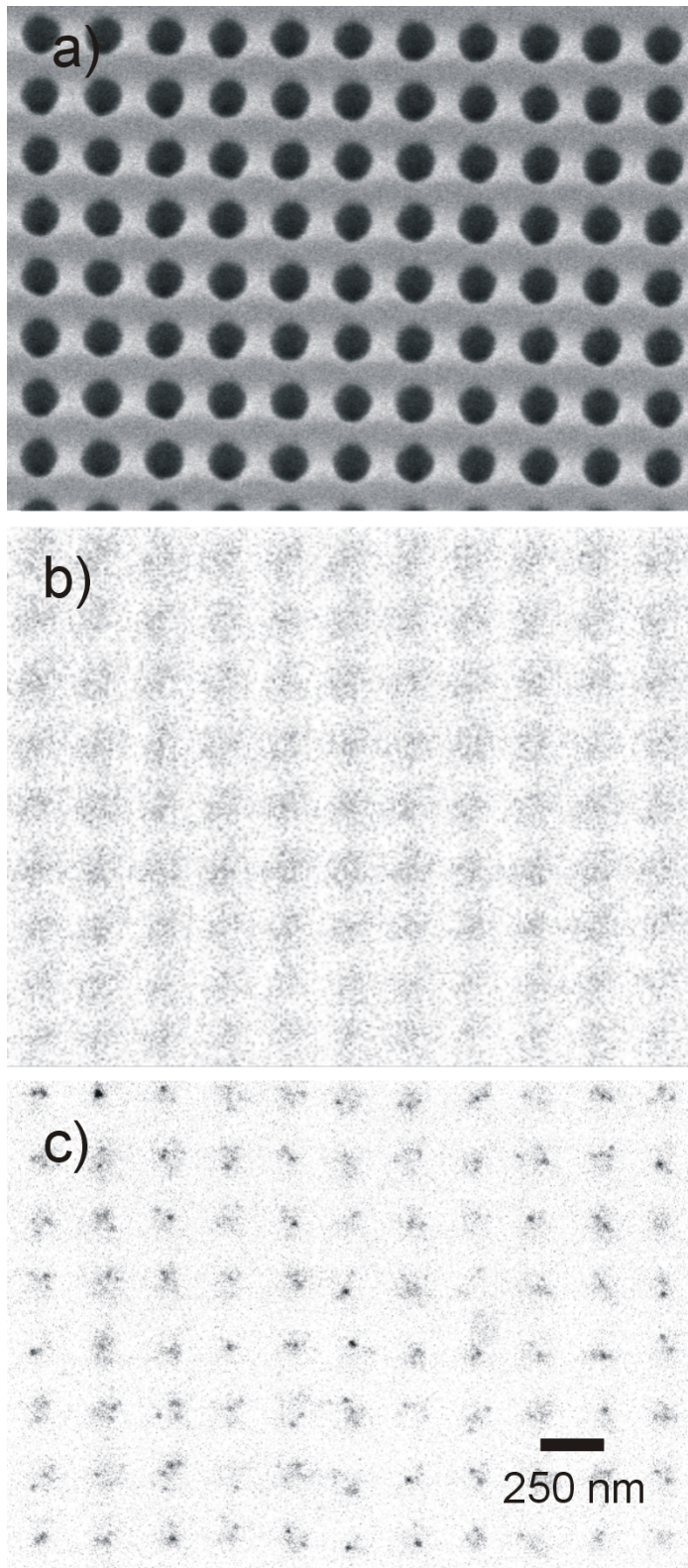


Fig. 6.2. Preliminary SEM results showing the sample at three stages of the experimental procedure: (a) after creation of the mask, (b) after ion irradiation and removal of the mask, and (c) after thermal annealing in air at a temperature of 1400 K during 3 hrs.

6.3. Outlook

Although the final goal of creating a single nanocluster per implanted area has not yet been achieved, the result displayed in Fig. 6.2(c) is very encouraging and shows the potential of this method. As mentioned in Section 1.1, embedded nanoclusters can also be used as memory devices by the charging and discharging of individual nanoclusters. The rectangular array shown in Fig. 6.2 allows straightforward addressing of the memory units. Of course, much more experimental work (TEM and electrical measurements) should be performed in order to fully assess the structural and electronic properties of these ordered nanocluster systems. Also, the quality of the optical properties should increase considerably when monodispersed, embedded Au or Ag nanoclusters are fabricated.

References

- [Allen et al. 1989] C.W. Allen, L.L. Funk, E.A. Ryan and A. Taylor, Nucl. Instrum. Meth. Phys. Res. B **40/41** (1989) 553.
- [Allen et al. 1992] W.R. Allen and S.J. Zinkle, J. Nucl. Mater. **191-194** (1992), 625.
- [Alivisatos 1996a] A.P. Alivisatos, Science **271** (1996) 933.
- [Alivisatos 1996b] A.P. Alivisatos, J. Phys. Chem. **100** (1996) 13226.
- [Andersen et al. 1987] O.K. Andersen, O. Jepsen and M. Šob, in *Electronic Band Structure and its Applications*, edited by M. Yussouff (Springer, Berlin, 1987), p. 1.
- [Asoka-Kumar et al. 1994] P. Asoka-Kumar, K.G. Lynn and D.O. Welch, J. Appl. Phys. **76** (1994) 4935.
- [Backhaus-Ricoult 2001] M. Backhaus-Ricoult, Acta Mater. **49** (2001) 1747.
- [Barbiellini et al. 1995] B. Barbiellini, M.J. Puska, T. Torsti and R.M. Nieminen, Phys. Rev. B **51**, 7341 (1995); B. Barbiellini, M.J. Puska, T. Korhonen, A. Harju, T. Torsti and R.M. Nieminen, *ibid.* **53**, 16201 (1996).
- [Birtcher et al. 1999] R.C. Birtcher, S.E. Donnelly, M. Song, K. Furuya, K. Mitsuishi and C.W. Allen, Phys. Rev. Lett. **83** (1999) 1617.
- [Boer et al. 2001] E.A. Boer, M.L. Brongersma, H.A. Atwater, R.C. Flagan and L.D. Bell, Appl. Phys. Lett. **79**, No. 6 (2001) 791.
- [Boev et al. 1987] O.V. Boev, M.J. Puska and R.M. Nieminen, Phys. Rev. B **36** (1987) 7786.
- [Bonafos et al. 2001] C. Bonafos, B. Colombeau, A. Altibelli, M. Carrada, G. Ben Assayag, B. Garrido, M. López, A. Pérez-Rodríguez, J.R. Morante and A. Claverie, Nucl. Instrum. Meth. Phys. Res. B **178** (2001) 17.
- [Boroński et al. 1986] E. Boroński and R.M. Nieminen, Phys. Rev. B **34**, 3820 (1986).
- [Boyd 2003a] R.W. Boyd, *Nonlinear Optics*, (Elsevier, San Diego, 2003).
- [Boyd 2003b] R.W. Boyd, *Nonlinear Optics*, (Elsevier, San Diego, 2003), Table 4.1.2. on pp. 194-195.
- [Britton et al. 1987] D.T. Britton, P.C. Rice-Evans and J.H. Evans, Phil. Mag. A **55** (1987) 347.

- [Busker et al. 2000] G. Busker, M.A. Van Huis, R.W. Grimes and A. van Veen, Nucl. Instrum. Meth. Phys. Res. B **171**, No. 4, (2000) 528.
- [Ceperley et al. 1980] D.M. Ceperley and B.J. Alder, Phys. Rev. Lett. **45** (1980) 566.
- [Chakraborty 1998] P. Chakraborty, J. Mater. Sci. **33** (1998) 2235.
- [Chen et al. 1998] J. Chen, R. Mu, A. Ueda, M.H. Wu, Y.-S. Tung, Z. Gu, D.O. Henderson, C.W. White, J.D. Budai and R.A. Zuhr, J. Vac. Sci. Technol. A **16**, No. 3 (1998) 1409.
- [Christensen et al. 2001] N.E. Christensen and D.L. Novikov, Phys. Rev. Lett. **86** (2001) 1861.
- [Claverie et al. 2002] A. Claverie, B. Colombeau, F. Cristiano, A. Altibelli and C. Bonafos, Nucl. Instrum. Meth. Phys. Res. B **186** (2002) 281.
- [Clement et al. 1996] M. Clement, J.M.M. de Nijs, P. Balk, H. Schut and A. van Veen, J. Appl. Phys. **79** (1996) 9029.
- [Cocuaud et al. 1997] N. Cocuaud, E. Picard, R.J.M. Konings, A. Conti and H. Matzke, Proceedings Global 97 (1997) 1044.
- [Coleman 2000] *Positron Beams and their Applications*, edited by P. Coleman (World Scientific, Singapore, 2000).
- [Crawford, Jr. 1984] J.H. Crawford, Jr., Nucl. Instrum. Meth. Phys. Res. **B1** (1984) 159.
- [Damen et al. 2003] P.M.G. Damen, A. van Veen, F. Labohm, H. Schut and M.A. van Huis, J. Nucl. Mater. **319** (2003) 65.
- [Davidovic et al. 1999] D. Davidovic and M. Tinkham, Phys. Rev. Lett. **83** (1999) 1644.
- [Deutsch 1951] M. Deutsch, Phys. Rev. **83** (1951) 866.
- [Downing et al. 1993] R.G. Downing and G.P. Lamaze, Neutron News **4**, No. 1 (1993) 15.
- [Doyle 1958] W.T. Doyle, Phys. Rev. **111**, No.4 (1958) 1067.
- [Dupasquier et al. 1995] *Positron Spectroscopy of Solids*, edited by A. Dupasquier and A.P. Mills Jr. (IOS Press, Amsterdam, 1995).
- [Eijt et al. (pc)] S.W.H. Eijt and C.V. Falub (private communication).
- [Eijt et al. 2001] S.W.H. Eijt, C.V. Falub, A. van Veen, H. Schut, P.E. Mijnders, M.A. van Huis and A.V. Fedorov, Mater. Res. Soc. Symp. Proc. **647** (2001) O14.11.
- [Ekardt 1999] *Metal Clusters*, edited by W. Ekardt (John Wiley & Sons Ltd., New York, 1999).
- [Eleveld et al. 1999] H. Eleveld, A. van Veen, F. Labohm and M.W. de Moor, J. Nucl. Mater. **212-215** (1994) 971.
- [Ellis et al. 1991] D.E. Ellis, J. Guo and D.J. Lam, Reviews of Solid State Science **5** (1991) 287.
- [Evans et al. 1985] J.H. Evans and D.J. Mazey, J. Phys. F: Met. Phys. **15** (1985) L1; Scripta Metall. **19** (1985) 621.
- [Evans et al. 1986] J.H. Evans and D.J. Mazey, J. Nucl. Mater. **138** (1986) 176.
- [Falub et al. 2001] C.V. Falub, S.W.H. Eijt, A. van Veen, P.E. Mijnders and H. Schut, Mater. Sci. Forum **363-365** (2001) 561.
- [Falub et al. 2002] C.V. Falub, P.E. Mijnders, S.W.H. Eijt, M.A. van Huis, A. van Veen and H. Schut, Phys. Rev. B **66** (2002) 075426.
- [Farjam et al. 1987] M. Farjam and H.B. Shore, Phys. Rev. B **36** (1987) 5089.

- [Fedorov et al. 2000] A.V. Fedorov, M.A. van Huis, A. van Veen and H. Schut, Nucl. Instrum. Meth. Phys. Res. B **166-167** (2000) 215.
- [Fedorov et al. 2001a] A.V. Fedorov, A. van Veen and H. Schut, Mater. Sci. Forum **363-365** (2001) 646.
- [Fedorov et al. 2001b] A.V. Fedorov, A. van Veen, M.A. van Huis, H. Schut, B.J. Kooi, J.Th.M. De Hosson and R.L. Zimmerman, AIP Conf. Proc. **576** (2001) 971.
- [Feldman 1991] L.C. Feldman, in *Ion Spectroscopies for Surface Analysis*, edited by A.W. Czanderna and D.M. Hercules (Plenum, New York, 1991) Chapter 6, pp. 311-361.
- [Forster et al. 1989] M. Forster, J.N. Mundy and H.-E. Schaefer, in *Positron Annihilation*, edited by L. Dorikens-Vanpraet, M. Dorikens and D. Segers (World Scientific, Singapore, 1989), p. 833.
- [Fukumi et al. 1994] K. Fukumi, A. Chayahara, K. Kodano, T. Sakaguchi, Y. Horino, M. Miya, K. Jujii, J. Hayakawa and M. Satou, J. Appl. Phys. **75**, No. 6 (1994) 3075.
- [Gale et al. 1992] J.D. Gale, C.R.A. Catlow and W.C. Mackrodt, Modell. and Sim. in Mater. Sci. and Eng. **1** (1992) 73.
- [Godey et al. 2000] S. Godey, E. Ntsoenzok, T. Sauvage, A. van Veen, F. Labohm, M.F. Beaufort and J.F. Barbot, Mater. Sci. and Eng. B **73**, No.1-3 (2000) 54.
- [Goldstein et al. 1992] A.N. Goldstein, C.M. Echer and A.P. Alivisatos, Science **256** (1992) 1425.
- [Griffioen et al. 1987] C.C. Griffioen, J.H. Evans, P.C. de Jong and A. van Veen, Nucl. Instrum. Meth. Phys. Res. B **27** (1987) 417.
- [Grimes et al. 1990a] R.W. Grimes and C.R.A. Catlow, J. of the Am. Ceram. Soc. **73**, No. 11 (1990) 3251.
- [Grimes et al. 1990b] R.W. Grimes, R.H. Miller and C.R.A. Catlow, J. of Nucl. Mater. **172** (1990) 123.
- [Grimes 1994] R.W. Grimes, J. of the Am. Ceram. Soc. **77**, No.2 (1994) 378.
- [Hakvoort et al. 1995] R.A. Hakvoort, A. van Veen, P.E. Mijnders and H. Schut, Appl. Surf. Sci. **85** (1995) 271.
- [Halperin 1986] W.P. Halperin, Rev. Mod. Phys. **58** (1986) 533.
- [Handbook 1986] Handbook of Chemistry and Physics, 66th ed. (CRC Press, USA, 1986).
- [Harding 1990] J.H. Harding, Rep. Prog. Phys. **53** (1990) 1403.
- [Hautojärvi et al. 1995] P. Hautojärvi and C. Corbel, in *Positron Spectroscopy of Solids*, edited by A. Dupasquier and A.P. Mills Jr. (IOS Press, Amsterdam, 1995), p. 491.
- [Hobbs et al. 1994] L.W. Hobbs, F.W. Clinard, Jr., S.J. Zinkle and R.C. Ewing, J. Nucl. Mater. **216** (1994) 291.
- [Hulse et al. 1980] J. Hulse, J. Kupperts, K. Wandelt and G. Ertl, Appl. Surf. Sci. **6** (1980) 453.
- [Ila et al. 1999] D. Ila, E.K. Williams, C.C. Smith, D.B. Poker, D.K. Hensley, C. Klatt and S. Kalbitzer, Nucl. Instrum. Meth. Phys. Res. B **148** (1999) 1012.

- [Ila et al. 2000] D. Ila, E.K. Williams, R.L. Zimmerman, D.B. Poker and D.K. Hensley, Nucl. Instrum. Meth. Phys. Res. B **166-167** (2000) 845.
- [Jacobi 1987] K. Jacobi, Surf. Sci. **192** (1987) 449.
- [Jacobs et al. 1992] P.W.M. Jacobs and E.A. Kotomin, Phys. Rev. Lett. **69**, (1992) 1411.
- [Jacobs et al. 2002] K. Jacobs, J. Wickham and A.P. Alivisatos, J. Phys. Chem. B **106** Lett. (2002) 3759.
- [JCPDS] JCPDS file 04-0829 (for MgO), file 04-0831 (for Zn), file 19-0191 (for sphalerite CdSe) and file 08-0459 (for wurtzite CdSe), International Centre for Diffraction Data.
- [Jensen et al. 1988] K.O. Jensen, M. Eldrup, N.J. Pedersen and J.H. Evans, J. Phys. F: Met. Phys. **18** (1988) 1703.
- [Jensen et al. 1990] K.O. Jensen, M. Eldrup, S. Linderoth and J.H. Evans, J. Phys.: Condens. Matter **2** (1990) 2081.
- [Kamat et al. 1997] *Semiconductor Nanoclusters*, edited by P.V. Kamat and D. Meisel (Elsevier, New York, 1997).
- [Kittel 1986] C. Kittel, *Introduction to Solid State Physics*, 6th ed. (John Wiley&Sons, New York, 1986) p. 134.
- [Kooi et. al. 2000] B.J. Kooi, A. van Veen, J.Th.M. De Hosson, H. Schut, A.V. Fedorov and F. Labohm, Appl. Phys. Lett. **76**, No. 9 (2000) 1110.
- [Kotomin et al. 1997] E.A. Kotomin, P.W.M. Jacobs, N.E. Christensen, T. Brudevoll, M.M. Kuklja and A.I. Popov, Defect and Diffusion Forum **143-147** (1997) 1231.
- [Kotomin et al. 1998] E.A. Kotomin and A.I. Popov, Nucl. Instrum. and Meth. in Phys. Res. B **141** (1998) 1.
- [Kreibig et al. 1995] U. Kreibig and M. Vollmer, *Optical Properties of Metal Clusters*, Springer Series in Materials Science; Vol. 25 (Springer, Berlin, 1995).
- [Kreibig et al. 1996] U. Kreibig, A. Hilger, H. Hövel and M. Quinten, in *Large Clusters of Atoms and Molecules*, edited by T.P. Martin (Kluwer, The Netherlands, 1996) pp. 475-493.
- [Krings et al. 1999] L.H.M. Krings, Y. Tamminga, J. van Berkum, F. Labohm, A. van Veen and W.M. Arnoldbik, J. Vac. Sci. Technol. A **17**, No. 1 (1999) 198.
- [Kuriplach et al. 1999] J. Kuriplach, M. Šob, G. Brauer, W. Anwand, E.-M. Nicht, P.G. Coleman and N. Wagner, Phys. Rev. B **59**, 1948 (1999).
- [Kuriplach et al. 2002] J. Kuriplach, W. Anwand, G. Brauer, and W. Skorupa, Appl. Surf. Sci. **194**, No. 1-4 (2002) 84.
- [Lang et al. 1982] N.D. Lang and A.R. Williams, Phys. Rev. B **25** (1982) 2940.
- [Langford et al. 1978] J.I. Langford and A.J.C. Wilson, J. Appl. Cryst. **11** (1978) 102.
- [Las et al. 1984] W.C. Las and T.G. Stoebe, Radiation Protection Dosimetry **8** (1984) 45.
- [Leslie 1982] M. Leslie, *Program CASCADE Documentation*, SERC Daresbury Laboratory Report DL/SCI/TM31T (1982).
- [Liu et al. 2002] Y.X. Liu, Y.C. Liu, D.Z. Shen, G.Z. Zhong, X.W. Fan, X.G. Kong, R. Mu and D. O. Henderson, Solid State Comm. **121** (2002) 531.

- [Lüth 1995] H. Lüth, *Surfaces and Interfaces of Solid Materials* (Springer, Berlin, 1995), 3rd ed., Sec. 3.1, p. 81.
- [Macrander 1980] A.T. Macrander, Phys. Rev. B **21** (1980) 2549.
- [Mahamuni et al. 1999] S. Mahamuni, K. Borgohain, B.S. Bendre, V.J. Leppert and S.H. Risbud, J. Appl. Phys. **85**, No. 5 (1999) 2861.
- [Marichy et al. 1979] G. Marichy, G. Chassagne and D. Durand, Phys. Stat. Sol. B **92**, 221 (1979).
- [Matzke 1982] H. Matzke, Radiation Effects **64** (1982) 3.
- [Mills, Jr., et al. 1986] A.P. Mills, Jr., and E.M. Gullikson, Appl. Phys. Lett. **49** (1986) 1121.
- [Munz et al. 1999] D. Munz and T. Fett, *Ceramics*, Springer Series in Materials Science Vol. **36** (Springer, Berlin, 1999).
- [Myers et al. 1994] S.M. Myers, D.M. Follstaedt and D.M. Bishop, in *Materials Synthesis and Processing Using Ion Beams*, edited by R.J. Culbertson, O.W. Holland, K.S. Jones and K. Maex, Mat. Res. Soc. Symp. Proc. **316** (1994) 33.
- [Nagai et al. 2000] Y. Nagai, M. Hasegawa, Z. Tang, A. Hempel, K. Yubuta, T. Shimamura, Y. Kawazoe, A. Kawai and F. Kano, Phys. Rev. B **61** (2000) 6574.
- [Nagai et al. 2001] Y. Nagai, T. Chiba, Z. Tang, T. Akahane, T. Kanai, M. Hasegawa, M. Takenaka and E. Kuramoto, Phys. Rev. Lett. **87** (2001) 176402.
- [Nagashima et al. 1996] A. Nagashima, N. Tejima, Y. Gamou, T. Kawai and C. Oshima, Surf. Sci. **357-358** (1996) 307.
- [Nagashima et al. 1998] Y. Nagashima, Y. Morinaka, T. Kurihara, Y. Nagai, T. Hyodo, T. Shidara and K. Nakahara, Phys. Rev. B **58** (1998) 12676.
- [Nakao et al. 2003] S. Nakao, S. Utsunomiya, K. Sun, L.M. Wang, Y. Miyagawa and S. Miyagawa, 17th Conf. on the Application of Accelerators in Research and Industry (CAARI 2002), to be published in AIP Conf. Proc. (2003).
- [Namba et al. 1984] H. Namba and Y. Murata, J. Phys. Soc. Japan **53** (1984) 1888.
- [Norton et al. 1992] M.G. Norton, C.B. Carter, E.L. Fleischer and J.W. Mayer, J. Mater. Res. **7** (1992) 3171.
- [Ore et al. 1949] A. Ore and J.L. Powell, Phys. Rev. **75** (1949) 1696.
- [Panda et al. 2000] B.K. Panda, G. Brauer, W. Skorupa and J. Kuriplach, Phys. Rev. B **61** (2000) 15848.
- [Pareja et al. 1985] R. Pareja, M.A. Pedrosa and R. Gonzalez, in *Positron Annihilation*, edited by P.C. Jain, R.M. Singru and K.P. Gopinathan, (World Scientific, Singapore, 1985) p. 708.
- [Pasche et al. 1989] S. Pasche and J.-P. Borel, Zeitschrift für Physik D **12** (1989) 401.
- [Pells 1982] G.P. Pells, Radiation Effects **64** (1982) 71.
- [Peng et al. 2000] X. Peng, L. Manna, W. Yang, J. Wickham, E. Scher, A. Kadavanich and A.P. Alivisatos, Nature **404** (2000) 59.
- [Perdew et al. 1981] J.P. Perdew and A. Zunger, Phys. Rev. B **23** (1981) 5048.
- [Puska et al. 1989a] M.J. Puska, P. Lanki and R.M. Nieminen, J. Phys.: Condens. Matter **1** (1989) 6081.

- [Puska et al. 1989b] M.J. Puska, S. Mäkinen, M. Manninen and R.M. Nieminen, *Phys. Rev. B* **39** (1989) 7666.
- [Puska et al. 1992] M.J. Puska and R.M. Nieminen, *Phys. Rev. B* **46** (1992) 1278.
- [Puska et al. 1994] M.J. Puska and R.M. Nieminen, *Rev. Mod. Phys.* **66** (1994) 841.
- [Qian et al. 1997] Y. Qian, D. Ila, R.L. Zimmerman, D.B. Poker, L.A. Boatner and D.K. Hensley, *Nucl. Instrum. Meth. Phys. Res. B* **127/128** (1997) 524.
- [Rajput et al. 1993] S.S. Rajput, R. Prasad, R.M. Singru, W. Trifhäufer, A. Eckert, G. Kögel, S. Kaprzyk and A. Bansil, *J. Phys.: Condens. Matter* **5** (1993) 6419.
- [Rechtin 1979] M.D. Rechtin, *Radiation Effects* **42** (1979) 129.
- [Rivera 2003] A. Rivera, *Hydrogen Interactions with Silicon-on-Insulator Materials*, PhD thesis (Delft University Press, The Netherlands, 2003); A. Rivera, A. van Veen, H. Schut, J.M.M. de Nijs and P. Balk, *Solid State Electronics* **46** (2002) 1775.
- [Roessler et al. 1991] D.M. Roessler and D.R. Huffman, in *Handbook of Optical Constants of Solids II*, edited by E.D. Palik (Academic Press, London, 1991), p. 919.
- [Ronchi 1981] C. Ronchi, *J. Nucl. Mater.* **96** (1981) 314.
- [Rubloff 1971] Rubloff, *Phys. Rev. B* **3** (1971) 285.
- [Sasajima et al. 1999] N. Sasajima, T. Matsui, S. Furuno, K. Hojou and H. Otsu, *Nucl. Instrum. Meth. Phys. Res. B* **148** (1999) 745.
- [Schut et al. 1999] H. Schut, A. van Veen, F. Labohm, A.V. Fedorov, E.A.C. Neeft and R.J.M. Konings, *Nucl. Instrum. Meth. Phys. Res. B* **147** (1999) 212.
- [Sferlazzo et al. 1987] P. Sferlazzo, S. Berko and K.F. Canter, *Phys. Rev. B* **35** (1987) 5315.
- [Skriver 1984] H.L. Skriver, *The LMTO Method* (Springer, Berlin, 1984).
- [Stepanov et al. 2002] A.L. Stepanov and D.E. Hole, *Recent Res. Devel. Appl. Phys.* **5** (2002) 1.
- [Studer et al. 1997] F. Studer, M. Hervieu, J.-M. Costantini and M. Toulemonde, *Nucl. Instrum. Meth. Phys. Res. B* **122** (1997) 449.
- [Tan et al. 1991] Z. Tan, J.I. Budnick, D.M. Pease and F. Namavar, *Phys. Rev. B* **43** (1991) 1987.
- [Tanaka et al. 2001] Y. Tanaka, Y. Sakurai, A.T. Stewart, N. Shiotani, P.E. Mijnders, S. Kaprzyk and A. Bansil, *Phys. Rev. B* **63** (2001) 045120.
- [Taylor et al. 1999] M.B. Taylor, C.E. Sims, G.D. Barrera, N.L. Allan and W.C. Mackrodt, *Phys. Rev. B* **59** (1999) 6742.
- [Thees et al. 2000] H.-J. Thees, M. Wittmaack, K.-H. Stegemann, J.v. Borany, K.-H. Heinig and T. Gebel, *Microelectronics Reliability* **40** (2000) 867.
- [Tiwari et al. 1996] S. Tiwari, F. Rhana, K. Chan, L. Shi and H. Hanafi, *Appl. Phys. Lett.* **69** (1996) 1232.
- [Treilleux et al. 1979] M. Treilleux and G. Chassagne, *J. Phys. (Paris)* **40**, L-283 (1979); M. Treilleux and G. Chassagne, *J. Phys. Coll. (Paris)* **41C**, No. 6 (1980) 391.
- [Ueda et al. 1997] A. Ueda, R. Mu, Y.S. Tung, D.O. Henderson, C.W. White, R.A. Zuhr, J.G. Zhu and P.W. Wang, *Materials Science Forum* **239-241** (1997) 675.
- [Ueda et al. 1998] A. Ueda, R. Mu, Y.-S. Tung, M. Wu, W.E. Collins, D.O. Henderson, C.W. White, R.A. Zuhr, J.D. Budai, A. Meldrum, P.W. Wang and Xi Li, *Nucl. Instrum. Methods Phys. Res. B* **141** (1998) 261.

- [Vaks et al. 1989] V.G. Vaks, M.I. Katsnelson, V.G. Koreshkov, A.I. Likhtenstein, O.E. Parfenov, V.F. Skok, V.A. Sukhoparov, A.V. Trefilov and A.A. Chernyshov, *J. Phys.: Condens. Matter* **1** (1989) 5319.
- [Van der Kolk et al. 1986] G.J. van der Kolk and A. van Veen, *Physica Scripta* **T13** (1986) 53.
- [Van Huis et al. 2001] M.A. van Huis, A.V. Fedorov, A. van Veen, F. Labohm, H. Schut, P.E. Mijnaerends, B.J. Kooi and J.Th.M. De Hosson, *Mater. Sci. Forum* **363-365** (2001) 448.
- [Van Huis et al. 2002] M.A. van Huis, A. van Veen, H. Schut, C.V. Falub, S.W.H. Eijt, P.E. Mijnaerends and J. Kuriplach, *Phys. Rev. B* **65** (2002) 085416.
- [Van Huis et al. 2003] M.A. van Huis, A. van Veen, H. Schut, S.W.H. Eijt, B.J. Kooi and J.Th.M. De Hosson, *Rev. Adv. Mater. Sci.* **4**, No. 1 (2003) 60.
- [Van Veen et al. 1990] A. van Veen, H. Schut, J. de Vries, R.A. Hakvoort and M.R. Ijpma, in *Positron Beams for Solids and Surfaces*, AIP Conf. Proc. **218**, edited by P.J. Schultz, G.R. Massoumi, and P.J. Simpson (AIP, New York, 1990), p. 171.
- [Van Veen 1991] A. van Veen, in *Fundamental Aspects of Inert Gases in Solids*, edited by S.E. Donnelly and J.H. Evans, NATO ASI Series B: Physics Vol. **278**, (Plenum Press, New York, 1991) 41.
- [Van Veen et al. 1995] A. van Veen, H. Schut, M. Clement, J.M.M. de Nijs, A. Kruseman and M.R. Ijpma, *Appl. Surf. Sci.* **85** (1995) 216.
- [Van Veen et al. 1999a] A. van Veen, H. Schut, A.V. Fedorov, F. Labohm, E.A.C. Neeft and R.J.M. Konings, *Nucl. Instrum. and Meth. in Phys. Res. B* **148** (1999) 768.
- [Van Veen et al. 1999b] A. van Veen, H. Schut, F. Labohm and J. de Roode, *Nucl. Instrum. Meth. Phys. Res. A* **427** (1999) 266.
- [Van Veen et al. 2000] A. van Veen, H. Schut and P.E. Mijnaerends, in *Positron Beams and their Applications*, edited by P. Coleman (World Scientific, Singapore, 2000), Chap. 6, p. 191.
- [Van Veen et al. 2001] A. van Veen, M.A. van Huis, A.V. Fedorov, H. Schut, C.V. Falub, S.W.H. Eijt, F. Labohm, B.J. Kooi and J.Th.M. De Hosson, *Mat. Res. Soc. Symp. Proc.* **647** (2001) O11.24.
- [Van Veen et al. 2002] A. van Veen, M.A. van Huis, A.V. Fedorov, H. Schut, F. Labohm, B.J. Kooi and J.Th.M. De Hosson, *Nucl. Instrum. Meth. Phys. Res. B* **191** (2002) 610.
- [Vergara et al. 1998] I. Vergara, R. González, R. Ramírez, J.E. Muñoz Santiuste and Y. Chen, *Phys. Rev. B* **58** (1998) 5236.
- [Von Barth et al. 1972] U. Von Barth and L. Hedin, *J. Phys. C* **5** (1972) 1629.
- [Vom Felde et al. 1988] A. Vom Felde, J. Fink and W. Ekardt, *Phys. Rev. Lett.* **61** (1988) 2249.
- [Watson et al. 1996] G.W. Watson, E.T. Kelsey, N.H. de Leeuw, D.J. Harris and S.C. Parker, *J. Chem. Soc. Faraday Trans.* **92** (1996) 433.
- [Weiss et al. 2000] A.H. Weiss and P.G. Coleman, in *Positron Beams and their Applications*, edited by P. Coleman (World Scientific, Singapore, 2000), p. 129.

- [Wengeler et al. 1981] H. Wengeler and F. Freund, *Ceram. Forum Int. - Ber. Dt. Kerm. Ges.* **58** (1981) 31.
- [West 1995] R.N. West, in *Positron Spectroscopy of Solids*, edited by A. Dupasquier and A.P. Mills, Jr. (IOS Press, Amsterdam, 1995), p. 75.
- [White et al. 1989] C.W. White, C.J. McHargue, P.S. Sklad, L.A. Boatner and G.C. Farlow, *Mater. Sci. Reports* **4** (1989) 41.
- [White et al. 1998] C.W. White, J.D. Budai, S.P. Withrow, J.G. Zhu, E. Sonder, R.A. Zuhr, A. Meldrum, D.M. Hembree, Jr., D.O. Henderson and S. Praver, *Nucl. Instrum. and Meth. in Phys. Res. B* **141** (1998) 228.
- [White et al. 1999a] C.W. White, A. Meldrum, J.D. Budai, S.P. Withrow, E. Sonder, R.A. Zuhr, D.M. Hembree Jr., M. Wu and D.O. Henderson, *Nucl. Instrum. Meth. Phys. Res. B* **148** (1999) 991.
- [White et al. 1999b] C.W. White, A. Meldrum, E. Sonder, J.D. Budai, R.A. Zuhr, S.P. Withrow and D.O. Henderson, in *Microstructural Processes in Irradiated Materials*, edited by S.J. Zinkle, G.E. Lucas, R.C. Ewing, J.S. Williams, *Mat. Res. Soc. Symp. Proc.* **540** (1999) 219.
- [Whited et al. 1973] R.C. Whited, C.J. Flaten and W.C. Walker, *Solid State Commun.* **13** (1973) 1903.
- [Wong et al. 1999] E.M. Wong and P.C. Searson, *Appl. Phys. Lett.* **74**, No. 20 (1999) 2939.
- [Zhang et al. 1999a] M. Zhang, C. Lin, X. Duo, Z. Lin and Z. Zhou, *J. Appl. Phys.* **85**, No. 1 (1999) 94.
- [Zhang et al. 1999b] W. Zhang, H. Wang, K.S. Wong, Z.K. Tang, G.K.L. Wong and R. Jain, *Appl. Phys. Lett.* **75**, No. 21 (1999) 3321.
- [Ziegler et al. 1985] J.F. Ziegler, J.P. Biersack and U. Littmark, *The Stopping and Range of Ions in Solids (TRIM)* (Pergamon, New York, 1985). See also www.srim.org for information on updated versions.
- [Zimmerman et al. 1999] R.L. Zimmerman, D. Ila, E.K. Williams, D.B. Poker, D.K. Hensley, C. Klatt and S. Kalbitzer, *Nucl. Instrum. Meth. Phys. Res. B* **148** (1999) 1064, and references therein.
- [Zinkle et al. 1997] S.J. Zinkle and C. Kinoshita, *J. Nucl. Mater.* **251** (1997) 200.
- [Zu et al. 1997] P. Zu, Z.K. Tang, G.K.L. Wong, M. Kawasaki, A. Ohtomo, H. Koinuma and Y. Segawa, *Solid State Comm.* **103**, No. 8 (1997) 459.

Summary

Bulk materials have properties very different from those of individual atoms. As more atoms are joined together to form a cluster, the material properties change until the number of atoms is so large (typically $> 10^5$) that the properties of the cluster are the same as the bulk properties of that material. The range over which the material properties change continuously is an interesting area of research. Size-dependent material properties include solid-solid structural phase transformations, metal-insulator transitions, linear and non-linear optical properties, changing melting temperatures and widening of the band gap of semiconductors. When clusters are implemented in nanotechnological devices, the material properties can be changed by tailoring the size of the clusters. A convenient way of creating clusters is by ion implantation followed by a thermal treatment to induce clustering of the implanted atoms. Nanoclusters are more stable when they are embedded in solid matrices and ion implantation is a straightforward way to achieve this. Very often, ceramic oxides (SiO_2 , MgO , Al_2O_3 , TiO_2) are used as embedding materials because of their stability (high melting temperatures) and because they are optically transparent so that the optical properties of the system can be easily investigated. In this work, the focus is both on the creation of the nanoclusters by ion implantation followed by thermal annealing, and on the study of the functional properties of these nanoclusters.

All nanocluster systems presented in this work were created by means of ion implantation and subsequent thermal annealing. The ion implantation energies varied from 30 keV for light elements to 1.0 MeV for heavy elements. The energies were adjusted to implant the ions within a depth of a few hundred nanometer so that positron beam techniques could be employed. The implanted dose was typically 10^{16} ions cm^{-2} . Clusters in the nanometer size range are formed after thermal annealing at temperatures varying from 900 to 1300 K, depending on the implanted ion species. A wide variety of experimental techniques was applied to monitor the evolution of defects in the target material and to investigate the

properties of the nanoclusters. These techniques include optical absorption spectroscopy (OAS), X-ray diffraction (XRD), transmission electron microscopy (TEM), neutron depth profiling (NDP), Rutherford backscattering spectrometry (RBS) and the positron beam analysis techniques (PBA) such as Doppler broadening (DB) and two-dimensional angular correlation of annihilation radiation (2D-ACAR). A special aspect of this work is the use of positron annihilation techniques as a complementary method to investigate embedded nanoclusters. If the positron affinity of the nanocluster material is lower than that of the host material, the vast majority of the positrons implanted in the material become trapped in the embedded nanoclusters, thereby becoming a self-seeking probe for nanoclusters. When a positron technique such as 2D-ACAR is used, the positrons reveal the electronic structure of the nanoclusters, which is very interesting when the structural and electronic properties of the nanoclusters start changing. The three-dimensional spatial confinement of the positron wavefunction in the nanoclusters is called *positron confinement*. Li in MgO is a very successfully investigated host-nanocluster system, as explained below.

Gaseous nanoclusters are usually referred to as bubbles and vacancy nanoclusters as cavities or nanovoids. The behaviour of gas atoms, gas bubbles and nanovoids in materials is often of technological interest; in particular, the behaviour of He atoms in ceramic oxides such as MgO, Al₂O₃ and MgAl₂O₄ is important. These materials are candidates for acting as an embedding matrix for the transmutation of actinides and must be able to resist long irradiations with α particles which come to rest in the form of He atoms. The formation and migration energies of the principal defects in MgO are determined by means of atomistic simulation calculations. The configuration of small vacancy clusters is also determined, and evidence is found that three-dimensional growth of vacancy clusters is energetically favoured over two-dimensional growth. This is in good agreement with experimental TEM observations which show that small, rectangularly shaped nanovoids are formed after accumulation of displacement damage in MgO. In He-implanted MgO the He is released at a temperature of 1325 K, leaving behind empty voids. The permeation energy (solution energy plus migration energy) for He in MgO is found from the atomistic simulation calculations as 3.6 eV. This is in good agreement with the permeation energy of 3.3 eV found from NDP experiments in combination with a stepwise annealing of the implanted crystals. In He-implanted Al₂O₃, the situation is quite different. The NDP/annealing experiments show that most of the He is released at a higher temperature of \sim 1750 K, which corresponds to a permeation energy of approximately 4.0 eV. The Doppler broadening results show that at this temperature the bubbles and nanovoids have already undergone shrinkage. The maximum bubble volume detected by means of Doppler broadening PBA was observed after annealing at a temperature of 1250 K. Solid Kr nanoclusters were also created by means of Kr ion implantation and subsequent annealing at 1100 K. By means of TEM it is found that the Kr nanoclusters are solid and have the fcc crystal structure. The lattice parameter of the Kr in

individual clusters is calculated from the moiré fringes observed in the TEM micrographs. It is found that the lattice parameter varies from 5.3 Å for small Kr clusters to 5.8 Å for the larger ones. These lattice parameters correspond to pressures of 2.5 down to 0.6 GPa, respectively (the smaller the cluster, the larger the pressure). Despite the very low value for the positron affinity of Kr (in comparison to that of MgO) as predicted in the literature, no evidence is found for positron confinement in Kr nanoclusters. One possible cause is that not enough electrons are available in the insulators MgO and Kr to establish equalisation of the Fermi levels of these two materials. In order to study the formation of nanovoids as a product of radiation damage, thin MgO(001) foils were irradiated with Kr ions in-situ in an electron microscope. Here the Kr ions completely pass the foil, leaving only displacement damage in the MgO. Accumulation of this displacement damage leads to the formation of nanovoids which can be formed in MgO without the presence of any gases.

For a long time metal nanoclusters have been examined, principally because of their linear and non-linear optical properties. Metallic nanoparticles give rise to optical absorption bands due to Mie surface plasmon resonance and show strongly nonlinear optical features. Another field of application where metal nanoclusters are used is in the development of memory devices. In this work, four metal nanocluster systems are studied: MgO:Li, MgO:Zn, MgO:Ag and MgO:Au. All nanoclusters exhibit Mie plasmon resonance. XRD and TEM investigations reveal that Ag and Au nanoclusters are very neatly embedded in the MgO host. The fcc Ag and Au clusters are in a cube-on-cube orientation relationship and have a small lattice mismatch with the rock-salt MgO. Li clusters larger than 40 nm have the bcc crystal structure and have a more complicated orientation relationship with the MgO. However, small Li clusters (smaller than 20 nm) adopt the unusual fcc crystal structure in order to fit better into the MgO matrix; again the orientation relationship is cube-on-cube and the lattice mismatch is small. Because of the very low positron affinity of Li compared to that of MgO, positrons can be very efficiently confined in the Li nanoclusters: it is observed that about 95 % of the positrons ending up in the ion implanted layer annihilate in Li nanoclusters, even though the atomic concentration of Li in that layer is only 1.3 at.%. This feature also enabled the department of Defects in Materials to investigate the Fermi surface of the unusual fcc Li crystal structure using the 2D-ACAR technique. It is found by means of optical absorption and NDP that the Li nanoclusters dissociate after annealing at a temperature of 1200 K. Zinc has the hcp crystal structure and is an example of a nanocluster that fits badly into the MgO matrix. It is observed by means of XRD and TEM that the *c*-axis of the Zn is aligned with one of the cubic MgO axes. The orientation relationship within the basal plane of the Zn is still to be determined. RBS and optical absorption spectroscopy reveal that the Zn dissolves into the MgO matrix upon annealing at a temperature of 1550 K.

Most of the recent scientific attention is dedicated to semiconductor nanoclusters. The electronic properties of semiconductor nanoclusters change already at relatively large cluster sizes (~ 10 nm) when compared to metal nanoclusters. One of the best-investigated features of semiconductor nanoclusters is the widening of the band gap with decreasing nanocluster size. For example, the band gap of the semiconductor CdSe can change from 1.8 eV for bulk CdSe to 2.5 eV for CdSe clusters with a size of 2 nm. In the present work, CdSe nanoclusters are created by sequential Cd and Se ion implantation and subsequent annealing at a temperature of 1300 K. Another size effect was encountered: TEM analysis revealed that CdSe nanoclusters smaller than 5 nm all have the rock-salt crystal structure, despite a large lattice mismatch with the MgO. The rock-salt structure is a high-pressure phase of CdSe. Nanoclusters larger than 10 nm clearly have a different crystal structure which is either the cubic sphalerite or the hexagonal wurtzite phase.

One disadvantage of the procedure of ion implantation and subsequent thermal annealing is the size distribution of nanoclusters. The department of Defects in Materials in Delft has started an ambitious project in collaboration with two German partners in order to create monodispersed nanoclusters of controlled size and position. With the aid of lithographic techniques a three-layer PMMA/Ge/PMMA mask is made, and e-beam pattern generation (EBPG) is used in combination with ion implantation in order to create implanted zones within small three-dimensional volumes of controlled size. The expectation is that upon thermal annealing, the implanted Au ions in such a small volume will converge into one single nanocluster. The preliminary results obtained using scanning electron microscopy (SEM) are very encouraging.

Overall, it can be concluded that nanoclusters consisting of open volume, noble gases, metals or semiconductors are easily created in ceramic oxides by ion implantation and subsequent thermal annealing. The small size of the nanoclusters and the interaction with the embedding matrix lead to many fascinating material properties, which are very different from the properties of bulk materials.

Samenvatting

Bulkmaterialen hebben eigenschappen die heel anders zijn dan die van atomen. Als atomen worden samengevoegd in een cluster, veranderen de materiaaleigenschappen totdat het aantal atomen zo groot is (in het algemeen meer dan 10^5) dat de eigenschappen van het cluster hetzelfde zijn als die van het bulkmateriaal. Het gebied waar de materiaaleigenschappen continu veranderen is een zeer interessant onderzoeksgebied. Grootte-afhankelijke materiaaleigenschappen zijn onder andere faseformaties, metaal-isolator overgangen, lineaire en niet-lineaire optische eigenschappen, en een verbreding van de energiekloof (*band gap*) van halfgeleiders. Als clusters worden geïmplementeerd in nanotechnologische *devices*, kunnen de materiaaleigenschappen worden veranderd door de grootte van de clusters aan te passen. Een geschikte manier om clusters te maken is door gebruik te maken van ionenimplantatie gevolgd door een thermische behandeling om het clusteren van de geïmplanteerde ionen te induceren. Nanoclusters zijn stabiel als ze zijn ingebed in vaste stoffen, en ionenimplantatie is een directe manier om dit te bewerkstelligen. Vaak worden keramische oxides (SiO_2 , MgO , Al_2O_3 , TiO_2) gebruikt als inbedmaterialen vanwege hun grote stabiliteit (hoog smeltpunt) en omdat ze optisch transparant zijn zodat de optische eigenschappen van het systeem makkelijk kunnen worden onderzocht. In dit werk gaat de aandacht zowel uit naar het creëren van nanoclusters met behulp van ionenimplantatie gevolgd door thermische verhitting, als naar het bestuderen van de eigenschappen van de nanoclusters.

Alle nanoclusters die in dit werk gepresenteerd worden zijn gecreëerd met behulp van ionenimplantatie en daaropvolgende thermische verhitting. De ionenimplantatieënergien varieerden van 30 keV voor lichte elementen tot 1.0 MeV voor zware elementen. De energien werden zo ingesteld om de ionen binnen een diepte van enkele honderden nanometers te implanteren, zodat gebruik gemaakt kon worden van positronenbundeltechnieken. De geïmplanteerde dosis was in de orde van 10^{16} ionen cm^{-2} . Clusters met nanometer-afmetingen worden gevormd na thermische verhitting op temperaturen variërend van 900 tot 1300 K,

afhankelijk van het soort geïmplantéerd ion. Een grote variëteit van experimentele technieken is gebruikt om de evolutie van defecten in het geïmplantéerde materiaal te volgen en om de eigenschappen van de nanoclusters te onderzoeken. Deze technieken zijn onder andere optische absorptie spectroscopie (OAS), Röntgendiffractie (XRD), transmissie elektronenmicroscopie (TEM), neutrondiepteprofilering (NDP), Rutherford terugverstrooiingspectrometrie (RBS) en positronenbundelanalysetechnieken (PBA) als Dopplerverbreiding (DB) en twee-dimensionale hoekcorrelatie van annihilatiestraling (2D-ACAR). Een speciaal aspect van dit werk is het gebruik van positronenannihilatietechnieken als een complementaire methode om ingebede nanoclusters te onderzoeken. Het overgrote merendeel van de positronen die in het materiaal zijn geïmplantéerd, wordt ingevangen in de ingebede nanoclusters als de positronenaffiniteit van het nanocluster materiaal lager is dan dat van het gastmateriaal. Daarbij worden de positronen een zelfzoekend onderzoeksdeeltje voor nanoclusters. Als een techniek zoals 2D-ACAR wordt gebruikt, leggen de positronen de elektronische structuur van de nanoclusters bloot, hetgeen interessant is als de structurele en elektronische eigenschappen van de nanoclusters beginnen te veranderen. De drie-dimensionale ruimtelijke beperking van de positronengolffunctie in de nanoclusters wordt positronenopsluiting (*positron confinement*) genoemd. Li in MgO is een gast-nanocluster systeem dat op die manier zeer succesvol is onderzocht, zoals hieronder wordt toegelicht.

Gasvormige nanoclusters worden doorgaans bellen genoemd, en vacatureclusters worden nanoholtes genoemd. Het gedrag van gasatomen, gasbellen en nanoholtes in materialen is vaak van technologisch belang, in het bijzonder is het gedrag van He atomen in keramische oxides zoals MgO, Al₂O₃ en MgAl₂O₄ belangrijk. Deze materialen zijn kandidaten om te fungeren als een inbeddingsmatrix voor de transmutatie van actinides en moeten lange bestralingen met α -deeltjes kunnen weerstaan, waarbij de α -deeltjes tot rust komen als He atomen. De formatie- en migratie-energiën van de basisdefecten in MgO werden bepaald met behulp van atomische simulatieberekeningen. De configuratie van kleine vacatureclusters is ook bepaald. Ook is er bewijs gevonden dat driedimensionale groei van vacatureclusters energetisch voordeliger is dan tweedimensionale groei, hetgeen in overeenstemming is met experimentele TEM waarnemingen die aantonen dat kleine, rechthoekige nanoholtes worden gevormd na accumulatie van verplaatssingsschade in MgO. In He-geïmplantéerd MgO komt het He vrij bij een temperatuur van 1325 K, waarbij lege holtes achterblijven. Met de atomistische simulatieberekeningen wordt een permeatie-energie (oplos-energie plus migratie-energie) voor He in MgO gevonden van 3.6 eV. Dit is in goede overeenstemming met de permeatie-energie van 3.3 eV die is verkregen uit NDP experimenten waarbij de geïmplantéerde materialen stapsgewijs werden verhit. In He-geïmplantéerd Al₂O₃ is de situatie heel anders. De NDP experimenten met stapsgewijze verhitting laten zien dat het meeste He vrijkomt bij een hogere temperatuur van ~1750 K, hetgeen overeenkomt met een permeatie-energie van ongeveer 4.0 eV. De Dopplerverbreidingsresultaten laten zien dat bij

deze temperatuur de bellen en nanoholtes al gekrompen zijn. Het grootste belvolume zoals gedetecteerd met behulp van Dopplerverbreiding PBA is waargenomen na verhitting op een temperatuur van 1250 K. Nanoclusters bestaande uit vast Kr zijn ook gemaakt met Kr ionenimplantatie gevolgd door verhitting op 1100 K. Uit de TEM resultaten blijkt dat de Kr nanoclusters vast zijn en de kubisch vlakgecentreerde (*fcc*) kristalstructuur hebben. De roosterconstante van het Kr in individuele clusters is berekend uit de *moiré fringes* waargenomen in de TEM opnames. De roosterconstante blijkt te variëren van 5.3 Å voor kleine Kr clusters tot 5.8 Å voor grote clusters. Deze roosterconstanten komen overeen met drukken van respectievelijk 2.5 en 0.6 GPa (hoe kleiner de cluster, hoe hoger de druk). Ondanks de hele lage waarde voor de positronenaffiniteit van Kr (in vergelijking met MgO) als voorspeld in de literatuur, is er geen aanwijzing gevonden voor positronenopsluiting in Kr nanoclusters. Een mogelijke oorzaak is het niet beschikbaar zijn van voldoende elektronen in de isolatoren MgO en Kr om de Fermi niveaus van deze twee materialen met elkaar in evenwicht te brengen. Om de vorming van nanoholtes als een produkt van stralingsschade te onderzoeken, werden dunne MgO(001) folies *in situ* in een elektronenmicroscop bestraald met Kr ionen. Hierbij gaan de Kr ionen helemaal door het folie heen, en blijft alleen stralingsschade achter in het MgO. Opeenhoping van deze stralingsschade leidt tot nucleatie en groei van nanoholtes die kunnen worden gevormd in MgO in afwezigheid van gassen.

Metaalnanoclusters zijn reeds lange tijd in onderzoek, voornamelijk vanwege hun lineaire en niet-lineaire optische eigenschappen. Metallische nanodeeltjes geven aanleiding tot optische absorptiebanden vanwege Mie oppervlakteplasmonresonantie en vertonen sterk niet-lineaire optische eigenschappen. Een ander toepassingsveld waar metaalnanoclusters worden gebruikt is de ontwikkeling van geheugenelementen. In dit werk worden vier metaalnanoclustersystemen bestudeerd: MgO:Li, MgO:Zn, MgO:Ag en MgO:Au. Alle nanoclusters vertonen Mie plasmonenresonantie. Uit XRD en TEM resultaten blijkt dat Ag en Au nanoclusters heel netjes ingebed zijn in het MgO gastmateriaal. De *fcc* Ag en Au nanoclusters zijn in een *cube-on-cube* oriëntatie-relatie en hebben een kleine mispassing met het MgO, dat de keukenzoutkristalstructuur heeft. Li clusters groter dan 40 nm hebben de kubisch lichaamsgecentreerde (*bcc*) kristalstructuur en hebben een ingewikkelder oriëntatie-relatie met het MgO. Kleine Li clusters echter (kleiner dan 20 nm) nemen de weinig voorkomende *fcc* kristalstructuur aan om beter in de MgO matrix te passen; de oriëntatie-relatie is weer *cube-on-cube* en de mispassing is klein. Vanwege de zeer lage positronenaffiniteit van Li ten opzichte van die van MgO kunnen positronen zeer effectief worden opgesloten in de Li nanoclusters: er wordt waargenomen dat ongeveer 95% van de positronen die terecht komen in de geïmplanteerde laag annihilieren in Li nanoclusters, terwijl de atomaire concentratie van Li in die laag slechts 1.3 at.% is. Dit verschijnsel heeft het mogelijk gemaakt voor de afdeling Defecten in Materialen om, gebruik makend van de 2D-ACAR techniek, het Fermi-oppervlak van de weinig voorkomende *fcc* Li kristalstructuur te

onderzoeken. Uit optische absorptie spectroscopie en NDP-metingen blijkt dat de Li nanoclusters dissociëren na verhitting op een temperatuur van 1200 K. Zink heeft de hexagonaal dichtgepakte (*hcp*) kristalstructuur en is een voorbeeld van een nanocluster dat slecht in de MgO matrix past. Met XRD en TEM wordt waargenomen dat de *c*-as van het Zn gelijkgericht is met een van de kubische MgO assen. De orientatie-relatie binnen het basale vlak van het Zn met het MgO moet nog worden bepaald. RBS en optische absorptiespectroscopie lieten zien dat het Zn oplost in de MgO matrix bij verhitting op een temperatuur van 1550 K.

De meeste wetenschappelijke aandacht gaat tegenwoordig uit naar halfgeleidernanoclusters. De elektronische eigenschappen van halfgeleidernanoclusters veranderen al bij relatief grote clusterafmetingen (~10 nm) in vergelijking met metaalnanostructuren. Een van de best onderzochte eigenschappen van halfgeleidernanoclusters is de verbreding van de energiekloof (*band gap*) met afnemende cluster grootte. De energiekloof van de halfgeleider CdSe bijvoorbeeld kan veranderen van 1.8 eV voor bulk CdSe tot 2.5 eV voor CdSe clusters met een afmeting van 2 nm. In dit werk worden CdSe nanoclusters gemaakt door opeenvolgende Cd en Se ionenimplantatie, gevolgd door verhitting op een temperatuur van 1300 K. Er werd een ander grootte-effect ontdekt: uit TEM analyse blijkt dat CdSe nanoclusters die kleiner zijn dan 5 nm alle de keukenzoutkristalstructuur hebben, ondanks een grote mispassing met het MgO. De keukenzoutstructuur is een hoge-druk fase van CdSe. Nanoclusters groter dan 10 nm hebben duidelijk een andere kristalstructuur die waarschijnlijk de kubische sfalerietstructuur is.

Een nadeel van de procedure van ionenimplantatie gevolgd door verhitting is de grootte-dispersie van de nanoclusters. De afdeling Defecten in Materialen is in samenwerking met twee Duitse partners aan een ambitieus project begonnen om monodisperse nanoclusters te maken waarbij controle bestaat over de grootte en de positie van de clusters. Langs lithografische weg wordt er een 3-laags masker van PMMA/Ge/PMMA, waarbij gebruik wordt gemaakt van elektronenbundelpatroongeneratie (EBPG). Hierbij worden geïmplanteerde gebieden gecreëerd in kleine, driedimensionale volumes met controle over de afmetingen. De verwachting is dat tijdens verhitting de Au-ionen die geïmplanteerd zijn in een dergelijk klein volume zullen convergeren tot een enkele nanocluster. De voorlopige resultaten die verkregen zijn met raster-elektronenmicroscopie (SEM) zijn veelbelovend.

Het geheel overziend kan worden geconcludeerd dat nanoclusters die bestaan uit open volume, edelgassen, metalen of halfgeleiders makkelijk kunnen worden gecreëerd in keramische oxides door ionenimplantatie gevolgd door thermische verhitting. De kleine afmetingen van de nanoclusters en de interactie met het inbeddingsmateriaal leiden tot vele fascinerende materiaaleigenschappen, die sterk verschillen van die van bulkmaterialen.

List of publications

2003

- M.A. van Huis, A. van Veen, A.V. Fedorov, F. Labohm and H. Schut, *Nucleation, growth and dissociation of He bubbles in Al₂O₃*, accepted for publication in Nucl. Instrum. Meth. Phys. Res. B.
- M.A. van Huis, A. van Veen, A.V. Fedorov, R.C. Birtcher, B.J. Kooi and J.Th.M. De Hosson, *In-situ TEM observation of gold nanocluster nucleation, coarsening and refining in Au implanted MgO(100) foils*, AIP Conf. Proc. **680** (2003) 735-740.
- M.A. van Huis, A. van Veen, H. Schut, S.W.H. Eijt, B.J. Kooi and J.Th.M. De Hosson, *Formation of CdSe nanoclusters in MgO by ion beam synthesis*, accepted for publication in Nucl. Instrum. Meth. Phys. Res. B (2003).
- M.A. van Huis, A. van Veen, H. Schut, S.W.H. Eijt, B.J. Kooi and J.Th.M. De Hosson, *Optical and structural properties of Li, Zn, Ag and Au nanoclusters embedded in MgO*, Reviews on Advanced Materials Science **4**, No. 1 (2003) 60-64.
- M.A. van Huis, A. van Veen, H. Schut, B.J. Kooi, J.Th.M. De Hosson, X.S. Du, T. Hibma and R. Fromknecht, *Formation and characterisation of Zn nanoclusters in MgO*, accepted for publication in Nucl. Instrum. Meth. Phys. Res. B (2003).
- M.A. van Huis, A. van Veen, H. Schut, B.J. Kooi and J.Th.M. De Hosson, *Formation of solid Kr nanoclusters in MgO*, Phys. Rev. B **67** (2003) 235409.
- H. Schut, H. van Gog, A. van Veen, M.A. van Huis and S.W.H. Eijt, *A positron beam study of hydrogen confined in nano-cavities in crystalline silicon*, accepted for publication in Nucl. Instrum. Meth. Phys. Res. B.
- P.M.G. Damen, A. van Veen, F. Labohm, H. Schut and M.A. van Huis, *Thermal annealing and defect evolution of helium in fully stabilised zirconia*, J. Nucl. Mater. **319** (2003) 65-73.

- S.W.H. Eijt, A. van Veen, P.E. Mijnaerends, C.V. Falub, H. Schut and M.A. van Huis, *Depth-selective 2D-ACAR and coincidence Doppler broadening investigation of embedded Au nanocrystals in MgO*, Conf. Proc. ICPA-13, accepted for publication in Mater. Sci. Forum.
- R. Fromknecht, G. Linker, L.M. Wang, S. Zhu, K. Sun, A. van Veen, M.A. van Huis, T. Weimann, J. Wang, J. Niemeyer, F. Eichhorn and T. Wang, *Crystalline nanosystems developed in TiO₂ by "conventional" and "patterned" Au ion implantation*, submitted to Nucl. Instrum. Meth. Phys. Res. B (2003).

2002

- M.A. van Huis, A.V. Fedorov, A. van Veen, C.V. Falub, S.W.H. Eijt, B.J. Kooi, J.Th.M. De Hosson, T. Hibma and R.L. Zimmerman, *Structural properties of Au and Ag nanoclusters embedded in MgO*, Nucl. Instrum. Meth. Phys. Res. B **191** (2002) 442-446.
- M.A. van Huis, A. van Veen, H. Schut, C.V. Falub, S.W.H. Eijt, P.E. Mijnaerends and J. Kuriplach, *Positron confinement in embedded lithium nanoclusters*, Phys. Rev. B **65** (2002) 085416.
- A. van Veen, M.A. van Huis, A.V. Fedorov, H. Schut, F. Labohm, B.J. Kooi and J.Th.M. De Hosson, *Nanocavity formation processes in MgO(100) by light ion (D, He, Li) and heavy ion (Kr, Cu, Au) implantation*, Nucl. Instrum. Meth. Phys. Res. B **191** (2002) 610-615.
- A.V. Fedorov, M.A. van Huis and A. van Veen, *A hot implantation study on the evolution of defects in He ion implanted MgO(100)*, Nucl. Instrum. Meth. Phys. Res. B **191** (2002) 452-455.
- C.V. Falub, P.E. Mijnaerends, S.W.H. Eijt, M.A. van Huis, A. van Veen and H. Schut, *Electronic structure and orientation relationship of Li nanoclusters embedded in MgO studied by depth-selective positron annihilation two-dimensional angular correlation*, Phys. Rev. B **66** (2002) 075426.
- C.V. Falub, P.E. Mijnaerends, S.W.H. Eijt, M.A. van Huis, A. van Veen and H. Schut, *Positron annihilation 2D-ACAR study of semi-coherent Li nanoclusters in MgO(100) and MgO(110)*, Nucl. Instrum. Meth. Phys. Res. B **191** (2002) 275-280.
- H. Schut, A. van Veen, A. Rivera, M.A. van Huis, A. Alba García, A.V. Fedorov and R. Escobar Galindo, *In situ mechanical, temperature and gas exposure treatments of materials combined with variable energy positron beam techniques*, Appl. Surf. Sci. **194** (2002) 239-244.
- S.W.H. Eijt, C.V. Falub, A. van Veen, H. Schut, M.A. van Huis and P.E. Mijnaerends, *Methods for defect characterisation in thin film materials by depth-selective 2D-ACAR*, Appl. Surf. Sci. **194** (2002) 234-238.

2001

- M.A. van Huis, A.V. Fedorov, A. van Veen, F. Labohm, H. Schut, P.E. Mijnaerends, B.J. Kooi and J.Th.M. De Hosson, *Lithium ion implantation effects in MgO(100)*, Mater. Sci. Forum **363-365** (2001) 448-450.
- van Veen, M.A. van Huis, A.V. Fedorov, H. Schut, C.V. Falub, S.W.H. Eijt, F. Labohm, B.J. Kooi and J.Th.M. De Hosson, *Lithium nanocluster formation in Li⁺-ion implanted MgO*, Mater. Res. Soc. Symp. Proc. **647** (2001) O11.24.
- A.V. Fedorov, A. van Veen, M.A. van Huis, H. Schut, B.J. Kooi, J.Th.M. De Hosson and R.L. Zimmerman, *Defects and nanocluster engineering in MgO*, AIP Conf. Proc. **576** (2001) 971-974.
- S.W.H. Eijt, C.V. Falub, A. van Veen, H. Schut, P.E. Mijnaerends, M.A. van Huis and A.V. Fedorov, *Ion-implantation generated nanovoids in Si and MgO monitored by high resolution positron beam analysis*, Mater. Res. Soc. Symp. Proc. **647** (2001) O14.11.

2000

- M.A. van Huis, A.V. Fedorov, A. van Veen, P.J.M. Smulders, B.J. Kooi and J. Th.M. De Hosson, *Copper implantation defects in MgO observed by positron beam analysis, RBS and X-TEM*, Nucl. Instrum. Meth. Phys. Res. B **166-167** (2000) 225-231.
- A.V. Fedorov, M.A. van Huis, A. van Veen and H. Schut, *Formation of gold nanoclusters in MgO by ion implantation at elevated temperatures*, Nucl. Instrum. Meth. Phys. Res. B **166-167** (2000) 215-219.
- G. Busker, M.A. van Huis, R.W. Grimes and A. van Veen, *Predicted vacancy cluster structures in MgO and their interaction with helium*, Nucl. Instrum. Meth. Phys. Res. B **171**, No. 4 (2000) 529-537.

Acknowledgements

First of all, I would like to thank my promoters, Prof. dr. A. van Veen and Prof. dr. J.Th.M. de Hosson, for their support and criticism throughout my PhD period. Tom, thank you for the continuous flow of fresh ideas and all the opportunities that you have offered me. You are much more a scientist than a manager, and you will always generate more ideas than your staff can handle. Jeff, thank you for making available all the expertise and equipment of your group in Groningen. The electron microscopy techniques became an indispensable tool in my research. From the members of the scientific staff of the department of Defects in Materials, I would like to thank Dr. H. Schut, Dr. S.W.H. Eijt and Dr. ir. P.E. Mijnaerends. Henk, thank you for all your help with the positron work and your no-nonsense, critical attitude in general. I would like to thank Stephan and Peter for their valuable input concerning the 2D-ACAR experiments and results. As a PhD student, I got the opportunity to collaborate with many scientists from various institutes. These scientists include:

- Prof. J.Th.M. de Hosson and Dr. B.J. Kooi from the Materials Science and Engineering Group, Department of Applied Physics, University of Groningen, The Netherlands. Bart, thank you for introducing me into the world of transmission electron microscopy (TEM). I would like to thank Uko Nieborg for teaching me the preparation techniques for cross-sectional TEM specimens.
- Prof. T. Hibma from the Inorganic Thin Films Group, Department of Applied Physics, University of Groningen, The Netherlands. Tjipke, thank you for your advice and for the XRD analyses that were performed on most of our nanocluster systems.
- Prof. R.W. Grimes and Dr. G. Busker from the Atomistic Simulation Group, Materials Science Department, Imperial College, London, UK. Your help was very important for gaining a fundamental understanding of the defect chemistry of MgO.
- Prof. R.C. Birtcher, Nonequilibrium Materials Group, Materials Science Department, Argonne National Laboratory (Argonne, IL, USA). I would like to thank Robert Birtcher

and the dedicated staff of the IVEM-TANDEM facility for giving us the opportunity to study ion implantation in-situ in the electron microscope.

- Dr. R. Fromknecht, Institut für Festkörperphysik, Forschungszentrum Karlsruhe, Eggenstein-Leopoldshafen, Germany: Rainer, thank you for being a partner in the lithography project and for your experimental contributions on RBS and work on TiO₂.
- Dr. J. Kuriplach, Department of Low Temperature Physics, Faculty of Mathematics and Physics, Charles University, Prague, Czech Republic. Jan has been very helpful for our research by calculating the positron affinity of MgO and of fcc and bcc Li. These results are presented in Section 4.1 of this thesis.
- Prof. D. Ila and Prof. R.L. Zimmerman, Alabama A&M University (Normal, AL, USA), where the 1 MeV Au and 600 keV Ag ions were implanted into MgO.

Ik zou Jan de Roode willen bedanken voor zijn veelzijdige inspanningen om de VARIAN implanter in elkaar te zetten en in goede conditie te houden. Bob Heijenga and Kees Westerduin, bedankt voor jullie hulp die ik kreeg als ik iets nodig had. Mijn meeste experimentele vaardigheden heb ik geleerd van mijn vriend en collega Alexander Fedorov. Sasha, dank voor alles. Verder wil ik alle studenten, promovendi, postdocs en technici van de groep Defecten in Materialen bedanken. Ik ben mijn ouders dankbaar voor alle steun die ze hebben gegeven gedurende mijn studieperiode. Lieve Heleen, er zijn dingen veel mooier, stralender en belangrijker dan wetenschap, en daar ben jij de vervolmaking van. Dank je voor je kritische houding en je inzicht.

Curriculum Vitae

Marijn Arnout van Huis was born in Managua, Nicaragua, on April 24, 1975. After living in Nicaragua for five years, in The Netherlands for three years and in Niger, Africa, for another three years, he returned to The Netherlands for secondary and academic education. An MSc degree in Applied Physics was obtained in September 1999 at the Delft University of Technology in The Netherlands. The final-year project was conducted in the Defects in Materials Group, which at the time was a section of the department of Reactor Physics of the Interfaculty Reactor Institute of the Delft University of Technology. He started his PhD project in November 1999 in the same Defects in Materials group.

